Numerical Hydrodynamics in Strong-Field General Relativity

William Edward East

A Dissertation
Presented to the Faculty
of Princeton University
in Candidacy for the Degree
of Doctor of Philosophy

Recommended for Acceptance
by the Department of
Physics
Adviser: Frans Pretorius

September 2013

Abstract

In this thesis we develop and test methods for numerically evolving hydrodynamics coupled to the Einstein field equations, and then apply them to several problems in gravitational physics and astrophysics. The hydrodynamics scheme utilizes high-resolution shock-capturing techniques with flux corrections while the Einstein equations are evolved in the generalized harmonic formulation using finite difference methods. We construct initial data by solving the constraint equations using a multigrid algorithm with free data chosen based on superposing isolated compact objects.

One application we consider is the merger of black hole-neutron star and neutron star-neutron star binaries that form through dynamical capture, as may occur in globular clusters or galactic nuclei. These systems can merge with non-negligible orbital eccentricity and display significant variability in dynamics and outcome as a function of initial impact parameter. We study the electromagnetic and gravitational-wave transients that these mergers may produce and their prospects for being detected with upcoming observations.

We also introduce a numerical technique that allows solutions to the full Einstein equations to be obtained for extreme-mass-ratio systems where the spacetime is dominated by a known background solution. This technique is based on using the knowledge of a background solution to subtract off its contribution to the truncation error. We use this to study the tidal effects and gravitational radiation from a solar-type star falling into a supermassive black hole.

Finally, we utilize general-relativistic hydrodynamics to study ultrarelativistic black hole formation. We study the head-on collision of fluid particles well within the kinetic energy dominated regime (Lorentz factors $\gamma = 8 - 12$). We find that black hole formation does occur at energies a factor of a few below simple hoop conjecture estimates. We also find that near the threshold for black hole formation, the collision

leads to two separate apparent horizons which then merge. Both of these phenomena can be understood in terms of a gravitational focusing effect.

Acknowledgements

I am indebted to many for their support during my time at Princeton. To begin with, I want to thank my advisor Frans Pretorius for his guidance and encouragement, and for in general exemplifying how to go about being a successful physicist. I am also grateful to Branson Stephens for guiding me through my first foray into numerical hydrodynamics, to Fethi Ramazanoglu for being an excellent research partner, and Sean McWilliams for fruitful collaboration and career advice, as well as to the rest of the research group, Hans Bantilan, Theo Brasoveanu, and Ben Lackey. I would like to thank Jim Stone for being a reader for this thesis, and the other members of my thesis committee, Jim Peebles and Suzanne Staggs. I also want to thank my fellow classmates, especially the old Red Hill Road gang, for keeping things interesting and making the transition to being a graduate student in New Jersey a pleasant one. Finally, throughout it all I have been bolstered by the love and support of my mother, my brother, and Annie.

During my graduate studies I was supported by an NSF Graduate Research Fellowship under grant DGE-0646086. The work presented here was made possible through computational resources provided by Teragrid/XSEDE under grant TG-PHY100053 as well as by the Woodhen and Orbital clusters at Princeton University.

Relation to Previously Published Work

The material in this thesis is based on previously published work. Chap. 2 comes from [1] written in collaboration with Frans Pretorius and Branson Stephens; Chap. 3 from [2] written in collaboration with Fethi Ramazanoglu and Frans Pretorius; Chap. 4 comes from [3] and incorporates some material from [4], both written in collaboration with Frans Pretorius and Branson Stephens; Chap. 5 from [5] written in collaboration with Frans Pretorius; Chap. 6 from [6] written in collaboration with Sean McWilliams, Janna Levin, and Frans Pretorius; Chap. 7 from [7] written in collaboration with Frans Pretorius; and Chap. 8 from [8] written in collaboration with Frans Pretorius. Material from this thesis was presented by the author at the following conferences: the 2011 Eastern Gravity Meeting and the 2011, 2012, and 2013 APS April Meetings.

To the memory of my father.

Contents

Chapter 1

Introduction

In this chapter we begin by briefly enumerating some of the topics in physics and astrophysics that can be addressed using general-relativistic hydrodynamics, emphasizing the particular applications addressed in this thesis. We also review the equations of general-relativistic hydrodynamics in the form used here, and then outline the remainder of the thesis.

1.1 Motivation

Since shortly after its formulation by Albert Einstein in 1915-1916, general relativity has been the reigning theory of gravity. Yet despite being around for nearly a century, most of our evidence for the veracity of general relativity comes from the weak field regime: from solar system tests or indirect evidence of gravitational waves [9]. The theory still remains largely untested in the strong-field regime where spacetime is highly curved and very dynamic. One of the most promising avenues to explore this regime is through the direct detection of gravitational waves. Several ground-based gravitational wave detectors utilizing laser interferometers including LIGO [10], VIRGO [11], and GEO600 [12] have been built and run. Though no detections have yet been made [13], these observatories are currently being upgraded to "advanced"

sensitivity and are expected to begin taking data in the next few years. Pulsar timing arrays are another promising method for detecting gravitational waves that is currently being pursued [14, 15] and there have also been proposals for a space-based laser interferometer gravitational wave detector to be launched in the coming decades [16].

The primary target for ground-based gravitational wave detectors is the merger of stellar mass compact object binaries: black hole-black hole, black hole-neutron star, and neutron star-neutron star binaries. Event rate estimates for these mergers are based on population synthesis models and have large uncertainties, but they indicate that Advanced LIGO should see somewhere between $\sim$ 1-1000 events per year [17]. The lack of analytical solutions of the general-relativistic field equations describing the mergers of these systems makes numerical methods necessary to understand them. Because gravitational wave signals are expected to have small magnitudes compared to the noise in the upcoming generation of detectors, match-filtering techniques which utilize waveform templates to pick the signal out of the noise will probably be necessary. This makes numerical solutions of the field equations necessary not only for interpreting gravitational wave signals, but potentially also for detecting them.

This thesis is concerned with general-relativistic systems that have matter, e.g. black hole-neutron star and neutron star-neutron star binaries, which are of interest for several reasons beyond the exploration of strong-field general relativity. It is thought that the cores of neutron stars contain matter exceeding nuclear density (3×10^{14} gm/cm^3) by a factor of a few. These densities are far beyond the reach of terrestrial experiments and there is considerable uncertainty about the properties of matter in this regime. It has been speculated that the cores of neutron stars could contain boson condensates, hyperons, or possibly even strange quark matter [18]. Since the properties of super-nuclear density matter, encoded in the neutron star's equation of state, determine the star's compactness, maximum mass,

tidal deformability, etc., observations of neutron star mergers could reveal crucial information about nuclear density physics. Studies of these effects in binary mergers indicate that the equation-of-state may be encoded in gravitational wave signals at a detectable level [19, 20, 21, 22, 23, 24, 25, 26, 27, 28, 29] (though percent-level characterization of equation-of-state parameters may not be possible until the next generation of detectors are developed).

Systems with matter also have the potential to source observable electromagnetic transients which might be seen as counterparts to gravitational wave signals. Indeed, there are already efforts underway to trigger searches for electromagnetic transients using potential gravitational wave sources [30, 31]. Merging black hole-neutron star or neutron star-neutron star binaries are one of the leading candidates for the progenitors of short gamma-ray bursts (SGRBs) [32, 33, 34]. In the hypothesized scenario, the merger would create a black hole surrounded by an accretion disk which would subsequently power a jet. A compact-object-merger origin of short gamma-ray bursts is consistent with the duration and millisecond variation observed in the signal, as well as the fact that SGRBs do not trace star formation [35]. However, the case is still inconclusive, which is something that the coincident detection of a gravitational wave and short gamma-ray burst could change. Though simulating the actual burst event is beyond the scope of this work, the properties of an accretion disk resulting from a compact object merger — and hence its viability to launch such a burst — will depend crucially on the strong-field dynamics of the merger, and thus is something which should be addressed by general-relativistic hydrodynamic simulations.

Besides short gamma-ray bursts, the high-energies of compact object mergers could power a number of other electromagnetic transients. During the merger process, some material will become unbound and ejected from the system. As the ejecta decompresses, it will undergo the r-process building up heavy elements which then decay by nuclear fission, sourcing infrared/optical emissions [36, 37, 38]. The collision

of this ejected material with the interstellar medium could also potentially produce radio wave emissions. Again, the amount of ejected material will depend crucially on the details of the merger dynamics [39]. Compact object mergers could also produce electromagnetic transients from magnetic field effects [40, 41] or flaring from the neutron star's crust cracking [42]. With a number of transient surveys underway or scheduled to come on-line, including PTF [43], Pan-STARRS [44], and LSST [45], understanding what these potential transients indicate about the strong-field dynamics which gave rise to them will be important.

Another target system for transient surveys in which strong-field gravity is important is tidal disruption events. Supermassive black holes with masses of roughly 10^5 to 10^{10} $M_\odot$ are thought to reside in the centers of most galaxies (including our own) and, on occasion, stars pass close enough to them to be captured and tidally disrupted [46]. The resulting accretion from the disrupted stellar material is conjectured to be the source of a number of candidate events observed in the optical through the X-ray bands [47, 48, 49, 50, 51, 52, 53, 54, 55, 56, 57, 58, 59, 60]. For solar-type stars encountering black holes of 10^7 to 10^8 solar masses, tidal disruption will occur near the innermost stable circular orbit of the black hole. These systems will therefore be sensitive to strong-field effects, including zoom-whirl type behavior and the spin of the black hole, which may imprint the flares we observe from such events. Hence, general-relativistic hydrodynamics can also contribute to the understanding of these systems.

There are numerous other examples of astrophysical systems that are being studied using general-relativistic hydrodynamics, including black hole accretion tori [61, 62, 63, 64], NS-white dwarf mergers [65], white dwarf-intermediate black hole disruption events [66], and core-collapse supernovae [67]. As the field matures this list will certainly grow.

Even beyond gravitational wave astronomy and high-energy astrophysics, there are a host of problems in theoretical general relativity and high-energy physics that can be addressed using general-relativistic hydrodynamics. This includes studying the ADS-CFT/gauge-gravity duality [68, 69, 70] and critical phenomena in gravitational collapse [71]. One example which we address here is the possibility of forming black holes in ultrarelativistic collisions. If two particles collide at sufficiently high speeds, they should form a black hole, because as the speeds of the particles approach the speed of light (in the center-of-mass frame) their kinetic energy will become arbitrarily large. According to general relativity, kinetic energy, like all other forms of energy, gravitates. Besides being an interesting theoretical topic in general relativity, it has been suggested that if our universe has small or warped extra dimensions [72, 73, 74] black hole formation could occur in proton collisions at the Large Hadron Collider [75, 76], and in the ultrarelativistic collision of cosmic rays with the Earth's atmosphere [77].

The numerous and diverse applications motivate the development of general and robust methods for simulating general-relativistic hydrodynamics. In the remainder of this chapter, we briefly review the Einstein equations and the general-relativistic hydrodynamic equations and outline the remainder of this thesis.

Note that throughout this thesis, unless otherwise stated, we will make use of geometric units where $G = c = 1$.

1.2 Einstein equations

In Einstein's theory of general relativity, gravity is described in terms of the geometry of spacetime. Spacetime is represented by a Lorentzian manifold with metric g_{ab} where distances are measured by the line element

$$ds^2 = g_{ab} dx^a dx^b \ . \tag{1.1}$$

The Christoffel connection Γ^a_{bc} for the spacetime manifold is given by

$$\Gamma^a_{bc} = \frac{1}{2} g^{ad}(\partial_b g_{cd} + \partial_c g_{bd} - \partial_d g_{bc}) \tag{1.2}$$

and can be used to define the covariant derivative on an arbitrary vector field V^a as

$$\nabla_a V^b = \partial_a V^b + \Gamma^b_{ac} V^c \ . \tag{1.3}$$

Spacetime curvature is encoded in the Riemann tensor $R^a{}_{bcd}$ which is usually defined in terms of the commutator of the covariant derivative operator:

$$(\nabla_a \nabla_b - \nabla_b \nabla_a) V^c = R^c{}_{dab} V^d \ , \tag{1.4}$$

i.e., the difference from changing the order when parallel transporting the vector field in first one direction and then another. Using (1.2), the Riemann tensor can then be written as

$$R^a{}_{bcd} = \partial_c \Gamma^a_{bd} - \partial_d \Gamma^a_{bc} + \Gamma^a_{ce} \Gamma^e_{db} - \Gamma^a_{de} \Gamma^e_{cb} \ . \tag{1.5}$$

Now the spacetime curvature in which gravity is manifested is governed by the field equations:

$$R_{ab} = 8\pi T_{ab} - 4\pi T g_{ab}. \tag{1.6}$$

Here T_{ab} is the stress-energy tensor of the matter, T is its trace, and $R_{ab} := R^c{}_{acb}$ is the Ricci tensor formed by contracting the Riemann tensor. Hence the field equations represent a set of 10 second-order partial differential equations for the metric. However, in this form, they have no fixed characteristic since they are merely statements about the geometry of 4-dimensional spacetime and are invariant under diffeomorphism.

The particular formulation of the Einstein field equations that we use in this thesis is the generalized harmonic formulation [78, 79] (c.f. BSSN [80, 81], another

popular formulation). In this formulation, we require the coordinates to satisfy an inhomogeneous wave equation $\Box x^a = H^a$ where H^a are specified functions (called the source functions) which encode the coordinate degrees of freedom. We can use these source functions to rewrite (1.6) as

$$g^{cd}\partial_c\partial_d g_{ab} + \partial_b g^{cd}\partial_c g_{ad} + \partial_a g^{cd}\partial_c g_{bd} + \partial_a H_b + \partial_b H_a - 2H_d\Gamma^d_{ab} + 2\Gamma^c_{db}\Gamma^d_{ca} = -8\pi(2T_{ab} - g_{ab}T). \quad (1.7)$$

We promote H^a to independent functions and specify additional equations for them. For example, the simplest choice would be the harmonic gauge, $H^a = 0$. In this work we only make use of gauge conditions where H^a is specified as some function of the metric and coordinates, though in general more complicated evolution equations are possible. As long as the evolution equations for the source functions and matter take a suitable form (i.e. do not change the principle part from being the first term), (1.7) is manifestly hyperbolic. In this formulation, we turn the Einstein equations into a Cauchy evolution problem by specifying initial values for the variables $\{g_{ab}, \partial_t g_{ab}, H_a, \partial_t H_a\}$ and evolving them forward in time.

Of course, this only gives a valid solution to the Einstein equations as long as the constraint $H^a = \Box x^a$ always holds. In fact, one can show using the Bianchi identity and conservation of stress-energy that the quantity $C^a := H^a - \Box x^a$ itself satisfies the evolution equation

$$\Box C^a = -R^a{}_b C^b. \quad (1.8)$$

This means that if on some initial time slice $C^a = 0$ (which we ensure by setting $H^a = \partial_b(\sqrt{-g}g^{ab})/\sqrt{-g} = \Box x^a$ initially, where g is the determinant of the metric) and $\partial_t C^a = 0$, then while evolving with (1.7), $C^a = 0$ will be satisfied for all time. The requirement that $\partial_t C^a = 0$ is actually equivalent to the standard Hamiltonian and momentum constraints which are obtained by projecting the Einstein field equa-

tions onto a time slice. In Chap. 3 we will elaborate on the constraint equations and how they can be cast as a set of coupled elliptic differential equations and solved numerically. Thus, evolving the Einstein equations in the generalized harmonic formulation entails the following: construct initial values for $\{g_{ab}, \partial_t g_{ab}\}$ that satisfy the constraint equations with the desired matter sources; evolve $\{g_{ab}, \partial_t g_{ab}\}$ using (1.7); in tandem evolve H^a according to an appropriate gauge choice; and evolve the matter according to its equations of motion.

1.3 General-relativistic hydrodynamics

For this thesis, we are concerned with coupling hydrodynamic matter to dynamical spacetime, primarily to model the bulk motion of stars. A hydrodynamical description is appropriate for a medium where the characteristic length scale of interest is much larger than the mean free path of particles to collide with their neighbors. For a perfect fluid we assume that for every fluid element there is a local inertial frame comoving with the element where the particles in the fluid element are in thermodynamic equilibrium and appear the same in every direction. This means that we can assign a single velocity and isotropic pressure to each fluid element. The stress-energy tensor for a perfect fluid is given in terms of the intrinsic fluid quantities ρ, the rest-mass density; P, the pressure; and ϵ, the specific energy as

$$T^{ab} = (\rho + \rho\epsilon + P)u^a u^b + g^{ab}P \ . \tag{1.9}$$

where u^a is the four-velocity (normalized so that $u^a u_a = -1$).

For matter consisting of a single fluid, the first part of the hydrodynamic evolution equations follows directly from the conservation of stress-energy,

$$\nabla_a T^{ab} = 0 \ . \tag{1.10}$$

The other part comes from conservation of rest-mass (or equivalently baryon number):

$$\nabla_a(\rho u^a) = 0 \ . \tag{1.11}$$

The final piece of information needed to close this system of equations is an equation of state which gives the pressure as a function of rest-mass density and specific energy, $P(\rho, \epsilon)$. In a hydrodynamical model of a neutron star, for example, this would encode the microphysical properties of the matter. Hence (1.10) and (1.11) give us five evolution equations for five hydrodynamic degrees of freedom.

The approach taken by most schemes (including the one presented in this thesis) for numerically evolving general-relativistic hydrodynamics is not to directly evolve the intrinsic fluid variables, but to instead introduce new variables that allow (1.10) and (1.11) to be rewritten in a form that more resembles the usual Newtonian Euler fluid equations. This idea has a long history going back to Wilson [82, 83]. The particular form of the hydrodynamic equations used in this thesis can be obtained as follows [84]. Using the identity that for an arbitrary vector field V^a, $\nabla_a(V^a) = \partial_a(\sqrt{-g}V^a)/\sqrt{-g}$, (1.11) can be rewritten as:

$$\partial_t(D) + \partial_i(Dv^i) = 0. \tag{1.12}$$

where the new variable is $D := \rho\sqrt{-g}u^t$, $v^i = u^i/u^t$ is the coordinate velocity, and the index i sums only over spatial directions. Something similar can be done with (1.10) to obtain

$$\partial_t S_a + \partial_i \left(\sqrt{-g}T^i{}_a\right) = \frac{1}{2}\sqrt{-g}T^{bc}\partial_a g_{bc} \tag{1.13}$$

where the new evolution variables encoding the fluid energy-momentum are $S_a := \sqrt{-g}T^t{}_a$. However, (1.13) contains source terms since the fluid can exchange energy and momentum with gravity.

Such a choice of evolution variables allows the extensive technology that has been developed for numerically simulating such systems to be imported to the general-relativistic case. Since (1.12) and (1.13) do not contain derivatives of fluid quantities in their source terms, the fluid evolution can be treated as a result of fluxes of conserved quantities passing between fluid cells in the numerical domain, thus numerically enforcing the conservative nature of the equations. We can also carry over from Newtonian hydrodynamics so called "high-resolution shock-capturing" techniques for handling discontinuities (i.e. shocks) that generically develop during evolution [85]. These techniques are based on calculating the fluxes at the interfaces of fluid cells by treating the fluid quantities as constant on either side of the interface with a discontinuity at the interface itself and then either exactly or approximately solving this problem (referred to as a Riemann problem) using the characteristic structure of the fluid equations. We will elaborate on this in Chap. 2.

1.4 Outline of thesis

The rest of this thesis is as follows. In Chap. 2 we describe a code for evolving hydrodynamics in full general relativity using the generalized harmonic formulation for the gravity and using high-resolution shock-capturing techniques and a conservative formulation of the hydrodynamic equations. One notable aspect of this code is the use of Berger-Collela style flux corrections to allow adaptive mesh refinement to be used without breaking the conservative nature of the hydrodynamics scheme. As noted above, creating initial data for general-relativistic evolutions requires solving the constraint part of the Einstein field equations, a set of coupled elliptic equations. In Chap. 3 we describe an initial data solver that uses a multigrid algorithm with mesh refinement and was designed to be applicable to generic setups through the use of a scheme based on superposing compact objects without assuming symmetries.

As a major application of these methods we study a particular subclass of compact object binaries that form through dynamical capture in dense stellar regions, such as globular clusters or galactic nuclei, and hence may merge with non-negligible orbital eccentricity. In Chap. 4 we present simulations of dynamical capture black hole-neutron star mergers, including an exploration the effects of black hole spin and neutron star equation of state, and in Chap. 5 we follow with a study of binary neutron star mergers. These systems are shown to exhibit large variability with impact parameter in the resulting dynamics and outcome, and in some cases make promising sources for potential observables like short gamma-ray bursts, r-process powered transients, or, in the case of binary neutron stars, precursor flaring events from crust-cracking during non-merger close encounters. Using the results from full numerical simulations as a guide, in Chap. 6 a model is presented for complete gravitational wave signals from highly eccentric mergers. This is used to explore the detectability of these signals by ground-based observatories, as well as to show how such signals may be missed by standard data analysis techniques.

In Chap. 7 a novel modification of the methods of Chap. 2 is presented that allows the accurate and efficient simulation of systems with a large disparity in mass, such as in stellar disruption events. The modification is based on a background error subtraction technique where the knowledge of the background solution is used to subtract off its contribution to the truncation error, while still evolving the full Einstein equations. This method is used to efficiently achieve high accuracy in simulations of a solar-type star falling into a supermassive black hole.

The same tools of general-relativistic hydrodynamics used for astrophysical simulations are applied in Chap. 8 to the quite different regime where kinetic energy makes up approximately 90% of the total mass/energy of the spacetime (i.e. Lorentz factors of $\gamma \approx 10$) to study head-on collisions of ultrarelativistic fluid particles. The simulations show that a focusing effect, where each boosted particle acts like a gravi-

tational version of a lens on the other particle, can lower the threshold for black hole formation compared to earlier estimates by causing matter to be focused into two trapped regions which then merge into a single black hole.

Finally, in Chap. 9 we conclude and summarize some directions for future work.

Chapter 2

Hydrodynamics in full general relativity

2.1 Introduction

As mentioned in Chap. 1, a new generation of gravitational wave detectors (LIGO [10], GEO [86],TAMA [87], and VIRGO [11]) are now operational, and within the next few years are expected to reach sensitivities that will allow observations of the Universe in gravitational radiation for the first time. The prime targets of these observations are compact object (CO) binaries composed of combinations of black holes (BHs) and neutron stars (NSs). Besides this, compact object mergers involving NSs are also possible progenitors for short-gamma-ray bursts (SGRBs) [32, 33, 34] and other electromagnetic and neutrino counterparts [88]. Thoroughly modeling systems like these would require evolution of the spacetime, the photon and neutrino radiation fields, and the magnetized, relativistic fluid. Even a minimalistic treatment, with the Einstein equations coupled to the equations of relativistic hydrodynamics, represents a complex, nonlinear system of partial differential equations. Numerical simulations are thus essential for exploring such strong-field, dynamical systems. There is a long

history of adapting successful techniques for simulating Newtonian hydrodynamics to relativistic and general relativistic fluids which we will not attempt to summarize (see [89] for a review of general relativistic hydrodynamics). Instead, we will briefly attempt to place the code described here in the context of other recent codes developed for fluids on evolving spacetimes.

Several of these codes [90, 91, 92, 93, 94] solve the field equations in the BSSN formulation [80, 81]. The remainder [95, 96] use the generalized-harmonic formulation [78, 79] which we also employ; unlike our code, however, these groups convert to a fully first-order formulation [97]. Most groups use finite-difference methods for the metric evolution and a conservative, high-resolution shock-capturing (HRSC) scheme for the hydro evolution; these unigrid algorithms are then interfaced with some sort of adaptive mesh refinement (AMR). A notable exception for the metric evolution is [95], which employs pseudospectral methods for the metric and then interpolates to a finite-volume grid for the fluid.

Some groups have implemented the MHD equations in full GR; since these codes all make use of conservative HRSC methods, they may be principally differentiated by how they meet the challenge of preserving the $\nabla \cdot \mathbf{B} = 0$ constraint. (A straightforward finite-difference evolution of the magnetic field would generically lead to magnetic monopoles and, hence, unphysical behavior.) `WhiskyMHD` employs constrained transport [92] for this purpose, which preserves the constraint to machine accuracy, whereas the code of [98] uses hyperbolic divergence cleaning. Constrained transport, however, requires special interpolation at refinement level boundaries in order to preserve the constraint. The Illinois group found that a vector-potential formulation of the MHD equations works well when coupled to AMR [99]. This is because the constraint is preserved by construction with the vector-potential, even with the restriction and prolongation operations of AMR (see also [100] for a thorough examination of the electromagnetic gauge condition). Studies indicate that magnetic fields

do not significantly affect the gravitational dynamics of CO mergers (see e.g. [98]), but they could be critical for understanding EM counterparts including the possible formation of a SGRB engine. A new method to treat the MHD equations was recently presented in [40], where ideal MHD is used in high matter density regions (e.g. inside a NS), while the force-free approximation is used elsewhere (e.g. the magnetosphere of a NS). The authors applied the method to study the collapse of magnetized hypermassive NSs (which could be formed via binary NS mergers) and suggested that intense EM outbursts could accompany such events.

Besides MHD, the other major advances in the physical model for numerical relativity codes have been in the arena of microphysics. While the $\Gamma = 2$ EOS was the community standard for quite some time, most codes now allow for a nuclear theory-based EOS [101, 102] and/or use various parametrized, piecewise polytropic EOSs inspired by the range of plausible nuclear EOSs [103, 104]. These advances in EOS description primarily affect the cold NS structure, but the group developing the `SACRA` code has also begun to account for neutrino transport via a simplified leakage scheme [21, 105]. The same group has also made available a formulation for a more accurate truncated moment scheme with a variable Eddington factor closure [106], which shows much promise for numerical relativity simulations with neutrino physics beyond the leakage approximation.

Another category of GR hydrodynamics codes employs the conformal-flatness approximation, which is particularly useful when supernova simulations are the target application. An example is CoCoNuT/VERTEX, which incorporates relativistic hydrodynamics, conformally flat gravity, and ray-by-ray neutrino transport [107]. The code of [108] employs a similar scheme for hydrodynamics and gravity but adds a test magnetic field; this code has been used to study the magnetorotational instability in supernovae.

Newtonian (and semi-Newtonian) [109, 110], conformally flat [111, 112], and fixed-background [113] SPH codes represent an important, orthogonal approach to studying CO interactions. SPH has an advantage over Eulerian schemes when a large range of spatial scales is involved. Such a situation may arise in CO mergers when material is stripped from a star in a tidal interaction and forms an extended tail. On the other hand, Eulerian codes are the standard approach when strong shocks are present, as would arise in binary NS mergers or disk circularization. (Recent progress has been made, however, in applying SPH to situations with relativistic shocks [114].) In addition, SPH has not (to our knowledge) yet been coupled to a code which evolves the full Einstein equations. Nonetheless, comparisons between Eulerian and SPH results could prove very useful on a problem-by-problem basis to characterize the errors in both methods.

Though current efforts in GR simulations involving matter tend to focus on increasingly complex physical models, there remain many unanswered questions in the astrophysics of compact objects that can be addressed with a code which solves the Einstein equations coupled to perfect fluid hydrodynamics. We have thus focused our code development on hydrodynamics in full GR, while maintaining a flexible infrastructure to accommodate additional physics modules in the future. We evolve the field equations in the generalized-harmonic formulation using finite differences. The fluid is evolved conservatively using one of several different shock-capturing techniques we test here. We have also implemented the hydrodynamical equations in a manner that is independent of EOS. We make use of AMR by dynamically adapting the mesh refinement hierarchy based on truncation error estimates of a select number of the evolved variables. We also utilize Berger and Colella [115] style flux corrections (also known as "refluxing") in order to make the use of AMR compatible with the conservative nature of the hydrodynamic equations. Though AMR flux corrections have been implemented in other astrophysical hydrodynamics codes (such as Athena [116],

CASTRO [117], `Enzo` [118], and FLASH [119]), to our knowledge this algorithm has not been used previously for hydrodynamics simulations in full general relativity.[1] A further noteworthy feature of our implementation is that we store corrections to the corresponding fluid quantity integrated in the volume of a given cell instead of the flux, allowing for easy implementation within a computational infrastructure that supports cell-centered but not face-centered distributed data structures.

In the remainder of this chapter we outline our computational methodology for simulating hydrodynamics coupled to the Einstein field equations and describe tests of this methodology. In Sec. 2.2 we review the generalized-harmonic approach to solving the field equations and present our methods for conservatively evolving a perfect fluid coupled to gravity, including our method for inverting the conserved quantities to obtain the primitive fluid variables and the implementation of flux corrections to enforce the conservation of fluid quantities across AMR boundaries. In Sec. 2.3 we present simulation results which test these methods, highlight the strengths and weaknesses of various shock -capturing techniques, and demonstrate the utility of the flux correction algorithm.

2.2 Computational methodology

In this section we begin by explaining the basic equations and variables we use to numerically evolve the Einstein equations in Sec. 2.2.1 and then discuss the conservative formulation of the hydrodynamics equations that we use in Sec. 2.2.2. The evolution of conserved fluid variables necessitates an algorithm for inverting these quantities to obtain the primitive fluid variables which we present in Sec. 2.2.3. Finally in Sec. 2.2.5 we present the details of our algorithm for AMR with flux corrections.

[1] Note that "flux correction" here refers to the enforcement of conservation at AMR boundaries, not the recalculation of fluxes with a more dissipative scheme to preserve stability as in Athena [120].

2.2.1 Solution of the Einstein equations

We solve the field equations in the generalized-harmonic formulation [78, 79] where we fix the coordinate degrees of freedom by specifying the evolution of the source functions $H^a = \Box x^a$. In this form the evolution equation for the metric, g_{ab}, becomes manifestly hyperbolic:

$$g^{cd}\partial_c\partial_d g_{ab} + \partial_b g^{cd}\partial_c g_{ad} + \partial_a g^{cd}\partial_c g_{bd} + 2H_{(a,b)} - 2H_d\Gamma^d_{ab} + 2\Gamma^c_{db}\Gamma^d_{ca} = -8\pi(2T_{ab} - g_{ab}T) \tag{2.1}$$

where Γ^a_{bc} is the Christoffel symbol, T_{ab} is the stress-energy tensor, and T is its trace. We evolve the metric, the source functions, and their respective time derivatives using fourth-order Runge-Kutta where the spatial derivatives are calculated using fourth-order accurate finite-difference techniques. In other words, we have reduced the evolution equations to first order in time so that there are 28 "fundamental" variables $\{g_{ab}, H_a, \partial_t g_{ab}, \partial_t H_a\}$, but we directly discretize all first and second spatial gradients without the introduction of additional auxiliary variables.

Analytically one can show [121] that if one begins with initial data that satisfies the Hamiltonian and momentum constraints, initially set $H^a = \Box x^a$, and then evolve the metric according to (2.1) and the source functions according to some specified differential equations, then the constraint equation $H^a - \Box x^a = 0$ will be satisfied for all time. Numerically this statement will only be true to within truncation error, which can grow exponentially in black hole space times; to prevent this we add constraint damping terms as in [122, 123]. In practice, ensuring that $H^a - \Box x^a$ is converging to zero for a given numerical simulation run at different resolutions provides an excellent check that the numerical solution is indeed converging to a solution of the field equations.

As described in [79], the computational grid we use is compactified so as to include spatial infinity. This way we can impose boundary conditions on the metric simply by requiring that it be Minkowski. However we evolve the metric of the uncompactified coordinates since the compactified metric is singular at spatial infinity.

2.2.2 Conservative hydrodynamics

Coupled to gravity we consider a perfect fluid with stress-energy tensor

$$T^{ab} = \rho h u^a u^b + g^{ab} P \ , \tag{2.2}$$

where $h := 1 + P/\rho + \epsilon$ is the specific enthalpy and u^a is the four-velocity of the fluid element. The intrinsic fluid quantities ρ, the rest-mass density; P, the pressure; and ϵ, the specific energy are defined in the comoving frame of the fluid element. As mentioned in Chap. 1, the equations of hydrodynamics are then written in conservative form as follows [84]:

$$\partial_t D + \partial_i (D v^i) = 0 \tag{2.3}$$

$$\partial_t S_a + \partial_i \left(\sqrt{-g} T^i{}_a \right) = \frac{1}{2} \sqrt{-g} T^{bc} \partial_a g_{bc} \tag{2.4}$$

where v^i is the coordinate velocity, g is the determinant of the metric, and the index i runs over spatial coordinates only. Note that (2.4) explicitly contains the time derivative of the metric for index $a = t$. The conserved variables D and S_a are defined as follows:

$$D := \sqrt{-g} \rho u^t \tag{2.5}$$

$$S_a := \sqrt{-g} T^t{}_a \tag{2.6}$$

where D is simply the time component of the matter 4-current.[2]

In some situations we wish to perform axisymmetric simulations where we use the symmetry to reduce the computational domain to two dimensions. We do this using a modification of the Cartoon method [125] as described in [79], where we take the x-axis as the axis of symmetry, and only evolve the $z = 0$ slice of the spacetime. For the hydrodynamics this means that effectively each fluid cell becomes a cylindrical shell, and we use the fact that the Lie derivative of the fluid fields with respect to the axisymmetric killing vector are zero to rewrite the coordinate divergences in the above equations as

$$\partial_i(Dv^i) = \partial_x(Dv^x) + 2\partial_{y^2}(yDv^y) \tag{2.7}$$

and similarly for $\partial_i(\sqrt{-g}T^i{}_a)$ for the t and x components. For the y component there is an additional source term

$$\partial_i(\sqrt{-g}T^i{}_y) = \partial_x(\sqrt{-g}T^x{}_y) + 2\partial_{y^2}(y\sqrt{-g}T^y_y) - (S_z v^z + \sqrt{-g}P/y). \tag{2.8}$$

By writing the y flux contribution in terms of ∂_{y^2} we ensure that when we discretize our evolution will be conservative with respect to the cylindrical shell volume element. We choose a special form for the equation for S_z:

$$\partial_t S_z + \partial_x(\sqrt{-g}T^x{}_z) + \frac{2}{y}\partial_{y^2}(y^2\sqrt{-g}T^y_z) = 0, \tag{2.9}$$

since in axisymmetry the quantity yS_z is exactly conserved (that is, it has no source term).

[2]In some implementations of the GR (magneto)hydrodynamic equations, see for e.g. [124], the analog of S_t in (2.6) that is evolved has the rest-mass density D subtracted off. This could provide improved results in situations where the rest-mass density is orders of magnitude larger than the internal or magnetic energy, and accuracy in these latter quantities is important. In the scenarios studied here (in particular since we are not looking at the behavior of magnetic fields) the added effect of a small amount of internal relative to rest energy on the dynamics of the fluid or metric will be negligible, and we expect either definition of S_t to give comparable accuracy results here. However in Chap. 7, where we study solar-type stars, we do make use of such a variable.

The conservative evolution system is solved numerically using HRSC schemes. We briefly summarize the different methods we have implemented and test in this chapter, though the references should be consulted for more complete details. For calculating intercell fluxes we have implemented HLL [126], the Roe solver [127], and the Marquina flux [128] method. The HLL method is straightforward to implement since it does not require the spectral decomposition of the flux Jacobian and is based on estimates for the largest and smallest signal velocities. The Roe solver works by solving the linearized Riemann problem obtained using the flux Jacobian at each cell interface (using the so-called Roe average of the left and right states). The Marquina flux method is an extension of this idea that avoids the artificial intermediate state and switches to a more viscous local Lax-Friedrich-type method from [129] when the characteristic speeds change sign across the interface. Since the latter two methods require the spectral decomposition of the flux Jacobian, we give it for our particular choice of conserved variables in Sec. 2.2.4. For reconstructing fluid primitive variables at cell faces we have implemented MC and minmod [85], PPM [130] [3], and WENO5 [132] [4], all of which may be used interchangeably with any flux method. MC and minmod are both slope limiter methods that reduce to linear reconstruction for smooth flows. Minmod is the more diffusive of the two. In comparison, PPM and WENO5 are higher-order reconstruction methods. PPM is based on parabolic reconstruction with modifications to handle contact discontinuities, avoid spurious oscillations from shocks by reducing order, and impose monotonicity. WENO5 combines three different three-point stencils with weights that are determined by a measure of the smoothness of the quantity being reconstructed. The specific fluid quantities that we reconstruct on the cell faces are ρ, u, and WU^i, where $u := \rho\epsilon$, W is the Lorentz factor between the local fluid element and an observer normal to the constant t hy-

[3] In particular we use the reconstruction parameters presented in [131].

[4] Specifically, we perform reconstruction with the stencils and weights presented in Section A2 of [133].

persurfaces, and U^i is the Eulerian velocity (the explicit form of which is given in the following section). We choose to reconstruct WU^i instead of simply U^i since any finite value of this quantity corresponds to a subluminal velocity.

The fluid is evolved in time using second-order Runge-Kutta. Since the fluid is evolved in tandem with the metric, the first and second substeps of the fluid Runge-Kutta time step are chosen to coincide with the first and third substeps of the metric time step. Since the spatial discretization of the fluid equations that we use is only second-order we choose to use second-order time stepping for the hydrodynamics and we have not yet experimented with higher-order methods. We still use fourth-order Runge-Kutta for nonvacuum metric evolution (even though for evolutions with matter the overall convergence rate will be no greater than second-order) both for convenience and because in vacuum dominated regions we may expect some improvement in accuracy. For general relativistic hydrodynamics we evolve the fluid on a finite subset (though the majority) of the total grid (which as mentioned extends to spatial infinity through our use of compactified coordinates), and at the outer boundary for the fluid we impose an outflow condition.

Finally, as is common practice for this method of simulating hydrodynamics, we require that the fluid density never drop below a certain threshold, adding a so-called numerical atmosphere. We give this numerical atmosphere a spatial dependence that makes it less dense approaching the boundaries[5] and choose a maximum value that makes it dynamically negligible (typically at least 10 orders of magnitude below the maximum density). The atmosphere is initialized using a cold equation of state (e.g. a polytropic equation of state).

[5]Specifically we let $\rho_{\rm atm}(x_c, y_c, z_v) = \bar{\rho}\cos^2(x_c)\cos^2(y_c)\cos^2(z_c)$ where $\bar{\rho}$ is a constant, and (x_c, y_c, z_c) are the compactified coordinates which range from -1 to 1.

2.2.3 Primitive inversion

The set of hydrodynamical equations is closed by an EOS of the form $P = P(\rho, \epsilon)$. While the conserved variables S_a and D are simply expressed in terms of fluid primitive variables (ρ, P, ϵ, and v^i) and the metric, the reverse is not true. This necessitates a numerical inversion to obtain the primitive variables following each update of the conserved variables. The method we use is similar to the one used in [134] for spherical symmetry. First, we decompose the 4-dimensional metric into the usual ADM space plus time form

$$\begin{aligned} ds^2 &= g_{ab}dx^a dx^b \\ &= -\alpha^2 dt^2 + \gamma_{ij}(dx^i + \beta^i dt)(dx^j + \beta^j dt) \end{aligned} \tag{2.10}$$

where γ_{ij} is the spatial metric, α the lapse function and β^i the shift vector. Then, from the metric and conserved variables we construct two quantities,

$$S^2 := \gamma^{ij} S_i S_j = \gamma H^2 W^2 (W^2 - 1) \tag{2.11}$$

$$E := \beta^i S_i - S_t = \sqrt{-g}(HW^2 - P) \ , \tag{2.12}$$

where $H := \rho h$ and γ is the determinant of the spatial metric. We reduce the problem of calculating the primitive fluid variables from the metric and conserved variables to a one-dimensional root problem, where we begin with a guess for H and iteratively converge to the correct value such that $f(H) = 0$ for some function. From (2.12) we can choose

$$f(H) = E/\sqrt{-g} - HW^2 + P. \tag{2.13}$$

Note that given the metric and conserved variables, $f(H)$ is only a function of H, and can be computed as follows. First, calculate $W^2 = (1 + \sqrt{1 + 4\Lambda})/2$ where

$$\Lambda := \frac{S^2}{\gamma H^2} = W^2(W^2 - 1) \ . \tag{2.14}$$

Then compute ρ and ϵ from

$$\rho = D/(\sqrt{\gamma}W), \tag{2.15}$$

and

$$\epsilon = -H(W^2 - 1)/\rho + WE/(D\alpha) - 1 \ , \tag{2.16}$$

respectively. Once ρ and ϵ are known, P can be obtained from the equation of state, and then $f(H)$ above. An iterative procedure for solving $f(H) = 0$, where $f(H)$ is calculated as just described, thus gives the primitive variables ρ, P, and ϵ. The three-velocity can then be computed from

$$U^i = \frac{\gamma^{ij} S_j}{\sqrt{\gamma} H W^2} \ , \tag{2.17}$$

where the Eulerian velocity U^i is related to the grid three-velocity through $U^i = (v^i + \beta^i)/\alpha$. This inversion scheme is implemented so as to allow any EOS of the form $P = P(\rho, \epsilon)$; thus, Γ-law, piecewise polytrope, and tabular equations of state such as the finite-temperature EOS of Shen et al. [135, 136] (for a given electron fraction Y_e) are all supported.

In practice we solve for $f(H) = 0$ numerically using Brent's method [137], which does not require knowledge of derivatives and is guaranteed to converge for any continuous equation of state as long as one begins with a bracket[6] around the correct solution. This can be useful when dealing with equations of state interpolated from

[6] The initial bracket for the root finding is chosen by first checking if $[H_0/(1+\delta), H_0(1+\delta)]$, where H_0 is the value of H computed for the primitive variables at the previous time step and $\delta > 0$ is a parameter we take to be 0.4, is a valid bracket around the zero of $f(H)$. If it is not, as a failsafe we try successively larger brackets with $[H_0/(1+\delta)^n, H_0(1+\delta)^n]$ for $n \geq 2$.

tabulated values. One can avoid losing accuracy in the ultrarelativistic and non-relativistic limit by Taylor expanding the above inversion formulas (see [134]), for example, in $1/\Lambda$ and Λ, respectively. We have implemented such expansions in our primitive inversion algorithm, though we have not yet made any significant study of the inversion calculation in these regimes.

In some cases the conserved variables will, due to numerical inaccuracies, evolve to a state that does not correspond to any physical values for the primitive variables. This causes the inversion procedure to fail. This can happen in very low density regions that are not dynamically important but still must be addressed. We handle such situations using a method similar to that of [84] by ignoring the value of S_t and instead requiring the fluid to satisfy a cold equation of state.

2.2.4 Spectral decomposition of the flux Jacobian

Our conservative formulation of the hydrodynamical equations (2.3,2.4) can be written in vector notation as $\partial_t \mathbf{q} + \partial_i(\mathbf{F}^i) = \mathbf{S}$ where $\mathbf{q}$ is a five dimensional vector of the conserved (in the absence of sources $\mathbf{S}$) fluid variables $\mathbf{q} = (D, S_t, S_x, S_y, S_z)^T$ and the flux $\mathbf{F}^i = (Dv^i, (S_t - \sqrt{-g}P)v^i, S_j v^i + \delta^i_j \sqrt{-g}P)^T$, where the index j in the flux is shorthand for the 3 components (x, y, z). Some flux calculation methods such as the Roe solver [127] and the Marquina flux [128] require the spectral decomposition of the Jacobian $\frac{\partial \mathbf{F}^i}{\partial \mathbf{q}}$ which we give here. (See [138] for the spectral decomposition for a similar formulation with slightly different conserved variables.) The eigenvalues are

$$\lambda_\pm = \alpha q(a \pm b) - \beta^i \tag{2.18}$$

and

$$\lambda_3 = \alpha U^i - \beta^i \tag{2.19}$$

(with multiplicity 3), where $a = (1 - c_s^2)U^i$, $b = c_s\sqrt{(1-U^2)[\gamma^{ii}(1-U^2c_s^2) - aU^i]}$, $q = (1 - U^2c_s^2)^{-1}$, c_s is the sound speed, and $\alpha, \beta^i, \gamma^{ij}$ are metric components as in (2.10). Here and throughout we use $i \in \{x, y, z\}$ to refer to the direction of the flux in the Jacobian with which we are concerned, $\frac{\partial \mathbf{F}^i}{\partial \mathbf{q}}$. In the following equations we use the index j as a shorthand for the three spatial components of the eigenvectors (that is, the components associated with S_x, S_y, and S_z). The indices l and m are fixed by i and the indices n and p are fixed by j as indicated below. The index k is the only index that is summed over. A set of linearly independent right eigenvectors is given by

$$\mathbf{r}_\pm = \Big(1, hW[U^k\beta_k - \{\alpha(\gamma^{ii} - U^iU^i) + A\beta^i\}/B], hW(U_j - \delta^i_j A/B)\Big)^T, \tag{2.20}$$

where $A = [U^ic_s^2(1-U^2) \mp b]q$ and $B = \gamma^{ii} - U^i(a \pm b)q$,

$$\mathbf{r}_3 = \Big(\kappa/(HW(\kappa/\rho - c_s^2)), U_k\beta^k - \alpha, U_j\Big)^T, \tag{2.21}$$

where $\kappa = \frac{\partial P}{\partial \epsilon}$, and,

$$\mathbf{r}_4 = \Big(WU_l, 2hW^2(U_k\beta^k - \alpha)U_l + h\beta_l, h(\gamma_{jl} + 2W^2U_jU_l)\Big)^T \tag{2.22}$$

where for $\mathbf{r}_4$, $l = y, z, x$ for $i = x, y, z$ respectively. The expression for $\mathbf{r}_5$ can be obtained simply by replacing l with m, where $m = z, x, y$ for $i = x, y, z$ respectively, in the above expression for $\mathbf{r}_4$. H and W are as defined following (2.12).

We also give the corresponding left eigenvectors. Component-wise, for $\mathbf{l}_\pm = (l^D_\pm, l^t_\pm, l^j_\pm)$,

$$\begin{aligned}
l^D_\pm &= \mp fhWV_\mp\xi \\
l^t_\pm &= \mp f\Big[(K-1)\{-\gamma U^i + V_\mp(W^2\xi - \Gamma_{lm})\} + KW^2V_\mp\xi\Big]/\alpha \\
l^j_\pm &= \mp f\Big[(\gamma_{ln}\gamma_{mp} - \gamma_{lp}\gamma_{mn})\{1 - KA^i - (2K-1)V_\mp U^i\} + (2K-1)V_\mp\xi W^2U^j\Big] \\
&\quad -\beta^j l^t_\pm
\end{aligned} \tag{2.23}$$

where $l = y, z, x$ and $m = z, x, y$ for $i = x, y, z$ respectively, and $n = y, z, x$ and $p = z, x, y$ for $j = x, y, z$ respectively and $\Gamma_{lm} = \gamma_{ll}\gamma_{mm} - \gamma_{lm}\gamma_{lm}$, $\xi = \Gamma_{lm} - \gamma U^iU^i$, $K = (1 - c_s^2\rho/\kappa)^{-1}$, $\Lambda_\pm = (a \pm b)q$, $V_\pm = (U^i - \Lambda_\pm)/(\gamma^{ii} - U^i\Lambda_\pm)$, $A^i = (\gamma^{ii} - U^iU^i)/(\gamma^{ii} - U^i\Lambda_\mp)$, and

$$f^{-1} = 2hWbq\xi(K-1)(\gamma^{ii} - U^iU^i)[(\gamma^{ii} - U^i\Lambda_+)(\gamma^{ii} - U^i\Lambda_-)]^{-1}.$$

Furthermore,

$$\mathbf{l}_3 = \frac{W}{c_s^2\rho}(\kappa - c_s^2\rho)\Big(h, W/\alpha, W(U^j - \beta^j/\alpha)\Big), \tag{2.24}$$

and the components of $\mathbf{l}_4$ and $\mathbf{l}_5$ are

$$\begin{aligned}
l^D_4 &= 0 \\
l^t_4 &= G_{lm}(\alpha h\xi)^{-1} \\
l^j_4 &= \Big[\delta^j_i U^i G_{lm} + \delta^j_l\{\gamma_{mm}(1 - U_iU^i) + \gamma_{im}U_mU^i\} \\
&\quad -\delta^j_m\{\gamma_{lm}(1 - U_iU^i) + \gamma_{im}U_lU^i\}\Big](h\xi)^{-1} - \beta^j l^t_4
\end{aligned} \tag{2.25}$$

where $G_{lm} = (\gamma_{mm} U_l - \gamma_{lm} U_m)$ and for $\mathbf{l}_4$, $l = y, z, x$ and $m = z, x, y$ for $i = x, y, z$ respectively. The expression for $\mathbf{l}_5$ can be obtained from the above expression for $\mathbf{l}_4$ simply by interchanging l and m.

2.2.5 Adaptive mesh refinement with flux corrections

Many of the problems we are interested in applying this code to involve a range of length scales, and in many cases we expect the small length scale features *not* to be volume filling, for example the individual compact objects in binary mergers. Such scenarios can be efficiently resolved with Berger and Oliger style adaptive mesh refinement [139]. A description of the variant of the algorithm we use can be found in [140]; here we mention some particulars to this implementation, and give a detailed description of the extension to ensure conservation across refinement boundaries.

The computational domain is decomposed into a hierarchy of uniform meshes, where finer (child) meshes are entirely contained within coarser (parent) meshes. The hierarchy is constructed using (primarily) truncation error (TE) estimates, which are computed within the Berger and Oliger time subcycling procedure by comparing the solution obtained on adjacent levels of refinement before the coarser levels are overwritten with the solution from the finer level. Typically we only use the TE of the metric variables, since fluid variables in general develop discontinuities as well as turbulent features that do not follow strict convergence. The layout of the AMR hierarchy is then periodically adjusted in order to keep the TE below some global threshold. In some situations we also require that a region where the fluid density is above a certain threshold always be covered by a minimum amount of resolution. This can be used to ensure, for example, that the resolution around a NS does not temporarily drop below some level even if the TE of the metric variables in the neighborhood of the star becomes small.

When setting the values of the metric variables on the AMR boundary of a given child level we interpolate from the parent level using third-order interpolation in time and fourth-order in space. For the cell-centered variables, the outer two cells in each spatial direction (for a refinement ratio of 2) on a child level are initially set using second order interpolation in time and space from the parent level. Following the evolution of the child level and flux correction applied to the parent level when they are in sync as described below, but before the cell-centered values on the child level are injected into the parent level, the values in the child boundary cells are reset using first-order conservative (spatial) interpolation from the parent level (i.e. the value in the child cell is set to be the same as that of the parent cell in which the child cell is contained). This ensures that the boundary cells on the child level are consistent with the corresponding flux-corrected cells on the parent level but does not affect the order of convergence of the scheme since these values are not used in the evolution step. During a regrid when adding cells to the domain of a refined level we also use first-order conservative interpolation from the overlapping parent level to initialize the values of the fluid variables at new cells (fourth-order interpolation is used for the metric variables). Note that the actual domain that is refined is larger than the volume where the TE estimate is above threshold by a given buffer in any direction. The buffer size and regridding interval are chosen so that if change in the region of high TE is associated with bulk motion of the solution (e.g. the NS moving through the domain), this region will never move by more that the size of the buffer between regrids. This ensures that new cells (for this kind of flow) are always interpolated from regions of the parent that are *below* the maximum TE threshold. Thus, though the interpolation operation to initialize new cells is first-order, we find the error it introduces is negligible (i.e., below the maximum desired TE).

AMR boundaries require special treatment in conservative hydrodynamics codes however, since the fluxes across the boundary of a fine-grid region will not exactly

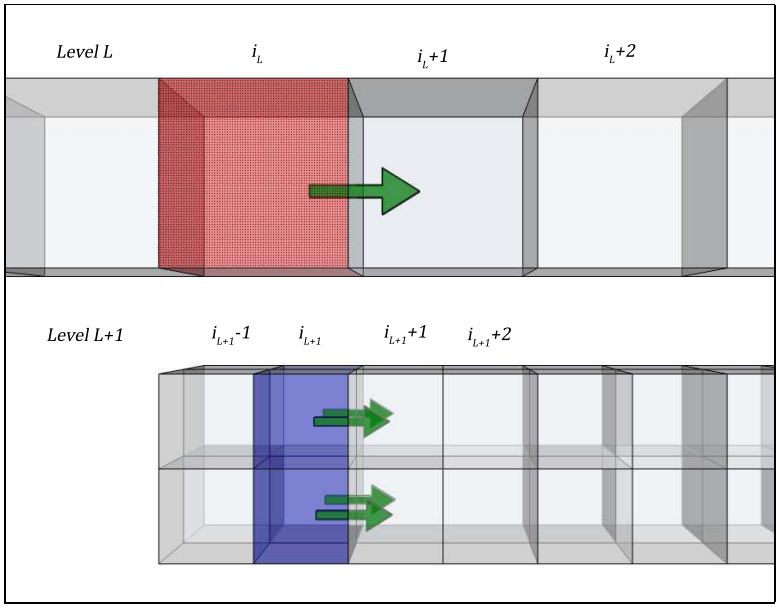

Figure 2.1: A visualization of a refinement level boundary and its treatment in the flux correction algorithm. The top shows cells in the x direction on refinement level L while the bottom shows equivalent cells for the $L+1$ refinement level (here the refinement ratio is 2). Fluxes are symbolized by arrows. On the bottom level the blue cells ("type B" in the discussion in the text) and those to the left on level $L+1$ are boundary cells and will have their values set by interpolation from level L following an evolution step on level L. Because of truncation error, subsequent evolution on level $L+1$ will give a flux differing from that computed on the parent level L. Consequently, when the new fine grid solution is injected back to the parent level (in cells to the right of the red/dotted pattern cell), the solution about the boundary will no longer be consistent with the flux previously computed there. The correct this, the fluid quantity in the red/dotted pattern cell is adjusted to exactly compensate for the difference in flux computed between the coarse and fine levels.

match the corresponding flux calculated on the coarse-grid due to differing truncation errors. To enforce conservation, we correct the adjacent coarse grid cells using the fine-grid fluxes according to the method of Berger and Colella [115]. In the remainder of this section we review the algorithm and outline our specific implementation.

We will concentrate on the evolution of D on a 3-dimensional spatial grid, though the remaining conserved fluid quantities are treated the same way, and modification to different numbers of spatial dimensions is trivial. Equation (2.3) is evolved

numerically at a given resolution as

$$\begin{aligned} D^{n+1}_{i,j,k} &= D^{n}_{i,j,k} - \Delta t\big[(F^{x}_{i+1/2,j,k} - F^{x}_{i-1/2,j,k})/\Delta x \\ &\quad +(F^{y}_{i,j+1/2,k} - F^{y}_{i,j-1/2,k})/\Delta y + (F^{z}_{i,j,k+1/2} - F^{z}_{i,j,k-1/2})/\Delta z\big] \end{aligned} \tag{2.26}$$

where $D^{n}_{i,j,k}$ is the volume average of D over the (i,j,k) cell at time $t = n\Delta t$; $F^{x}_{i+1/2,j,k}$ is the flux $F^{x} = Dv^{x}$ through the $(i+1/2,j,k)$ cell face; Δx is the x length of each cell and so on for the y and z direction. In practice the flux values will be calculated with some HRSC technique combined with Runge-Kutta, but the specifics are not relevant here. Now consider a situation with two sequential levels of refinement, L and $L+1$, where level $L+1$ has a higher resolution with spatial refinement ratio of r in each direction, and its domain is a subset of level L. (In practice, we always take $r = 2$.) Here we focus the discussion on a left boundary in the x direction, as illustrated in Fig. 2.1; boundaries along the right face and other coordinate directions are treated in a like manner.

When evolving according to the Berger-Oliger algorithm, after each time step of length Δt is taken on level L, r steps of length $\Delta t/r$ are taken on level $L+1$. Then the results obtained on $L+1$ are injected into level L where the levels overlap i.e., the restriction operation is performed conservatively by setting the value in the parent cell to the (coordinate) volume-weighted average of the child cells that make up the parent cell. Now on level L, the change in D due to flux going through the cell face $(i_L + 1/2, j_L, k_L)$ on a timestep will be

$$\delta D_L = -\frac{\Delta t}{\Delta x} F^{x}_{i_L+1/2,j_L,k_L}(t_n). \tag{2.27}$$

On level $L+1$, the change in D in one fine-level time step due to flux passing through one of the r^2 cell faces that make up this same interface is

$$\delta D_{L+1,j,k,m} = -\frac{\Delta t/r}{\Delta x/r} \times F^x_{i_{L+1}+1/2, j_{L+1}+j, k_{L+1}+k}(t_n + m\Delta t/r).$$

for j, k, and $m \in \{0, 1, \ldots, r-1\}$. Now because of truncation error, in general the change in the net "mass" [7] $\delta M_L := \delta D_L V_L$ within the coarse-level cell at (i_L, j_L, k_L) computed with the coarse-level fluxes will not equal the corresponding quantity $\delta M_{L+1} := \sum_{j,k,m} \delta D_{L+1,j,k,m} V_{L+1,j,k,m}$ computed with the fine-level fluxes, where V_L is the coordinate volume of the cell (i_L, j_L, k_L) and $V_{L+1,j,k,m}$ is the coordinate volume of the cell $(i_{L+1}, j_{L+1}+j, k_{L+1}+k)$. Thus, after the values of D on level $L+1$ are injected into level L (in cells (i_L+1, j_L, k_L) and to the right in this example), the solution on level L will suffer a violation of mass conservation proportional to $\delta M_L - \delta M_{L+1}$. To restore the conservative nature of the algorithm, the idea, described in detail below, is to adjust the conservative variable D in the cell (i_L, j_L, k_L) post-injection by an amount to exactly compensate for this truncation error induced difference.

The scheme originally proposed in [115] is to define an array that keeps track of a correction to the fluxes through cell faces on level L that make up the boundary of the evolved cells on level $L+1$. Consider the case where $(i_L + 1/2, j_L, k_L)$ is such a face. This face-centered flux correction array, δF, is initialized with the inverse of the flux in (2.27), $\delta F = -F^x_{i_L+1/2, j_L+j, k_L+k}$, and then during the course of taking the

[7] For the conserved fluid variable D which we focus on for specificity, the value of the quantity integrated within the volume of a cell in fact represents the rest mass in that cell. Throughout this section we will therefore use the term 'mass' to refer to the value of a conserved fluid variable volume integrated within a cell, though for other conserved fluid variables this will not correspond to a physical mass.

r time steps on level $L+1$ receives corrections from the terms in (2.28)

$$\delta F \rightarrow \delta F + \frac{1}{r^3} \sum_{j,k,m} F^x_{i_{L+1}+1/2, j_{L+1}+j, k_{L+1}+k}(t_n + m\Delta t/r). \tag{2.28}$$

After the cell values on level L are overwritten by the injected values on level $L+1$ where they overlap, the cells on level L that abut level $L+1$ though are not themselves covered by level $L+1$ cells are corrected with the flux stored in δF.

The way we implement the flux correction algorithm is slightly different from this. In particular we wish to avoid the added computational complexity of implementing face-centered grid functions, and therefore we keep track of a cell-centered correction. The correction is thus also more naturally represented as a correction to the fluid quantity integrated within the volume of the cell (e.g. for D the rest-mass) rather than a flux. Again referring to Fig. 2.1, we define the first few cells at the boundary of level $L+1$ as buffer cells since the calculation of flux requires knowledge of the state on both sides of the interface. These cells will have their values set by interpolation from those in level L. The innermost buffer cells for the boundary on level $L+1$ we call type B cells (blue cells in the lower half of the figure). These are the cells where the level $L+1$ contribution to the mass correction will be stored. The cell on level L which contains the type B cell we will refer to as a type A cell (red, dotted-pattern cell). Type A cells are the ones that receive mass corrections in this algorithm. For each cell on each refinement level we use a bitmask grid function that indicates whether the cell is one of the above types (A or B), and if so which of the six possible faces ($+x$, $-x$, $+y$, $-y$, $+z$, $-z$) abut the boundary. For simplicity in the implementation we do not allow grid hierarchies where a cell would be both type A and type B[8].

[8]In other words, an inner (non-physical) boundary on level L must be at least one cell away from any inner boundary on level $L-1$. If the hierarchy is generated by truncation error which is sufficiently smooth, inner boundaries will typically not be coincident. Also, experience suggests it

In the following we outline the additional tasks relative to the basic Berger-Oliger algorithm that need to be performed with our implementation of Berger-Colella. Following the spirit of these algorithms, we break down the tasks into those the AMR "driver" code implements, which do not require knowledge of the specific equations being evolved or what physical quantities the variables represent, and conversely the "application" steps that would need to be implemented by a unigrid application code plugging into the driver to become AMR-capable. The driver tasks include the following:

(i) For the conserved fluid density D, allocate a storage grid function to keep track of the associated mass correction δM, i.e. the total correction to D within the volume of a given cell.

(ii) Upon initialization set all correction arrays δM to zero, and compute the bitmask for the current refinement hierarchy.

(iii) After any regrid, recompute the bitmask array for the new hierarchy.

(iv) During the stage when buffer cells are set for variable D at interior boundaries on level $L+1$ via interpolation from level L, also interpolate the correction variable δM, where the latter's interpolation operator simply sets δM in a child cell to be $1/r^3$ that of the parent cell (for a three-dimensional spatial grid).

(v) Following injection of arrays D and δM from level $L+1$ to level L, where the injection operator for δM is an algebraic sum over child cells (a) zero all type B cells in δM on level $L+1$, (b) call the application routine (first item in the next list) to apply the mass corrections to D stored in the injected δM to type A cells on level L, (c) zero all type A cells in δM on level L.

The following are new tasks that the unigrid application code needs to implement:

is often more challenging to get an AMR evolution stable if inner boundaries are too close, so in all this restriction is not particularly limiting.

(i) A routine that will add the mass corrections stored in δM to D for all type A cells on a given grid (i.e., set $D_L \to D_L + \delta M/V_L$)[9].

(ii) When taking a single time step on a grid, for any cell marked type A, set δM to minus the change in mass of the cell from fluxes through cell faces indicated by the bitmask. For example, with the case illustrated in Fig.2.1 and discussed above around Eqs. (2.27) and (2.28), set $\delta M_L = -V_L \delta D_L$.

(iii) When taking a single time step on a grid, for any cell marked type B, add to δM the change in mass of the cell from fluxes through cell faces indicated by the bitmask. For example, with the same example above, set $\delta M_{L+1,j,k} \to \delta M_{L+1,j,k} + V_{L+1,j,k,m} \delta D_{L+1,j,k,m}$.

For the GR-hydro equations we have five conserved fluid variables, D and S_a. Though the latter do have nonzero source terms — since gravity can be a source (or sink) of energy-momentum — the above algorithm ensures there will be no artificial loss/gain in the presence of AMR boundaries due to truncation error from the advection terms.

2.3 Tests

In this section we present a number of tests of the methods presented above. We begin by demonstrating the fourth-order convergence of the evolution of the Einstein equations for vacuum spacetimes before moving on to a number of flat space, relativistic hydrodynamics tests that probe the treatment of fluid discontinuities. We conclude with several tests of hydrodynamics in curved spacetimes.

[9]Since we consider D a density and δM a mass, this requires normalization by the volume element V_L, which the application knows. Note that in our code even though we have included the uncompactified metric volume element $\sqrt{-g}$ in the definition of the conservative variables and fluxes, compactification (and in axisymmetry, the cylindrical shell volume element) effectively makes the grid non-uniform and so the volume scaling is non-trivial. An alternative implementation could move this correction step to the driver list of tasks, though then the application would need to supply the driver with the array of local volume elements.

2.3.1 Vacuum evolution

In [79, 141] several tests of convergence of an earlier version of the code (without hydrodynamics) were presented. However, since then we have updated the evolution of the Einstein equations to fourth-order spatial differencing and fourth-order Runge-Kutta time differencing, so we first show two vacuum tests: a Brill wave evolution [142, 143] and a boosted BH evolution.

Brill wave

For the Brill wave test we begin with initial data where the spatial line element is given by

$$ds^2 = \psi^4 \Big(e^B dx^2 + \frac{e^B y^2 + z^2}{r^2} dy^2 + \frac{(e^B - 1) yz}{r^2} (dydz + dzdy) + \frac{e^B z^2 + y^2}{r^2} dz^2 \Big) \quad (2.29)$$

where $r = \sqrt{y^2 + z^2}$, $B = 2Ar^2 \exp(-(r/\sigma_r)^2 - (x/\sigma_x)^2)$, and the value of the conformal factor Ψ is determined by solving the Hamiltonian constraint. We choose $A = 40$, $\sigma_r = 0.16$, and $\sigma_x = 0.12$. The initial data is chosen to be time symmetric ($\dot{\gamma}_{ij} = 0$) and maximally sliced ($K = 0$) with the conformal lapse $\tilde{\alpha} := \Psi^{-6}\alpha = 1$. The remaining metric components are chosen to satisfy the harmonic gauge ($\Box x^a = 0$). This describes a gravitational wave that initially collapses inward before dispersing. In Fig. 2.2 we show results from convergence tests in axisymmetry at three resolutions where the medium and high runs had, respectively, 1.5 and 2 times the resolution of the low run. The constraint equations ($H_a - \Box x_a = 0$) as well as the metric components show the expected fourth-order convergence.

Boosted BH evolution

As an additional vacuum spacetime test we evolved a boosted BH in three dimensions. We began with initial data describing a BH in harmonic coordinates [144] with

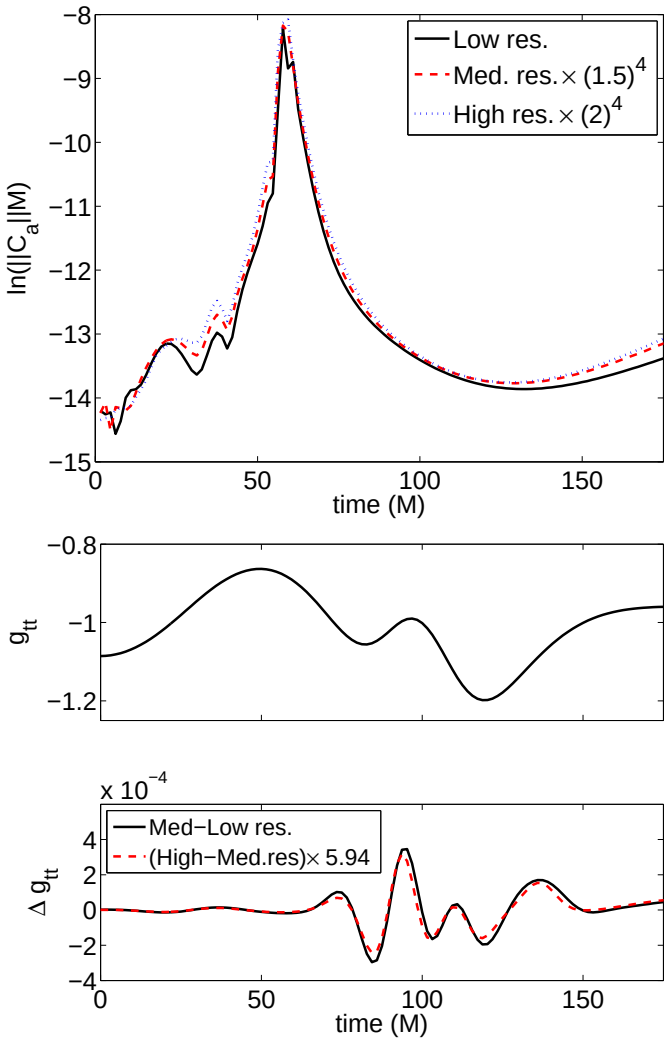

Figure 2.2: **Top**: The natural log of the L^2 norm of the constraint violation, $C_a := H_a - \Box x_a$, for a Brill wave evolution (i.e. natural log of $\sqrt{\int |C_a|^2 d^2x / \int d^2x}$). The three resolutions shown are scaled assuming fourth-order convergence. Time is shown in units of M, the total ADM mass of the spacetime, and the constraints are multiplied by M to make them dimensionless. The lowest resolution has a grid spacing of $h = 1.56M$. **Middle/Bottom**: The value of the metric component g_{tt} evaluated at $(x, y, z) = (0, 50M, 0)$ (middle) and the difference in this quantity between low and medium resolution, and medium and high resolution (bottom), the latter scaled so that the two curves should coincide for fourth-order convergence.

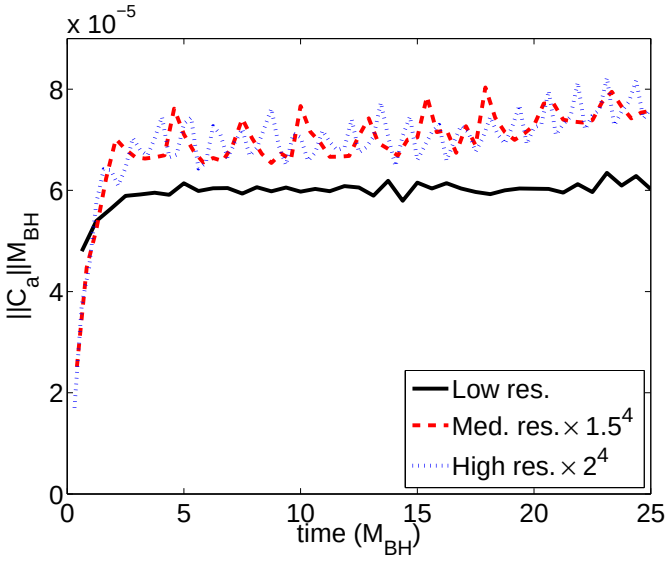

Figure 2.3: The L^2-norm of the constraint violation ($C_a := H_a - \Box x_a$) in the equatorial plane for a boosted BH simulation with $v = 0.25$. The three resolutions shown are scaled assuming fourth order convergence. Time is shown in units of $M_{\rm BH}$, the ADM mass of the BH in its rest frame, and the norm of the constraints is multiplied by $M_{\rm BH}$ so as to make it dimensionless.

boost parameter $v = 0.25$. As described in [79], during the evolution we avoid the BH singularity by searching for an apparent horizon and excising a region within. To demonstrate convergence we performed this simulation at three resolutions, the lowest of which has approximately 30 points covering the diameter of the BH. The medium (high) resolution has 1.5 (2.0) times the number of points in each dimension, respectively. For all resolutions we used the same AMR hierarchy, determined based on truncation error estimates at the lowest resolution, with six levels of 2:1 refinement. In Fig. 2.3 we demonstrate that the constraint equations are converging to zero at fourth-order. When hydrodynamics is included the theoretical limiting convergence rate of our code will drop to second-order (in the absence of shocks). However in vacuum dominated regions, for example the gravitational wave zone, one can expect that for the finite resolutions we can practically achieve the convergence will be somewhere between second- and fourth-order.

Test	Γ^a	P_L	ρ_L	v_L	P_R	ρ_R	v_R
RT1	5/3	13.33	10.0	0.0	10^{-8}	1.0	0.0
RT2	5/3	1000.0	1.0	0.0	10^{-2}	1.0	0.0
RT3	4/3	1.0	1.0	0.9	10.0	1.0	0.0
TVT	5/3	1000.0	1.0	0.0	1.0	1.0	$(0.0, 0.99)^b$

Table 2.1: The initial left and right states for the 1D Riemann problems. [a] Adiabatic index of EOS [b] In this case v_x=0 but the transverse velocity $v_y = 0.99$ is nonzero.

2.3.2 Relativistic hydrodynamic tests in flat spacetime

We have performed a number of standard tests for relativistic, inviscid hydrodynamics that probe how well a given numerical scheme handles the various discontinuities that arise. The best combination of reconstruction and flux calculation methods depends on the problem under consideration. We have thus implemented several options and maintained a modular code infrastructure so that they are readily interchangeable and upgradable. While strong shocks such as the ones considered here are not expected to play an important dynamical role in binary BH-NS mergers, they might be important in other potential applications of interest (such as NS-NS grazing impacts, or understanding EM emission from collisions). Thus, the ability to tailor the reconstruction and flux methods to the problem at hand may prove important in the future. In this section, we closely follow the sequence of tests used in the development of the `RAM` code of Zhang and MacFadyen [145], so that our results may be compared with theirs. Though they focus on more sophisticated flux-reconstruction algorithms, their simpler methods (labeled U-PPM and U-PLM, denoting reconstruction of the unknowns with piecewise parabolic and linear reconstruction, respectively) are comparable to the ones we employ.

1D Riemann problems

Reconstruction	Flux method	RT1		RT2		RT3		TVT	
		Error[a]	Convergence[b]	Error	Convergence	Error	Convergence	Error	Convergence
MC	HLL	0.034	0.82	0.110	0.59	0.062	0.77	0.238	0.72
	Roe	0.032	0.82	0.110	0.60	0.052	0.80	0.233	0.72
	Marquina	0.036	0.82	0.127	0.59	0.056	0.79	0.227	0.76
Minmod	HLL	0.061	0.86	0.169	0.42	0.054	0.71	0.395	0.76
WENO5	HLL	0.033	0.84	0.093	0.76	0.039	0.61	0.191	0.83
	Roe	0.032	0.85	0.096	0.79	0.039	0.60	0.198	0.81
	Marquina	0.036	0.85	0.093	0.76	0.038	0.66	0.183	0.82
PPM	HLL	0.041	0.88	0.133	0.67	0.024	1.01	0.248	0.78

Table 2.2: 1D Riemann test results. [a]The L1 norm of the error for resolution $N = 400$. [b]The average convergence rate between runs with $N = 200$, 400, 800, and 1600. The ideal rate is unity for problems such as these containing discontinuities.

We first present a series of four relativistic, one-dimensional (1D) Riemann problem tests for which the exact solution is known (see Sections 4.1-4.4 of [145]). In all cases, the domain is $x \in [0, 1]$ and there are initially two fluid states, a left and a right, initially separated by an imaginary partition at $x = 0.5$. At $t = 0$, the partition is removed and the fluid evolves to some new state. A Γ-law EOS is used for all the tests. In Table 2.1 we summarize the initial states and adiabatic indices used for the four tests, which we label as RT1 (Riemann Test 1), RT2, RT3, and TVT (Transverse Velocity Test). We compare the performance of the various combinations of reconstruction schemes and flux methods to the exact solution and summarize the errors and convergence rates in Table 2.2. Exact solutions to these four tests were generated using a solver provided by B. Giacomazzo, which is described in [146]. Taking HLL as our basic flux method, we performed this series of Riemann problem tests with four reconstruction methods: MC, minmod, WENO5, and PPM. For MC and WENO5, we also explored the effect of the flux method by running the tests with the Roe solver and Marquina's method. Most cases have a Courant-Friedrichs-Lewy (CFL) factor of 0.5. However, the Roe solver, when combined with WENO5, does not seem to work well for problems with very strong shocks, such as RT2 and TVT. For a CFL factor of 0.5, we obtain acceptable results with Roe only by using a more diffusive limiter (like MC). For RT2 and TVT, we thus use Roe combined with WENO5 with a CFL factor of 0.1.

All of the methods we considered perform well on RT1, which is a fairly easy test. The lowest overall error occurs for WENO5 reconstruction (though the density profile between the shock and the contact discontinuity seems not to be as flat as in the other cases). The overall success of WENO5 may be due to the fact that the shock is relatively mild and there is an extended rarefaction that benefits from the high-order reconstruction. In Fig. 2.4 we compare the density profile obtained using HLL and various reconstruction methods to the exact solution. We note that the

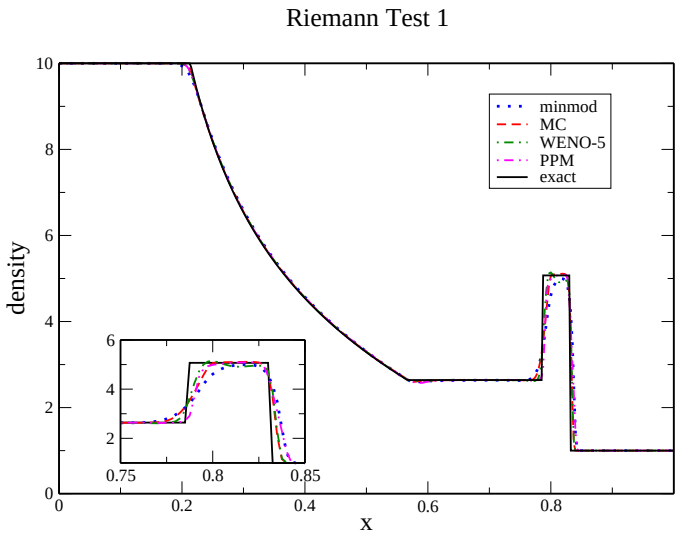

Figure 2.4: Density at $t = 0.4$ for Riemann Test 1 (RT1) with different reconstruction methods and the HLL flux scheme at resolution $N = 400$. The inset shows the shock and contact discontinuity. The exact solution was generated using the code of [147].

tests which used the Roe or Marquina flux calculation with WENO5 do not have the oscillation visible in the plot around $x = 0.8$ in the HLL-WENO5 case.

The second Riemann test (RT2) is more difficult than the first, with the blast wave resulting in a very thin shell of material bounded by a shock on the right and a contact discontinuity on the left (see Fig. 2.5). The average convergence rates for this test show a marked difference between the piecewise-linear and higher-order reconstruction methods. WENO5 seems to perform best, but there is not much difference between HLL and Marquina or the Roe solver (with diminished CFL factor) with WENO5. As in RT1, the reconstruction method seems to be more important to the solution than the flux scheme.

RT3 is a challenging problem in which the fluid on the left collides with the initially stationary fluid on the right, resulting in two shocks separated by a contact discontinuity. Our numerical solutions suffer from significant oscillations (particularly in the reverse shock) for all reconstruction schemes except PPM, which was specifically designed to suppress such post-shock oscillations (see Fig. 2.6). PPM also has the

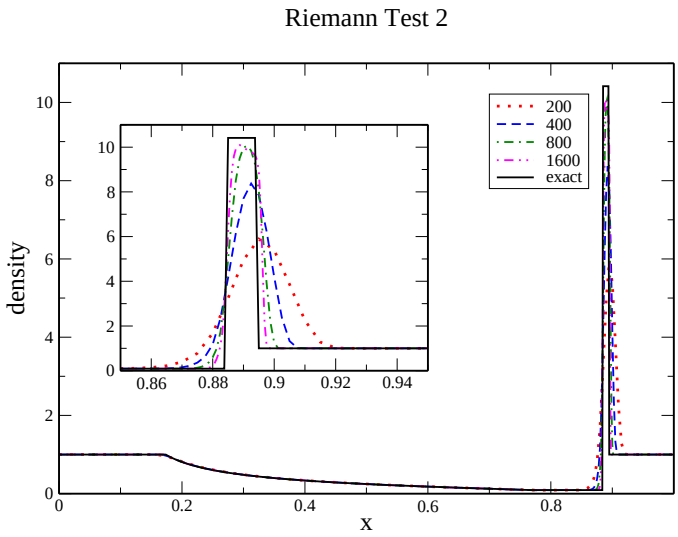

Figure 2.5: Density at $t = 0.4$ for Riemann Test 2 (RT2) at different resolutions for HLL-WENO5. The average convergence rate in this case is 0.76. The thin shell of material between the shock and the contact is particularly difficult to resolve.

best convergence properties (0.85-1.16), with an average rate close to the expected value of unity. (Finite-volume hydrodynamic schemes such as this should converge at first order to a weak solution of the equations when discontinuities are present.)

For the transverse velocity test, the initial data are set up as in RT2, except that there is a transverse velocity $v^y = 0.99$ on the right side of the partition. The strong shock propagates *into* the boosted fluid, and the structure of the shock is altered, since the velocities in all directions are coupled through the Lorentz factor [148]. Again, the reconstruction technique influences the result more than the flux calculation. For WENO5 reconstruction, the errors for HLL, Roe, and Marquina are all very close in magnitude. WENO5 and PPM yield the best results overall. In Fig. 2.7 we show the density profile at different resolutions for HLL combined with WENO5.

1D shock-heating problem

We next consider a one-dimensional shock-heating problem as in [145], which tests a code's conservation of energy as well as the ability to handle strong shocks. For

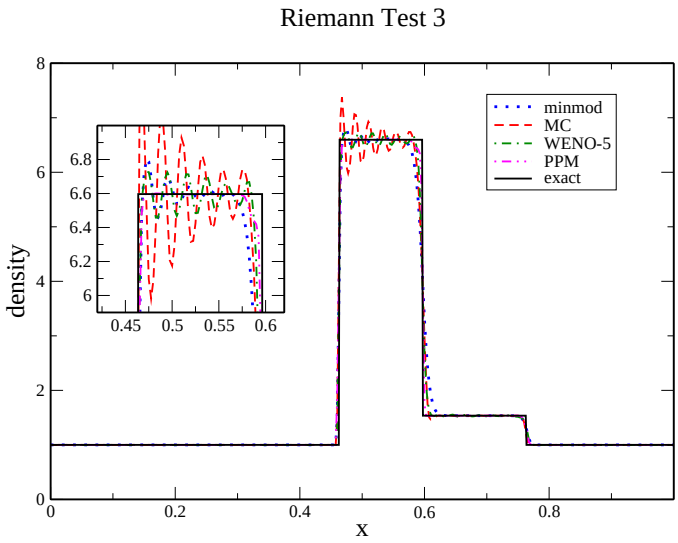

Figure 2.6: Density at $t = 0.4$ for Riemann Test 3 (RT3), a collision problem, for different reconstruction methods with HLL at resolution $N = 400$. The post-shock oscillations are largest in the MC case and smallest for PPM.

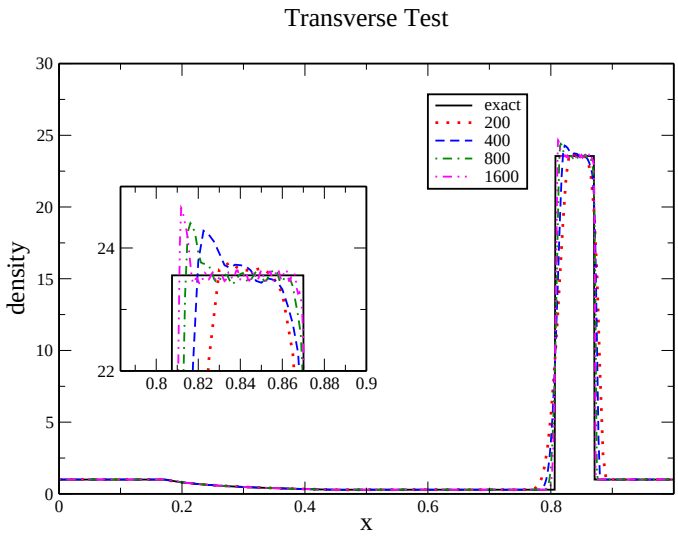

Figure 2.7: Density at $t = 0.4$ for the transverse test (TVT) at different resolutions for HLL-WENO5. The average convergence rate in this case is 0.83.

Reconstruction	Error[a]	Convergence[b]
ZERO	950	0.94
Minmod	801	0.92
MC	1500	0.85
PPM	824	0.96
WENO5	1670	0.53

Table 2.3: Shock -heating test results. For this test we also compare to zero slope reconstruction, labeled "ZERO." [a] The L1 norm of the error for resolution $N = 400$. [b] The average convergence rate between runs with $N = 200$, 400, 800, and 1600.

this problem, the computational domain is $x \in [0, 1]$ with a reflecting boundary at $x = 1$. The fluid moves toward this boundary with an ultrarelativistic initial velocity of $v = 1 - 10^{-10}$. The fluid has an initial density of $\rho = 1.0$ and a very small amount of specific internal energy, $\epsilon = 0.003$. The EOS is a gamma-law with $\Gamma = 4/3$. When the relativistic fluid slams into the wall, its kinetic energy is converted into internal energy behind a shock which propagates to the left. Because the fluid is initially cold, essentially all of the heat is generated through this conversion. As explained in [145], the shock speed and the compression ratio of the shock (or equivalently, the post-shock density) is known analytically. We evaluate our errors by calculating the L1 norm of the density errors on the entire computational domain. The average rate of convergence is also calculated using this measure of error.

We performed this test using HLL with five different reconstruction methods at four different resolutions (200, 400, 800, and 1600 zones). Results are shown in Table 2.3. We find that, due to the extremely strong shock, there is a tendency for post-shock oscillations to form with less diffusive reconstruction schemes (see Fig. 2.8). The WENO5 solution is afflicted with severe post-shock oscillations and exhibits poor convergence to the exact compression ratio. Very diffusive reconstruction schemes (zero slope and minmod) are comparatively quite successful and converge rapidly to the exact compression ratio. PPM, with its flattening step, gives the best convergence rate overall.

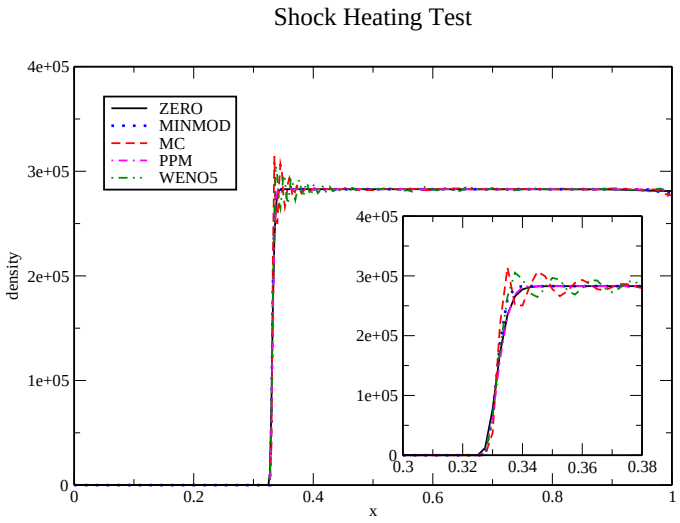

Figure 2.8: Density at $t = 2.0$ for the shock-heating test with different reconstruction methods and the HLL flux scheme. The inset focuses on the shock front.

Emery step problem

Next we consider the two-dimensional (2D) Emery step problem [149, 130], with the setup as in [145]. In this scenario, a fluid flows through a wind tunnel at relativistic speed and hits a step, which is represented by a reflecting boundary condition. The computational domain is $(x, y) \in [0, 3] \times [0, 1] - [0.6, 3] \times [0, 0.2]$ where the subtracted region represents the step. At the left boundary, inflow conditions are enforced (as in the initial data), while at the right, outflow conditions are enforced. All remaining boundaries are reflecting. The fluid is initialized with density $\rho = 1.4$, velocity $v_x = 0.999$, and a $\Gamma = 1.4$ EOS. The pressure is set to 0.1534, giving a Newtonian Mach number of 3.0.

Higher-order reconstruction methods seem to be essential for this test problem. We find that the MC limiter performs poorly, regardless of the flux method. Although the MC simulation is stable, the bow shock formed as the fluid reflects off the step is distorted by large amplitude post-shock oscillations. These propagate downstream, rolling up the boundaries between the different solution regions. The higher resolution runs with MC also have these features, but at shorter wavelengths

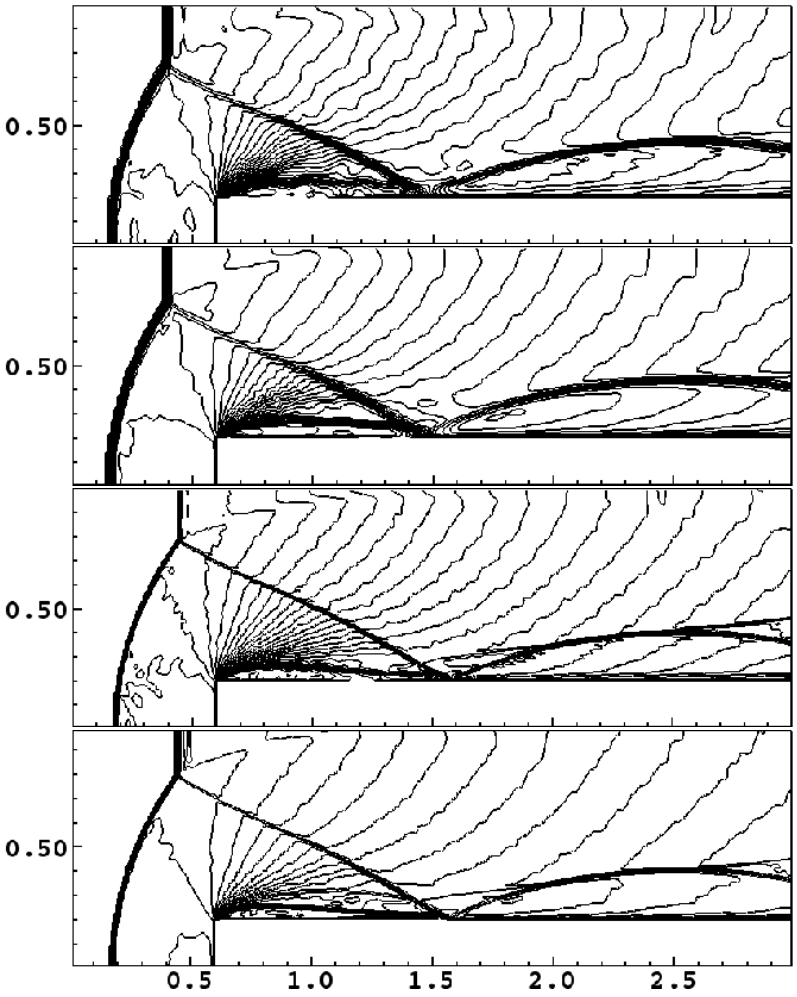

Figure 2.9: Density contours (30 equally spaced in the logarithm) for the Emery step problem. The upper (lower) two plots show results for resolution 240×80 (480×160). For each resolution, the upper plot shows results for WENO5 reconstruction, and the lower for PPM. The respective minimum and maximum densities, $(\rho_{\min}, \rho_{\max})$, are $(1.0, 1.0 \times 10^2)$, $(0.55, 1.1 \times 10^2)$, $(0.82, 1.1 \times 10^2)$, and $(6.8 \times 10^{-2}, 1.1 \times 10^2)$.

and lower amplitude. PPM and WENO5 reconstruction performs much better, and these results are shown at two resolutions in Fig. 2.9. (This figure can be compared to those of [150, 145].) The PPM results appear slightly better than WENO5 at a given resolution, likely because of the deliberate oscillation suppression in the PPM algorithm.

2D shock tube problem

As an additional test of these algorithms' ability to propagate strong, multidimensional shocks we consider a 2D shock tube test. The computational domain $(x, y) \in [0, 1] \times [0, 1]$ is divided into four equal quadrants. The initial fluid states in the lower/upper, left/right quadrants are

$$\begin{aligned}
(\rho, P, v_x, v_y)^{LL} &= (0.5, 1, 0, 0) \\
(\rho, P, v_x, v_y)^{LR} &= (0.1, 1, 0, 0.99) \\
(\rho, P, v_x, v_y)^{UL} &= (0.1, 1, 0.99, 0) \\
(\rho, P, v_x, v_y)^{UR} &= (0.1, 0.01, 0, 0).
\end{aligned}$$

In this simulation the lower-right and upper-left quadrants converge on the upper-right quadrant creating a pair of curved shocks. We use a $\Gamma = 5/3$ EOS. In Fig. 2.10 we show results from simulations using HLL or the Marquina flux method combined with WENO5 or the MC limiter. The first three panels are from runs with resolution of 400×400 and a CFL factor of 0.5 and are comparable to [145] and the references therein. Though the main shock features are captured by all of the methods we considered, oscillations arising from the curved shock fronts are evident in varying degrees. The fourth panel is similar to the first but contains a refined mesh in the center that has the same resolution as the other three panels, while the remainder of the domain has half the resolution. Though the majority of the flow is thus effectively derefined, the principal features remain the same. This is despite the fact that the shocks must travel through or along refinement boundaries, and the numerical shock speeds differ slightly on either side of such boundaries due to the different truncation errors.

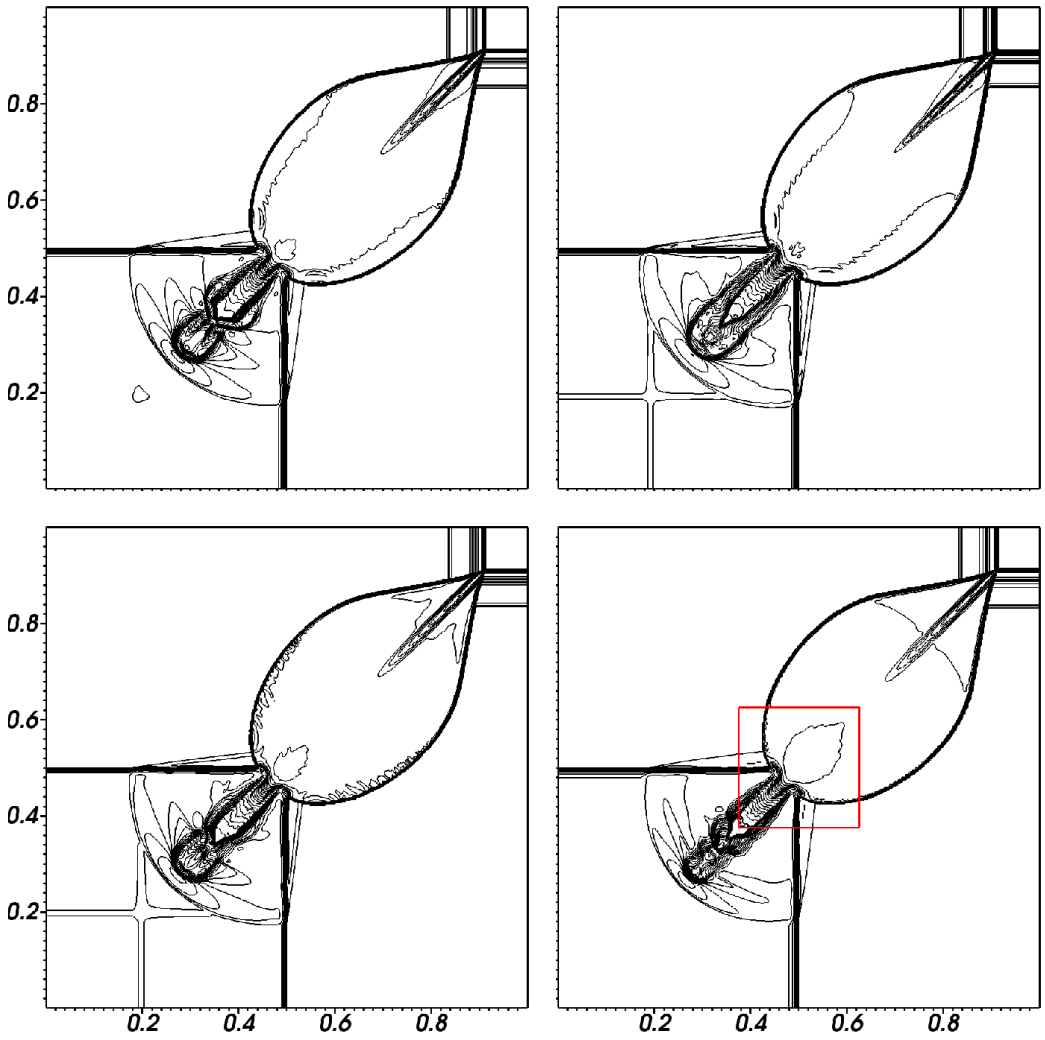

Figure 2.10: Density contours (30 equally spaced in the logarithm) for the 2D Riemann problem with, from left to right, top to bottom: HLL and MC, HLL and WENO5, Marquina and MC, and HLL and MC with mesh refinement. The respective minimum and maximum densities, $(\rho_{\min}, \rho_{\max})$, are $(1.1 \times 10^{-2}, 7.0)$, $(8.2 \times 10^{-3}, 8.1)$, $(9.1 \times 10^{-3}, 7.1)$, and $(7.6 \times 10^{-3}, 7.0)$. For the first three simulations a resolution of 400×400 was used. For the final simulation, a refinement region (red box) was placed in the middle with equivalent resolution, while the remaining grid has half the resolution (i.e. this simulation has lower resolution overall). A CFL factor of 0.5 was used throughout.

2.3.3 Hydrodynamic tests in curved spacetime

Bondi accretion

As a first test of our code's ability to simulate relativistic hydrodynamics in the strong field regime, we consider Bondi flow. We set up our initial conditions with a stationary solution to spherical accretion onto a black hole [151]. We use Kerr-Schild coordinates for the black hole metric. In order to test our code's ability to converge to the correct solution we measured how the conserved density D differed from the exact solution as a function of time for three resolutions. The lowest resolution has a grid spacing of $h = 0.078M_{BH}$, while the medium and high resolutions have twice and 4 times the resolution respectively. As shown in Fig. 2.11, $||D - D_{\rm exact}||$ converges to zero at second-order. For this test we tried both the MC and WENO5 limiters (with HLL for the flux calculation). Though both had similar levels of error and showed the expected convergence, WENO5 had larger errors at low and medium resolutions. This is probably because, at lower resolutions, the larger WENO5 stencil extends farther inside the black hole horizon where there is larger truncation error.

Boosted NS

As an additional test of our evolution algorithm, we considered a single TOV star with a boost of $v = 0.5$, with astrophysically relevant EOS (the HB EOS of [23]) and mass (1.35 $M_\odot$). We performed a convergence study at three resolutions, the lowest of which has approximately 50 points covering the diameter of the star. The medium (high) resolution has two (three) times the number of points in each dimension, respectively. The AMR hierarchy is identical in all cases, with 7 levels of 2:1 refinement, and was determined using truncation error estimates from the low resolution run. Figure 2.12 shows that the constraint violations show the expected second-order convergence to zero. We also compared the performance of different reconstruction

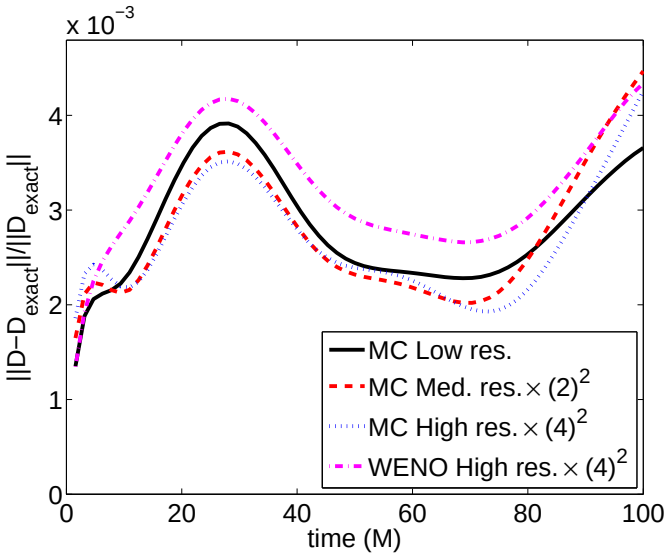

Figure 2.11: The L^2 norm of the difference between the numerical and exact value of the fluid quantity D (divided by the norm of the exact solution) for Bondi accretion with MC and WENO5. The low resolution was run with a grid spacing of $h = 0.078M_{BH}$ while the medium and high has twice and 4 times the resolution respectively. The results are scaled for second-order convergence.

methods (though using the HLL flux method throughout). In Fig. 2.13, we show the maximum density of the NS as a function of time for various reconstruction methods. Though the drifts and oscillations in density converge away for all methods, we find that WENO5 gives the least density drift compared to MC and PPM at a given resolution. The drift in maximum density with PPM has to do with the way this particular implementation enforces monotonicity at extrema, which results in a loss of accuracy (see for example [152]). Modifying the way the algorithm handles smooth extrema can reduce this effect. We implemented one such modification (Eqs. 20-23 from [152]), the results of which are labeled 'PPM alt.' in Fig. 2.13.

Boosted NS flux correction test

As a demonstration of the flux correction algorithm (outlined in Sec. 2.2.5) to enforce conservation across AMR boundaries, we perform an additional boosted NS test. We

use the same conditions as the low resolution simulation outlined above in Sec. 2.3.3 but with a different AMR hierarchy. In particular, we keep the hierarchy fixed so that the boosted NS will move to areas of successively lower refinement. In Fig. 2.14, one sees that without flux corrections there is a $\approx 0.1\%$ loss in fluid rest-mass as the NS moves off the highest refinement level, and a $\approx 0.8\%$ loss as the NS moves off the next to highest refinement level. This change in the conserved fluid rest-mass comes from the fact that there is a slight mismatch in fluxes at the mesh refinement boundaries due to truncation error. With the flux correction routine activated, this error is eliminated, and the only change in the total rest-mass is due to the density floor criterion (i.e., the numerical atmosphere). As an indication of how the use of flux corrections affects energy and momentum we can also compare the integrated matter energy and momentum as seen by a set of Eulerian observers. The matter energy density is given by $T^{ab}n_a n_b$ and the momentum density is given by $p_i = -T^a_i n_a$ where n_a is the timelike unit normal to the constant t slices. These quantities involve combinations of the conserved fluid variables and the metric and are subject to truncation error, especially since in this simulation the NS is allowed to move to lower resolution. In addition, these quantities can vary with time due to gauge effects (though in this case, the variation due to gauge effects is subdominant to the variation mentioned below), so we use them as an indication of the effect of flux corrections by comparing them for the simulations with and without flux corrections to a similar simulation where the AMR tracks the NS and there is therefore essentially no flux across AMR boundaries. At the end of the simulation the run without flux corrections has 0.91% less energy compared to a similar simulation where the AMR tracks the NS, while the run with flux corrections has only 0.13% less energy. The run without flux corrections has 4.0% less momentum (in the boost direction) while with flux corrections the comparative loss is 2.5%.

This test is somewhat artificial since we have deliberately prevented the AMR algorithm from tracking the NS. As long as the AMR algorithm can keep the boundaries away from areas of non-negligible flux (as it does when following the boosted NS in the test described in Sec. 2.3.3) the effect of the flux correction algorithm is small, at the level of the numerical atmosphere that gets pulled along with the star. However, in astrophysical applications, situations may generically arise in which fluid crosses AMR boundaries. For example, the tidal tails formed by the disruption of a NS by a BH will cross refinement boundaries, and likewise for the subsequent accretion disk that forms, since it would be much too costly to keep these entire structures on the finest mesh. Of course, the hydrodynamic solution is still subject to truncation error, which could in principle affect aspects of the dynamics at the same order of magnitude as putative nonconservative effects. Though for certain problems, such as calculating the amount of unbound material following a BH-NS merger, or studying the late time accretion, it could be quite advantageous to ensure conservation within the hydrodynamic sector. It would be an interesting computational science problem to systematically study the efficacy of AMR boundary flux conservation in such scenarios.

Finally, we note that additional convergence test results from this code are shown in subsequent chapters for the particular applications discussed there.

2.4 Conclusions

Numerous scenarios that fall within the purview of general relativistic hydrodynamics are still mostly unexplored—especially CO mergers involving neutron stars. There is a rich parameter space, of which large areas remain uncharted due to uncertainty or potential variability in BH and NS masses, BH spin and alignment, the NS EOS, and other aspects. Beyond the pure hydrodynamics problem, the roles of magnetic

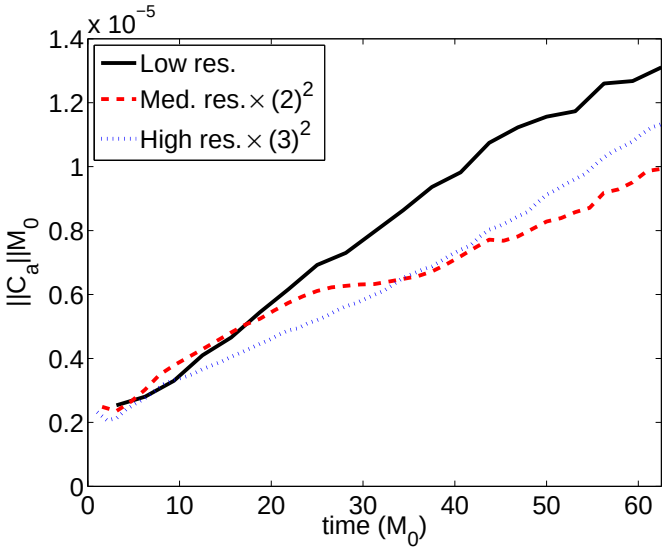

Figure 2.12: The L^2-norm of the constraint violation ($C_a := H_a - \Box x_a$) in the equatorial plane for a boosted NS simulation with $v = 0.5$ (using HLL flux calculation and WENO5 limiter). The three resolutions shown are scaled assuming second-order convergence. Time is shown in units of M_0, the ADM mass of the NS in its rest frame, and the norm of the constraints is multiplied by M_0 so as to make it dimensionless.

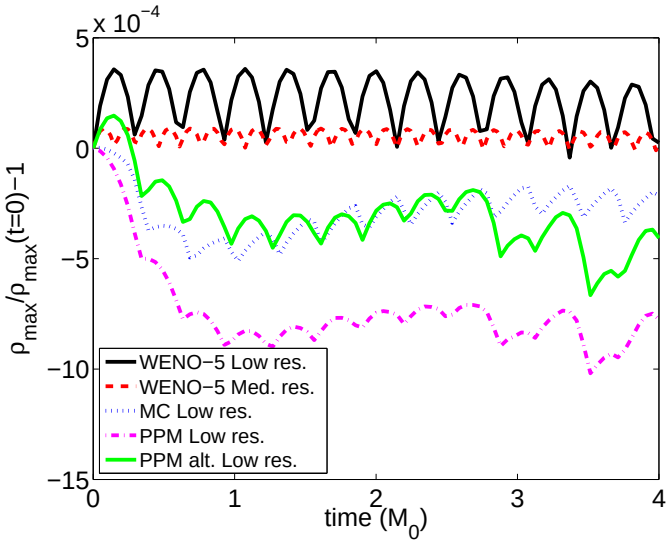

Figure 2.13: The relative variation of the maximum central density from its initial value ($\rho_{\max}/\rho_{\max}(t=0)-1$) during a boosted NS simulation with $v = 0.5$ for various reconstruction methods and for two different resolutions in the case of WENO5.

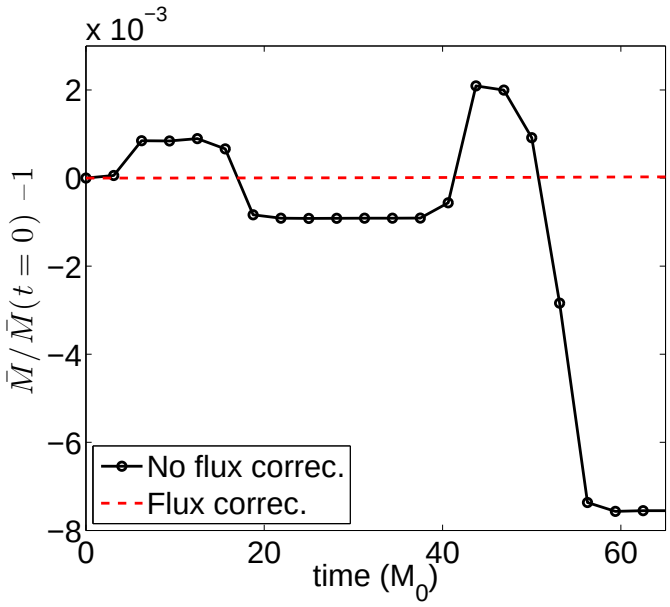

Figure 2.14: The relative variation of the fluid rest-mass ($\bar{M}/\bar{M}(t=0)-1$) for a boosted NS test with (dotted, red line) and without (solid black line) flux corrections at mesh refinement boundaries. For this test, the mesh hierarchy is fixed so that at $t \approx 20\ M_0$ the NS has moved from being contained entirely on the finest resolution to being contained entirely on the second finest resolution. At $t \approx 60\ M_0$ the NS has moved from the second to the third finest resolution.

fields and neutrino physics are just beginning to be explored by various groups, and we expect to add support for such physics to our code in the future. In Chap. 7 we describe additional modifications of this code that allow it to be efficiently used for studying extreme-mass-ratio systems.

The potential applications of robust and flexible numerical algorithms for evolving hydrodynamics together with the Einstein field equations are manifold. With this in mind, we have implemented methods for conservatively evolving arbitrary EOSs, in particular for converting from conserved to primitive variables without knowledge of derivatives; and we have implemented numerous reconstruction and flux calculation methods that can be used interchangeably to meet problem specific requirements. Though accurate treatment of shocks may not be crucial for BH-NS mergers (where shocks are not expected to be dynamically important), the same is not true of NS-

NS binaries, especially eccentric ones where the stars may come into contact during nonmerger close encounters [153]. We have also taken care to implement a flux correction algorithm that preserves the conservative nature of hydrodynamical advection across AMR boundaries. Though strict conservation is not, strictly speaking, essential (since any nonconservation would be at the level of truncation error), it is an especially appealing property when studying, for example, CO mergers as potential SGRB progenitors. After merger, material that did not fall into the black hole — typically on the order of a few percent of the original NS mass — will fill a large volume making up an accretion disk and potentially unbound material. Though accurately tracking this material is not important for the gravitational dynamics, it is critical for characterizing potential EM counterparts to the merger.

Chapter 3

Conformal thin-sandwich solver for generic initial data

3.1 Introduction

The purview of numerical relativity has extended to include not only relativity theory, but also a wide range of other topics. Motivated by current and upcoming efforts to detect gravitational waves [10, 11, 86, 154, 155], there has been extensive work on mergers of binary compact objects (BCOs) [156] including binary black holes (BH-BH) [157, 158, 159, 160], binary neutron stars [161], and black hole-neutron star (BH-NS) systems [162, 163]. In addition to binaries in quasicircular orbits, there have also been studies of eccentric binaries [164, 165, 4, 3, 166, 167, 168, 169, 153, 170] as may arise, for example, from dynamical capture. Other works of interest to astrophysics include gravitational collapse of stars [171, 172], black hole accretion [89], and the nature of cosmological singularities [173, 174]. Aside from astrophysical systems, numerical relativity has also emerged as a useful tool to explore various concepts in gravity and high energy physics [175], such as critical collapse [71], ultrarelativistic collisions [176, 177, 178, 179, 180], the gauge/gravity duality [68, 181, 182, 69, 70],

gravity and black holes in higher dimensions [183, 184, 185], and the (in)stability of anti-de-Sitter spacetime [186]. In all these applications, a necessary ingredient is a good method for constructing initial data (ID). In this chapter we present a new initial data solver, based on the conformal thin-sandwich (CTS) [187] formulation, which we have designed to be more generally applicable to a range of physical scenarios by avoiding symmetry or simplifying assumptions.

There has been extensive research on the problem of constructing ID for general relativity, and detailed reviews can be found in [188, 189, 190, 191]. Early attempts at solving the initial data problem relied on certain assumptions to make the mathematical formulation of the problem more tractable, such as conformal flatness and maximal slicing. The widely used Bowen-York solution [192] is one such example. These assumptions are restrictive since, for example, the isolated Kerr black hole does not admit conformally flat slices [193], and consequently the Bowen-York solution cannot be used to construct black holes with spin higher than $S/M_{\rm ADM}^2 = 0.928$ [194, 195]. Other examples include the use of quasiequilibrium assumptions for constructing ID for binary systems (such as approximate helical Killing vectors or the like, and approximate hydrostatic equilibrium for any matter in the system); see, for example, [196, 197, 198, 199, 200, 201, 202, 203, 204, 205, 206, 207, 208, 209, 210, 211]. This serves as a good approximation for astrophysically motivated quasicircular inspiral sufficiently far from merger, though it is not valid for eccentric mergers (except possibly near the turning points of the orbit [212]) or the ultrarelativistic scattering problem. Many of these studies made further simplifying assumptions, such as conformal flatness, which does not have an astrophysical motivation. Attempts to supply more realistic conformal initial data include superposition of isolated black hole spacetimes [213, 214, 215, 216, 217, 195, 218], and in addition using post-Newtonian solutions [219, 220] and matched asymptotic expansions to supply an initial outgoing radiation field [221, 222, 223]. Using superposed data allowed evolution of binary

black holes in quasicircular orbits with spins exceeding the Bowen-York limit [224]. A further alternative approach, initially applied to binaries including neutron stars, involves solving the full Einstein-Euler system of equations with a waveless and/or near-zone helical symmetry approximation [208, 225, 226, 227, 228].

Since our goal is to have a more general purpose numerical initial data solver that can be used for a range of applications, as outlined in the first paragraph, we will use the CTS formalism with arbitrary conformal metric and other free data to be chosen as needed for the particular application. For our first version of the code, as presented here, we restrict to four-dimensional, asymptotically flat spacetimes, with application to BCO interactions. For the free data we use superposed, boosted single CO spacetimes. At large separation this is a good approximation for the physical metric of dynamical capture binaries and the ultrarelativistic scattering problem, and the nonlinear corrections from solving the CTS equations are small. For quasicircular binaries, again at large separation this is a good approximation. However, unlike the scattering problems, at practical (because of limited computational resources) initial separations to allow evolution through merger, the simple superposition we use at present will not give improved astrophysically relevant ID compared to current quasiequilibrium approaches. Compared to existing studies using superposed data, a couple of novel aspects about our work is we include the matter and metric in the superposition of COs involving fluid stars (as opposed to solving the Euler equations on a flat background in the studies mentioned earlier, or conformal to a single black hole solution [210]) and the consideration of ultrarelativistic initial boosts with Lorentz factors up to 10.

Another notable aspect of this work is how we handle black hole singularities. Most existing approaches either use some form of boundary condition on a trapped surface on or inside each black hole (see, for example, [188, 196, 205]), or use a slice that maps the interior region of the computational domain for each black hole to either

part (so-called "trumpets" [229, 230, 231, 232]) or all ("punctures" [233]) of a different asymptotically flat region spanned by an Einstein-Rosen bridge (for a novel variant that does not require separation of the metric into a background piece and conformal factor see [234]). Here we follow an alternative approach where some distance inside the apparent horizon of each black hole we replace the vacuum interior with an (unphysical) distribution of stress-energy to regularize the interior metric. This is similar to a "stuffed black hole" [235] or the "turduckening" evolution scheme [236, 237] (see also [238]). However, since we use excision to subsequently evolve the initial data, with the excision surface chosen to entirely contain the unphysical matter, here it is merely a device to set up a simple initial data problem without explicit interior boundary conditions or singularities. Note, however, that if we were to solve the ID on a domain with traditional excision surfaces inside each black hole, we would (assuming a well-posed elliptic problem) obtain the same solution exterior with appropriate excision boundary conditions, though the mapping between some unphysical interior and appropriate boundary conditions would be nontrivial and in general nonunique.

An outline of the rest of the chapter is as follows. In Sec. 3.2 we review the CTS formulation, describe our method for choosing the metric and fluid free data, outline the scheme for regularizing black hole solutions, and describe how we numerically solve the constraint equations using a multigrid solver. In Sec. 3.3 we present examples of initial data obtained with our solver for quasicircular, eccentric, and ultrarelativistic mergers of compact objects. Finally, we comment on our results and discuss possible future improvements in Sec. 3.4. We use geometric units where Newton's constant $G = 1$ and the speed of light $c = 1$.

3.2 Computational methodology

3.2.1 Conformal thin-sandwich equations

To formulate the initial data problem for general relativity, we start by foliating spacetime with a family of spacelike hypersurfaces Σ_t parametrized by t. The normal vector to these surfaces n^μ and the generator of time translations t^μ satisfy

$$t^\mu = \alpha n^\mu + \beta^\mu, \tag{3.1}$$

where α is the lapse and β^μ is the shift, which is tangent to Σ_t ($n_\mu \beta^\mu = 0$). We use the standard convention where Greek indices run through $\{0, 1, 2, 3\}$ and represent the full spacetime coordinates, while Latin indices run through $\{1, 2, 3\}$ and represent coordinates intrinsic to a given spatial hypersurface. Using the orthogonal projection operator $\perp^\mu{}_\nu := \delta^\mu{}_\nu + n^\mu n_\nu$, we obtain the induced metric on Σ_t, $\gamma_{ij} := g_{\mu\nu} \perp^\mu{}_i \perp^\nu{}_j$, where $g_{\mu\nu}$ is the four-dimensional spacetime metric. The line element can be written in terms of these quantities as

$$ds^2 = -\alpha^2 dt^2 + \gamma_{ij}(dx^i + \beta^i dt)(dx^j + \beta^j dt). \tag{3.2}$$

The extrinsic curvature of a slice Σ_t can be written in terms of a Lie derivative as

$$K_{ij} := -\frac{1}{2}\mathcal{L}_n \gamma_{ij} \ . \tag{3.3}$$

Projecting the Einstein equations onto the hypersurface Σ_t, one obtains the constraint equations

$$R + K^2 + K_{ij}K^{ij} = 16\pi E, \tag{3.4}$$

$$D_j K^{ij} - D^i K = 8\pi p^i, \tag{3.5}$$

where $K = \gamma^{ij} K_{ij}$, R, and D_i are the Ricci scalar and covariant derivative associated with γ_{ij}, respectively, and E and p^i are the energy and momentum density as measured by an Eulerian observer, respectively.

In the language of the $3+1$ decomposition, initial data for the Einstein field equations (and any matter evolution equations) are a set of 20 functions representing the components of α, β^i, γ_{ij}, K_{ij}, E, and p^i on the initial slice Σ_t that together satisfy the constraints (3.4)–(3.5). Though, in principle, there are numerous conceivable ways of coming up with consistent initial data, it is challenging to separate freely specifiable versus constrained degrees of freedom in a manner where the underlying physical interpretation of the free data is transparent, and where the choice of the free data leads to a well-posed set of constraint equations. The CTS method [187] is a prescription for this separation of degrees of freedom that begins with a conformal decomposition of the spatial metric and the extrinsic curvature. Introducing the conformal factor Ψ, we define

$$\begin{aligned} \tilde{\gamma}_{ij} &:= \Psi^{-4} \gamma_{ij}, & (3.6) \\ \hat{A}^{ij} &:= \Psi^{10} \left(K^{ij} - \frac{1}{3} K \gamma^{ij} \right) \\ &= \frac{1}{2\tilde{\alpha}} \left[\dot{\tilde{\gamma}}^{ij} + \tilde{D}^i \beta^j + \tilde{D}^j \beta^i - \frac{2}{3} \tilde{\gamma}^{ij} \tilde{D}_k \beta^k \right], & (3.7) \end{aligned}$$

where $\dot{\tilde{\gamma}}^{ij} := \Psi^4 (\dot{\gamma}^{ij} - \frac{1}{3} \gamma^{ij} \gamma_{kl} \dot{\gamma}^{kl})$ is defined to be traceless, the overdot indicates a time derivative, $\tilde{\alpha} := \Psi^{-6} \alpha$, and $\tilde{R}$ and $\tilde{D}_i$ are the Ricci scalar and covariant derivative associated with $\tilde{\gamma}_{ij}$, respectively. With these definitions we can rewrite (3.4) and (3.5) in the CTS form as

$$\begin{aligned} \tilde{D}_i \tilde{D}^i \Psi - \frac{\tilde{R}}{8} \Psi + \frac{1}{8} \hat{A}_{ij} \hat{A}^{ij} \Psi^{-7} - \frac{K^2}{12} \Psi^5 &= -2\pi \Psi^{-3} \tilde{E} & (3.8) \\ \tilde{D}_j \hat{A}^{ij} - \frac{2}{3} \Psi^6 \tilde{D}^i K &= 8\pi \tilde{p}^i & (3.9) \end{aligned}$$

with $\tilde{p}^i := \Psi^{10} p^i$, $\tilde{E} := \Psi^8 E$. Initial data is obtained by solving this system of four elliptic equations for Ψ and β^i [upon substitution of (3.7) into (3.9)], where $\tilde{\gamma}_{ij}$, $\dot{\tilde{\gamma}}^{ij}$, K, $\tilde{\alpha}$, $\tilde{E}$, and $\tilde{p}^i$ are the "free data" that can be freely specified to reflect the physical system under investigation.

3.2.2 Superposed free data

Under the conformal thin-sandwich method one is free to choose any values for $\tilde{\gamma}_{ij}$, $\dot{\tilde{\gamma}}^{ij}$, $\tilde{\alpha}$, K, $\tilde{E}$, and $\tilde{p}^i$ for which a solution can be found. In this section we outline our method for determining this free data in order to construct initial data representing binary systems. The basic idea is as follows. Since solutions to the Einstein equations representing isolated compact objects (black holes, stars, etc.) are well known, and since if the separation between the objects is not too small the solution describing two compact objects is well-approximated by superposing the two isolated solutions, we therefore set our free data using such a superposed solution and then solve the constraint equations in order to obtain the nonlinear correction.

There are many ways to combine the metrics representing isolated compact objects. The method we use is based on the $3+1$ splitting. Let $\gamma_{ij}^{(1)}$, $\dot{\gamma}_{ij}^{(1)}$, $\alpha^{(1)}$, and $\beta^{i(1)}$ represent the spatial metric, time derivative of the spatial metric, lapse, and shift, respectively, of the first isolated solution (e.g. a boosted black hole or neutron star solution) and similarly for the second isolated solution. Then, we construct the following quantities:

$$\gamma_{ij}^{(\mathrm{sup})} = \gamma_{ij}^{(1)} + \gamma_{ij}^{(2)} - f_{ij} \tag{3.10}$$

$$\dot{\gamma}_{ij}^{(\mathrm{sup})} = \dot{\gamma}_{ij}^{(1)} + \dot{\gamma}_{ij}^{(2)} \tag{3.11}$$

$$\alpha^{(\mathrm{sup})} = \alpha^{(1)} + \alpha^{(2)} - 1 \tag{3.12}$$

$$\beta^{i(\mathrm{sup})} = \beta^{i(1)} + \beta^{i(2)} \tag{3.13}$$

where f_{ij} is the flat-space metric. This particular construction will break down if $\alpha^{(\mathrm{sup})} \leq 0$ or $\det[\gamma_{ij}^{(\mathrm{sup})}] \leq 0$ anywhere in the domain, which would then require some other way of combining the metrics, for example, using distance-weighted attenuation functions as in [239]. (In [217] it was also found necessary to enforce a desired asymptotic falloff of the superposed metric, owing to the use of a corotating frame.) However, these conditions are not violated for the cases considered here. From the above quantities, we then calculate the free data we will use when solving the CTS equations from the usual relations:

$$\tilde{\gamma}_{ij} = \gamma_{ij}^{(\mathrm{sup})} \tag{3.14}$$

$$\dot{\tilde{\gamma}}^{ij} = -\tilde{\gamma}^{ik}\tilde{\gamma}^{jl}\left(\dot{\gamma}_{kl}^{(\mathrm{sup})} - \frac{1}{3}\tilde{\gamma}^{mn}\dot{\gamma}_{mn}^{(\mathrm{sup})}\tilde{\gamma}_{kl}\right) \tag{3.15}$$

$$\tilde{\alpha} = \alpha^{(\mathrm{sup})} \tag{3.16}$$

$$K = \frac{1}{2\tilde{\alpha}}(2\partial_i\beta^{i(\mathrm{sup})} + \dot{\tilde{\gamma}}^{ij}\tilde{\gamma}_{ij} + \tilde{\gamma}^{ij}\beta^{k(\mathrm{sup})}\partial_k\tilde{\gamma}_{ij}). \tag{3.17}$$

For initial data with matter we use a similar method. We set $\tilde{E}$ and $\tilde{p}^i$ by superposing the energy and momentum density of the two objects (we do not consider situations where they would both be nonzero at the same point). For some cases (in particular for the ultrarelativistic boosts), we rescale the momentum density so that its magnitude with respect to the superposed metric $\tilde{\gamma}_{ij}$ is equal to the magnitude of the original momentum density with respect to the metric of the isolated object ($\gamma_{ij}^{(1)}$ or $\gamma_{ij}^{(2)}$). This ensures that $\tilde{E}^2$ and $\tilde{p}^i\tilde{p}_i$ have the same ratio as the isolated objects. This is important since the choice of conformal scaling of the energy $\tilde{E} = E\Psi^8$ was designed to ensure that if the conformal quantities satisfy the dominant energy condition, $\sqrt{\tilde{\gamma}_{ij}\tilde{p}^i\tilde{p}^j} \leq \tilde{E}$, then so will the rescaled quantities following the solution of the constraints.

3.2.3 Regularizing black hole solutions

In cases where black holes are a part of the physical system, the divergences at the black hole's singularity must be addressed. As discussed in the Introduction, there are several ways to deal with this issue in the initial data problem; the approach we take here is to explicitly modify the metric of an isolated (prior to superposition) black hole solution inside the horizon to take a prescribed, regular form. The regularized region will not in general satisfy the vacuum constraint equations, and to avoid a singular conformal factor and shift vector components when solving the constraints with such background data, we introduce unphysical energy-momentum in the union of black hole interiors so that these regions automatically satisfy the constraints, albeit with the unphysical interior matter source.

We start with a single, unboosted spinning black hole spacetime in horizon penetrating coordinates (for the results described here we use the harmonic form of Kerr derived in [144], though we have also tried it using Kerr-Schild coordinates without difficulty), so that the only divergences in the metric components are well within the horizon. We then choose a surface that encloses the singular region, yet is strictly inside the event horizon. The interior of this surface we call the *regularization region*. Outside the regularization region we do not modify the metric. Inside, there are many conceivable ways to alter the metric to eliminate the divergences. The simple approach we take is to promote the black hole mass M and spin a constants to functions of space and smoothly decrease them from their bare values at the regularization surface to zero at some surface interior to this.

Specifically, we introduce a regularization function

$$f_{\text{reg}}(x) = \begin{cases} 1, & x > 1, \\ x^3 \left(6x^2 - 15x + 10\right), & 1 > x > 0, \\ 0, & 0 > x, \end{cases} \tag{3.18}$$

chosen to be twice continuously differentiable so that the consequent unphysical energy is well behaved. We use a Cartesian grid[1] and define $r^{(E)}(x,y,z) = \sqrt{x^2+y^2+z^2}$ as the Euclidean radius for a point with coordinates x, y, z. We then replace the mass M and the spin parameter a with $\xi(x,y,z)M$ and $\xi(x,y,z)a$, respectively, in all the metric components, where

$$\xi(x,y,z) = f_{\rm reg}\left(\frac{(r^{(E)}(x,y,z)/r_+^{(E)}(x,y,z)) - q_{\rm in}}{q_{\rm out} - q_{\rm in}}\right), \tag{3.19}$$

$r_+^{(E)}(x,y,z)$ is the Euclidean radius for the point on the event horizon at the same angular direction as (x,y,z), $q_{\rm out}$ defines the outer surface of the regularization region, and $q_{\rm in}$ is the inner surface inside of which the metric is Minkowski, with $1 > q_{\rm out} > q_{\rm in} > 0$. The shape of the regularization region, namely a shrunken form of the interior of the event horizon, was motivated by the similar volume excised during evolution (though that is based on the apparent horizon, and the excision surface is a best-fit ellipsoid rather than the exact shape of the apparent horizon). The particular values of $q_{\rm out}$ and $q_{\rm in}$ are not too important (i.e., give essentially the same solutions), the only practical requirements being that $q_{\rm out}$ represents a surface within the excision surface we will use during evolution and that $q_{\rm in}$ is not to be too close to $q_{\rm out}$; otherwise excessive resolution is needed to resolve the transition.

Once we have an everywhere-regular metric, we superpose it with any other COs to construct the free data as described in Sec. 3.2.2. We then compute the unphysical energy and momentum we will add to the regularization regions simply by evaluat-

[1]Note that in the harmonic coordinates of [144] only the region with $r_K > M$ is represented on the Cartesian grid $r \geq 0$, where r_K is the radial coordinate of the the metric in ingoing null Kerr form. Hence the physical singularity is not on the grid; however, the metric components are discontinuous at $x = y = z = 0$ ($r_K = M$), and hence regularization is still required.

ing (3.4) and (3.5) with the background, superposed data

$$E_{\text{unphys}} := \tfrac{1}{16\pi}(R + K^2 + K_{ij}K^{ij})^{(\text{sup})}, \tag{3.20}$$

$$p^i_{\text{unphys}} := \tfrac{1}{8\pi}(D_j K^{ij} - D^i K)^{(\text{sup})}. \tag{3.21}$$

E_{unphys} and p^i_{unphys} are then added to $\tilde{E}$ and $\tilde{p}^i$ within the regularization regions, and we can then solve the CTS equations as usual without any additional special treatment of these regions. It is also possible to calculate the unphysical energy-momentum before the superposition and add E_{unphys} and p^i_{unphys} directly. The former method gives a small discontinuity of E_{unphys} and p^i_{unphys} at the boundary of the regularization region, whereas the latter one gives continuous quantities. Either approach leads to similar results, but the former gives more rapid relaxation of the elliptic equations and is the choice for the cases presented here.

During evolution, we choose black hole excision surfaces that entirely contain the regularization regions and unphysical matter. Thus, one can think of the unphysical matter as serving as a proxy for what would otherwise be boundary conditions for Ψ and β^i on excision surfaces. Given a solution to the constraints with regularized interiors it is trivial to read off what the equivalent (Dirichlet) boundary conditions would have been, though the inverse problem of mapping some set of desired boundary conditions to interior sources is less trivial and likely not well posed in general.

3.2.4 Fluid solutions

For the applications with (physical) matter considered here we use Tolman-Oppenheimer-Volkov (TOV) star solutions in isotropic coordinates to construct the metric free data quantities as well as $\tilde{E}$ and $\tilde{p}^i$. Such solutions are derived by assuming a relationship between the pressure and density $P(\rho)$, e.g. as given by a polytropic condition. Once the constraint equations have been solved and E

and p^i found, we determine the new density and pressure profiles using this same relationship and solving the equation

$$(E + P(\rho))(E - \rho) - p_i p^i = 0 \tag{3.22}$$

for ρ, which follows directly from the expressions for the energy and momentum density of a perfect fluid. For the applications considered here, we do not explicitly impose any additional constraints on the fluid quantities (e.g. that the fluid be in hydrostatic equilibrium). We leave that to future extensions.

3.2.5 Multigrid elliptic solver

To numerically solve the CTS equations we discretize (3.8) and (3.9) using standard second-order finite difference operators and solve them using a full approximation storage implementation of the multigrid algorithm with adaptive mesh refinement (AMR) as described in [240]. A multigrid algorithm is characterized by a smoothing operation and by a choice of restriction and prolongation operators. We use Newton-Gauss-Seidel relaxation for smoothing, and half-weight restriction and linear interpolation for the restriction and prolongation operators, respectively. These latter operators require special treatment on mesh refinement boundaries which we outline in Sec 3.2.6. Unlike in the evolution code, we do not use a compactified coordinate system extending to spatial infinity. Rather, the initial data numerical grid extends to a large but finite radius. This is to avoid numerical problems attributable to large Jacobian factors needed in compactification which become especially problematic near the corners of the boundary. At the outer boundaries we impose boundary conditions that $\Psi = 1$ and $\beta^i = \beta^{i(\mathrm{sup})}$. Since the use of mesh refinement enables us to put the outer boundary far away from the compact objects, these boundary conditions can be made sufficiently accurate compared to numerical error (though for future applica-

tions they could also be replaced with, e.g., Robin boundary conditions). Any points outside this domain on the evolution grid are initialized via extrapolation, assuming a leading order $1/r$ approach to an asymptotically flat spacetime.

For some applications we wish to solve for initial data with axisymmetry. To efficiently solve the constraint equations in these situations we have implemented a modified version of the Cartoon method [125] similar to that used in [79]. Letting the y axis be the axis of symmetry, we restrict our computational domain to a subset of the half-plane $(x, y) \in (-\infty, \infty) \times [0, \infty)$. We use the existence of an axisymmetric Killing vector to express derivatives in the z direction in terms of derivatives in the x and y directions. On the y axis we impose regularity, which gives the following conditions for the constrained variables: $\partial_y \Psi = 0$ and $\partial_y \beta^x = \partial_y \beta^y = \beta^z = 0$.

3.2.6 Multigrid AMR interpolation

A multigrid algorithm requires a restriction operator to inject quantities from finer to coarser grids as well as a prolongation operator to interpolate corrections from coarser grids to finer grids (see e.g. [241]). For our multigrid algorithm we use half-weight restriction as our restriction operator. In three dimensions half-weight restriction can be written as

$$f_{\mathrm{HW}} = f_{i,j,k} + \frac{1}{12}(\Delta f_{xx} + \Delta f_{yy} + \Delta f_{zz}), \tag{3.23}$$

where

$$\Delta_{xx} f = f_{i+1,j,k} - 2 f_{i,j,k} + f_{i-1,j,k}, \tag{3.24}$$

and similarly for the y and z directions. Note that $\Delta_{xx} f$ divided by h^2 (where h is the grid spacing) is a second-order approximation for $\partial_x^2 f$. On AMR boundaries where the full stencil is not available we must modify the above expression. For example, on

a negative x boundary we replace $\Delta_{xx} f$ by a right-handed second derivative stencil

$$\Delta_{xx} f = 2f_{i,j,k} - 5f_{i-1,j,k} + 4f_{i-2,j,k} - f_{i-3,j,k} \tag{3.25}$$

and so on for the other directions. This ensures not only that $f_{\rm HW}$ is a second-order representation of f, but also that $f_{\rm HW}$ is smooth to $O(h^4)$ on AMR boundaries. Hence if second derivatives of $f_{\rm HW}$ are computed including restricted boundary points in the stencil, the error will be $O(h^2)$.

We use linear interpolation as our prolongation operator. However, after applying a correction from a coarse grid, we reset the values on the AMR boundaries of the fine grid for the points that do not exist on the coarse level with fourth-order interpolation using those points that do. We found this higher order interpolation to be beneficial as we do not relax the points on the boundary.

3.3 Applications

3.3.1 Quasicircular binary black holes

As a first application of our technique, we generate and evolve ID for the (approximate) quasicircular inspiral of two nonspinning, equal-mass black holes. Our present method for providing free data is not designed to easily give initial data for quasicircular inspiral (though presumably with sufficient fine-tuning of the boost vectors this could be achieved), and this basic example is mainly to provide a relatively low eccentricity binary, a couple of orbits before merger, for comparison to past studies. Specifically, we are interested in seeing how close the masses, etc., of the black holes obtained following the solution of the constraints are to the corresponding parameters used in constructing the free data, and how much "spurious" gravitational radiation is present in the initial data.

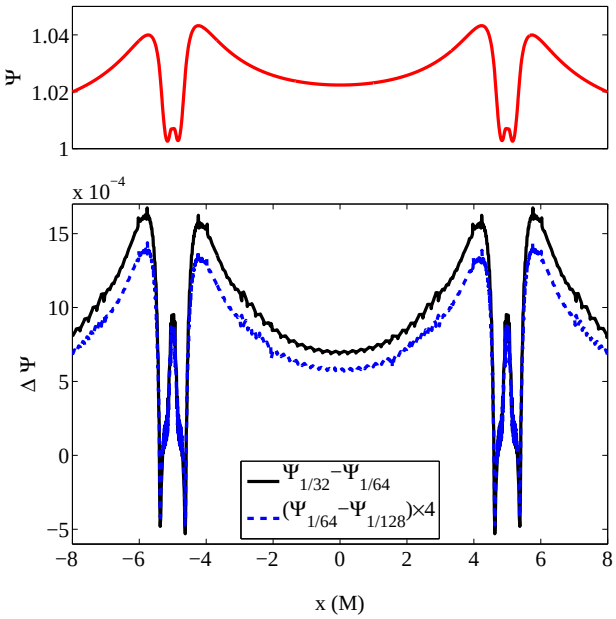

Figure 3.1: The conformal factor Ψ from BH-BH ID. Upper: Ψ on the x axis which lies on the orbital plane and goes through the centers of the black holes. Lower: Differences in Ψ with resolution on the x axis, scaled assuming second-order convergence.

For the initial data, we use free data set by superposing two boosted nonspinning equal mass black holes at a coordinate separation of $10M$, where M is the sum of the isolated black hole masses (which in general will be different from the irreducible masses of the black holes once the constraint equations are solved). The black holes are given purely tangential boost velocities chosen so that, when evolved, the black holes undergo a few orbits with monotonically decreasing proper separation. The initial data grid extends to $\pm 2048M$ in all three directions. For convergence studies of the initial data solver, we use three base grid sizes of 33^3, 65^3, and 129^3 and 12 levels of mesh refinement with identical grid structures in each case. As expected, the conformal factor and shift vector exhibit second-order convergence as shown in Figs. 3.1 and 3.2, as does the residual of (3.4) and (3.5). For evolution, we use the highest resolution initial data. The ID is evolved using the generalized harmonic formulation of the field equations, choosing harmonic coordinates at $t = 0$ and transitioning to

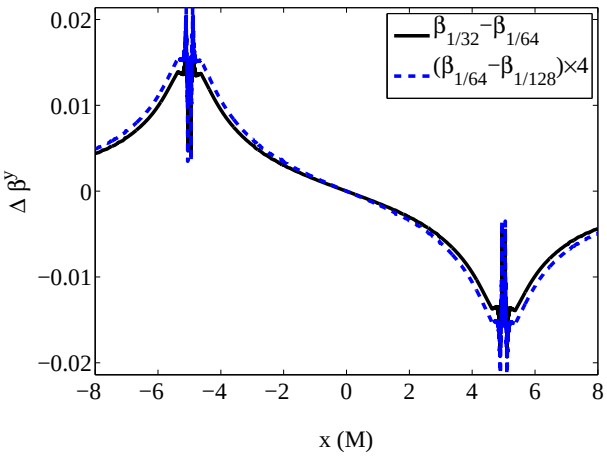

Figure 3.2: Differences in the shift component β^y with resolution on the x axis from BH-BH ID, scaled assuming second-order convergence.

a damped harmonic gauge as described in Chap. 2. The eccentricity is estimated to be $e \approx 0.05$ based on the evolution of the coordinate distance between the centers of the apparent horizons as shown in Fig. 3.3. Though the orbital eccentricity could presumably be reduced further by tuning the initial velocities using methods such as the one proposed in [242] or using the post-Newtonian approximation as in [243], we did not attempt to do so for this basic comparison. Because of corrections from solving the constraints, the sum of the masses of the isolated black holes whose space-times we superpose M is different from the sum of irreducible masses computed from their apparent horizons at the beginning of the evolution $M_{\rm irr}$. For this particular case $M_{\rm irr}/M = 1.21$. The ID is constructed using free data with nonspinning black holes, and the initial spin calculated from the apparent horizons is zero to within truncation error ($|S/M_{\rm BH}^2| < 6 \times 10^{-3}$). The ratio of the irreducible mass of the final black hole after the merger to the sum of the irreducible masses of the initial black holes is $M_{{\rm irr},f}/M_{\rm irr} = 0.885$, and the dimensionless spin parameter of the final black hole is $a_f/M_f = 0.678$. Both of these values are in good agreement (considering the mild initial eccentricity here) with the high accuracy results of 0.88433 and 0.68646,

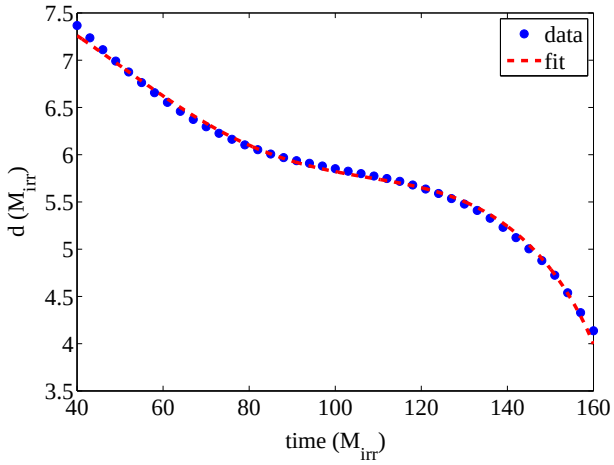

Figure 3.3: Coordinate separation of the centers of the two black holes fitted to a function $(A - B(t - t_0))^{1/4} + C\cos(\omega(t - t_0) + \phi)$. This function combines the decaying orbit attributable to quadrupole radiation with the effects of eccentricity, given by $e = C/d(t = t_0) \approx 0.05$. Because of early-time gauge effects (a transition from harmonic to damped harmonic gauge) we exclude the first $t = 40M_{\rm irr}$ from the fit.

respectively, from [244]. In Fig. 3.4 we show the gravitational waves from the BH-BH merger. The initial spurious part of the signal is of comparable magnitude to other ID approaches that do not attempt to include gravitational waves from the prior inspiral; see, for example, [223].

3.3.2 Eccentric compact object mergers

As another application of this technique, we consider constructing initial data describing a dynamical capture BH-NS binary. We set the free data using a boosted harmonic black hole solution and a neutron star with the HB equation of state [23]. Let M be the sum of the masses of the isolated black hole and neutron star. We construct initial data for a 4:1 BH-NS binary by setting the boost velocities to correspond to a Newtonian orbit with eccentricity $e = 1$ and periapse distance $r_p = 5M$ at various initial separations d. We keep the mass and spin that we use for the black hole component of the free data fixed at $0.8M$ and $-0.4M$, respectively (where the

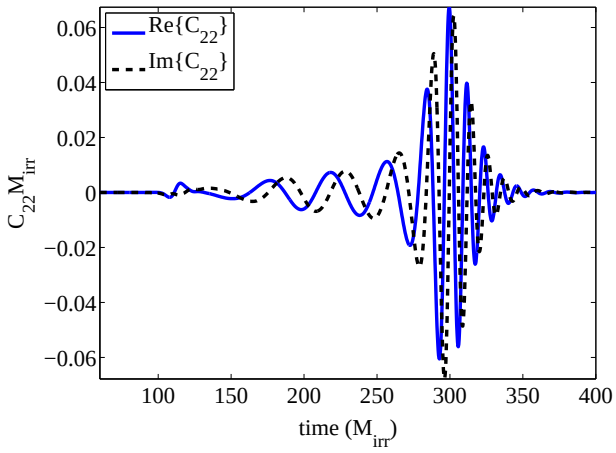

Figure 3.4: The real and imaginary components of the $l = 2$, $m = 2$ spin-weight -2 spherical harmonic of $r\Psi_4$ extracted at a radius of $105M$. Time is measured from the beginning of the simulation.

negative sign indicates that the spin is retrograde with respect to the orbital angular momentum) and the mass of the neutron star component of the free data fixed at $0.2M$. The spin and masses will receive corrections from solving the constraint equations and with decreasing d these will differ more and more from the input parameters of the free data. The input parameters can, of course, be tuned to achieve desired values in the final solution. However, since here we are mainly interested in quantifying this difference, we keep them fixed. We use a grid extending from $-1600M$ to $1600M$ in each dimension where the base level is covered by 257^3 points and there are nine additional levels of mesh refinement, each with a refinement ratio of two. We solve for data with initial separations $d/M = 15$, 25, and 50. In Table 3.1 we show the maximum difference of the conformal factor from unity as well as the actual ADM (Arnowitt-Deser-Misner) mass, black hole mass and spin, neutron star rest mass, and induced neutron star density oscillations for these three different separations. We can see that even at a separation of 15 M the difference between input and final parameters is small—at the level of a few percent. At such separations, however, the oscillations induced in the neutron star by the initial setup become large. This prob-

lem could be remedied by adding additional constraints to the matter, for example, requiring it to satisfy an equilibrium version of the Euler equations.

We evolve the initial data past merger using three different resolutions. To give some sense of the smallest scales resolved in these runs, the low (medium, high) resolution run has two finest-level meshes centered around the BH and NS of roughly 80^3 (100^3, 150^3) cells each, resolving the diameter of the NS with approximately 40 (50, 75) cells and the BH horizon diameter with roughly 70 (85, 130) cells. Unless otherwise stated, all quantities are from the high resolution runs. In Fig. 3.5 we show the norm of the constraints throughout the evolution of the $d = 15M$ ID at the different resolutions. The single highest, resolution ID is used for all evolution runs, so the fact that evolution constraints are converging to zero indicates that the truncation error of the ID is at least as small as that of the highest resolution evolution. In Fig. 3.6 we plot the amplitude of the gravitational waves measured from the three different evolutions to show the amount of spurious gravitational radiation this method of constructing ID introduces. The level of spurious gravitational radiation decreases with increasing separation and in all three cases is small—an order of magnitude or more below the physical signal of interest. After the passage of the spurious gravitational radiation, the gravitational wave signal from all three initial separations is approximately the same, though there are small differences owing to the changes in parameters indicated in Table 3.1, and because we are starting the systems along different points of a Newtonian trajectory.

3.3.3 Ultrarelativistic initial data

As a final application, we consider the problem of specifying ID for ultrarelativistic collisions. The study of the collision of objects where kinetic energy dominates the dynamics of the spacetime is of considerable interest to super-Planck scale particle collisions, as arguments suggest classical Einstein gravity will be adequate to describe

d/M	$\max(\lvert\Psi-1\rvert)$	$M_0/M_{0,\infty}$	$M_{\rm BH}/M$	$a_{\rm BH}/M$	$M_{\rm ADM}/M$	$\rho_{\rm oscill.}$ (%)
15	0.0155	1.077	0.832	−0.398	1.051	14.3
25	0.0092	1.049	0.818	−0.402	1.030	9.0
50	0.0046	1.028	0.808	−0.399	1.017	4.5

Table 3.1: Characteristics of BH-NS initial data with Newtonian orbital parameters $r_p = 5M$ and $e = 1$ with three initial coordinate separations d. Here $\max(|\Psi - 1|)$ is the maximum deviation over the entire domain of the conformal factor from the background free-data value of unity, $M_0/M_{0,\infty}$ is the rest mass of the neutron star compared to its isolated rest mass, $M_{\rm BH}/M$ and $a_{\rm BH}/M$ are the black hole mass and spin parameters measured from the apparent horizon relative to the initial total mass M of the free data, $M_{\rm ADM}/M$ is the relative ADM mass of the solution, and $\rho_{\rm oscill.}$ is the relative magnitude of the oscillation in time of the maximum rest mass density of the neutron star induced by the ID construction.

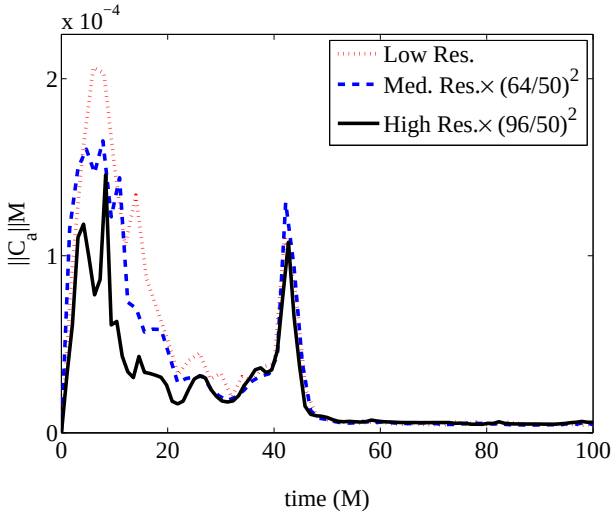

Figure 3.5: The L^2 norm of the constraint violation, $C_a := H_a - \Box x_a$, in units of $1/M$ for the $d = 15M$ BH-NS merger in the $100M \times 100M$ region around the center of mass in the equatorial plane (i.e. $\sqrt{\int \|C_a\|^2 d^2x / \int d^2x}$). This is shown for low, medium, and high resolutions where the latter two are scaled assuming second-order convergence.

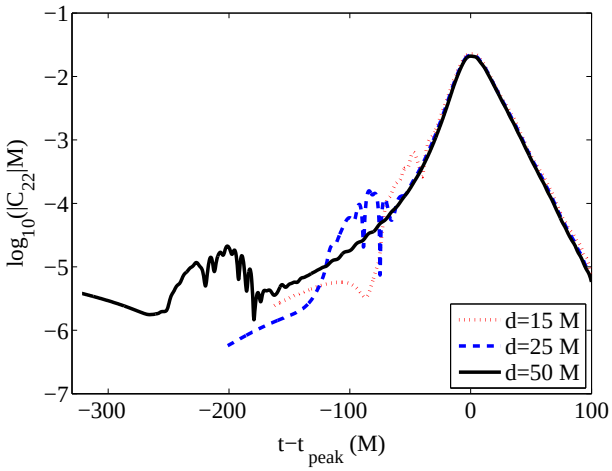

Figure 3.6: The log of the magnitude of the $l = 2$, $m = 2$ spin-weight -2 spherical harmonic of $r\Psi_4$ for BH-NS simulations with different initial separations d. The value of Ψ_4 was extracted on a sphere of radius $100M$ and is shown starting at the beginning of the simulation and continuing past merger. The waveforms have been aligned so that the peaks occurs at time 0.

the process [245, 246, 247]. The hoop conjecture [248] predicts that the generic outcome of a sufficiently ultrarelativistic collision will be black hole formation, and this, together with suggestions of a tera-electron-volt Planck scale [72, 74], imply that, if such a scenario describes nature, the Large Hadron Collider or cosmic ray collisions with Earth could produce black holes [75, 76, 77]. Though to date no signs of black hole production have been observed [249, 250], the nature of the kinetic energy dominated regime in general relativity is of interest in its own right and has largely been unexplored.

Initial data describing such systems will be far from equilibrium, and one cannot assume that the solution is time symmetric or quasistatic. It is instructive to recall the Aichelburg-Sexl [251] solution describing a gravitational shock wave. The solution can be obtained from a boosted Schwarzschild solution by simultaneously taking the mass to zero and the boost parameter to infinity, while keeping their product constant and finite. Two such oppositely boosted solutions can be superposed to obtain a new solution that is valid up until collision. Though it is not clear how applicable this is to

the nonlimiting case, this suggests that superposition may be a good approximation to describing such spacetimes.

Here we consider the specific example of the setup for a head-on collision of two fluid star solutions. We use the method described in Sec. 3.2.2 to construct free data from two $\Gamma = 2$ polytropic TOV star solutions that have unboosted mass M_* and a compactness (ratio of mass to radius) of $C = 0.01$. The stars are boosted toward each other with boost factor $\gamma = 10$. We consider a sequence of solutions at various initial coordinate separations d. We take advantage of the axisymmetry of the problem and use $[-2000M, 2000M] \times [0, 2000M]$ where $M := 2\gamma M_*$ as our computational domain. The base level is covered by 1025×513 points, and there are nine additional levels of mesh refinement. To test convergence we also consider two lower resolutions with grid spacing 2 and 4/3 times as coarse.

Using the method for specifying free data described in Sec. 3.2.2, as $d \to \infty$ we expect the corrections from solving the constraints will go to zero: $\Psi \to 1$, the magnitude of the coordinate velocities of the stars $|v|$ will approach $\sqrt{1-\gamma^{-2}}$, the ADM mass $M_{\rm ADM}$ will approach M, and the total rest mass M_0 will approach the sum of the rest masses of the isolated stars $M_{0,\infty}$. In Fig. 3.7 we show how all these quantities change with coordinate separation. We can see that it is possible to solve for ID where the stars are quite close together, though the corrections become large, and in particular the ADM mass decreases quite significantly.

To give an indication of the numerical errors on these quantities, we can compare the values obtained at the highest resolution to the Richardson extrapolated values using all three resolutions. For example, for the smallest separation $d = 1.56M$, we have $\max(|\Psi - 1|) = 0.05326$ (0.05325) and $\max|\mathrm{v}| = 0.530149$ (0.530153) where the values in parentheses are the Richardson extrapolated quantities (which are consistent with approximately second-order convergence).

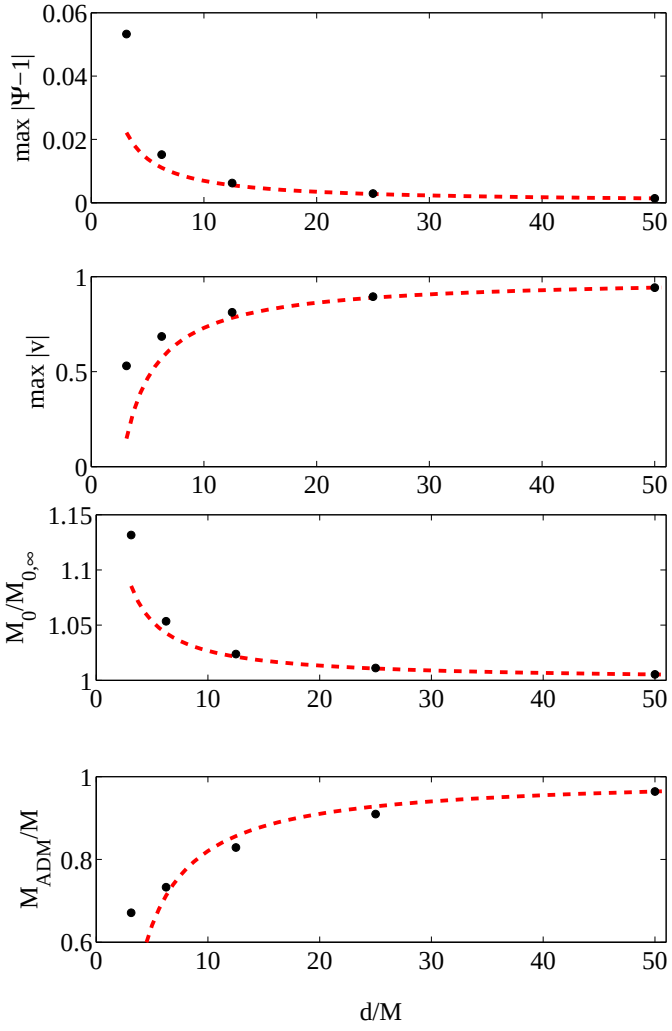

Figure 3.7: Various quantities from ultrarelativistic collision ID with $\gamma = 10$ made using the superposition method for constructing free data. From top to bottom the quantities shown are the maximum (over the entire domain) difference of the conformal factor from unity, the maximum coordinate velocity of the fluid, the total rest mass, and the ADM mass. All quantities are shown as a function of d, the coordinate separation between the two stars. For all these cases the maximum of $|\Psi - 1|$ occurs for values of Ψ that are less than unity. One might expect these quantities to approach their infinite separation limits as $1/d$ for large d; the dotted lines show such $1/d$ curves for each quantity matched to the $d/M = 50$ point.

We can compare the above method of constructing free data for this case to a conformally flat method. Specifically, we set all the metric free data quantities to their flatspace values and set $\tilde{E}$ and $\tilde{p}^i$ for each star to a special-relativistically boosted density and pressure profile taken from the TOV solution. In Fig. 3.8 we show the same quantities as in Fig. 3.7 but using this conformally flat method. In this case the corrections from solving the constraints will not go to zero with infinite separation since all the nontrivial geometry is coming from the conformal factor. Hence the energy-momentum will be substantially rescaled at any separation. Also in contrast to the first method, the maximum of $|\Psi - 1|$ occurs for $\Psi > 1$ instead of $\Psi < 1$, which means E and p^i will be smaller than their conformal counterparts. With conformally flat ID it is also possible to solve for stars close together, though, as in the previous method, the ADM mass decreases steeply. It should also be noted that because of the large shift vector obtained with the second method, the coordinate velocity is substantially greater than one, which may make it more challenging to numerically evolve.

A full characterization of this ultrarelativistic collision ID requires evolution, which we present in Chap. 8.

3.4 Conclusions

We have outlined a general method for constructing initial data based on superposition and the CTS formulation of the constraint equations, and demonstrated the method with some example solutions. Though there are numerous existing applications of the CTS method, and superposition has been proposed before, some of the notable aspects of the work presented here include adding the matter and metric of neutron stars to the prescription, regularizing the interiors of black holes with (unphysical) matter sources, and applying it to regimes not yet studied before,

namely, initial data for generic high-eccentricity binary mergers and ultrarelativistic collisions. For astrophysically relevant binaries we find that superposition of single, isolated compact object solutions works well in the sense that nonlinear correction from solving the constraints are relatively small for larger initial separations, implying that superposition is a good start to attain more astrophysically realistic initial data (for example, by adding prior gravitational wave information as in [223] to the superposed background data for quasicircular or low eccentricity inspirals). Including neutron stars, we find that the superposition effectively induces oscillations in the stars. This again is small for large separations and hence a good approximation to dynamical capture binaries. However, practical application to low eccentricity inspirals will likely require that the CTS equations be supplemented with some form of quasiequilibrium equations for the hydrodynamics (as in many existing ID methods, for example [200, 208, 225]).

For the ultrarelativistic boost examples we are able to obtain solutions to the CTS equations with superposed and conformally flat data well into the kinetic energy dominated regime ($\gamma = 10$) for sufficiently large initial separations. At smaller separations we are still able to obtain solutions. However, for these initial data sets the corrections to the metric and fluid properties become large, and it is less clear how to separate the total energy of the spacetime into kinetic energy, rest mass energy, etc. This will require evolution to resolve, and we leave that to future work. Nevertheless, given that there are few results on the uniqueness and existence of solutions to the conformal constraint equations beyond constant mean curvature slicing [252] (and in some cases, such as the extended CTS equations [253] there are known examples of nonuniqueness [254]), it is interesting that we are able to obtain solutions in this highly nonlinear regime.

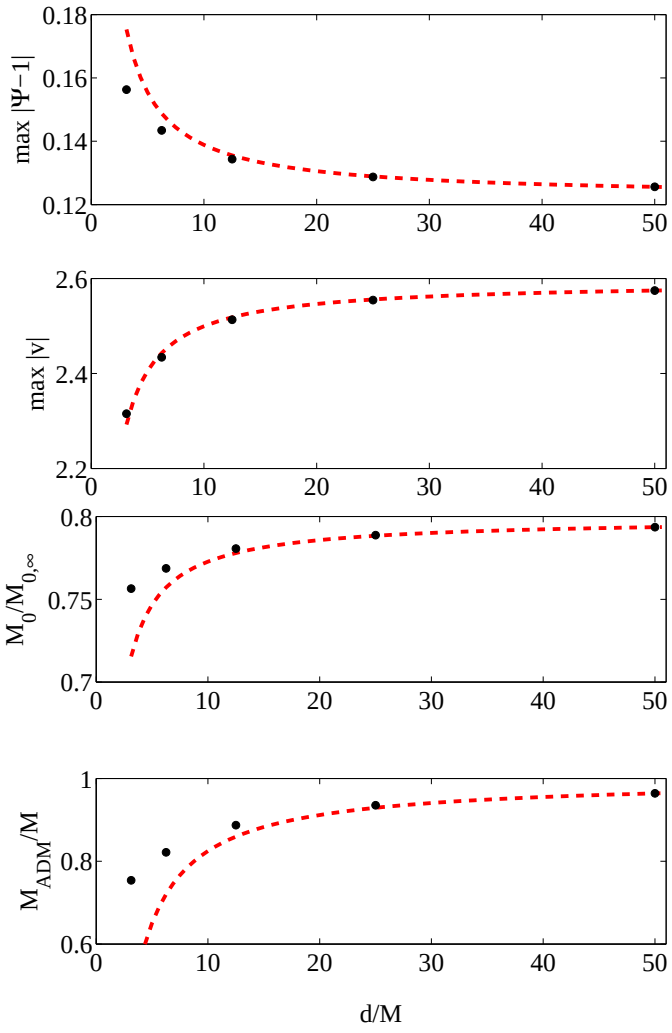

Figure 3.8: Same as Fig. 3.7 but with conformally flat data. For all these cases the maximum of $|\Psi - 1|$ occurs for values of Ψ that are greater than unity.

Chapter 4

Dynamical capture black hole-neutron star mergers

4.1 Introduction

It is important to understand mergers of black holes (BHs) and neutron stars (NSs) not only because they are a chief source for ground-based gravitational wave (GW) detectors (such as LIGO [10]) but also because they may be accompanied by a diverse range of electromagnetic (EM) and neutrino emission. One of the more interesting possibilities in this regard is that BH-NS mergers may be progenitors of a fraction of observed short-hard gamma-ray bursts (sGRBs) [32, 33, 34]. Furthermore, existing and planned wide-field survey telescopes such as PTF [43], Pan-STARRS [44], and LSST [45] are beginning to observe and classify fainter EM transient events, some of which are expected to be produced in BH-NS mergers from a variety of mechanisms (see [88] for a recent, detailed exploration of the possibilities). Coincident observation of these EM events with a gravitational wave signal from a binary coalescence would provide a wealth of additional information about the system beyond any individual observation, even, for example, providing an independent way to measure cosmologi-

cal parameters [255]. However this depends on having a good understanding of how to map the particular observations to the underlying astrophysical processes governing the merger.

The great diversity in sGRBs hints at the possibility that there will be a corresponding diversity in the associated GW and EM signals, and motivates the exploration of all viable channels for binary compact (BCO) mergers. BCOs may form through the evolution of primordial binaries or through dynamical capture in dense stellar systems, such as nuclear or globular clusters. BCOs formed through the latter channel, which could merge with non-negligible eccentricity, are the focus of this and the subsequent two chapters. In this chapter we study dynamical capture BH-NS evolution using full general relativistic hydrodynamics (following-up and extending the first such study performed in [4]). Before delving into the details, we briefly summarize the motivation for studying this class of BCO. In contrast, most studies of BH-NS mergers to date have focused on the quasicircular inspiral case; see [162] for a review of these efforts.

A chance close-encounter of two compact objects in a stellar cluster could result in a bound system if the energy loss due to GW emission is sufficiently large. (Tidal interaction with the NS is also a source of energy loss [256], though due to the relative scalings with distance, to leading-order the total cross section for *capture* is dominated by the GW emission.) Because of gravitational focusing, a sizable fraction of binding encounters will result in highly eccentric binaries that merge within a few orbits of the initial encounter. For Newtonian hyperbolic orbits of systems with total mass M and relative velocity w at infinity, the pericenter separation r_p is related to the impact parameter at infinity b by $r_p = b^2 w^2/2M + O(w^4)$ (unless otherwise stated we employ geometric units with $G = c = 1$ throughout). Thus, since the capture rate is linearly proportional to the cross sectional area, it is linearly proportional to r_p. For the 4:1 BH to NS mass ratio systems studied here (with $w = 1000$ km/s), estimates of

the energy lost to GW based on the work of [257] shows binding encounters occur at $r_p \lesssim 40$ M (and scales with mass ratio as $\mu^{4/7}$). The results presented here show that cases with initial $r_p \lesssim 7M$ (for the canonical nonspinning BH), or close to 20% of binding encounters (of a 4:1 system with $w = 1000$ km/s), result in "direct collisions," i.e., merging on the first close-encounter.

4.1.1 Event rates

At first glance it may seem that encounters resulting in dynamical capture would be too rare to be of any relevance as possible GW or EM transient sources; however, recent studies have suggested otherwise. Here we briefly review the event rates for dynamical capture binaries. (We consider NS-NS and BH-BH in addition to BH-NS rates since we will be interested in these systems in subsequent chapters.) [1]

Galactic nuclei are one promising setting for the formation of dynamical capture binaries. Mass segregation around a central massive BH can lead to large densities of stellar mass BHs and stars. For example, the Fokker-Planck model used in [258] suggests that our galactic nucleus should have $\sim$ 2000 BHs and $\sim$ 400 NSs in the central 0.1 pc. In [259, 260], the event rate for the formation of BH-BH binaries from GW capture in this setting was estimated to be roughly between 0.01 and 1.0 yr^{-1} Gpc^{-3}, with corresponding Advanced LIGO detection rates of $\approx 1 - 10^2$ yr^{-1}. This rate assumes that the number density n of BHs in galactic nuclei has a scatter with $\langle n^2 \rangle / \langle n \rangle^2 = 30$. Assuming no scatter would reduce the above rate by a factor of 30. This also assumes a number density of contributing galaxies of 0.05 Mpc^{-3}; i.e. it includes all galaxies as contributing roughly equally. Lower mass galaxies are not as well understood, though if a significant number of them have total cluster mass fractions above the 2.5% used in the aforementioned calculation, this rate would increase. Other unaccounted for effects, such as steeper profiles from light-dominated

[1] Some of the material in this subsection originally appeared in [6]

mass functions [261], could also potentially increase this rate. The formation of BH-NS binaries is estimated to be $\sim 1\%$ of this rate [259].

Dynamical capture binaries may also form in globular clusters (GCs) that undergo core collapse [262, 263]. In [264] binary formation through tidal capture was studied. Using M15 as a prototypical GC, it was calculated that the NS-NS tidal capture rate would peak at ~ 50 yr^{-1} Gpc^{-3} at $z = 0.7$ (falling to ~ 30 yr^{-1} Gpc^{-3} by $z = 0$) for their default model of core collapse. They also provide a scaling to BH-NS and BH-BH mergers which (assuming $M_{\rm BH} = 4.5 M_\odot$ and a relative fraction of BHs to NSs $f_{\rm BH}/f_{\rm NS} \approx 0.28$) gives rates that peak at ~ 70 yr^{-1}Gpc^{-3} and ~ 20 yr^{-1}Gpc^{-3} for BH-NS and BH-BH mergers, respectively. This scaling does not include complications due to BH ejection [265, 266, 267, 268, 269]. Also, these calculations do not include the likely reduction in compact object (CO) populations within the GC due to natal kicks. In [270] it was found that including a 5% NS retention fraction when fitting simulation results to observations of M15, and assuming no central BH, reduced the estimated number of NSs in the inner 0.2 pc by $\sim 1/4$ compared to a similar study that did not include natal kicks [271]. The calculated NS-NS merger rate is quite sensitive to the fraction f of NSs in the core, scaling as $\sim f^2$, which means the aforementioned rates could be too large by an order of magnitude if retention rates are this low. However, observations suggest that in some GCs the NS retention fraction could be as high as 20% [272]. Also, note that the tidal capture cross section used in [264] is more than an order of magnitude smaller than the GW capture cross section for compact objects, and using the latter would increase the rates by the same factor. Tidal capture is estimated to occur in [264] for periapse values $r_p/M \leq 32$, 25, and 13 for NS-NS, BH-NS, and BH-BH binaries, respectively.

In [273] NS-NS binary formation in GCs via exchange interactions was studied, giving a merger rate of ~ 2 yr^{-1} Gpc^{-3}. A similar mechanism was explored in [274] for BH-NS systems; the results depend sensitively on the initial mass fraction of BHs,

with more massive BHs leading to higher event rates. For example, models where the GC contained $M = 35_{\odot}$ BHs lead to advanced LIGO detection rates of 0.04–0.7 yr^{-1}. Though in contrast to tidal or GW capture discussed in the previous paragraph, the mechanisms looked at in both these studies typically produce binaries with periods of 0.1 days or longer, and they will effectively circularize before entering the LIGO band.

There is also the possibility that eccentric mergers could result from hierarchical triples through the Kozai mechanism. This has been suggested to occur in BH-BH mergers in GCs [275, 276, 269] and CO mergers around supermassive BHs in galactic nuclei [277], as well as in coeval or dynamically formed BH-NS or NS-NS binaries [278]. Though dynamically different from direct capture two-body systems, in Kozai-accelerated evolution the merger itself could take place with significant eccentricity [275] and have comparable behavior at late times to the systems studied here. However, we are unaware of any systematic studies of expected populations and corresponding LIGO-event rates for such Kozai triple systems. Efforts to understand this mechanism in the general-relativistic regime are ongoing (see e.g. [279]), and we are unaware of any systematic studies of expected populations and corresponding LIGO-event rates for such Kozai triple systems (though see [280]).

In comparison, population synthesis models [281] find primordial BH-NS merger rates from $\sim$ 0.1 yr $^{-1}\mathrm{Gpc}^{-3}$ (pessimistic) to $\sim$ 120 yr $^{-1}\mathrm{Gpc}^{-3}$ (optimistic). To estimate Advanced LIGO detection rates requires full templates for these events, which we present in Chap. 6; however, here we briefly mention that in [260] the signal-to-noise ratio was computed using post-Newtonian-based models of the early stages of the mergers, which showed that a subset (depending upon the component masses) could be observed out to 200-300 Mpc for an average orientation, even excluding the final stages of the merger in the templates. This suggests detection rates of $\sim 0.3-10/\mathrm{yr}$. For comparison to primordial BH-NS binaries, [17] quotes an Advanced

LIGO optimal detection distance of 927 Mpc for a 10 $M_\odot$ BH to 1.4 $M_\odot$ NS merger, which scales to $\sim$ 400Mpc when averaging over orientation and sky location; the corresponding detection rates range from 0.2/yr to 300/yr for pessimistic to optimistic source population estimates.

Though far from conclusive, there is also observational evidence for multiple sGRB progenitors, which could, in part, be due to dynamical capture vs primordial mergers. Of sGRBs with identified host galaxies, $\sim 25\%$ have offsets of $\gtrsim 15$ kpc from their hosts [282]. This subset of sGRBs with large offsets would be consistent with kicked, primordially formed BCOs or with dynamically formed binaries in globular clusters. The latter may be preferred for the largest offsets [283], especially if primordial BCOs experience weak kicks [284]. Analysis of x-ray afterglows observed by Swift/X-Ray Telescope suggests that different progenitors may be responsible for sGRBs with and without extended emission [285]; again, one possible explanation is dynamical capture (with extended tidal tails leading to long-term emission) vs primordial. There has also been a claim that a very high-energy gamma-ray source observed in Terzan 5 may, in fact, be the remnant of a BCO merger-powered sGRB [286]; if true, this would support the claim that dense cluster environments can be significant sources of BCO mergers.

4.1.2 Effects of orbital eccentricity

Merging with moderate to high eccentricity could have significant effects on all the GW and EM observables from the event. In contrast to a low-eccentricity inspiral, the GWs are emitted primarily around periapsis, resulting in waveforms that resemble a sequence of bursts more than a continuous signal. Consequently, for mass ratios relevant to stellar mass BH-NS mergers, the evolution of effective orbital parameters describing the binary does not occur quasistatically as in the early inspiral of low-eccentricity binaries. Regarding effects associated with tidal disruption of the NS, an

interesting coincidence for this class of BH-NS systems is that the typical radii inside of which tidal stripping begins, depending upon the NS compactness and, hence, equation of state (EOS), roughly coincides with the range of pericenter separations where the orbit becomes unstable due to general relativistic effects ($r_p \lesssim 10M$ depending upon on the spin of the black hole where M is the total mass of the system). The resultant dynamics could thus be very different from Newtonian expectations. Of course, these two zones also roughly correspond for quasicircular inspiral. However, highly eccentric binaries have significantly more angular momentum (at a given orbital separation) than quasicircular binaries. This additional angular momentum could strongly affect the matter dynamics relative to the quasicircular case, for example, resulting in comparatively massive disks and/or in multiple and prolonged episodes of mass transfer and ejection. Ejected mass will decompress and form heavy elements through the r-process [36, 37, 38], and thus these systems could account for a significant fraction of such elements in the Universe. Furthermore, subsequent decay of the more radioactive isotopes could lead to observable EM counterparts [287, 88].

4.1.3 Outline of remainder of chapter

In this chapter we perform simulations of BH-NS dynamical capture and merger using general relativistic hydrodynamics (GRHD) (see [264] for an earlier related study using a Newtonian-based hydrodynamics code) for several values of BH spin and NS equation of state. Astrophysical BHs are expected to form with a range of spins, (see e.g. [288, 289]) and in the quasicircular case spin was found to be crucial in obtaining significant accretion disks [290, 291, 292, 98]. Additionally, there is significant uncertainty about the NS equation of state. Since the EOS determines the NS compaction and, hence, the point at which the NS will become tidally disrupted, it is also an important determinant of the merger outcome. In addition to non-spinning BHs, we consider initial BH-spins aligned and antialigned with the orbital angular

momentum (with dimensionless spin parameter $a = 0.5$ and $a = -0.5$, respectively), as well as different EOSs (the "2H", "HB" and "B" models from [23]). Note that there is no *a priori* reason to expect alignment of the BH spin with orbital angular momentum in dynamical-capture binaries; this particular choice of spin direction and magnitude was purely motivated as a first, simple exploration of the effects of spin on the merger. Certainly in future studies a broader expanse of parameters will need to be considered. There is also much room for improvement with the matter description, including more realistic EOSs and additional physics beyond GRHD. For quasicircular BH-NS inspiral [293], EOS effects were studied in [101, 22, 294, 20], the effects of magnetic fields in [98, 295], and higher mass ratio systems (up to 7:1) in [296].

In the remainder of the chapter we begin with a brief review of our numerical methods (Sec.4.2); In Sec. 4.3, we describe the particular cases we study. We focus on systems with small initial periapsis r_p, in part for the practical reason that these binaries merge quickly and are thus computationally tractable, this is the regime where full general-relativistic (GR) effects will be most strongly manifested, and because maximum complementary information to post-Newtonian studies (e.g. [260] or [264]) can be obtained. We present the results of the simulations in Sec. 4.4. We find that the rich variability in the dynamics and merger outcome as a function of impact parameter is compounded by considering different EOSs and values of BH spin. For example, we find that with prograde spin or a stiffer EOS significant episodes of mass transfer may occur during nonmerger close-encounters. Systems where the BH has retrograde spin or that are somewhat less eccentric (than parabolic) can undergo sustained whirling phases before merger that are evident in the GW signal. As in the eccentric binary NS mergers studied in [153], we also find that strong f-mode oscillations in the NS can be excited in close, nonmerger encounters (see also an earlier study of a head-on BH-NS collision [297], though here the presence of the f-mode is

largely a consequence of the initial data). In Sec. 4.5 we use the results of the simulations to calibrate a simple model for the non-quasistatic evolution of effective orbital parameters during each close-encounter. This model will be extended in Chap. 6 to explore the detectability of these systems with gravitational wave observations. We conclude in Sec. 4.6.

4.2 Numerical methods

In this section, we briefly outline our numerical methods for solving simulating eccentric binaries.

4.2.1 Evolution

We model the evolution of BH-NS binaries by solving the Einstein field equations coupled to a perfect fluid using the code described in Chap. 2. In order to avoid singularities we excise within any apparent horizons. In evolving eccentric binaries, we find that a damped harmonic gauge similar to the one described in [178] (see also [298]) is beneficial for achieving stable evolutions through merger. Specifically a damped harmonic gauge takes the form $H^a = \xi(n^a - \bar{n}^a)$, where n^a is the four-vector normal to the constant coordinate time slices, $\bar{n}^a$ is another timelike unit vector, and ξ is a constant controlling the magnitude of the damping. The particular form for $\bar{n}^a$ that we found to work well is from [298],

$$\bar{n}^a = \frac{1}{\alpha}\left(\frac{\partial}{\partial t}\right)^a + \log\left(\frac{\alpha}{h^{1/2}}\right) n^a. \tag{4.1}$$

We use a value of $\xi \approx 0.2/M$, though include a spatial dependency so that ξ goes to zero at spatial infinity. In addition, we begin with initial data in the harmonic gauge and transition to this damped harmonic gauge before the two objects begin to strongly interact. The use of this gauge seems to smooth out sharp features in

the lapse that develop near merger when harmonic gauge is used, however, we have not studied the pure harmonic case in sufficient detail to conclude whether or not harmonic time slicing is developing a coordinate singularity.

We describe the neutron star material as a perfect fluid. The fluid equations are written in conservation-law form and solved using high-resolution shock-capturing schemes as described in Chap 2. Though we have implemented several methods for calculating intercell fluxes and for reconstructing fluid primitive variables at cell faces, we used HLL [126] combined with WENO-5 [133] for the results presented here.

Truncation error estimates are used to generate the AMR-level structure. All initial data were evolved with a fiducial "medium" resolution run, where the coarsest-level has 128^3 cells and covers the entire domain (we use a compactified coordinate system, so this includes spatial infinity). We also chose a maximum truncation error so that initially six additional levels of refinement (seven total) are generated to resolve the BH and NS. Given the computational expense of these simulations, we limited the total number of levels to seven during evolution, and did not allow regridding on the two coarsest-levels to prevent the algorithm from tracking the outgoing gravitational waves beyond the largest extraction sphere of $100M$. For several representative cases we also ran a "low" and "high" resolution simulation for convergence testing, where on each level the low (high) resolution run had a mesh spacing of 64/50 (64/96) of the medium resolution run, and we scaled the corresponding maximum local-truncation error threshold-parameter used by the AMR algorithm assuming second-order convergence. Note that this procedure will not generate identical hierarchies between different resolution runs (except for the two coarsest levels in the wave zone, which we keep fixed), but on average the highest-resolution grid covering a given coordinate cell will have the above refinement ratios between the different runs. To give some sense of the smallest scales resolved by the hierarchy, before tidal disruption, the low (medium, high) resolution run has two finest-level meshes centered around the BH

and NS of roughly 80^3 (100^3, 150^3) cells each, resolving the diameter of the NS with approximately 40 (50, 75) cells and the BH horizon diameter with roughly 70 (85, 130) cells. Unless otherwise noted, results will be reported for medium resolution with error bars (where appropriate) computed from convergence calculations.

4.2.2 Initial data

We construct initial data by superimposing a boosted BH with a boosted nonspinning Tolman-Oppenheimer-Volkoff (TOV) star solution separated by $d = 50M$. Though this superposition does not strictly satisfy the constraint equations except in the limit of infinite separation, we have performed tests at various separations in order to verify that the superposition-induced constraint violation is comparable to truncation error at our resolution, in particular following an initially slightly larger transient that propagates away (and is partly damped due to the use of constraint damping) on roughly the light-crossing time d of the binary. In Fig. 4.1, we show the level of constraint violation ($C_a := H_a - \Box x_a$) following the transient for various separations and resolutions for the $r_p = 10M$ case. At these resolutions, we can still achieve convergence of the constraints with this superposed data, and increasing the initial separation to $d = 100M$ does not significantly affect the level of constraint violation at the same resolution. This implies that the error introduced by the superposition is on the order of or smaller than the numerical truncation error at this resolution. We note that the work described in the chapter was originally carried out prior to the development of the code described in Chap. 3 and does not make use of it. However, comparison of select evolutions with initial data constructed as in Chap. 3 confirm that the superposition error is comparable to the truncation error.

The fact that we are beginning the binary at finite separation as a simple superposition of boosted single-compact object solutions and that there is a transient early time constraint-violation, both effectively introduce systematic errors in the param-

eters of the binary. To give some idea of the possible magnitude of this error, the effect on the apparent horizon-mass of the BH at early times and the amplitude of the density oscillation induced in the NS are both $\lesssim 2\%$. Though it is difficult to exactly quantify how this will translate to modified-binary parameters, we expect it to be comparable to or smaller than the error introduced by setting initial orbital parameters at a finite distance based on a Newtonian approximation (as described in the next section). As we report later, the truncation error in quantities of interest that we do measure such as energy emitted in GWs is percentwise larger than this, implying that solving the constraints or attempting more accurate initial representations for the metric and NS fluid distribution may only offer marginal improvement in the overall accuracy of the results at these resolutions. However, for future higher-resolution studies it would be important to solve the constraints and improve the model of the physical initial conditions for the system.

Finally, we briefly comment that since our simulations employ compactified coordinates such that the outer boundaries extend to spatial infinity, the global [Arnowitt-Deser-Misner (ADM)] M and J should be conserved. In practice, however, we must evaluate these quantities at a finite distance, making them subject to gauge artifacts, some propagating outward from the central BH-NS region from $t = 0$. For $t < 200M$, an extraction sphere of $300M$ is free of propagating artifacts, hence M (J) is conserved to better than 0.3 (2.0)% for all cases at medium resolution.

4.3 Cases

Motivated by possible BH-NS interactions in cores of galactic nuclei and globular clusters, we create initial data for hyperbolic encounters with varying impact parameter. These encounters are hyperbolic since the two bodies have nonzero kinetic energy at (effectively) infinite separation. We will take their relative velocity at infinity to be

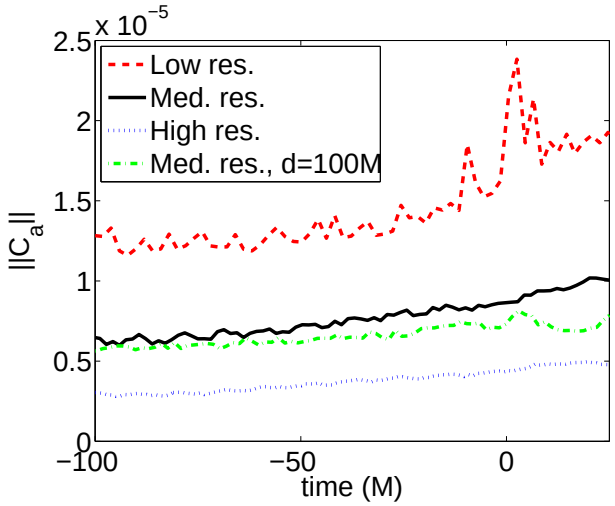

Figure 4.1: L^2-norm of the constraint violation, $C_a := H_a - \Box x_a$, in units of $1/M$ from the $r_p = 10M$ case in the $100M \times 100M$-region around the center of mass in the equatorial plane (i.e. $\sqrt{\int \|C_a\|^2 d^2x / \int d^2x}$). This is shown for low, medium, and high resolutions for the standard initial separation between the BH and NS of $d = 50M$; the relative magnitudes at a given time are consistent to good approximation with second-order convergence. Also shown is a medium resolution run with an initial separation of $d = 100M$. The time is shifted so that the point of closest approach occurs at approximately $t = 0$ for all cases.

$w = 1000$ km/s since this is the expected magnitude of the virial velocity in the core of a nuclear cluster [299, 300].

In practice, this initially positive total energy is small compared to the kinetic energy of the encounter itself, so that the orbits are nearly parabolic and have eccentricities $1 + O(10^{-5})$. In this study we also restrict our attention to BH-NS systems with a 4:1-mass ratio (referring to the isolated ADM masses of the BH and NS). The reasons for choosing this mass ratio are in part because it is within the range of astrophysically plausible values given current observations of NS and candidate BH masses (see, for example, [301, 302]), and in part because within this range it is also a value where we expect to see strong tidal-disruption effects. Certainly it would be of interest to explore a broader range of mass ratios, however, due to limited computational resources we leave that to a future study.

We choose the initial positions and velocities for the BH and the NS according to the Newtonian equations for a hyperbolic orbit (see, e.g., [303]) with $w = 1000$ km/s and an initial separation of $d = 50M$. We vary the initial spin of the BH, considering the values $a = -0.5, 0$, and 0.5 where negative (positive) values indicate retrograde (prograde) spin in relation to the orbital angular momentum. We also consider three different broken Γ-law model EOSs labelled 2H, HB, and B in [23]. For the prototypical 1.35 $M_\odot$ NS that we use, these EOSs give compactions $M_{NS}/R_{NS} = 0.13, 0.17$, and 0.18, respectively. Note that while the compaction of the B EOS NS is only slightly smaller than that of the HB, it has a maximum mass of 2.0 $M_\odot$ (the 2H and HB have maximum masses of 2.83 and 2.12 $M_\odot$, respectively). Given recent observations [304], B is therefore on the soft end of the allowed range for the EOS family considered here. We include a thermal component in the EOS, a Γ-law with $\Gamma_{\rm th} = 1.5$ to allow for shock heating.

We do not consider large impact parameters corresponding to initial $r_p > 15M$. Even so, for impact parameters at the upper end of the range we do evolve the eccentricity is sufficiently large (though < 1) after the first close-encounter that it would be very expensive to evolve to the second encounter. To help calibrate our model for orbital parameter evolution that will be introduced in Sec. 4.5, we also consider a set of runs with initial orbital parameters for a bound orbit with eccentricity $e = 0.75$ instead of the hyperbolic orbit with $e \approx 1$. These simulations can be seen as corresponding to systems that have already undergone one or more close-encounters and evolved to these orbital parameters.

To keep the parameter space at a manageable size, we vary only one of the three parameters of BH spin, NS-EOS, and initial eccentricity at a time from our base case — an initially nonspinning BH ($a = 0$), a NS with the HB EOS, and the two objects initially with Newtonian orbital parameters corresponding to a marginally unbound orbit ($e \approx 1$) — and then consider a range of impact parameters. See Fig. 4.2 for

plots of the NS trajectory for several cases, and Fig. 4.3 for snapshots of the rest-mass density at select times illustrating aspects of the matter dynamics.

4.4 Results

Varying the parameters as discussed in the previous section, there is much degeneracy in the qualitative features that arise (which will need to be addressed in future studies investigating extraction of source properties from GW and EM observations). This is essentially because the leading-order source of the variability is rooted in the following two properties of the system: (1) the NS radius, varied by altering the EOS (as the NS mass is fixed in this study), (2) the location of the innermost stable orbit (ISO) varied by changing the spin of the BH or the eccentricity of the encounter. For equatorial geodesics on a black hole background, the ISOs asymptote to circular orbits, though these should not be confused with the innermost *stable* circular orbit (at $r = 6M$ in Schwarzschild), or ISCO. The circular orbits (in the range $r = 3M$ to $6M$ in Schwarzschild) associated with the ISOs with nonzero eccentricity are *unstable*, and under infinitesimal perturbation their noncircular nature is manifest in the form of zoom-whirl behavior [305]. Specifically, depending upon the size of the perturbation, the geodesic will undergo a number of near circular orbits (the "whirls"), followed either (depending upon the sign of the perturbation) by a plunge into the BH or by a single near elliptical orbit (the "zoom"), and in the latter case the motion repeats. Away from the geodesic limit there is still an effective ISO, where qualitatively similar behavior occurs [167], though radiation reaction will eventually drive the system to a merger for all bound systems.

In terms of the gravitational dynamics, the closer the periapsis is to the ISO, the more whirling that occurs, resulting in enhanced GW emission and more rapid evolution of effective orbital parameters. Regarding the matter dynamics, the ISO is

essentially the "event horizon" for fluid elements following geodesics, or being close to geodesic. What this implies is on a close-encounter, if the NS is not disrupted and the periapsis of the orbit is within the ISO a merger will result and the entire NS will fall into the BH. If the NS is disrupted, following the essentially Newtonian redistribution of angular momentum that results, fluid elements within an ISO corresponding to their effective eccentricity will immediately plunge into the BH, while the rest will either move out onto eccentric orbits to later fall back onto an accretion disk or be ejected from the system. If the majority of the NS mass ends up outside the ISO following disruption, once it moves beyond the tidal-disruption zone there will be sufficient self-gravity for the material to recoalesce into a NS core. Similarly, in a partial disruption where only the outer layers are stripped from the NS, some stripped material will accrete into the BH, some back onto the NS, and a portion will be flung out unbound.

In the following subsections, we break down the discussion of phenomenology of the encounters by first summarizing the results from the base case presented in [4] (Sec. 4.4.1), then describe in turn what happens when spin (Sec. 4.4.2), EOS (Sec. 4.4.3), and eccentricity (Sec. 4.4.4) are changed relative to the base case. In order to have some intuitive understanding of why the changes have the effects they do, it is useful to keep the above discussion in mind. This can also allow one to anticipate what would happen if parameters we are not altering here are changed, for example, the BH or NS mass.

4.4.1 Zero-spin survey with HB EOS

Here we summarize the results obtained for simulations with an initially nonspinning BH and a NS with the HB EOS. We considered a range of periapsis separations from $r_p/M = 5.0$ to 15 (*i.e.,* 50 to 150 km). Henceforth, we will consider r_p to be normalized by M. In all of these cases, sufficient energy is carried away by GWs to

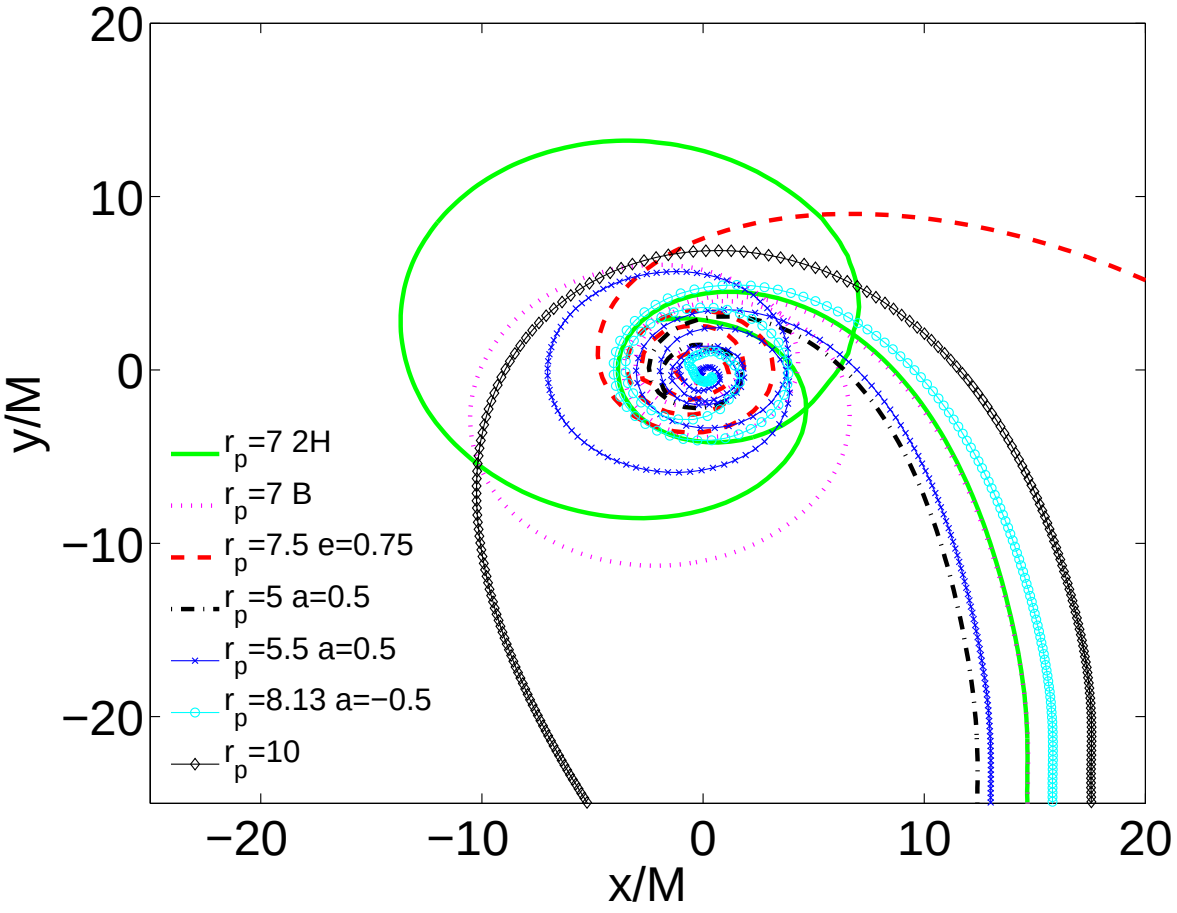

Figure 4.2: Trajectories of the NS center-of-mass for various simulations. The $r_p = 7.0$ with 2H EOS, $r_p = 7.0$ with B EOS, and $r_p = 5.5$ $a = 0.5$ (HB EOS) both undergo a close-encounter followed by a short elliptic orbit before merging. Note that while in both the $r_p = 7.0$-cases the NS approaches the BH on essentially the same orbit, the dynamics around the close-encounter and subsequent orbits are very different due to EOS effects (see Sec. 4.4.3). The $r_p = 10$ (HB EOS) undergoes a long-period elliptical orbit following the initial periapsis passage. The remainder of the cases shown merge on the first encounter while displaying various degrees of whirling behavior.

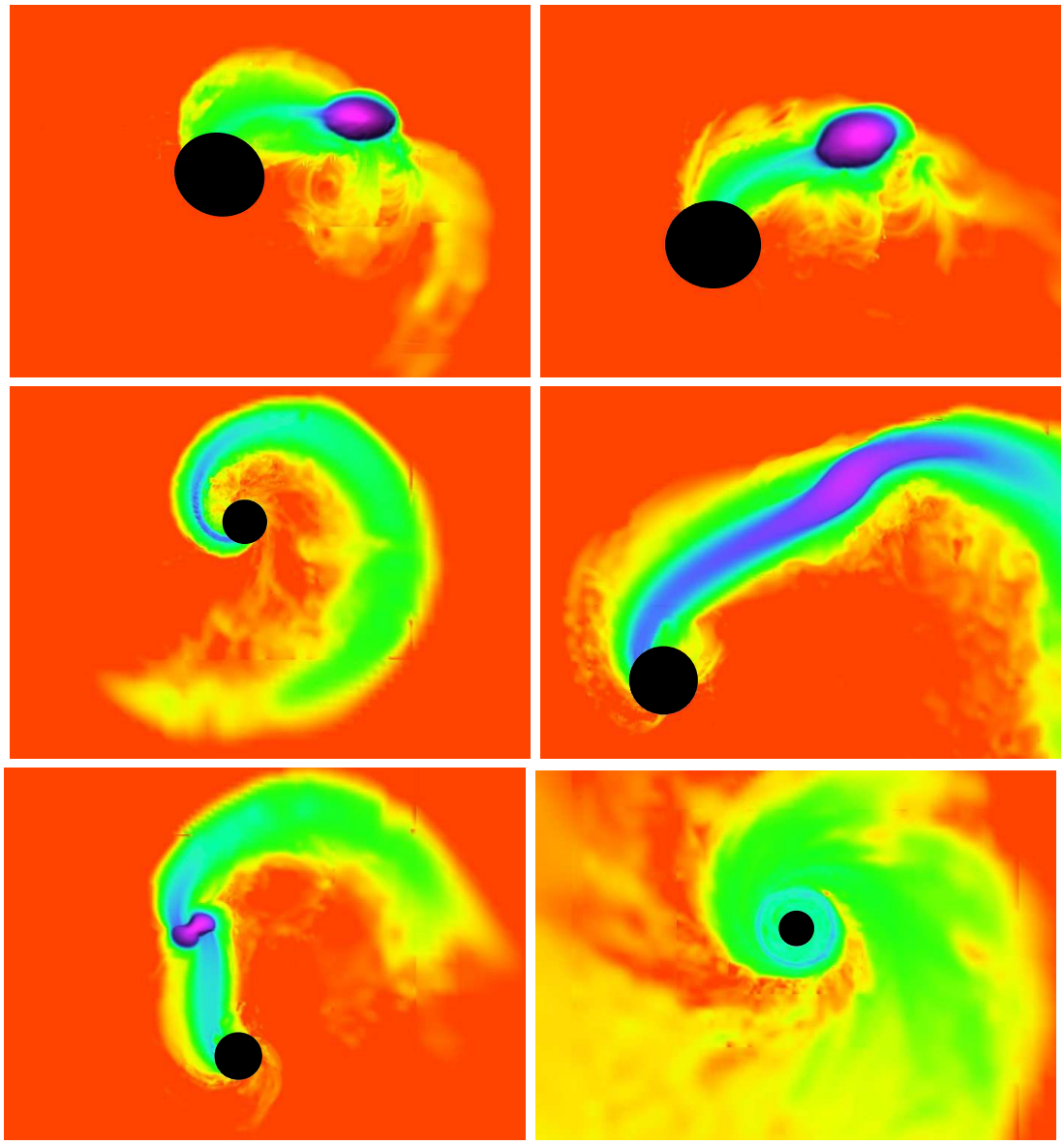

Figure 4.3: Rest-mass density in the equatorial plane from various BH-NS simulations, left to right, top to bottom: (1) the BH and NS undergoing a close-encounter ($t = 242$ M, $r_p = 7.0$, B EOS), (2) the NS undergoing a whirling-phase before merging ($t = 269$ M, $r_p = 8.13$, $a = -0.5$), (3) the NS stretched into a long tidal stream during merger ($t = 506$ M, $r_p = 7.5$, $e = 0.75$), (4) a mass transfer episode ($t = 292$ M, $r_p = 7.0$, 2H EOS), (5) towards the end of a mass-transfer episode during the NS's first periapsis passage ($t = 272$ M, $r_p = 5.5$, $a = 0.5$), and (6) a nascent accretion disk ($t = 388$ M, $r_p = 5$, $a = 0.5$). Recall that r_p is reported in units of total mass M. The color scale is logarithmic from 10^{-6} to 1 times the initial maximum density ($\rho_{\rm max} = 8.3$ (3.7,9.8) $\times 10^{14}$ g cm^{-3} for the HB (2H, B) EOS). The BH is roughly the same coordinate size (with diameter ≈ 3 M) in all panels, which can be used to infer the relative scale of each snapshot.

result in a bound system. Our simulations exhibit three types of behavior: (1) a direct plunge ($r_p = 5.0, 5.83, 6.67, 6.81$); (2) following the initial periapsis passage, a single elliptical orbit and then a plunge ($r_p = 6.95, 7.22, 7.5$); and (3) following the initial periapsis passage, a long-period elliptical orbit ($r_p = 8.75, 10.0, 12.5, 15.0$). For the latter group (and the high-resolution $r_p = 7.5$ run), we do not simulate the entire orbit since the length of such simulations would make them very computationally expensive [2], and we focus on the burst of GWs associated with the first periapsis passage. For one case in each class ($r_p = 5.0, 7.5, 10.0$) we performed a convergence study which showed approximately second-order convergence and allowed us to perform a Richard extrapolation to estimate errors in the resulting GWs. To give further indication of the truncation error in these runs, in Fig. 4.4 we plot the error in the trajectory of the NS in a fly-by case $r_p = 10$ (see Fig. 4.2 for the medium resolution trajectory). The GW energy and angular momentum emitted (including extrapolated values from the resolution studies) as well as the disk properties of those cases followed through merger are summarized in Table 4.1. Table 4.2 shows the spin of the post-merger BH (for this base set of runs as well as the subsequent parameter survey) for the cases we followed through merger. As the threshold in r_p dividing (1) and (2) is approached there is a dramatic enhancement in the gravitational energy and angular momentum released during the close-encounter.

The amount of material remaining after merger, which could potentially form an sGRB-powering accretion disk also depends significantly on impact parameter. Below the threshold dividing (1) and (2), there is a sizable amount of remaining material in excess of 20% in the $r_p = 6.81$ case. In most cases $\approx 50\%$ of the material is unbound. As seen in Fig. 4.5, a simple numerical estimate of the fallback time for the bound

[2]For example, based on an estimate using the emitted GWs and assuming a Newtonian orbit the $r_p = 8.75$ case will undergo another close-encounter after ~ 7000 M, which would take 2-3 months of wall clock time to simulate at medium resolution (while the larger r_p cases will take even longer). Though such long runs are not unheard of, we chose to use our limited computational resources to explore a greater number of parameters.

material based on when the elliptic orbit will return to the accretion disk shows the characteristic $t^{-5/3}$ scaling [46].

r_p	$M_0/M_0(t=0)$ [a]	$M_{0,u}/M_0(t=0)$ [b]	$\tau_{\rm acc}$ (ms) [c]	First periapsis [d]		Total [e]	
				$\frac{E_{GW}}{M}\cdot 10^2$	$\frac{J_{GW}}{M^2}\cdot 10^2$	$\frac{E_{GW}}{M}\cdot 10^2$	$\frac{J_{GW}}{M^2}\cdot 10^2$
5.00	0.005[g]	0.0	25	–	–	0.67(0.87)[f]	4.14(4.86)[f]
6.67	0.107	0.056	130	–	–	1.29	9.10
6.81	0.221	0.101	40	–	–	1.19	9.60
6.95	0.018	0.003	47	0.697	7.33	1.65	13.9
7.22	0.013	0.001	16	0.358	4.48	1.18	10.2
7.50	0.009	0.003	7.6	0.242(0.147)[f]	3.44(2.46)[f]	1.03	44.7
8.75	...	...	...	0.073	1.58	...	...
10.0	...	...	...	0.033(0.027)[f]	0.97(0.88)[f]	...	...
12.5	...	...	...	0.011	0.46	...	...

Table 4.1: Disk properties and GW energy and angular-momentum losses for an initially hyperbolic ($e \approx 1$) encounter of a zero-spin BH and NS with HB EOS. Dashed entries correspond to cases that merge during the first encounter, and hence have no "first periapsis"; dotted entries correspond to binaries that were only evolved through first periapsis passage.

[a] Rest-mass remaining outside the BH shortly (~ 50 M) after the end of merger, normalized by the initial total rest-mass.

[b] Unbound rest-mass estimated using local fluid velocities and assuming a stationary metric.

[c] Rough *initial* accretion timescale ($\tau_{\rm acc} = M_0/\dot{M}_0$) evaluated shortly after merger.

[d] Energy and angular momentum lost to GWs during the first close-encounter.

[e] Total GW energy and angular-momentum losses for cases which were followed through merger.

[f] Results are from medium-resolution runs; values in parentheses are Richardson-extrapolated estimates using low and high resolutions, where available. Note that the relatively large error for $r_p = 7.5$ (and to a lesser extent $r_p = 5, 10$) is due in part to truncation error altering the actual periapsis by a small amount, and in this regime the GW emission is highly sensitive to binary separation.

[g] For the $r_p = 5$ case $M_0/M_0(t=0)$ was the same at the three resolutions to within $\approx 5 \times 10^{-4}$; however, for such low disk masses we expect systematic effects, e.g., the numerical atmosphere to be important.

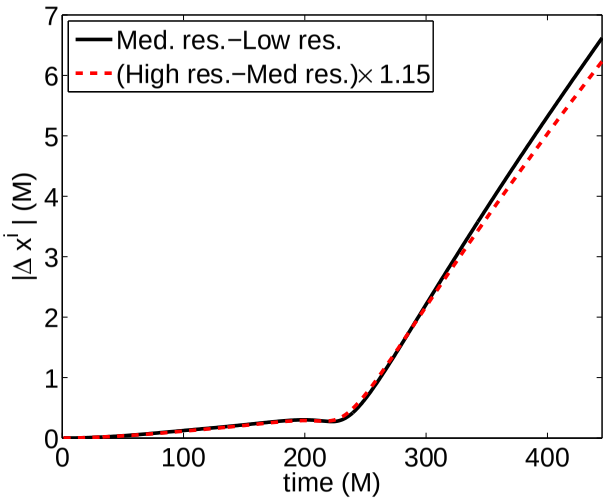

Figure 4.4: Convergence of the NS trajectory for the $r_p = 10, a = 0$-case (see Sec. 4.4.1). What is plotted is the magnitude of the difference in the center of rest-mass position of the NS between the low and medium-resolution runs, and between the medium and high-resolution runs scaled assuming second-order convergence. The close-encounter occurs near $t = 230M$, where the largest "perturbation" of the orbit due to truncation error happens; the relatively large growth of the difference in trajectories following this is mostly just a reflection of this change in the orbital parameters that occurred around periapsis.

4.4.2 Effects of black hole spin

As expected from Kerr geodesics, prograde BH spin results in a smaller critical-impact parameter below which the NS merges with the BH on the first encounter than in the nonspinning case; the converse is expected for cases with retrograde initial BH-spin. For the cases with initial BH-spin $a = 0.5$ (top of Table 4.3), only the $r_p = 5.0$ case merges on the first encounter while $r_p = 5.5$, 6.0, and 6.25 go back out on a short elliptic orbit before merging. The $r_p = 7.5$ and 10.0 cases go out on a long elliptic orbit after the initial periapsis passage, and we did not follow these through merger. For the $r_p = 5$ case, we also performed convergence tests in order to estimate truncation error for a spinning BH where the effective ISO is closer to the BH. From this we compute Richardson extrapolated values for the energy and angular momentum of the resulting GW as well as for the amount of matter left over post-merger; these

$a = 0$ HB EOS								
r_p	5.00	6.67	6.81	6.95	7.22	7.50		
$a_{\rm final}$	0.49[a]	0.45	0.37	0.47	0.50	0.50		
$a_{\rm eff}$	0.40	0.46	0.47	0.47	0.48	0.49		
	$a = 0.5$				$a = -0.5$			
r_p	5.00	5.50	6.00	6.25	5.00	7.50	8.13	8.28
$a_{\rm final}$	0.74	0.71	0.71	0.70	0.16	0.25	0.22	0.24
$a_{\rm eff}$	0.72	0.74	0.77	0.77	0.08	0.17	0.19	0.19
	2H EOS				B EOS			
r_p	5.00	6.75	7.00		5.00	6.25	7.00	
$a_{\rm final}$	0.50	0.29	0.33		0.48	0.52	0.48	
$a_{\rm eff}$	0.40	0.46	0.47		0.40	0.45	0.47	
	$e = 0.75$							
r_p	7.50	7.81						
$a_{\rm final}$	0.44	0.49						
$a_{\rm eff}$	0.46	0.47						

Table 4.2: Post-merger BH spin (dimensionless) for various initial conditions. Also shown is the effective spin $a_{\rm eff}$, used in the model described in Sec. 4.5 and calculated from initial conditions using (4.3).
[a] $a_{\rm final} = 0.49 \pm 0.01$

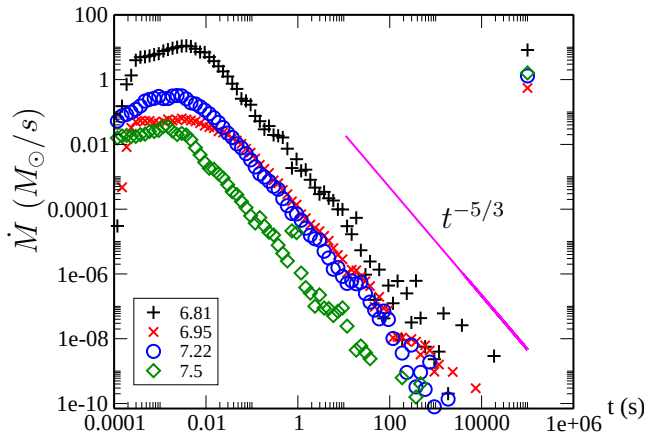

Figure 4.5: Approximate fallback accretion rates for $r_p = 6.81$, 6.95, 7.22, and 7.5 cases with HB EOS. Time is plotted in seconds. For this diagnostic, we consider the fluid in each cell as a ballistic particle and take its orbital period as the approximate fallback timescale. The instantaneous BH accretion rates evaluated at the same time are shown at the upper right (arbitrary abscissa).

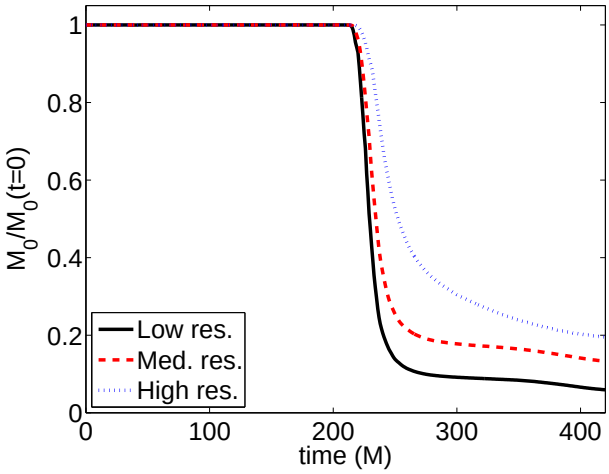

Figure 4.6: Effect of resolution on the disruption and subsequent accretion of NS material, as measured by the total rest-mass exterior to the BH horizon, for the $r_p = 5, a = 0.5$ case (see Sec. 4.4.2). The amount of rest-mass remaining at late times at the different resolutions is consistent with approximately second-order convergence.

values are reported in the table. In Fig. 4.6 we also show the amount of rest-mass exterior to the BH horizon as a function of time and resolution for this case.

One important consequence of the reduced critical-impact parameter in the prograde case is that around this threshold, the tidal forces on the NS are greater and the resulting accretion disks consequently larger. Even more striking, the enhanced tidal interaction can lead to significant mass transfer from the NS to the BH even in nonmerger close-encounters, as, for example, with the $r_p = 5.5$, $a = 0.5$ case. Here the NS becomes highly distorted and loses approximately 16% of its mass to the BH (see Fig. 4.7). However, a compact (albeit highly distorted) star remains (see Fig. 4.3 middle, bottom) until it merges with the BH on its second close-encounter.

For the $a = -0.5$ cases (see bottom of Table 4.3), $r_p = 5.0$, 7.5, and 8.13 are direct mergers while the $r_p = 8.28$ case goes through a single elliptic orbit before merging. The $r_p = 8.44$, 8.75, and 10.0 cases go out on longer elliptic orbits which we did not follow to completion. Because of the larger critical-impact parameter for merger on the first encounter, there is less tidal disruption and, hence, the accretion disks

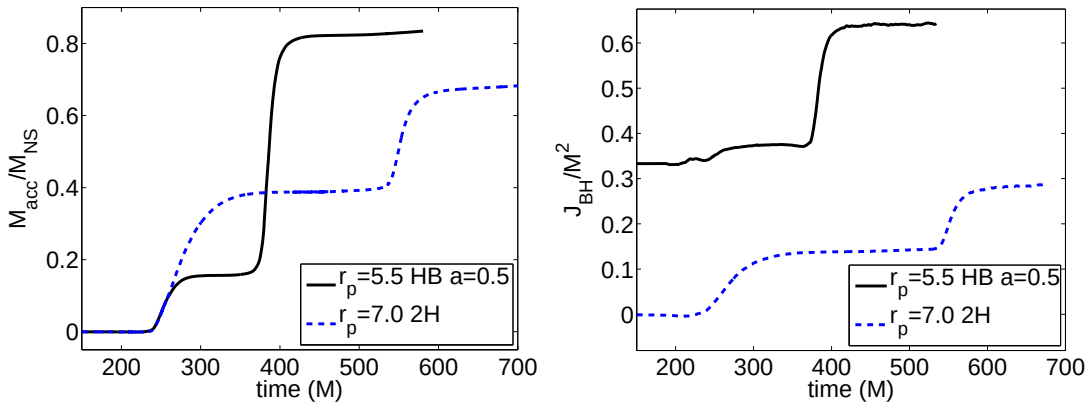

Figure 4.7: **Left:** The amount of rest-mass (normalized to the total rest-mass of the NS) accreted by the BH as a function of time for the $r_p = 7.0$ 2H-case and for the $r_p = 5.5$, $a = 0.5$ HB-case. In both cases there are two significant episodes of mass transfer. **Right:** The angular momentum of the BH horizon in units of the total ADM-mass squared, M^2, as a function of time for the same two cases.

contain $\leq 1\%$ of the total NS rest-mass for all the cases followed through merger. However, this also means that the BH and NS can undergo more whirling behavior in the critical regime before merger. This is especially evident in the waveform for the nearer threshold merger case of $r_p = 8.13, a = -0.5$ as shown in Fig. 4.8. The gravitational wave signal shows several cycles of almost constant amplitude and frequency, indicative of a nearly circular orbit. Compared to the near-threshold nonspinning case ($r_p = 6.81$, also shown in Fig. 4.8), this whirling period is much more pronounced in the waveform.

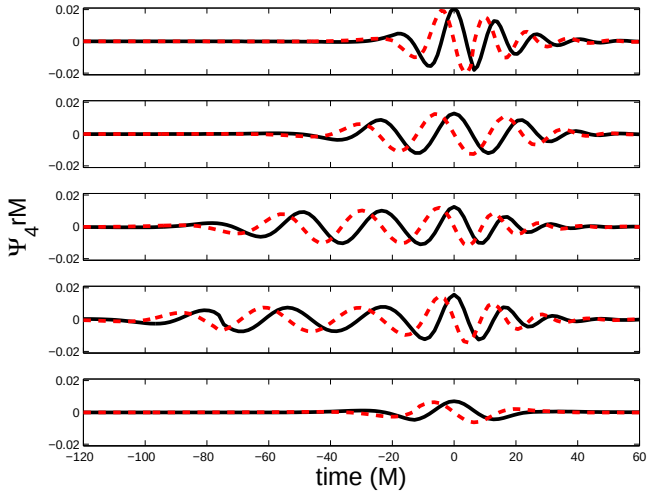

Figure 4.8: The real and imaginary components (solid, black-lines and red, dotted-lines) of Ψ_4 on the z-axis (perpendicular to the orbital plane) during merger for the following cases (top to bottom): $r_p = 5$, HB; $r_p = 6.81$, HB; $r_p = 7.5, e = 0.75$, HB; $r_p = 8.13, a = -0.5$, HB; and $r_p = 7.0$, 2H (see Fig. 4.10 for the full signal). The waveforms are aligned so that the peak occurs at $t = 0$ with zero phase.

r_p	$M_0/M_0(t=0)^a$	$M_{0,u}/M_0(t=0)^b$	$\tau_{\rm acc}$ (ms) ^{c}	First periapsis ^{d}		Total^e	
				$\frac{E_{GW}}{M}\cdot 10^2$	$\frac{J_{GW}}{M^2}\cdot 10^2$	$\frac{E_{GW}}{M}\cdot 10^2$	$\frac{J_{GW}}{M^2}\cdot 10^2$
$a=+0.5$							
5.00	$0.165(0.295)^f$	$0.021(0.107)^g$	4.8	–	–	$1.25(1.41)^f$	$7.14(9.04)^f$
5.50	0.174	0.088	40	0.800	7.14	1.40	10.9
6.00	0.181	0.029	26	0.360	4.16	1.53	14.7
6.25	0.080	0.014	33	0.347	4.11	1.29	12.0
7.50	...	...	...	0.104	1.90	...	...
10.0	...	...	...	0.025	0.82	...	...
$a=-0.5$							
5.00	0.007	0.0	36	–	–	0.33	2.32
7.50	0.008	0.0	71	–	–	0.82	5.91
8.13	0.010	0.0	0.12	–	–	1.57	13.7
8.28	0.002	0.0	2.8	0.385	5.12	1.25	12.8
8.44	...	...	...	0.268	3.98	...	...
8.75	...	...	...	0.167	2.85	...	...
10.0	...	...	...	0.052	1.32	...	...

Table 4.3: Disk properties and GW energy and angular-momentum losses for an initially hyperbolic ($e \approx 1$) encounter of a BH with spin $a = \pm 0.5$ and NS with HB EOS. The same comments and set of footnotes ^{a} to ^{f} apply as in Table 4.1.
^{g} For the $r_p = 5$, $a = +0.5$ case the Richardson extrapolated value of $M_{0,u}/M_0(t=0)$ was computed using just the medium and high-resolution results and assuming second-order convergence due to the low amount of unbound material in the low-resolution case.

4.4.3 Effects of equation of state

We also consider the B EOS, which is softer than the HB, and the 2H EOS, which is stiffer. Though the different EOSs have only a slight effect on the critical impact parameter, they can have a dramatic effect on the near-threshold behavior. For the B EOS, we chose four different impact parameters (bottom of Table 4.4): $r_p = 5.0$ and 6.25 (direct mergers); $r_p = 7.0$ (after periapsis passage, a short elliptic orbit and then merger); and $r_p = 7.5$ which we did not follow through its full elliptic orbit after the first close-encounter. The more compact B EOS NS experiences less tidal disruption and forms accretion disks with $\leq 1\%$ of the total NS rest-mass for all cases followed through merger. For the 2H EOS, we considered five different impact parameters (see top of Table 4.4): direct mergers $r_p = 5.0$ and 6.75; $r_p = 7.0$ (after periapsis passage, a short elliptic orbit and then merger); and $r_p = 7.25$ and 7.5 which we did not follow through the full elliptic orbit after the first close-encounter.

The less compact 2H EOS NS experiences significant tidal deformation, and for the $r_p = 6.75$ and 7.0 cases there is $\approx 30\%$ of the NS material leftover post-merger. In the case of $r_p = 7.0$ the deformation and tidally-induced oscillations of the NS are especially severe (see Fig. 4.3, bottom left) and there is a period of significant mass transfer (Fig. 4.7) from the NS to the BH during the first close-encounter. This is very similar to the $r_p = 5.5, a = 0.5$ case, though more pronounced. For both the 2H EOS and the $a = 0.5$ with HB EOS simulations no significant mass transfer is found for runs with r_p slightly above 7.0 and 5.5, respectively, so we can use these as an effective measure of the separation d_R at which the star begins to overflow its Roche lobe. Though the individual values are somewhat higher than expected from Newtonian theory, it predicts a scaling with compaction $d_R \propto \mathcal{C}_{NS}^{-1}$, where $\mathcal{C}_{NS} := M_{NS}/R_{NS}$; this does approximately hold here since $\mathcal{C}_{HB}/\mathcal{C}_{2H} = 1.3$. This ignores any relativistic effects, both gauge and physical, the latter including, for example, the effect of BH spin on tidal disruption. In Fig. 4.9 we show the mass profiles of an isolated star

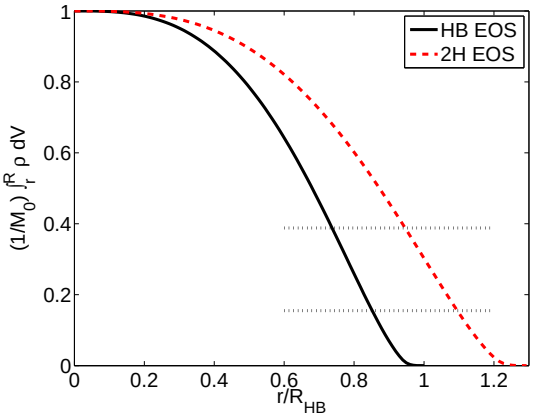

Figure 4.9: The fraction of rest-mass outside a given radius $(1/M_0)\int_r^R \rho dV$ for an isolated star with the HB or 2H EOS and $M = 1.35\ M_\odot$. Here radius r is normalized to the radius of the HB star ($R_{\rm HB}$). The horizontal, dotted-lines indicate the amount of material accreted into the BH during the initial close-encounter for the $r_p = 5.5$-case with HB EOS (bottom) and the $r_p = 7.0$-case with 2H EOS (top) as shown in Fig. 4.7.

with the 2H and HB EOS. This shows that the outer spherical shell that contains the approximately 40% of the NS material that is accreted into the BH during the first close-encounter for 2H corresponds to a volume containing almost no material in the HB case. Again, though we are ignoring the complicated details of mass-transfer dynamics, this is suggestive as to why, for the BH-NS system studied here, there is significant mass transfer for the 2H EOS around $r_p = 7.0$ but very little for the HB EOS.

Since for the 2H $r_p = 7.0$ case so much mass is transferred before the merger and there is a strong disruption during merger, the gravitational wave signal resulting from merger itself is significantly weaker than for other cases (see Fig. 4.8). The full waveform from Fig. 4.10 also shows that the GW pulse from the fly-by dominates the signal compared to the merger part of the waveform.

Between the initial close-encounter and merger there is also evidence in the GW signal of excited f-modes within the NS; this was also observed in eccentric-binary NS encounters [153]. Here we give a qualitative account of the stellar dynamics to show

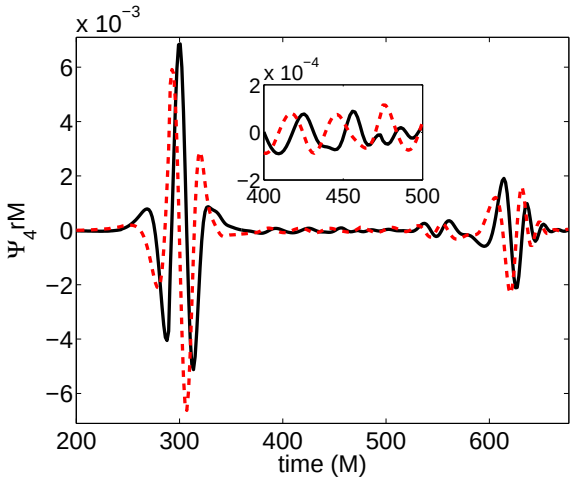

Figure 4.10: The real and imaginary components (solid black lines and red dotted lines) of Ψ_4 on the z-axis (perpendicular to the orbital plane) at $r = 70$ M for the $r_p = 7.0$ 2H simulation. The large burst at $t \approx 300$ M comes from the initial fly-by, where the NS becomes extremely distorted (Fig. 4.3) and loses a significant portion of its mass (Fig. 4.7). The smaller pulse at $t = 600$ M comes from the merger. In between, there is a smaller component of the signal coming from the tidally induced oscillation of the NS.

that the dominant oscillation is akin to that of an f-mode of an isolated, perturbed star—a detailed study, aside from the difficulty of applying a perturbative analysis in such a transient and in some cases highly distorted star, is beyond the scope of this study. Figure 4.11 demonstrates the density and velocity distortions for the $r_p = 7.0$, 2H case (right panel) as well as the $r_p = 6.95$ HB case in which the distortion is less extreme (left panel). The latter bears a particularly strong resemblance to the pure $l = m = 2$ f-mode flow pattern (see, e.g., Fig. 19 of [306]). In both cases, an animation of the density field seems to suggest a rotating, distorted NS. However, as Fig. 4.11 demonstrates, the velocity pattern is not one of overall rotation but rather that of an oscillatory mode. Indeed, the circulation theorem should hold to a good approximation in the bulk of the NS material (though there are entropy-generating shocks near the surface). Thus, the tidal interaction with the BH would not induce rotation in the usual sense, but rather oscillatory modes with rotating patterns. Many such modes are likely to be excited, but the $l = m = 2$ f-mode seems to dominate.

We performed a spherical-harmonic decomposition of the star's rest-mass density $\rho = \sum C_{lm} Y_{lm}$ at select times and found C_{22} to be the largest coefficient next to C_{00}. We also checked that the perturbation amplitude grows monotonically with radius. For the $r_p = 6.95$ simulation with the HB EOS $|C_{22}/C_{00}| \approx 0.01 - 0.02$ at $r = 0.4M$ grows to $|C_{22}/C_{00}| \approx 0.15 - 0.20$ at $r = 0.8M$. Here r is the radius of the sphere centered on the NS center-of-mass on which the coefficients are calculated. The next largest coefficient C_{20} is smaller by a factor of $\gtrsim 2$. The $r_p = 7.0$ simulation with the 2H EOS shows similar behavior although the coefficients are somewhat larger with $|C_{22}/C_{00}| \approx 0.03$ and 0.25 at $r = 0.4M$ and $0.8M$, respectively.

We briefly comment on the possible detectability of such an f-mode excitation in GWs. Such an observation in principle could provide a wealth of information about the structure of the NS, in particular, since f-mode frequencies are quite sensitive to the EOS (see for example [307]). However, here, (a) the amplitudes are quite low relative to the dominant GW emission (see Fig. 4.10), (b) for the cases where the largest amplitudes are excited, the initial r_p is sufficiently small that only a few cycles of waves will be emitted before subsequent merger, limiting the signal-to-noise that could be built up, and (c) the frequency is quite high (above 1 kHz) and thus not in a regime where the AdLIGO-class detectors are very sensitive. Thus, even if there is a sizable population of eccentric merger events as studied here, it is unlikely that any corresponding f-mode excitation will be observed with the current generation of GW detectors.

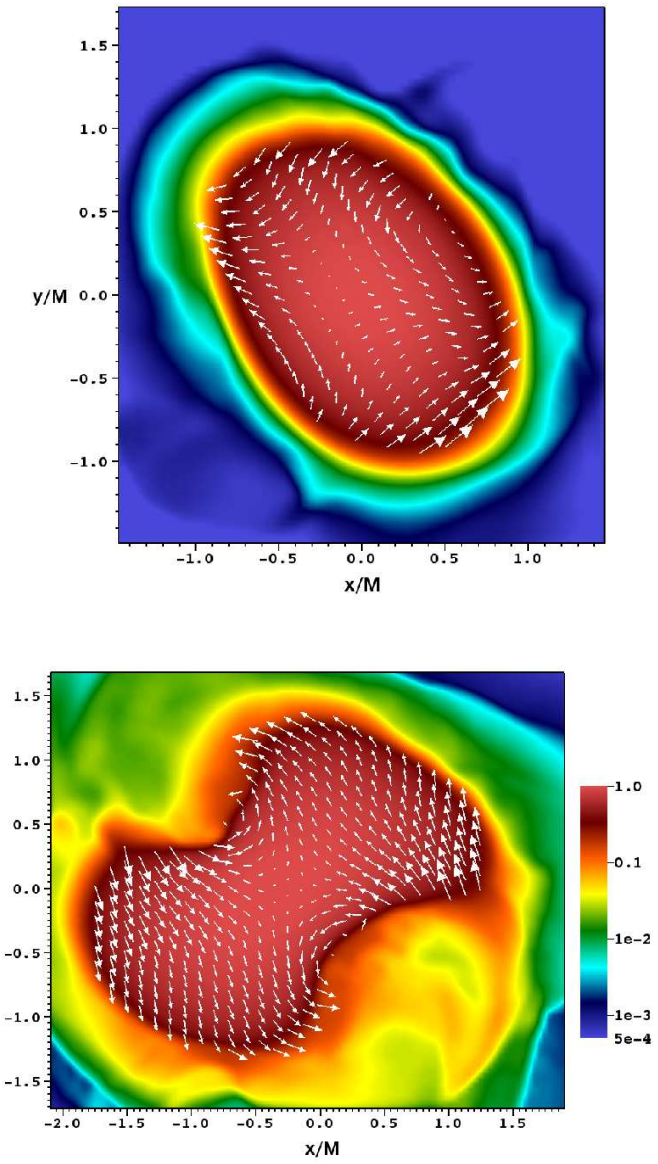

Figure 4.11: NSs exhibiting large-amplitude f-mode oscillations following the first interaction with the (nonspinning) BH. The cases shown are $r_p = 6.95$ with the HB EOS at $t = 341M$ (top) and $r_p = 7.0$ with the 2H EOS at $t = 356M$ (for the latter case, see the bottom left-panel of Fig. 4.3 for a snapshot of the density near the time of closest approach to the BH when this large oscillation is excited). The color map shows the rest-mass density in the equatorial plane on a logarithmic scale, normalized to the instantaneous maximum density. The arrows show the velocity in the NS center-of-mass frame. The longest velocity arrows correspond to velocity magnitudes 0.084 (top) and 0.17 (bottom). Though the two cases have similar periapsis radii, the lower compaction in the 2H-case leads to a much stronger tidal interaction and an f-mode which shows nonlinear characteristics.

r_p	$M_0/M_0(t=0)^a$	$M_{0,u}/M_0(t=0)^b$	$\tau_{\rm acc}$ (ms) ^{c}	First periapsis ^{d}		Total ^{e}	
				$\frac{E_{GW}}{M}\cdot 10^2$	$\frac{J_{GW}}{M^2}\cdot 10^2$	$\frac{E_{GW}}{M}\cdot 10^2$	$\frac{J_{GW}}{M^2}\cdot 10^2$
2H EOS							
5.00	0.008	0.0	56	–	–	0.58	3.61
6.75	0.278	0.117	18	–	–	0.47	4.65
7.00	0.303	0.149	60	0.387	4.53	0.43	5.41
7.25	...	...	...	0.283	3.90	...	...
7.50	...	...	...	0.200	3.07	...	...
B EOS							
5.00	0.008	0.0	57	–	–	0.60	3.83
6.25	0.008	0.0	64	–	–	0.87	5.63
7.00	0.010	0.001	10	0.718	7.69	1.73	10.7
7.50	...	...	...	0.268	3.72	...	...

Table 4.4: Disk properties and GW energy and angular-momentum losses for an initially hyperbolic ($e \approx 1$) encounter of a BH with zero-spin and a NS with 2H and B EOS. The same comments and set of footnotes ^{a} to ^{f} apply as in Table 4.1.

4.4.4 Bound eccentric evolution

Finally, we simulated binaries where the BH and NS have initial-orbital parameters corresponding to a bound orbit with $e = 0.75$ for a range of values of r_p. These simulations can be viewed as corresponding to systems that have already become bound through one or more close-encounters and lost some of their initial eccentricity. In practice, the length of such evolutions would be very computationally expensive to follow in full. Of the impact parameters considered (see Table 4.5), $r_p = 7.5$ is the only direct-plunge, and $r_p = 7.81$ is the only case we followed past periapsis passage to merge on the second close-encounter. For the remaining cases ($r_p = 8.13$, 8.75, and 10.0), we only followed partially through their elliptic orbits after the first close-encounter. The threshold for merger on the first encounter moves out slightly in this case as an appeal to geodesics in Schwarzschild would suggest. In Fig. 4.12, we plot the gravitational waveforms from two fly-by close-encounters $r_p = 8.13$ and 10.0. In addition, we fit the expected waveform according to a Newtonian-order quadrupole approximation [257, 303, 308] (NQA) to our numerical results by multiplying by an overall factor. As found in [4] and in our other simulations here for the marginally unbound case, though the shape of the waveforms agree quite well, the numerical results exhibit a significant amplitude enhancement that is larger the closer one gets to the threshold for merger during the close-encounter. In addition, from Fig. 4.8 we can see that the near-threshold merger waveform shows more evidence of whirling than the initially unbound case.

r_p	$M_0/M_0(t=0)^a$	$M_{0,u}/M_0(t=0)^b$	$\tau_{\rm acc}$ (ms) ^{c}	First periapsis ^{d}		Total ^{e}	
				$\frac{E_{GW}}{M}\cdot 10^2$	$\frac{J_{GW}}{M^2}\cdot 10^2$	$\frac{E_{GW}}{M}\cdot 10^2$	$\frac{J_{GW}}{M^2}\cdot 10^2$
7.50	0.109	0.062	32	–	–	1.47	13.6
7.81	0.007	0.001	7.1	0.410	5.25	1.58	16.1
8.13	...	...	...	0.248	3.67	...	...
8.75	...	...	...	0.125	2.34	...	...
10.0	...	...	...	0.049	1.28	...	...

Table 4.5: Disk properties and GW energy and angular-momentum losses for an initially eccentric $e = 0.75$ encounter of a zero-spin BH with a NS with HB EOS. The same comments and set of footnotes ^{a} to ^{f} apply as in Table 4.1.

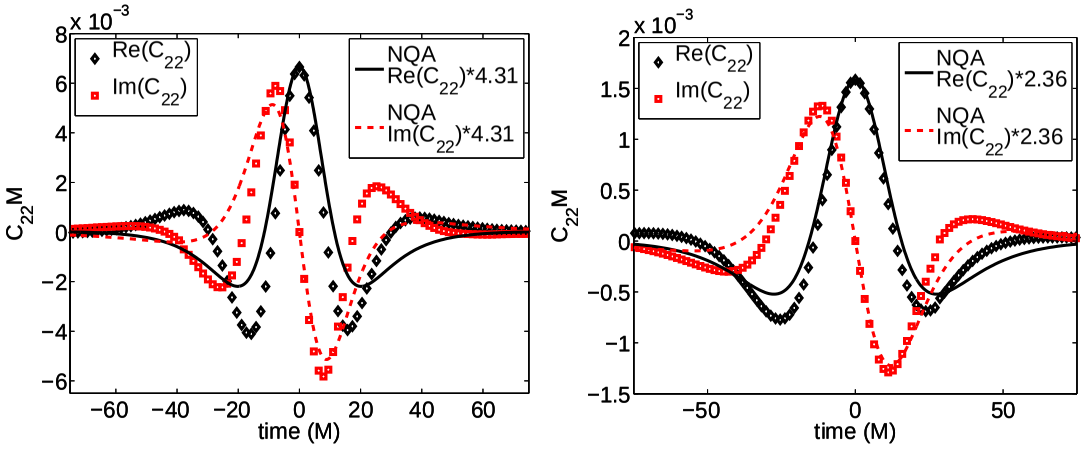

Figure 4.12: The real and imaginary components (black diamonds and red squares) of the $l = 2$, $m = 2$ spherical-harmonic of $r\Psi_4$ for $e = 0.75$ and $r_p = 8.125$ (left) and $r_p = 10$ (right). For comparison the NQA analytical results are shown multiplied by an overall factor so that the magnitude and phase match at peak ($t = 0$).

4.5 Evolution of orbital parameters

There is a dramatic enhancement in gravitational-wave energy and angular momentum emitted in a BH-NS close-encounter that occurs as the threshold for merger on the first encounter is approached. In this section, we will attempt to explain this enhancement by analogy to the zoom-whirl orbits in Kerr spacetimes, and extrapolate this behavior to close-encounters with different eccentricities and spins. Then we will use these results to approximate the evolution of orbital parameters for BH-NS systems undergoing a series of close-encounters.

4.5.1 Zoom-whirl enhancement

As discussed in the previous section and as can be seen in Fig. 4.13, though different values of initial spin or eccentricity may shift the critical value of r_p, which we shall call r_c at which the NS merges with the BH during a first encounter, for all the cases considered there is a significant enhancement in the energy of the gravitational waves emitted as this threshold is approached. This can be understood by analogy

to the zoom-whirl orbits in Kerr spacetimes. As the BH-NS approaches the critical-impact parameter, it is closer and closer to the unstable orbit dividing plunging and nonplunging orbits and will, therefore, exhibit more and more whirling behavior. Though the effect is most dramatic near threshold, this zoom-whirl analog is a way to understand the significant enhancements over the NQA predictions that persist till $r_p \approx 10$ (see Fig.4 in [4]). This motivates a fit to the GW energy emitted in a whirling close-encounter with the functional form (see Fig. 4.13)

$$E_{\rm GW} = E_0(1 - (\delta r_p/\Delta)^\gamma) \tag{4.2}$$

where $\delta r_p = r_p - r_c$, E_0 is the difference in energy between a quasicircular orbit and an eccentricity e orbit both with $r_p = r_c$, Δ is the range over which zoom-whirl-like behavior dominates the GW- emission energetics, and γ is a parameter that in the geodesic analogue is related to the instability exponent of the corresponding unstable circular orbit. Given the limited number of points we have, we choose to use γ as our single fitting parameter. We set r_c to the average of the closest sub and supercritical values of r_p from the simulations. We choose $\Delta = 3$ by inspection so that values of r_p outside this range are well-approximated by the NQA model. Certainly, in future work once more data points are available it would be preferable to more systematically fit to the other parameters as well, and refine the model.

The left panel of Fig. 4.13 shows this fitting performed individually to each set (e, a) of simulations run. We should note that due to limited computational resources we have not been able to perform this fitting at multiple resolutions in order to be able to estimate the effect of truncation error on γ. However, due to the sensitivity of $E_{\rm GW}$ on r_p that can be seen in Fig. 4.13, one would expect that the truncation error in these values will be dominated by the resolution dependence of r_c as opposed to the error in γ. In the remainder of this section we will use the data from the $e \approx 1$, $a = 0$

set to calibrate geodesic-inspired extensions to arbitrary values of (e, a), which can then be compared to the other three sets of simulation data (right panel of Fig. 4.13) to test how well this extrapolation works.

To extend this model to different values of eccentricity e and BH spin a, we assume that the dependency of r_c and γ on these values is the same as in the geodesic case on a Kerr background. We will use $a_{\rm eff}$ to refer to the effective spin parameter we use in the Kerr formulas. For better correspondence with the Kerr spacetime, we want to take $a_{\rm eff}$ to be the approximate spin of the BH that would form if a merger occurred. We do this rather then use the initial spin of the BH based on results from [167], which suggest that far from the geodesic limit the total angular momentum of the binary is more important than the BH spin. We estimate $a_{\rm eff}$ using

$$a_{\rm eff} = a_0 \frac{\sqrt{(1+e)r_p}}{\sqrt{2r_{c0}}} + a(M_{\rm BH}/M)^2. \tag{4.3}$$

where $M_{\rm BH}$, a, r_p, and e are the initial BH-mass, initial BH-spin, periapsis, and eccentricity, respectively, of the encounter for which we want to compute an $a_{\rm eff}$, and $a_0 \approx 0.5$ is the final spin measured from the $e \approx 1$, $a = 0$, $r_p = r_{c0} \approx 6.9$ simulation. In Table 4.2, we show how $a_{\rm eff}$ compares to the final BH-spins in the simulations that we followed through merger. This simple formula based on the total angular momentum of the system does not attempt to capture any of the complications due to differences in matter dynamics or gravitational radiation between the different cases, and as can be seen does not always capture the trends with r_p seen in the simulations. We use $a_{\rm eff}$ because it has a simple motivation, and it does a decent job of estimating the final BH-spin for the purposes of this model. This allows us to extend this model to other values eccentricity e and BH-spin a that were not simulated.

Recall that for equatorial geodesics with eccentricity e in Boyer-Lindquist coordinates with BH-spin parameter a, there is a value for the periapsis that corresponds

to a marginally unstable orbit $r_c^{\rm BL}(e,a)$. It can be found by solving the equation (see, for example, [305]) $(r_c^{\rm BL})^2 = (J-aE)^2(1+e)/(3-e)$, where E and J are the orbit's specific energy and angular momentum, respectively. For our model, we assume that $r_c(e,a_{\rm eff}) \propto r_c^{\rm BL}(e,a_{\rm eff})$, and we fit the proportionality constant using our numerical results for $e \approx 1$, $a = 0$.

The instability exponent for unstable circular orbits in Boyer-Lindquist coordinates is given by [309, 167]

$$\gamma^{\rm BL}(e,a) = \frac{r}{2\pi}\left[3r^2 D + \frac{4M}{\omega^2}(rR^2\omega^2 - 4Ma\omega - r + 2m)\right]^{-1/2} \tag{4.4}$$

where $R = r^2 + a^2(1+2M/r)$, $D = r^2 + a^2 - 2Mr$, $\omega = M/(Ma \pm \sqrt{Mr^3})$ ($\pm$ for prograde and retrograde, respectively), and we set $r = r_c^{\rm BL}(e,a)$. Again, we assume that $\gamma(e,a_{\rm eff}) \propto \gamma^{\rm BL}(e,a_{\rm eff})$ and fit the proportionality constant using our numerical results for $e \approx 1$, $a = 0$. For the angular momentum lost to gravitational waves in a close-encounter we assume a similar expression

$$J_{\rm GW} = J_0(1 - (\delta r_p/\Delta)^\gamma) \tag{4.5}$$

where again J_0 is the difference in angular momentum of a quasicircular orbit and an eccentricity e orbit evaluated at the same separation r_p.

This simple prescription for estimating gravitational-wave energy and angular-momentum loss has some obvious limitations. We are extrapolating the critical impact parameter and instability exponent based on a Kerr spacetime to a BH-NS spacetime that is dynamic and nonperturbative. We are also ignoring tidal effects or dependence on EOS in this model. Nevertheless, in Fig. 4.13, we compare how closely this predicted scaling with spin and eccentricity matches that from simulation results. Given its simplicity, as well as the numerical error in these results, this model does a satisfactory job of capturing the trends in these scalings.

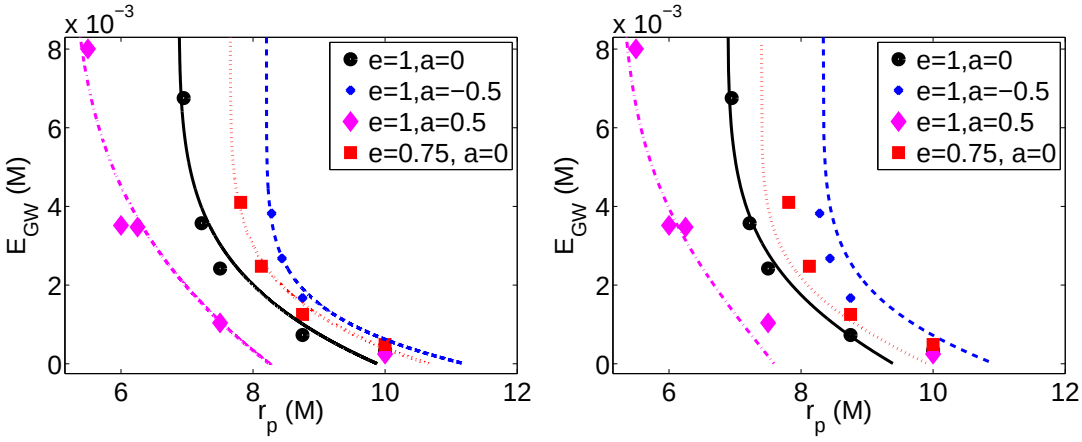

Figure 4.13: **Left:** Energy lost to GWs during the initial close-encounter (i.e. excluding merger) as a function of r_p for initial BH spin $a = 0, -0.5$, and 0.5 and for initial eccentricity $e = 1$ and 0.75. The functional form $E_0(1 - (\delta r_p/\Delta)^\gamma)$ (lines) motivated by zoom-whirl dynamics is a fit to the simulation results (points). $\delta r_p = r_p - r_c$ where r_c is the threshold value for merger during the encounter. E_0 is the difference in energy between a quasicircular orbit and an $e \approx 1$ (0.75) orbit, both having $r_p = r_c$. Δ is the range over which zoom-whirl-like behavior dominates the GW-emission energetics. γ is a parameter that in the geodesic analogue is related to the instability exponent of the corresponding unstable circular orbit, here, we use it as our fitting parameter. We obtain $\gamma = 0.19$, 0.13, 0.25, and 0.16 for $(e, a) = (1, 0)$, (1,-0.5), (1,0.5), and (0.75,0), respectively. **Right:** This shows the same simulation data points as the left figure, though here we use the $e = 1$, $a = 0$ case (solid, black points) to determine the free parameters for the method described in the text to extrapolate the values of r_c and γ to the other three cases.

4.5.2 Systems undergoing multiple close-encounters

The enhanced GW energy and angular-momentum losses during a close-encounter for a given r_p result in more rapid loss of eccentricity and larger rate of decrease of r_p of the next encounter. Figure 4.14 shows approximate trajectories in e and r_p for binaries on initially marginally unbound (i.e., $e = 1 + \epsilon$) orbits for a range of initial BH spin. These results were obtained using the above model for energy and angular momentum lost to GWs and assuming e and r_p follow the Newtonian relationship to energy and angular momentum. We approximate these losses as occurring in discrete steps during close-encounters. (This approximation will break down as $e \to 0$.) Trajectories computed with the NQA amplitude and eccentricity-dependence [257, 303, 308] are

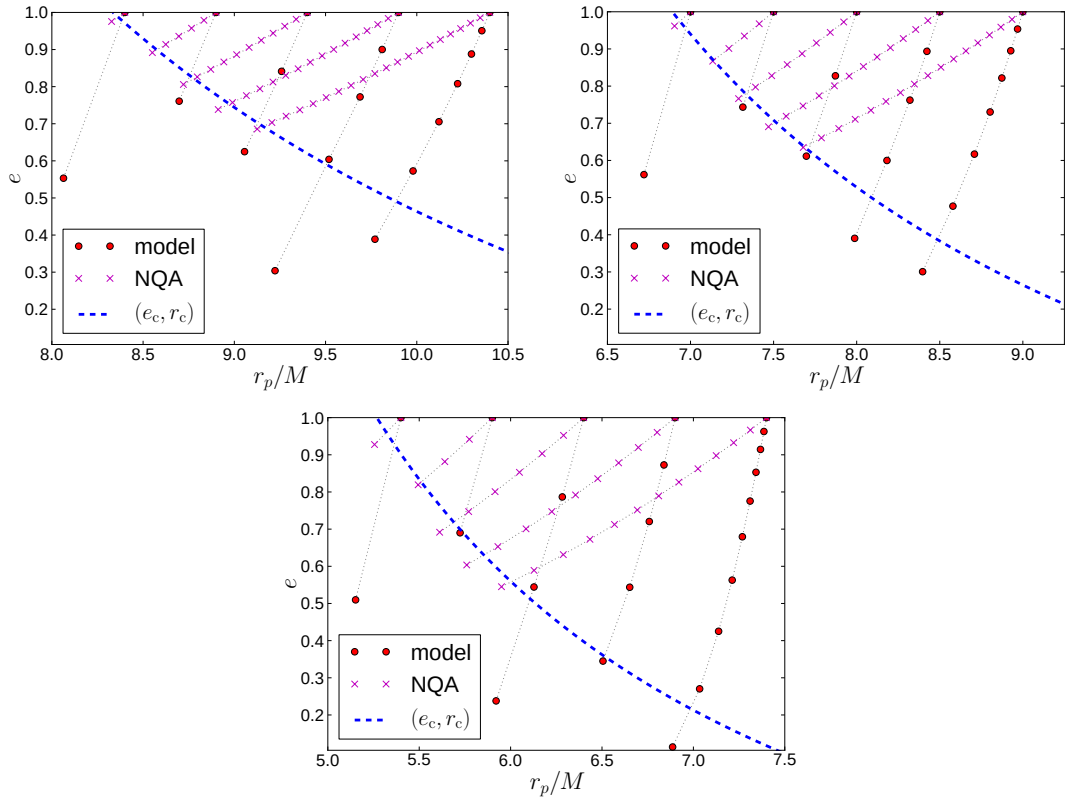

Figure 4.14: The evolution of the eccentricity and periapsis separation of various $4:1$ mass ratio BH-NS binaries that begin marginally unbound and undergo a series of close-encounters (large red points) before merging. For comparison, we also plot the results using the NQA expressions from [257, 303] (magenta x's). We also plot the critical eccentricity for a given r_p for a close-encounter to result in merger (blue, dotted-line). Hence, the points below this curve correspond to merger events. From left to right, top to bottom, the plots correspond to an initial BH-spin of $a = -0.5$, 0, and 0.5, respectively.

also shown in the figure. The NQA execute many more orbits before merger. This clear departure from the NQA prediction at small r_p due to strong field-GR effects should thus be apparent in the gravitational waveform. This model can also be used to predict approximately the critical-initial impact parameter for the BH-NS system to merge on the second close-encounter, the third close-encounter, and so on. We expect interesting dynamics around each of the thresholds up until the point where the system has undergone enough close-encounters that it circularizes.

4.6 Conclusions

We have performed an initial survey of eccentric BH-NS mergers including the effects of black hole spin and varying the NS EOS. Though the limited number of values we considered in this work does not begin to exhaust the parameter space, what is immediately apparent is the strong diversity in the resulting gravitational and matter dynamics. Though we have not yet studied the consequences of this on gravitational-wave detectability and parameter extraction, or possible electromagnetic counterparts, it is clear that the outcome can depend sensitively on the binary parameters and matter EOS.

In order to understand the effects of large eccentricity, these simulations can be compared to the quasicircular BH-NS merger simulations of [294, 292], which used the same piecewise polytrope equations of state. In [294], it was found that for a nonspinning BH and a 3:1-mass ratio, the resulting disk masses where 0.044, 0.0015, and $< 10^{-5}\ M_\odot$ for the 2H, HB, and B EOSs, respectively. Hence eccentric mergers with certain ranges of impact parameters is one way to achieve significantly larger accretion disks compared to the quasicircular case without BH spin. The effects of BH spin were considered in [292], where for a 4:1-mass ratio and the HB EOS they found disk masses of 0.024 and 0.18 $M_\odot$ for BH spins of $a = 0.5$ and 0.75, respectively (and even larger values for stiffer EOSs or lower mass ratios). They also only found a non-negligible amount of unbound material ($\geq 0.01 M_\odot$) for stiff EOSs like the 2H. Thus, an important characteristic of eccentric mergers is the larger amount of ejected material found for some parameters. This could be a significant source of r-process elements [36, 37, 38], and give rise to EM counterparts, e.g. through nuclear decay of the radioactive r-process isotopes [287, 88]. The amount of energy radiated away in gravitational waves for the quasicircular case is somewhat higher than the values found here (for example, $E_{GW} = 1.7\%$ of the total mass for a 4:1 mass ratio, HB EOS, and $a = 0.5$ in [292]). The gravitational-wave signal is of course completely

different for eccentric mergers, which are dominated by bursts from close-encounters or merger of the two compact objects.

Whether dynamical capture BH-NS mergers occur with sufficient frequency in the Universe to constitute a decent event rate for ground-based GW detectors is another question; at the least, failure to observe such events will place constraints on these sources, while if several are observed given the sensitivity of the outcome to properties of the binary, they could be ideal environments to reveal the structure of neutron stars. And again, we should emphasize that excessive fine tuning of parameters is not required for significant variability. Taking the relative velocity at large separations in a typical nuclear-cluster cusp as an example (≈ 1000 km/s), roughly 25% of such encounters will have $r_p \lesssim 10$, (following the same line of reasoning discussed in the introduction for the percentage of direct collisions) corresponding to the cases studied here. Certainly some of the most extreme examples of mass transfer, large accretion disks, or multiple whirl orbits will be rare; perusing Tables 4.1-4.5 will give some idea of the distribution with r_p. (Recall that the cross section scales linearly with r_p due to gravitational focusing, and that one would also expect some cases with larger initial r_p than we followed through merger to exhibit similar variability.) It is not trivial to calculate a transition value of initial r_p above which the qualitative behavior at late times is described by a quasicircular inspiral, though our study suggests at least a quarter of dynamical-capture binaries will merge with high eccentricity.

In Chap. 6 we elaborate on the detectability of the GW signals from BH-NS mergers that arise from dynamical capture in the strong-field regime. This complements the first study of such systems presented in [260], in that we intend to focus on the later stages of high-eccentricity mergers, including the merger/ringdown part of the signal. Future work includes expanding the parameter space to different BH and NS masses, BH-spin orientations, and (as computational resources permit) evolution of systems that exhibit more than two close-encounters before merger. Performing

higher-resolutions simulations will also be important to coming up with a more quantitatively accurate model of the behavior of the BH-NS binary near the threshold for merger during a given close-encounter. Doing so will not only require additional computational resources but a better method for creating initial data describing such eccentric binaries, since the superposition method used here imposes an effective floor on the accuracy that be reached. It would also certainly be interesting to investigate EM counterparts to these events; such simulations would require extensions to the code used here beyond the present GRHD.

Chapter 5

Dynamical capture binary neutron star mergers

5.1 Introduction

In addition to the black hole-neutron star binaries explored in Chap. 4, merging binary neutron stars (NSs) also promise to be rich sources of both gravitational and electromagnetic (EM) radiation, probing strong-field gravity and nuclear density physics, and hence warrant their own detailed study. NS–NS mergers are a primary source targeted by gravitational wave (GW) detectors such as [10] and they are also candidates for short gamma-ray burst (SGRB) progenitors and several other EM counterparts [88, 310, 311].

There have been numerous studies of primordial binary NS mergers (see e.g. [161]), which will have essentially zero orbital eccentricity when they enter the frequency band of ground-based GW detectors. However, binaries may also arise via n-body interactions in dense stellar regions and some fraction of them will have sizable eccentricity at merger. Recall from Chap. 4 that such binaries may form in globular clusters (GCs) undergoing core collapse [262, 273] or in galactic nuclei [299, 260, 277]

through dynamical capture, as well as possibly through Kozai resonance in a triple system [278], or exchange interactions [273]. It is far from certain that high eccentricity mergers occur frequently enough to expect observation with the upcoming generation of GW detectors. However, it is also not implausible that they do, and as eccentric NS mergers may also produce distinguishable EM emission compared to quasi-circular mergers, it behooves us to understand both systems from a multi-messenger perspective.

In Chap. 4, black-hole–neutron-star (BH–NS) mergers formed through dynamical capture were found to exhibit a rich variation with impact parameter, in some cases producing sizable disks and amounts of unbound material. In [153], several eccentric NS–NS mergers were studied using a $\Gamma = 2$ equation of state (EOS) and shown to exhibit f-mode excitation during close encounters. There have also been studies of BH–NS and NS–NS collisions with Newtonian gravity [264, 312] showing similar variation in the outcomes.

In this chapter, we study dynamical capture NS–NS mergers for a range of impact parameters using general-relativistic hydrodynamics (GRHD). We also consider several different NS EOSs because of the uncertainty regarding the correct description of matter above nuclear densities. One of the important issues we address for the first time is if these mergers can produce hypermassive neutron stars (HMNSs). In studies of quasi-circular systems it was found that thermal energy from the merger, as well as differential rotation, could support long-lived HMNSs for some EOSs e.g., [105] and that this would be imprinted in the GW signal and resulting disk properties. HMNSs with longer lifetimes can also build up significant magnetic fields which can power strong EM transients during the collapse to a BH [40]. For dynamical capture binaries, the amount of angular momentum, and likely the amount of shock heating, will be strong functions of impact parameter, suggesting HMNS formation will be as well.

Another notable feature of dynamical capture NS–NS mergers is their potential to produce unbound nuclear material which will decompress and form heavy nuclei via the r-process [36, 37, 38]; subsequent radioactive decay could produce observable emission. Recent work [313, 314] suggests processes like NS–NS mergers may be needed to supplement the supernovae r-process yield in accounting for the observed abundances. Though simulations of quasi-circular NS–NS mergers using Newtonian or conformally flat gravity have found suitable ejecta, they seem to be in tension with fully general-relativistic results which find negligible amounts of ejecta [161]. This is *arguably* because of strong-field GR effects, such as BH formation and the existence of innermost stable orbits. As we show, dynamical capture mergers are more promising sources of ejecta, presumably as the stars are less bound when disruption occurs.

In the remainder of this chapter, we outline our methods for simulating NS–NS mergers with GRHD, discuss the merger dynamics for a range of impact parameters and three different EOSs, and comment on potential GW and EM counterparts. We find that, while the GW signals from these mergers may be challenging to detect with upcoming ground-based detectors, they have the potential to source numerous EM transients. Non-merging close encounters can induce tidal deformations strong enough to crack the NSs' crusts; a merger where the total mass is above the maximum mass of a single NS can either promptly collapse to a BH or produce a hot, rapidly rotating HMNS, where the latter outcome tends to have more massive disks and ejected material.

5.2 Numerical approach

We numerically solve the Einstein equations, discretized with finite differences, in the generalized harmonic formulation. The hydrodynamics are evolved in a conservative formulation using high-resolution shock-capturing techniques. Details are given in

Chap. 2. We use the same gauge, slope limiters, and flux methods as in Chap. 4. In particular, we use WENO-5 [133] for reconstructing fluid variables at cell interfaces and HLL [126] for calculating intercell fluxes.

We use adaptive mesh refinement with up to seven levels that are dynamically adjusted according to truncation error (TE) estimates. To measure convergence and TE, we perform a select number of simulations at three different resolutions. The low, medium, and high resolutions, respectively, have base levels covered by 129^3, 201^3, and 257^3 points (with the maximum TE threshold adjusted accordingly), and approximately 64, 100, and 128 points across the diameter of the NSs on the finest level at the initial time (for the HB EOS). In Figure 5.1, we show an example of convergence of NS trajectories as well as the constraints of the field equations. All simulations are performed at medium resolution and results quoted below are from this resolution, with Richardson extrapolated values given in parenthesis (indicating the quantity's TE) where multiple resolution data are available.

We use the piece-wise polytropic EOS models labeled 2H, HB, and B from [23] and include a thermal component $P_{\rm th} = (\Gamma_{\rm th} - 1)\epsilon_{\rm th}\rho$ with $\Gamma_{\rm th} = 1.5$. These EOSs were designed to span the range of possible EOSs. The 2H, HB, and B EOSs, respectively, give NSs with compactions $M_{\rm NS}/R_{\rm NS}$ of 0.13, 0.17, and 0.18 for $M_{\rm NS} = 1.35\ M_\odot$ and maximum masses of 2.83, 2.12, and 2.0 $M_\odot$ (unless otherwise stated we use geometric units with $G = c = 1$).

We construct initial data by solving the constraint equations in the conformal thin-sandwich formulation as described in Chap. 3. We begin the two NSs at a separation of $d = 50M$, where $M = 2.7\ M_\odot$ is the total mass of the system (hence $d = 200$ km), and consider various initial velocities which we label by r_p, the periastron distances of parabolic Newtonian orbits with the same velocities (which will be different from the actual periastron distance of the simulated binaries). We performed the majority of the simulations using the middle compaction HB EOS but ran select impact

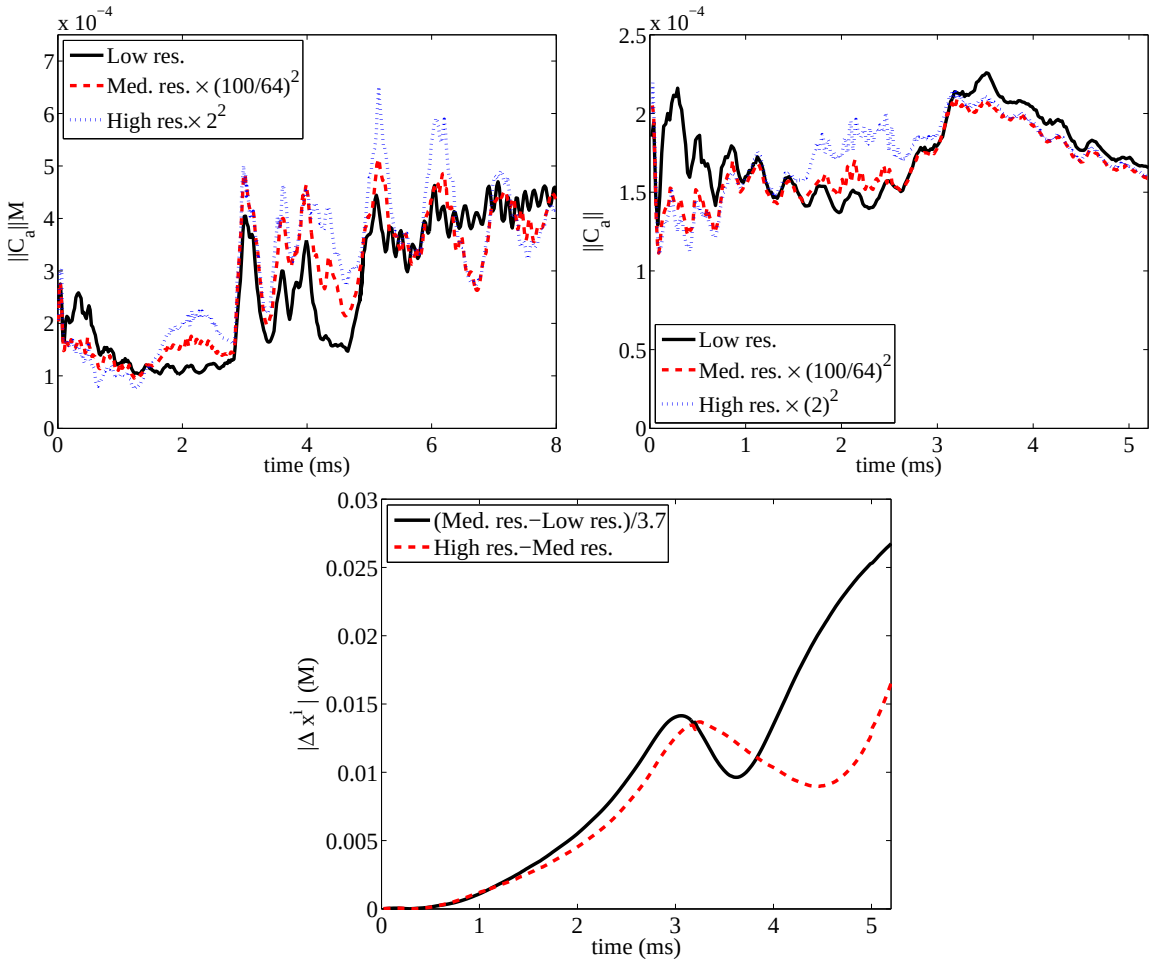

Figure 5.1: Top: L^2-norm of the constraints ($C_a := H_a - \Box x_a$) in the $100M \times 100M$ region around the center of mass in the equatorial plane for the $r_p = 7.5$ (left) and $r_p = 10$ (right) HB cases, with the three resolutions scaled assuming second-order convergence. Bottom: the difference in the NS center of mass as a function of time from the different resolution runs for the $r_p = 10$, HB case, scaled assuming second-order convergence.

parameters using all three EOSs. For all simulations except one we used NSs that both have a mass of 1.35 $M_\odot$; the other case has a mass ratio of $q = 0.8$ and a total mass of 2.88 $M_\odot$. We leave a more detailed study of mass-ratio dependence to future work.

5.3 Results and discussion

5.3.1 Effect of impact parameter

Using the HB EOS, we consider a range of impact parameters from $r_p/M = 2.5$ (we henceforth quote r_p in units of M) to $r_p = 20$ (i.e., 10 to 80 km). This is well within the range to form a bound system as [257] indicate that for equal masses, GW capture occurs for $r_p \lesssim 1.8/w^{4/7}$ where w is the velocity at infinity. (Tidal energy loss [256], because of the relative scalings with distance, is subdominant in determining *capture*.) Binaries that approach with small impact parameters ($r_p = 2.5$ and 5) promptly merge and collapse to a BH. For $r_p = 2.5$ the mass and dimensionless spin of the final BH is $M_{\rm BH}/M = 0.998(0.995)$ and $a = 0.537(0.538)$ while the energy and angular momentum in GWs is $E_{\rm GW}/M = 3.7(4.0) \times 10^{-3}$ and $J_{\rm GW}/M^2 = 2.60(2.75) \times 10^{-2}$. For $r_p = 5$, $M_{\rm BH}/M = 0.985$, $a = 0.719$, $E_{\rm GW}/M = 1.06 \times 10^{-2}$, and $J_{\rm GW}/M^2 = 6.74 \times 10^{-2}$; Figure 5.2 shows the corresponding GW signals. For both these cases, the amount of material leftover after merger is $\lesssim 10^{-6}$ the original rest mass of the NSs. The dearth of matter post-merger, and the fact that most of the power of the GW signal is at a relatively high frequency ($\sim$ 5 kHz), makes these scenarios less promising sources of observable EM or gravitational radiation.

Binaries with larger impact parameters ($r_p = 10$, 15, and 20) result in non-merging close encounters followed by long elliptic orbits which we did not follow in their entirety due to limited computational resources. The close encounters result in pulses of GW radiation and excite f-mode oscillations in the stars, which are also evident

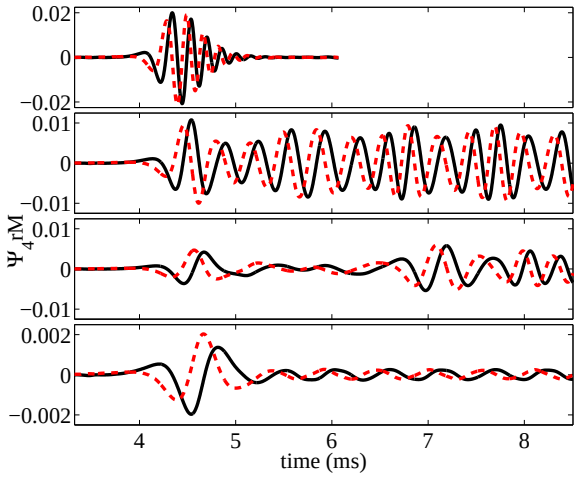

Figure 5.2: Real (solid black) and imaginary (dotted red) components of the Newman–Penrose scalar Ψ_4 on the axis orthogonal to the orbit measured at $r = 100M$ for the $r_p = 5$, 7.5, 8.75, and 10 cases with HB EOS.

in the GW signal (see Figures 5.2 and 5.3). This f-mode excitation was studied in detail in [153] and also found in similar BH–NS encounters (see Chap. 4). The induced tidal ellipticity in the $r_p = 10$ case is greater than the $\delta R/R \approx 0.1$ value required to induce a strain of $u_{\rm strain} \simeq 0.1$ and shatter the NS crust ([315]; though we are not modeling the crust here). The energy and angular momentum radiated in the $r_p = 10$ close encounter is $E_{\rm GW}/M = 1.472(1.474) \times 10^{-3}$ and $J_{\rm GW}/M^2 = 3.545(3.546)\times10^{-2}$; for $r_p = 15$ and 20 $(E_{\rm GW}/M, J_{\rm GW}/M^2) = (1.64\times10^{-4}, 8.69\times10^{-3})$ and $(3.8 \times 10^{-5}, 2.8 \times 10^{-3})$, respectively. Taking this as orbital energy and angular momentum loss gives a Newtonian estimate for the time to the next close encounter of 65 ms for the $r_p = 10$ case. For the next largest impact parameter simulated, $r_p = 15$, the tidal deformation is negligible, and the estimated time to the next close encounter is 1.8 s. This suggests precursor EM transients associated with crust shattering for these systems could be produced of order hundreds of milliseconds, but probably not more than a few seconds, before merger.

For the intermediate cases ($r_p = 7.5$ and 8.75), the stars come into contact and form a single object. For $r_p = 7.5$, this happens at the first close encounter; for

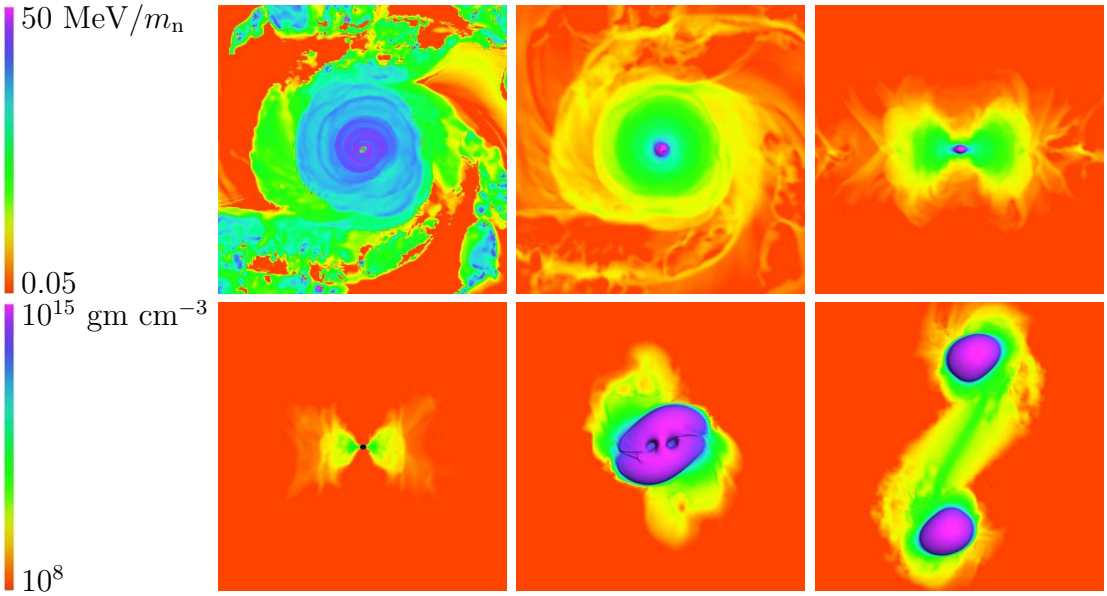

Figure 5.3: Snapshots of thermal specific energy (top left panel) with a logarithmic color scale from 0.05 to 50 MeV/$m_{\rm n}$ and rest-mass density (other five panels) from 10^8 to 10^{15} gm cm^{-3}. The top left and top middle, and bottom middle and bottom right panels show the equatorial plane, while the other two show a perpendicular plane through the center of mass. The top panels show an HMNS with surrounding disk and unbound material from the $r_p = 8.75$, HB EOS case at $t = 13.3$ ms. The bottom panels show, from left to right, a BH and a surrounding disk for the $r_p = 7.5$ B EOS case at $t = 10.2$ ms; a merger from the $r_p = 7.5$, HB EOS case at $t = 3.2$ ms; NSs with excited f-mode perturbations post close encounter from the $r_p = 10$, HB EOS case at $t = 4.1$ ms. The first four panels have the same distance scale, where the coordinate radius of the HMNS and BH are ≈ 13 and ≈ 6 km, respectively. The last two panels share a second distance scale; the coordinate separation between the NSs in the last panel is ≈ 73 km.

$r_p = 8.75$, the stars briefly fly apart before merging. When the stars come into contact they undergo shock heating and develop features similar to the Kelvin–Helmholtz vortices observed in [312] (see Figure 5.3). Though the total mass is above the maximum for a cold, static star with this EOS, the stars are highly spun-up and have a significant thermal component (22%–25%) to their internal energy (see Table 5.1). In the vicinity of these objects the (density-weighted) average thermal specific energy is $\epsilon_{\rm th} \approx 10$–$20$ MeV$/m_n$ where m_n is the neutron mass.

These HMNSs produce quasi-periodic GWs with frequency ~ 3.2 kHz (see Figure 5.2). Though these hypermassive configurations survive the duration of our simulations (≈ 13 ms), they presumably will eventually collapse to form BHs. In Table 5.1, we indicate the rate of energy and angular momentum loss to GWs at the end of the simulation. From this one can roughly estimate the time it will take for the HMNS to radiate its remaining angular momentum to GWs assuming a constant $dJ_{\rm GW}/dt$ (e.g., for the $r_p = 7.5$, HB case, it will take ~ 70 ms). However, magnetohydrodynamic effects, such as the Kelvin-Helmholtz [316, 317, 318] the magnetorational instability, [319] — as well as cooling by neutrino emission, (which could take seconds) [105], none of which we take into account, will also be important in determining when these stars collapse. Table 5.1 also lists data from the unequal mass ratio ($q = 0.8$), $r_p = 7.5$ case, which shows qualitatively similar behavior to the equal mass case.

r_p	EOS	$J_{\rm tot}/M^2$ [a]	$\langle\epsilon_{\rm th}\rangle$ [b]	$E_{\rm th}/E_{\rm int}$ [c]	$M_{0,u}$ [d]	$\frac{E_{\rm GW}}{M}\times 100$ [e]	$\frac{J_{\rm GW}}{M^2}\times 100$ [f]	$dE_{\rm GW}/dt$ [g]	$dJ_{\rm GW}/dt/M$ [h]
7.5	HB	0.96	20	0.22	0.64	3.78(3.91)	30.5(31.2)	1.56×10^{-5}	1.23×10^{-4}
7.5 ($q=0.8$)	HB	0.96	14	0.17	0.57	3.36	27.5	7.60×10^{-6}	6.22×10^{-5}
7.5	2H	0.95	14	0.31	4.39	0.70	10.8	3.45×10^{-7}	3.20×10^{-6}
8.75	HB	1.05	17	0.25	2.65	2.07	24.0	1.50×10^{-5}	1.14×10^{-4}
10	2H	1.11	11	0.27	6.65	0.50	9.28	2.70×10^{-6}	3.48×10^{-5}

Table 5.1: Properties of Hypermassive NS Cases, Measured at $t \approx 13.3$ms

[a] Global angular momentum.

[b] Density-weighted average of the thermal component of the specific energy in units of MeV/m_n.

[c] Fraction of internal (Eulerian) energy that is thermal.

[d] Rest mass that is unbound in percent of $M_\odot$.

[e] The total energy emitted in GWs through the $r = 100M$ surface.

[f] The total angular momentum emitted in GWs.

[g] Average GW flux of energy.

[h] Average GW flux of angular momentum.

5.3.2 Effect of equation of state

In addition to the HB EOS, we also simulated an intermediate impact parameter $r_p = 7.5$ using the B (softer) and 2H (stiffer) EOSs. For the B EOS, a BH forms soon after merger with $M_{\rm BH}/M = 0.988$ and $a = 0.766$; the total radiated energy and angular momentum are $E_{\rm GW}/M = 3.55 \times 10^{-2}$ and $J_{\rm GW}/M^2 = 0.239$, respectively. For the 2H EOS, the total mass is below the maximum for a stable cold NS and the stars fly apart after the first collision before eventually settling down to a single massive star.

We also performed simulations with the B and 2H EOSs and $r_p = 10$. With the softer B EOS, the NSs undergo a close encounter that is qualitatively similar to the HB EOS. However, because of the greater compactness of the NS, the amplitude of the resulting GW pulse is larger with 19% and 13% more energy and angular momentum, respectively. Due to the large eccentricity, this will have a significant effect on the subsequent orbit of the NSs. Ignoring any other contributions to orbital energy loss and assuming the Newtonian expression for the orbital period suggests that the time to the next close encounter is 50 ms with the B compared to 65 ms for the HB EOS. Binaries with impact parameters in this range may undergo multiple close encounters before merging, with the time between the GW bursts a sensitive function of (in this example) the EOS. For the 2H EOS, the stars have larger radii and graze during the close encounter, merging to a massive star soon after.

5.3.3 Possible post-merger transients

Intermediate impact parameters ($r_p = 7.5$ for the various EOSs and mass ratios, $r_p = 8.75$ HB, and $r_p = 10$ 2H EOS) form HMNSs with non-negligible accretion disks, thought to be necessary for an SGRB progenitor, and unbound material which could potentially power other EM transients (as would presumably a subset of larger impact parameter systems were we to follow them through merger). Figure 5.4 shows

the amount of matter, total and unbound (fluid cells with outward radial velocity and four-velocity time component $u_t < -1$; see also Table 5.1), outside a given radius from the center of mass and the velocity distribution of the unbound matter. The various cases have 0.005–0.07$M_\odot$ unbound material, and roughly 2–3 times more in a disk. As expected, cases with less compact NSs have more unbound material compared to more compact cases. Larger impact parameters (which have more angular momentum) also have comparatively more unbound material with the most occurring in cases where the NSs first come into contact in non-merger close encounters ($r_p = 8.75$ HB and $r_p = 7.5$ and 10 2H). The unequal mass-ratio merger with $q = 0.8$ produces slightly less unbound material than the comparable equal mass merger. In all cases, the ejecta is mildly relativistic with asymptotic velocity that peaks in the range 0.1–0.3c. This ejecta is presumably neutron rich and will convert to heavy elements through the r-process, the heaviest of which will undergo fission, emitting photons [38, 320, 287]. The arguments from [287] estimate the time scale as

$$t_{\rm peak} \approx 0.6 \text{ d} (M_{\rm u}/3 \times 10^{-2} M_\odot)^{1/2} (v/0.2c)^{-1/2}$$

with a luminosity, peaking in the optical/near UV, of

$$L \approx 4 \times 10^{42} \text{ erg s}^{-1} (M_{\rm u}/3 \times 10^{-2} M_\odot)^{1/2} (v/0.2c)^{1/2}$$

normalized here to the approximate values from the $r_p = 8.75$ case. However, recent calculations using more detailed heavy element opacities suggest that the timescale may be up to a week with emission peaking in the IR [321].

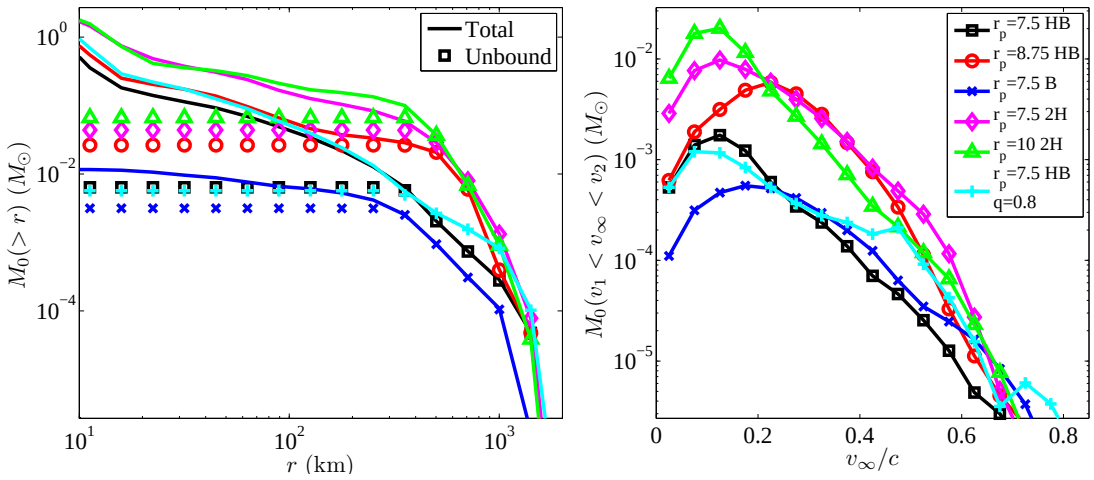

Figure 5.4: **Left**: The total and unbound rest mass outside a given radius from the center of mass for various cases at $t \approx 13$ ms. **Right**: Unbound rest mass with asymptotic velocity grouped in $0.05c$ bins. The legend applies to the left panel as well. By this time, the $r_p = 7.5$, B case has collapsed to a BH, the $r_p = 7.5$, 2H case is an NS below the maximum mass for this EOS, while the rest are HMNSs that will presumably collapse to BHs within 10's of ms to a few seconds.

This ejecta is also expected to collide with the interstellar medium producing radio waves that will peak on timescales of weeks with brightness [39]

$$F(\nu_{\rm obs}) \approx 0.4(E_{\rm kin}/2\times10^{51}\ {\rm erg})(n_0/0.1{\rm cm}^{-3})^{7/8} (v/0.2c)^{11/4}(\nu_{\rm obs}/{\rm GHz})^{-3/4}(d/100{\rm Mpc})^{-2}\ {\rm mJy}$$

where n_0 is the density of the surrounding environment (we use $n_0 \sim 0.1$ cm^{-3} for GC cores; [312]), $\nu_{\rm obs}$ is the observation frequency, d the distance, and we have normalized the kinetic energy and velocity to the $r_p = 8.75$, HB simulation. We assume the same electron distribution power index and energy fraction in relativistic electrons and magnetic fields as in [88].

5.4 Conclusions

We have performed GRHD simulations modeling dynamical capture NS–NS mergers, giving direct estimates of the corresponding GW emission and merger outcome varying impact parameter, EOS, and mass ratio. By measuring pre-merger tidal deformation and post-merger stripped material (bound and ejected), we have also speculated on related EM transients.

Regarding transients that may precede the merger, non-merging close encounters can lead to tidal deformations strong enough to crack the NSs' crust and tap into the $\sim 10^{46}$ erg stored in elastic energy [322], potentially causing flaring activity from milliseconds up to possibly a few seconds before merger. Though a different mechanism and time scales, the signature could be similar to resonance induced cracking for quasi-circular inspirals proposed in [42]. The cracking of the NS crust is one possible explanation for SGRB precursors observed by *Swift* [323].

We find that dynamical capture mergers can result in prompt BH formation or the formation of an HMNS depending on impact parameter and EOS. The HMNSs will be long lived due to their rapid rotation and thermal energy, giving them the potential to seed large magnetic fields and source intense transients during collapse.

In contrast to what was found in general-relativistic studies of quasi-circular NS–NS mergers, we find that dynamical capture mergers can result in massive disks even for equal mass binaries, and can result in up to a few percent of a solar mass in ejecta. This mildly relativistic ejecta can produce potentially observable optical and radio transients. The amount of ejecta found here is similar to the 0.009–0.06 $M_\odot$ found with Newtonian gravity [312], though not for comparable impact parameters ($r_p \leq 5$). However, what is qualitatively consistent with the Newtonian setups is that we observe the largest amounts of unbound material for grazing collisions.

Regarding GW detectability, the high frequency of the merger-ringdown or quasi-periodic signals from the HMNS will be difficult to observe with AdLIGO. Individual

bursts from close encounters would also not be detectable except for very nearby events. For example, an $r_p = 10$, HB EOS merger at $d = 100$ Mpc has sky-averaged SNR for AdLIGO of ≈ 0.9. This implies that if dynamical capture NS–NS mergers constitute a fraction of SGRB progenitors, a further subset of these will not have a detectable GW counterpart. GW signals from larger r_p binaries undergoing numerous close encounters would have larger SNR, and the timing between bursts will be a sensitive function of the orbital energy, containing information about the EOS, for example. We defer a detailed study of GW detectability to Chap. 6.

Chapter 6

Observing gravitational waves from dynamical capture binaries

6.1 Introduction

As recounted in Chap. 4 and Chap. 5, in dense stellar regions, such as galactic nuclei or globular clusters, individual black holes (BHs) or neutrons stars (NSs) can become gravitationally bound as energy is lost to gravitational radiation during a close passage. These dynamically captured pairs may be additional sources for gravitational wave (GW) detectors, as well as sources of electromagnetic (EM) transients such as short gamma-ray bursts (SGRBs). Eccentric pairs will be distinguishable from quasicircular coeval binaries, which are born in a bound system and have had time to circularize before reaching the sensitive bandwidths of ground-based GW observatories such as LIGO [10], VIRGO [11], GEO600 [12], and KAGRA(LCGT) [324].

The primary purpose of this chapter is to study the detectability of sources that retain eccentricity while in the LIGO band (for simplicity, we only employ LIGO sensitivity curves). We focus on mergers with initial periapse $r_p \lesssim 10M$, where M is the total mass, making this study complementary to previous studies [259, 260].

As we show later, in this regime essentially all mergers occur with non-negligible eccentricity ($e \gtrsim 0.2$). This is also the regime where strong-field effects such as black hole spin and zoom-whirl behavior can influence the dynamics. To estimate the fraction of dynamical capture binaries that retain high eccentricity, we can use Newtonian dynamics with quadrupolar energy loss following [257, 325, 303]. First, for a hyperbolic orbit with a small velocity at infinity $v \ll 1$, the relationship between impact parameter b and r_p is $r_p \approx b^2 v^2/2M$. In other words, the cross section $\sigma \propto b^2$ scales *linearly* with r_p. The maximum pericenter passage that leads to a bound system through gravitational radiation loss[1] is $r_{p,m} \approx (31\eta)^{2/7} v^{-4/7} M$, where $\eta = m_1 m_2/M^2 = q/(1+q)^2$ is the symmetric mass ratio, with q the mass ratio. For a galactic nuclear cluster where $v \approx 1000$ km/s, between 20% and 30% of dynamical capture binaries (where the range is from $q = 1$ to $q = 0.1$) will have $r_p/M < 10$; for a globular cluster with $v \approx 10$ km/s, this drops to 1.5%–2.0%.

Although we focus on those with small initial periapse, *all* dynamical capture binaries will have a repeated burst phase [260]. For a large fraction of expected binary masses the repeated bursts will be within the Advanced LIGO band. The burst frequency is $\nu_b \approx r_p^{-1}(r_p/M)^{-1/2}$; the lowest frequency occurs at $r_p = r_{p,m}$, which ranges from $(1-100\text{Hz})/M_{10}$ for $q = 0.1$ encounters in globular clusters to $q = 1$ encounters in nuclear clusters, with $M_{10} = M/10M_\odot$. To estimate the percentage of systems that will end with a low-eccentricity inspiral phase, if the initial periapse is $r_{p,i}$, and we consider the repeated burst phase to end at a periapse of $r_{p,f}$ with eccentricity e_f, from [325] $r_{p,i} \approx 0.57 r_{p,f}(1+e_f)e_f^{-12/19}[1 + O(e_f^2)]$. For example, if a binary with $e_f < 0.1$ by $r_{p,f} = 10M$ can be considered to have a low eccentricity inspiral phase, then this corresponds to all systems with $r_{p,i} > 27M$. For nuclear

[1] As mentioned earlier, for the COs considered here, energy lost to tidal effects is much less than GW emission at these separations, so the latter process determines the cross section. Also, when a bound system is formed, the fraction that has a semimajor axis large enough to have the binary tidally unbound by a subsequent interaction with the surrounding cluster potential is insignificant.

clusters, this is between 20% and 40% for $q = 1 - 0.1$, while the corresponding range for globular clusters is 94% and 96%.

Multimessenger exploration, combining gravitational wave signals with detections of electromagnetic transients, is of course an exciting possibility. Binary NS or BH-NS mergers are thought to be progenitors for SGRBs, and may also source a number of other EM transients [88, 311]. As illustrated in Chap. 4 and Chap. 5, simulations of eccentric BH-NS and NS-NS mergers have shown a rich variation in outcome with impact parameter, with the possibility of large accretion disks as well as ejecta that could undergo the r-process [264, 4, 3, 5, 312]. The time scales between close encounters in eccentric mergers may also explain observed delays between precursors and SGRBs [323]. For example, as noted in Chap. 5 NS crust cracking on a non-merging close encounter could potentially cause flares that precede the merger by an interval ranging from milliseconds to possibly a few seconds. Even a null GW detection provides astronomical information as it rules out compact object mergers as the source of an observed GRB, but only if the detectability of these types of signals is understood. Given the disparate nature of the waves from dynamical capture vs coeval mergers, data analysis methods designed specifically for each are required for this kind of astronomy. Methods to search for quasicircular inspiral (of relevance to the majority of coeval binaries, and a subset of dynamical capture binaries that form with a sufficiently large periapse to circularize before merger) have been the predominant focus of the GW community over the past decades [326]. Comparatively, there is a dearth of studies on the detectability of highly eccentric mergers [2]. In [328] the single burst from a parabolic close encounter was studied, while [259] included the additional signal provided by subsequent bursts. This repeated burst phase was studied in [260] using 2.5 and 3.5 order post-Newtonian (PN) equations of motion. It was found that GWs from this phase may be detectable by Advanced

[2]Though see [327] for a recent study of the efficacy of quasicircular templates to detect lower eccentricity NS binaries.

LIGO out to 200–300 Mpc for BH-NS binaries and 300–600 Mpc for BH-BH binaries. Since the PN approximations begin to break down close to merger, the evolution was only followed to $r_p = 10M$. To model the last stages of merger requires numerical relativity (NR), and there have been a number of numerical studies of eccentric mergers [167, 164, 165, 329, 153, 4, 3, 5, 170]. However, because of the computational expense of these simulations, it is not possible with current computer resources to follow high-eccentricity binaries through multiple close encounters. The challenge is compounded by a large parameter space, including the impact parameter, mass ratio, BH spin, and NS equation of state. It is thus not reasonable to expect that brute-force numerical simulations will be able to provide templates before the Advanced LIGO era, even accounting for expected increases in computer power.

To begin to bridge the gap between large periapse PN solutions and late-time numerical solutions, we introduce a model for the inspiral, merger, and ringdown of dynamical capture compact binaries. This model is based on geodesic equations of motion in an effective Kerr spacetime, combined with quadrupole radiation (Sec. 6.2.1) and a version of the Implicit Rotating Source (IRS) model [330, 331] for the merger and ringdown parts of the GW signal (Sec. 6.2.3). (Except for the IRS extension, and the comparable masses, our hybrid is reminiscent of the "kludge" introduced to study extreme mass ratio inspirals [332, 333, 334, 335], based in part on the "semirelativistic" approach of [336].) We validate this model through a comparison to full numerical simulations in the strong-field regime (Sec. 6.2.2) and to the PN approximation for $r_{\rm p} > 10\,M$ (Sec. 6.2.4).

The waveforms we produce here are likely not accurate enough for optimal template-based detection of multiple-burst events. Indeed, creating improved accuracy waveforms will probably require a different approach, for example, using the effective one body (EOB) formalism which has recently been extended to generic orbits [337] and calibrating it using full numerical simulations. However, our waveforms

capture the relevant features with sufficient faithfulness that we can use them to assess the efficacy of existing LIGO search strategies. We can also use our waveforms to investigate new search strategies that may be better suited to highly eccentric mergers. In Sec. 6.3 we use this model to evaluate how well these GW signals could be seen with each generation of the LIGO detectors, varying impact parameter (equivalently r_p), total mass, and mass ratio. We use various analysis methods: matched filtering with the model templates, filtering with ringdown templates, and a burst search with sine-Gaussian templates. We also estimate how well a hypothetical search using incoherent stacking of bursts following [338] would perform. Though not as optimal as matched filtering, stacking is likely more robust to timing uncertainties in the burst sequence. We find that if capture binaries do exist, in many cases their GW signals will be missed by single-burst or ringdown searches (and, as we argue, quasicircular templates), whereas these sources would be detectable with a full template or a stacked burst search. In particular, GRB051103 [339] had a measured distance of 3.6 Mpc, and no coincident GW signal was found using traditional searches [340, 341]. However, there is a sizable region of the parameter space of dynamical capture binaries that existing searches would have missed. The possibility that the GRB was preceded by an eccentric merger remains a viable possibility.

In Sec. 6.4 we make concluding remarks and comment on the direction of future work.

6.2 Waveform Model

In this section we describe our model for high-eccentricity merger waveforms. We first look at the inspiral phase in Sec. 6.2.1, which can be considered a sequence of GW bursts, each generated at a periapse passage. In Sec. 6.2.2 we compare the model expressions we use for the bursts to full numerical simulations. In Sec. 6.2.3

we discuss the IRS model for the merger and ringdown phase, and in Sec. 6.2.4 we present examples of the full signal, and make further comparisons to PN results for the inspiral phase.

6.2.1 Repeated burst phase

Our objective here is to model the GW signal from an eccentric binary that passes through a series of close encounters prior to merger. To this end, we use a prescription based on the equations of motion of a geodesic in a Kerr spacetime, coupled with the quadrupole formula for gravitational radiation. We identify the mass and total angular momentum of the binary with the mass and spin parameters of the effective Kerr spacetime and the orbital angular momentum and energy with that of the geodesics. This approach has the advantage of reproducing the correct orbital dynamics in the Newtonian limit and general-relativistic test particle limit, while still incorporating strong-field phenomena such as pericenter precession, frame dragging, and the existence of unstable orbits and related zoom-whirl dynamics. For simplicity, in this first study we restrict our attention to equatorial orbits and, for the most part, nonspinning BHs (we compare the IRS model to a merger involving a spinning BH in Sec. 6.2.3).

The equations for an equatorial geodesic in a Kerr spacetime with mass M and dimensionless spin a can be written in first order form using Boyer-Lindquist coordinates as

$$\begin{aligned}
\dot{\tau} &= \frac{\Delta}{\tilde{E}R_0^2 - 2M^2a\tilde{L}/r} := Q, \\
\dot{\phi} &= \frac{1}{R_0^2}\left[\tilde{L}Q + 2M^2a/r\right] := \Omega, \\
\dot{r} &= \Delta Q P_r/r^2, \\
\dot{P}_r &= \frac{1}{r^2Q}\left[\Omega^2(r^3 - M^3a^2) + M(2Ma\Omega - 1)\right] + \frac{P_r^2Q}{r^3}\left[M^2a^2 - Mr\right] \qquad (6.1)
\end{aligned}$$

where $R_0 = r^2 + 2M^3a^2/r + M^2a^2$, $\Delta = r^2 - 2Mr + M^2a^2$, $P_r = r^2\dot{r}/(\Delta Q)$, τ is proper time, and the overdot indicates a derivative with respect to the coordinate time. Here $\tilde{E}$ and $\tilde{L}$ are the energy and angular momentum of the geodesic.

In order to apply these equations to a binary system we go to the center-of-mass frame and let $\mathbf{r}$ be the separation between the objects. Then we identify the geodesic parameters $\tilde{E}$ and $\tilde{L}$ with the reduced energy and angular momentum of the system and promote these quantities to time-dependent variables. To determine the amount of energy and angular momentum radiated away to gravitational waves, we use the quadrupole formula

$$\begin{aligned} \dot{\tilde{E}} &= -\frac{\mu}{5}\dddot{\mathcal{I}}_{ij}\dddot{\mathcal{I}}_{ij} \\ \dot{\tilde{L}} &= -\frac{2\mu}{5}\epsilon^{zij}\ddot{\mathcal{I}}_{ik}\dddot{\mathcal{I}}_{jk} \end{aligned} \tag{6.2}$$

where μ is the reduced mass, $\mathcal{I}_{ij}$ is the reduced quadrupole moment, and $\ddot{\mathcal{I}}_{ij}$ and $\dddot{\mathcal{I}}_{ij}$ are written in terms of the variables $\{r, \phi, P_r, \tilde{E}, \tilde{L}\}$ using (6.1). We set M in (6.1) to the total mass (neglecting orbital energy contributions), and we set $a = \mu\tilde{L}/M^2 + a_{BH}$, where a_{BH} is the net spin of any BHs (though again for this study we focus on non-spinning BHs, where $a_{BH} = 0$). The use of an effective spinning BH spacetime based on total angular momentum is motivated by [167], where it was found that the properties of zoom-whirl-like dynamics exhibited in equal mass mergers in full numerical relativity are better approximated by geodesics on the effective Kerr spacetime than Schwarzschild spacetime, and it differs from the EOB approach which uses deformations of the Schwarzschild metric for the merger of nonspinning objects [342]. We note that when the orbital angular momentum is large we will have $a > 1$. However, this will occur only when the separation r is also large, so general-relativistic effects are small, and no unusual behavior arises from exceeding the Kerr limit. We numerically integrate the coupled set of equations (6.1) and (6.2).

The remaining element is to calculate the observed gravitational radiation, which will depend on the intrinsic source parameters (i.e. the mass, mass ratio, eccentricity, and initial periapse distance), and will also vary with sky location and relative orientation of the source to the detector. At linear order and in the transverse traceless gauge, the complex gravitational wave strain $h_{\rm opt}$ a distance d from an optimally oriented source is simply related to changes in the quadrupole moment through

$$h^{\rm opt} := h_+^{\rm opt} + i h_\times^{\rm opt} := \frac{2}{d}\left(\ddot{\mathcal{I}}_{x\,x} + i\ddot{\mathcal{I}}_{y\,x}\right) . \tag{6.3}$$

For general orientations, the emitted strain can be represented through a mode decomposition as

$$\bar{h} := h_+ + i h_\times = \sum_{\ell=2}^{\infty}\sum_{m=-\ell}^{\ell} h_{\ell m}(t,d)\,{}_{-2}Y_{\ell m}(\theta,\phi)\,, \tag{6.4}$$

where ${}_{-2}Y_{\ell m}$ are the spherical harmonics of spin weight -2 [343], and θ and ϕ are the polar and azimuthal angles of orientation, respectively. For the comparable mass, nonspinning systems that we are primarily interested in, the quadrupole (i.e., $\ell = 2$, $m = \pm 2$) component dominates the strain, so that

$$\bar{h} \approx h_{22}(t,d)\,{}_{-2}Y_{22}(\theta,\phi) + h_{2-2}(t,d)\,{}_{-2}Y_{2-2}(\theta,\phi). \tag{6.5}$$

This completes the approach for calculating the source waveform that reaches a detector. In a later section we will include the sensitivity of the detector in the analysis.

6.2.2 Comparison to fully general-relativistic numerical simulations

To provide some validation for this model we compare several waveforms of single high-eccentricity fly-by encounters from full general-relativistic numerical simulations

to those obtained from the geodesic equation with the quadrupole formula. The simulations include a 4:1 mass ratio BH-NS system (see Chap. 4), an equal mass NS-NS system (see Chap. 5), and an equal mass BH-BH system. The NR simulations were all performed using the code described in Chap. 2.

In Fig. 6.1 we show several such examples from NR simulations of the 4:1 BH-NS system alongside corresponding waveforms from our model with best-fit parameters. The peak amplitude of the geodesic is scaled to be the same as in the simulations. The fit is performed by finding the initial orbital parameters that maximize the phase overlap between the waveforms (see e.g. [344]). In this regime the match between the waveforms is most sensitive to r_p as opposed to e. As can be seen, the fly-by waveforms from our model provide a good match to those from simulations. Even close to the effective innermost stable orbit (ISO) for the BH-NS system (the bottom panels of Fig. 6.1), where the system begins to show evidence of whirling behavior, our model is able to approximately capture the shape of the waveform.

In Table 6.1 we give the fit parameters, amplitude enhancement, and overlap. We also show the approximate initial orbital parameters (r_p and e) of the simulation obtained by equating a Newtonian estimate of the reduced orbital energy and angular momentum at the beginning of the simulation with the $\tilde{E}$ and $\tilde{L}$ parameters of the geodesic model described above. (Note, this is different from the *Newtonian* values for r_p and e used in [3, 5].) For most of the BH-NS systems in Table 6.1 we can see that the enhancement required to match the amplitude of our model to the simulation results is $\sim 4\%$–11%. This is presumably due to aspects not captured by this simple model, such as finite-size effects, as well as truncation error from the simulations. The one case where the amplitude of the simulation waveform was below the model result was a simulation with strong whirling behavior (bottom-right panel of Fig. 6.1) where the NS had large f-mode oscillations excited as described in [3].

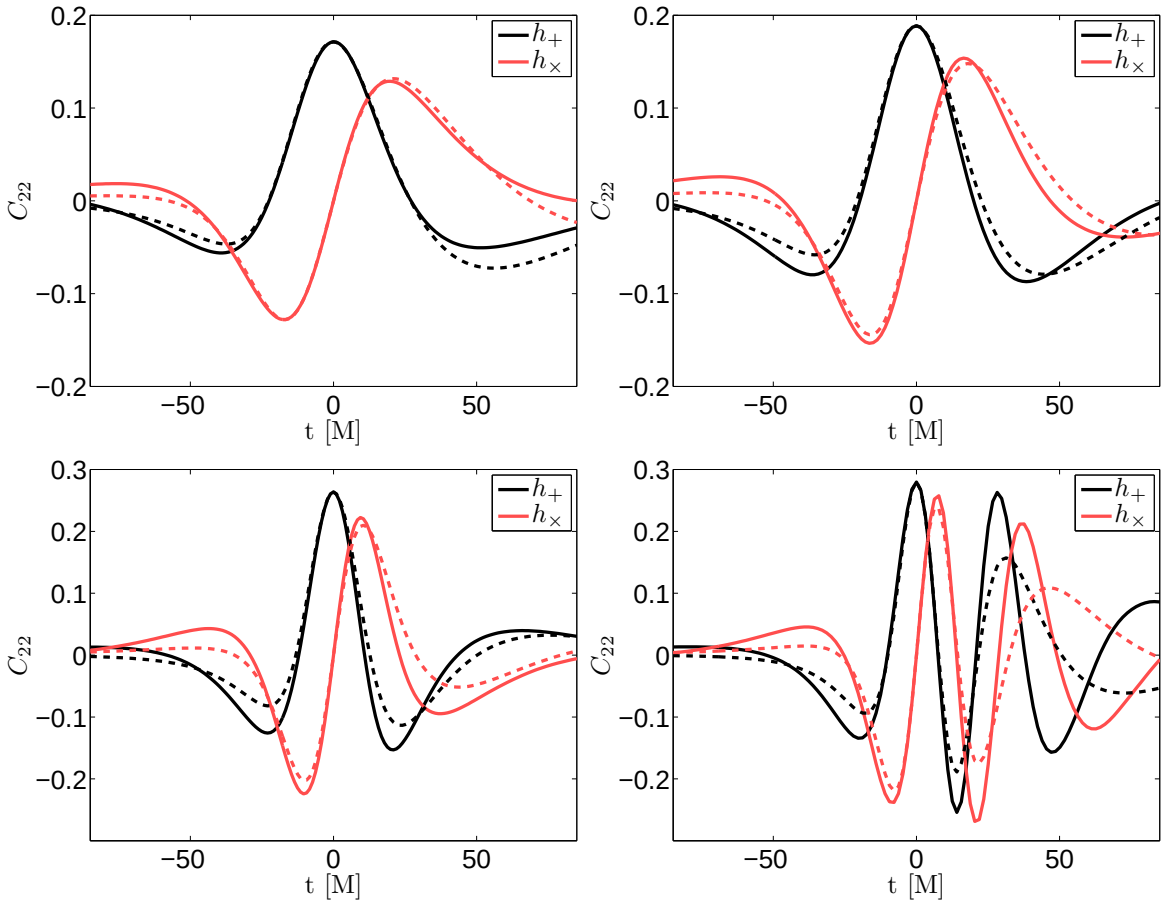

Figure 6.1: Comparison of the $\ell = 2$, $m = 2$ component of $\bar{h}$ for fly-by waveforms from 4:1 BH-NS simulations (solid line) and our model with best-fit periapse distance (dashed line). The approximate effective geodesic orbital parameters of the simulated system (left to right, top to bottom) are $(r_p, e) = (8.3, 1.0)$, $(8.0, 0.8)$, $(5.6, 1.0)$, and $(5.0, 1.0)$. The fit parameters are given in Table 6.1.

We also compare the geodesic model with an equal mass BH-BH and an equal mass NS-NS system as shown in Fig. 6.2. Although one would expect a geodesic approximation to be most accurate in the limit that one mass is much larger than the other, it still provides good fits for equal masses. This model, however, does not attempt to include finite-size effects (such as the f-mode excitation visible in the later part of the bottom of Fig. 6.2), which would be required to address questions related to measuring the NS equation of state from such GW signals.

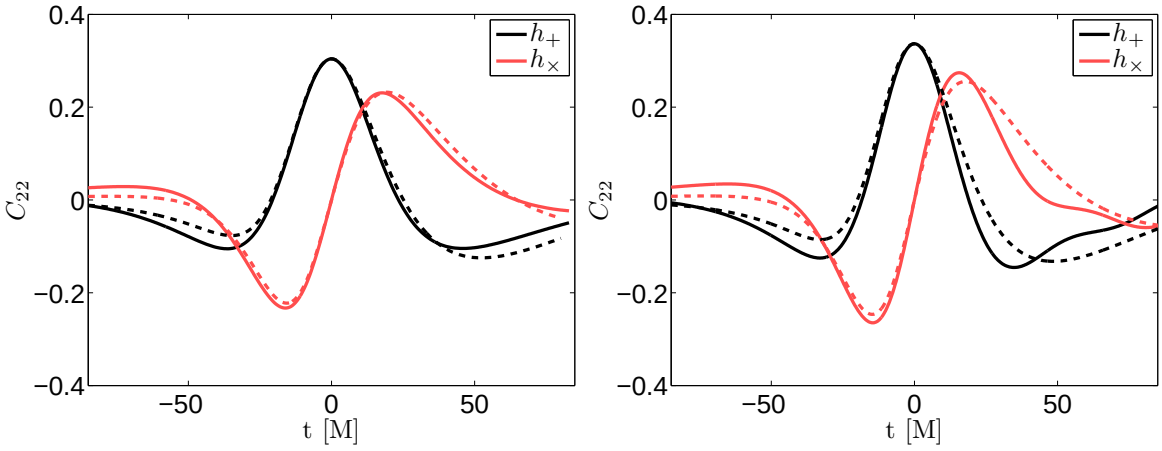

Figure 6.2: Comparison of the $\ell = 2, m = 2$ component of $\bar{h}$ for fly-by waveforms from equal mass BH-BH (left panel) and NS-NS (right pannel) simulations (solid lines) and our model (dotted lines) with best-fit parameters. The approximate effective geodesic orbital parameters of the simulated systems are $(r_p, e) = (8.7, 1.0)$ for both cases. The fit parameters are given in Table 6.1. The feature in the waveform after the peak in the NS-NS simulation is from f-mode excitation that occurs during the close encounter.

	Simulation[a]		Fit[b]			
Binary	r_p	e	r_p	e	A^c	Overlap[d]
NS-BH	8.30	1.00	8.77	1.00	1.04	0.99
NS-BH	8.00	0.80	7.97	0.81	1.11	0.98
NS-BH	5.62	1.00	5.61	1.00	1.11	0.97
NS-BH	5.04	1.00	4.26	1.00	0.61	0.74
BH-BH	8.71	1.00	8.23	1.00	1.16	0.99
NS-NS	8.71	1.00	7.82	1.00	1.28	0.96

Table 6.1: Fit parameters for close-encounter GWs.
[a] Approximate initial parameters of the geodesic model based on the initial orbital energy and angular momentum of the simulation.
[b] Initial parameters of the geodesic model that best fit the simulation data.
[c] Amplitude enhancement applied to the waveform from the best-fit geodesic model.
[d] Overlap between simulation and the best-fit geodesic model.

6.2.3 Merger model

After a binary has evolved through some number of close encounters, it will merge. In order to include the waveforms resulting from merger, we supplement the model outlined in Sec. 6.2.1 with a version of the IRS model [330, 331] for the merger and ringdown part of the GW signal. Note that the IRS assumes the waveform is circularly polarized. This is not strictly valid for the complete merger-ringdown phase of eccentric binaries, though as we show below, it does provide a reasonably good approximation to results from numerical simulations. As with other aspects of our waveform model, this assumption could be refined in the future, but it is adequate for the purpose of testing the efficacy of existing search strategies for detecting eccentric binaries.

In particular, we model the phase evolution to asymptotically approach the least damped quasinormal mode frequency of the final BH, $\omega_{\rm QNM}$, via

$$\omega(t) = \omega_{\rm QNM}(1 - \hat{f}) \tag{6.6}$$

where

$$\hat{f} = \frac{c}{2}(1 + \frac{1}{\kappa})^{1+\kappa}\left(1 - (1 + \frac{1}{\kappa}e^{-2t/b})^{-\kappa}\right). \tag{6.7}$$

Here $b = 2Q/\omega_{\rm QNM}$ is determined by the quality factor and frequency of the final BH, and κ and c are free parameters of the model. The amplitude is given, up to an overall factor A_0, by

$$A = \frac{A_0}{\omega(t)}\left(\frac{|\dot{\hat{f}}|}{1 + \alpha(\hat{f}^2 - \hat{f}^4)}\right)^{1/2} \tag{6.8}$$

where $\dot{\hat{f}} = d\hat{f}/dt$, and α is a free parameter. We find that $\alpha = 72.3/Q^2$ provides a reasonably good fit to our numerical simulations.

In Fig. 6.3 we show a comparison between simulation results of BH-NS mergers and the best-match IRS model waveforms, where we let κ and c be fitting parameters.

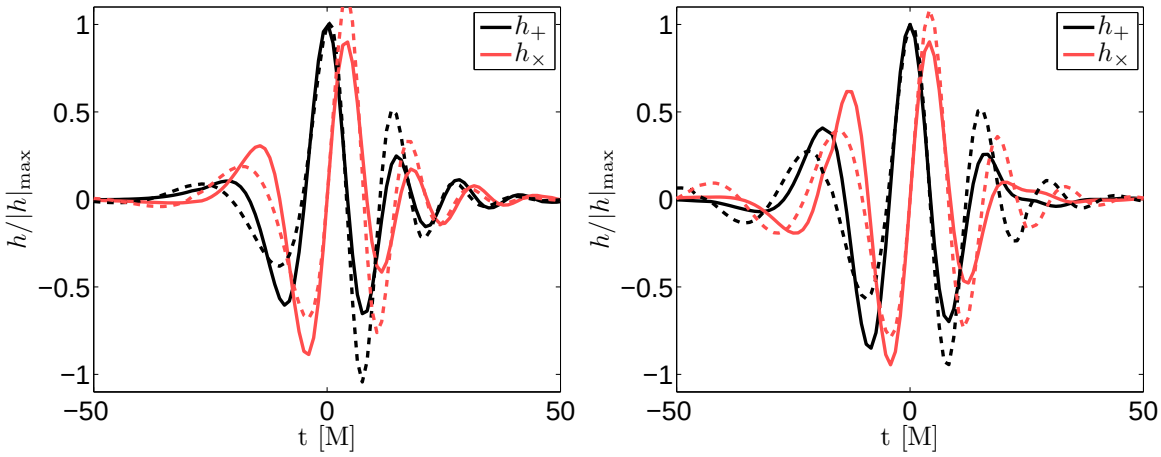

Figure 6.3: Comparison of the merger GW strain from a 4:1 BH-NS simulation (solid lines) and the IRS model (dotted lines) with best-fit parameters. The left panel shows a case where the initial BH was nonspinning. The right panel shows a case with $a_{\rm BH} = 0.5$, which results in more whirling behavior and tidal disruption of the NS. The best-fit parameters in (6.7) are $(\kappa, c) = (0.66, 0.28)$ (left) and $(0.46, 0.18)$ (right), and the matches are 0.98 and 0.96, respectively. The match is weighted based on the "whitened" waveforms as described in Sec. 6.3 assuming a total mass of 10 $M_\odot$.

In Fig. 6.4 we show the same thing for equal mass NS-NS and BH-BH mergers. This simple model will not capture disruption or other matter effects, and best-fit values for κ and c will have some dependence on the parameters of the binary, such as the impact parameter preceding merger. However, when studying signal detectability we fix $\kappa = 0.64$ and $c = 0.26$, which empirically provides reasonably good fits to a large number of simulated waveforms, and therefore provides an adequate representation of a generic eccentric merger. We attach the IRS part of the waveform to the model from Sec. 6.2.1 when the separation reaches the light ring of the effective Kerr spacetime.

6.2.4 Model properties and comparison to post-Newtonian

Combining the inspiral and merger models allows us to generate complete waveforms for dynamical capture binaries. In Fig. 6.5 we show one such example for a 4:1 mass ratio system with initial orbital parameters corresponding to $r_{\rm p} = 8\,M$ and $e = 1$. The

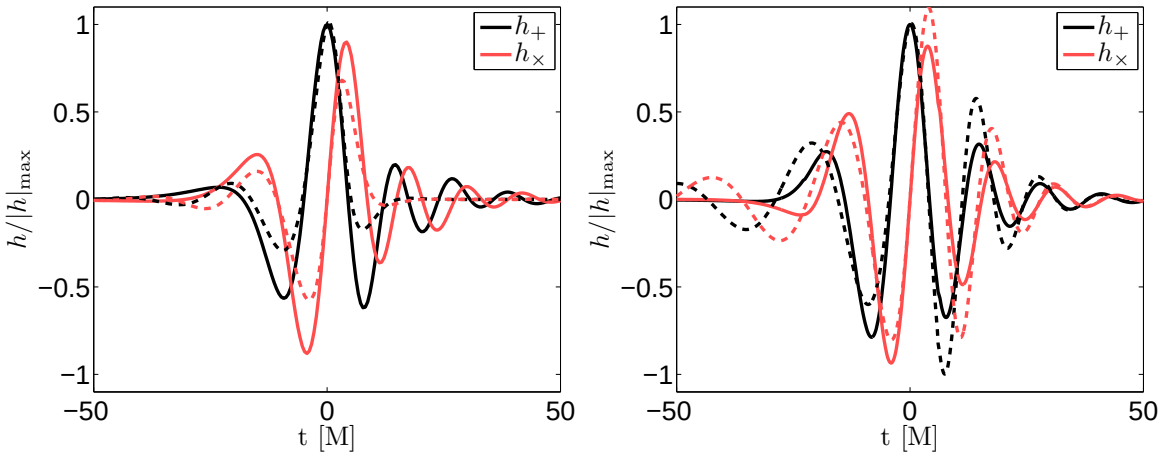

Figure 6.4: Comparison of merger waveforms from an equal mass BH-BH simulation (left panel) and NS-NS simulation that forms a BH (right panel) with the IRS model (dotted lines) with best-fit parameters. The best-fit parameters in (6.7) are $(\kappa, c) = (0.31, 0.03)$ (left) and $(0.36, 0.19)$ (right), and the matches are 0.98 and 0.97, respectively. The match is weighted based on the "whitened" waveforms as described in Sec. 6.3 assuming a total mass of 20 $M_\odot$ and 2.8 $M_\odot$ for the BH-BH and NS-NS binaries, respectively.

waveform shows the decreasing time interval between bursts from close encounters as $r_{\rm p}$ and e decrease due to gravitational radiation. The number and timing of the bursts is a sensitive function of the amount of energy and angular momentum radiated in each close encounter. In Fig. 6.6 we show how $r_{\rm p}$ and e evolve according to this model for some example binaries. It can be seen that the binaries considered here, which begin on parabolic orbits with $r_p \leq 10\,M$, still have non-negligible eccentricity all the way to merger.

We can also compare this model to that given by the 2.5 and 3.5 order PN approximation as used in [260]. In Fig. 6.7 we show how the difference in the energy and angular momentum radiated away in a close encounter for 2.5 or 3.5 PN relative to our model changes with the initial impact parameter. The geodesic model predicts less energy and momentum loss than 2.5 PN but more than the 3.5 PN. At large impact parameters the three different models converge. At smaller impact parameters the 2.5 and 3.5 PN approximations begin to diverge. As shown in [345], the PN

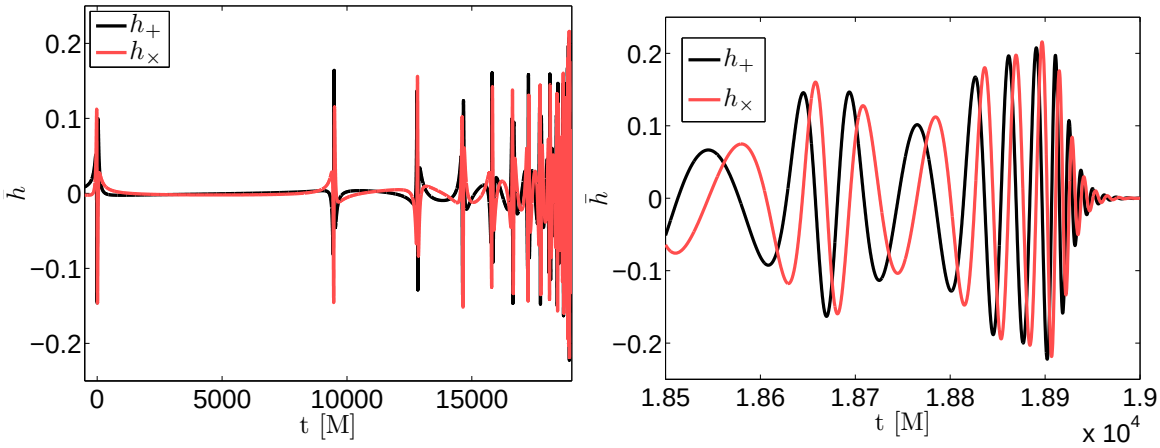

Figure 6.5: GW strain generated with our model and initial conditions $r_{\rm p} = 8\,M$ and $e = 1$. The left panel shows the entire waveform, while the right panel shows a zoomed-in view of the end of the waveform.

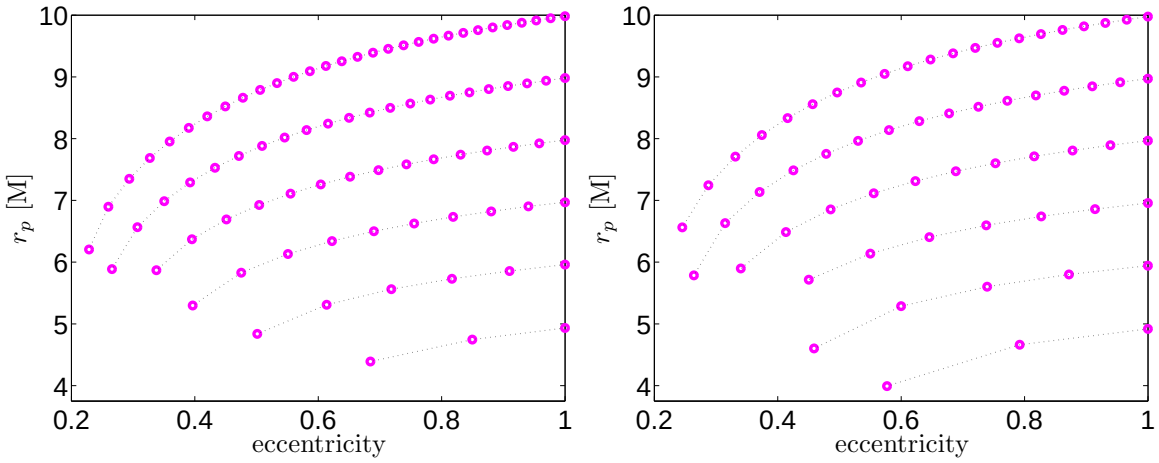

Figure 6.6: Evolution of orbital parameters for a 4:1 (left panel) and an equal mass ratio (right panel) binary. The effective eccentricity is calculated from successive apoapse and periapse distances as $e = (r_a - r_p)/(r_a + r_p)$.

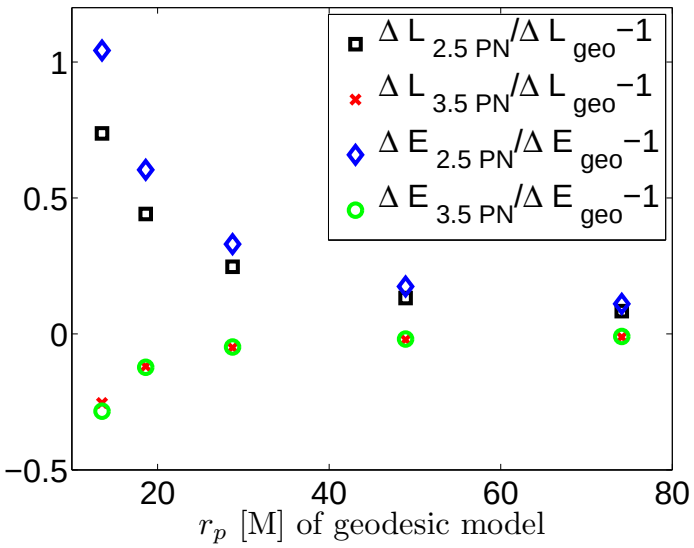

Figure 6.7: Relative difference in energy and angular momentum lost in a close encounter for the 2.5 and 3.5 PN approximations versus our model. For this comparison the orbits are chosen to initially have zero energy and the same value of angular momentum which, for a geodesic with the same initial conditions, corresponds to the value of r_p indicated on the x axis.

approximation fails to converge (or even to provide physically sensible results in the case of 3.5 PN) for $r_p \lesssim 10\,M$.

The gravitational wave model we have outlined in this section is relatively simple and could be improved upon by, for example, adding more sophisticated conservative dynamics, including finite-size effects for NSs, as well as going beyond the quadrupole approximation in determining gravitational radiation. However, given the decent match between this model and the full numerical simulations, as well as its consistency with the PN approximation as described above, it can be used to investigate issues of detectability, as we do in the next section.

6.3 Detectability

6.3.1 Detector modeling

Having developed a model for the gravitational waveforms emitted by high-eccentricity binaries, we can now assess the detectability of these signals for different source parameters and detectors. The measured strain h is given by

$$h = \Re\left[F\bar{h}\right] = F_+ h_+ + F_\times h_\times \,, \tag{6.9}$$

where $F := F_+ - iF_\times$ is the sky-dependent detector response. The signal-to-noise ratio (SNR) ρ using a perfectly matched filter is given by

$$\rho^2 = \langle h|h\rangle, \tag{6.10}$$

where $\langle\cdot|\cdot\rangle$ denotes a noise-weighted inner product given by

$$\langle h_1|h_2\rangle := 2\int_0^\infty df\, \frac{\tilde{h}_1^*\tilde{h}_2 + \tilde{h}_1\tilde{h}_2^*}{S_n}\,, \tag{6.11}$$

where $S_n(f)$ is the power spectral density of the detector noise, and $\tilde{h}$ denotes the Fourier transform of the original h time series. Because we limit our model to the quadrupole component of the signal, and we focus on detectors (like LIGO) for which the gravitational wavelength is much longer than the detector's armlength, we can trivially relate the SNR of an optimally oriented and located source to the SNR of an orientation- and sky-location-averaged source. For such detectors, the response function to the two waveform polarizations, F_+ and $F_\times$, is simply the root-mean-squared (rms) average over the sky location and polarization angles, $\sqrt{\langle F_{+,\times}^2\rangle} = \sqrt{1/5}$ [346]. Likewise, the rms average over source orientations is $\sqrt{\langle {}_{-2}Y_{2,\pm 2}\rangle} = \sqrt{1/5}$, so that $\sqrt{\langle\rho^2\rangle} = \rho_{\rm opt}/5$. We can further define the characteristic strain $h_{\rm c}$ for both the signal

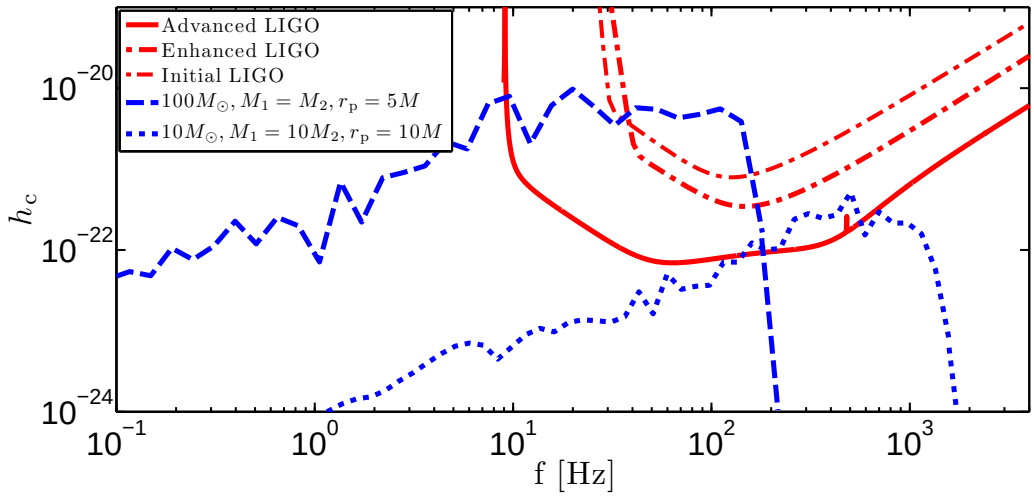

Figure 6.8: The characteristic strain h_c is shown for the initial (thin dash-dotted line), Enhanced (dash-dotted line), and Advanced LIGO (solid line) detectors, as well as for two example signals at $D_L = 1$ Gpc. The first signal corresponds to an orientation-averaged source with $M = 100$ $M_\odot$, $q = 1$, and $r_p = 5M$ (dashed line), and the second signal is from a source with $M = 10$ $M_\odot$, $q = 0.1$, and $r_p = 10M$ (dotted line). Both signal spectra are smoothed to diminish fluctuations and make the trend more clear. The system with $q = 0.1$ has little contribution from the merger, so the repeated burst phase dominates the spectra, with $h_c \propto f$, whereas the $q = 1$ system signal comes largely from the merger, where $h_c \approx$ constant over a small band of frequencies.

and detector noise. Given Eq. (6.11) and the typical practice of plotting sensitivity curves logarithmically, it is useful to define $h_c := \sqrt{\langle {}_{-2}Y_{2,\pm 2}\rangle} f\tilde{h}_{\rm opt}$ for signals and $h_c := \sqrt{fS_n/\langle F^2\rangle}$ for detector noise, so that both signal and noise are characterized as a dimensionless strain, and the ratio of signal-h_c to noise-h_c is the square root of the integrand for ρ^2 when integrated over logarithmic frequency intervals df/f. We show this characterization of signal and noise in Fig. 6.8.

For assessing the relative contribution of different waveform segments to the SNR, it is often convenient to work in the time domain by constructing "whitened" waveforms [347], which weight the amplitude of the waveform as a function of frequency

to account for the presence of noise in the detector,

$$h' = \int_{-\infty}^{+\infty} df \, \frac{\tilde{h}}{\sqrt{S_n}} \, e^{-i2\pi ft}. \tag{6.12}$$

With these whitened vectors, the noise-weighted inner product (6.11) can be reexpressed in the time domain:

$$\langle h_1 | h_2 \rangle := \int_{-\infty}^{\infty} dt \, h_1'^{*}(t) \, h_2'(t). \tag{6.13}$$

Figure 6.9 shows portions of the whitened waveform for two example cases with the same mass ratio and initial r_p and e, but different masses. The upper panel shows the burst with the largest SNR contribution for a source with total mass $M = 10$ $\mathrm{M}_\odot$, while the lower panel shows the loudest burst for $M = 100$ $\mathrm{M}_\odot$. The different masses change the frequency of the signal, so different bursts are emphasized by the detector sensitivity; in particular, for larger masses the final burst and merger are emphasized. We also show best fits for two types of templates that are described below.

6.3.2 Templates and detection strategies

While quasicircular sources are searched for using matched filtering, eccentric systems are far more susceptible to modeling errors in the relative timing and phase of signal bursts, which is why we focus our attention on alternative approaches to detection. For example, a small modeling error in the energy lost during a particular periapse passage δE will induce a timing error in the arrival time of the subsequent burst δT given by $\delta T \propto \delta E (1-e)^{-5/2}$. Therefore, dynamical capture binaries are far more challenging to model with sufficient accuracy to apply matched filtering due to their large eccentricities.

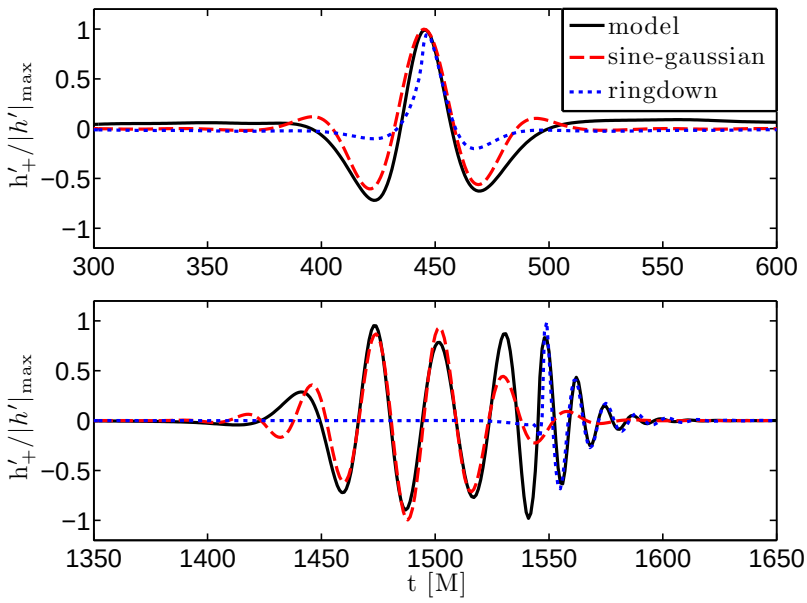

Figure 6.9: Whitened waveforms for a 10 $M_\odot$ (top panel) and a 100 $M_\odot$ (bottom panel) binary with initial $e = 1$ and $r_p = 5M$, along with the (whitened) best–fit template among sine-Gaussian and ringdown templates.

We assess detection prospects of GWs from capture binaries for two currently used templates, sine-Gaussian (SG) and ringdown (RD) templates, as well as an idealization of a third strategy based on combining an excess power search with stacking. The SG and RD both take the form

$$\bar{h} = A \exp\left[-\left(\frac{t - t_o}{\tau}\right)^{\gamma} + i\omega(t - t_o) - i\phi_o \right], \tag{6.14}$$

where $\gamma = 1$ and $t \geq t_o$ for the RD templates, and $\gamma = 2$ with $-\infty < t < \infty$ for the SG templates. Here A is the overall amplitude, t_o and ϕ_o are the time and phase of the template's amplitude peak, τ sets the e-folding of the amplitude, and ω is the constant frequency.

In addition to assessing the performance of two burst templates, we calculate a rough approximation of the potential performance for an excess power search that accumulates power from the entire signal [338], which we will call a power-stacking

search. Here, the data would be transformed to a time-frequency (TF) tiling using a basis suitable for capturing individual bursts within a tile, and then power from different tiles corresponding to bursts, as informed by our model, would be combined. Whereas in most existing TF searches an individual element must have enough power to exceed some threshold, with that threshold being large enough to avoid many false alarms, the approach we describe does not require that the signal be detectable in any single TF element. In the case of a monochromatic signal, the SNR from optimal filtering will accumulate with the number of cycles N as $\sqrt{N}$, while the excess power in stacking TF elements (constructed using any basis) overlapping the given frequency will accumulate as $N^{1/4}$. The signals from high-eccentricity binaries are not monochromatic, but given the typically large number of bursts occurring in band, and the relative flatness of both the source spectrum and the detector sensitivity across its most sensitive band, we expect the aforementioned scalings to hold approximately for realistic signals.

This search would be very similar to the stacked search proposed for combining potential GW counterparts to observed electromagnetic signals from soft gamma repeaters [338]. There, TF elements were aligned in time based on the observed bursts, and they demonstrated the $N^{1/4}$ SNR scaling when adding power for identical injected signals. Since we do not have a separate observational trigger, our proposed search would sum power along elements overlapping bursts as indicated by our waveform model. We leave it to future work to fully investigate this, though here we assume we can achieve the $N^{1/4}$ SNR scaling, and thus can estimate the performance of a power-stacking search by noting that optimal filtering should outperform power stacking by $N^{1/4}$. Hence, we can approximate the effective excess power SNR as $\rho_{\mathrm{EP}} \approx N^{-1/4}\rho$. This simple estimate will constitute our third search technique in our subsequent analysis.

We do not employ quasicircular (QC) templates, although they have thus far been the only tool employed to search for long-lived signals. QC templates will generically fail to match the performance of any of the above methods for the repeated burst phase of eccentric sources for the following reasons. First, during the long intervals between eccentric bursts a QC template will still be integrating power from the data, which is predominantly noise. Specifically, the ratio of the characteristic time scale of an eccentric burst to the period between bursts is roughly

$$\frac{\tau_{\rm GW}}{T} \approx (1-e)^{3/2}\,. \tag{6.15}$$

In other words, there will be $\sim (1-e)^{-3/2}$ additional cycles between bursts in a QC signal with the same periapse. Moreover, even if the QC template is phase aligned to a particular burst, since the time between bursts is much larger than the GW period, the rest of the template will effectively have random phase alignment with other bursts in the sequence and, on average, no additional SNR will be acquired. To summarize, typically the best-matched QC template will only integrate signal about the loudest burst, but even so, the performance will not be as good as a single-burst search due to the larger integrated noise accumulated over the period of the QC template (expect for the higher mass systems where only the final merger/ringdown signal is in band).

6.3.3 Results

We calculate two useful quantities related to the SNR: the detectability horizon and the detection probability. Since $h \propto D_L^{-1}$, where D_L is the luminosity distance, we can use (6.10) to calculate the distance (which we call the detection horizon) at which a sky- and orientation-averaged source could be observed with a SNR of 8 using optimal filtering. The detection probability for a given strategy is simply the ratio of

the volume in which the strategy could detect a source with some SNR to the volume in which the source could be seen with the same SNR using optimal filtering. In the remainder of this section, we will calculate these quantities for various cases of interest. We consider the following configurations:

- three detector sensitivities, corresponding to initial, Enhanced, and Advanced LIGO;
- three detection strategies, including SGs, RDs, and power stacking, and how they compare to optimal filtering;
- three intrinsic system parameters:
  - total system mass M, ranging from 1 $M_\odot$–2000 $M_\odot$;
  - mass ratio q of the binary components, ranging from 0.01–1;
  - initial r_p, ranging from $5M$–$10M$ (with initial $e = 1$; we exclude $r_p < 5M$ simply because in most cases it is a direct collision qualitatively similar to $r_p = 5$, and see [260] for a study of $r_p > 10M$).

In Fig. 6.10, we show contours of constant horizon distance as a function of q and r_p for initial LIGO, assuming optimal filtering, SG templates, and power stacking. Two contours of note, at 0.77 and 3.6 Mpc, correspond to the distances of GRB070201 [348] and GRB051103 [339], respectively. These were two nearby gamma-ray bursts observed by Swift during the S5 initial LIGO run, while two interferometers were actively collecting data at or near initial LIGO's design sensitivity. However, no signal was found in the LIGO data using the methods applied (specifically, various burst and quasicircular inspiral templates) for these GRBs, nor for any of the 137 GRBs (35 with measured redshifts) that occurred while initial LIGO was taking science data during its S5 run at or near design sensitivity [340, 341]. Thus in Fig. 6.10 we restrict the mass ratio to the range 0.1–1, with one of the masses fixed at 1.35 $M_\odot$,

to focus on systems including a neutron star that are expected to generate GRBs. In the case of a dynamical capture binary source at 0.77 Mpc, the signal is sufficiently loud that even suboptimal searches like SG templates would detect them. However, for a source at 3.6 Mpc, whereas an optimal filter would have detected a signal from a large region of the parameter space, including all cases with $q < 0.5$ or $r_p > 7.5\,M$, and power stacking would recover signals with $q < 0.4$, SG templates are far less effective, and would only recover a small sliver of parameter space with $q < 0.2$. This suggests the possibility that the searches applied to the LIGO data would not have found the gravitational wave counterpart to GRB051103 if it was in the form of a dynamical capture binary. Furthermore, across the full parameter space explored, the difference in performance among these three searches is substantial, with optimal filtering detecting sources as far as $D_L = 50$–100 Mpc, while power stacking only reaches $D_L \approx 30$ Mpc, and SG templates only reach $D_L \approx 15$ Mpc.

Figures 6.11 and 6.12 show, for Enhanced and Advanced LIGO respectively, contours of detection horizon as a function of mass and mass ratio at a fixed $r_p = 6\,M$ using an optimal filter and SG and RD templates. The primary difference in both cases is the degradation of performance for higher mass ratios (smaller q), with the SG performing as well as or better than the RD templates across much of the parameter space, with the exception of comparable mass ratios, where the ringdown signal is most emphasized. For each search, Enhanced LIGO could detect an equal mass binary with $M = 100$ $\mathrm{M}_\odot$ out to $D_L = 1$ Gpc, and Advanced LIGO will see the same sources beyond 10 Gpc.

The relative performance of SG and RD is further demonstrated in Figs. 6.13 and 6.14, which show the detection probabilities of each template (equivalently, the ratio of the detectable volume using the templates to the volume using optimal filtering). SG templates perform best for $M \approx 200$ $\mathrm{M}_\odot$ systems using Enhanced LIGO and $M \approx 1000$ $\mathrm{M}_\odot$ systems using Advanced LIGO, largely independent of the mass ratio.

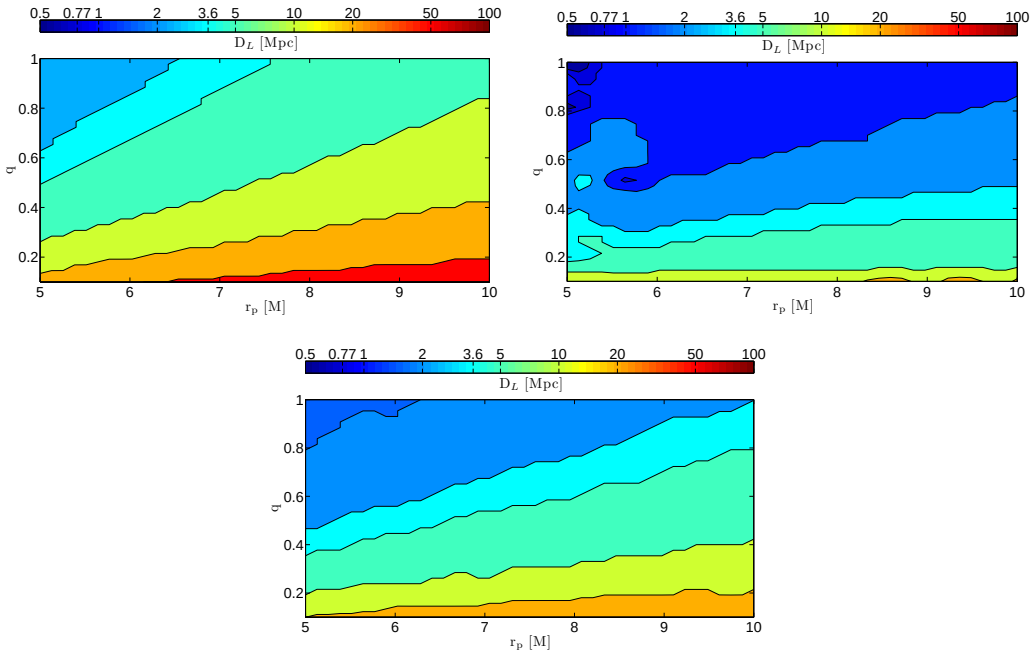

Figure 6.10: Contours of horizon distance ($\rho = 8$) as a function of mass ratio q and pericenter separation r_p for initial LIGO using an optimal filter (top-left panel), sine-Gaussian templates (top-right panel), and an estimate of a power-stacking search (bottom panel) as described in the text. We fix one component to be a 1.35 $M_\odot$ neutron star and change the total mass with mass ratio accordingly. We include a contour at $D_L = 0.77$ Mpc and another at 3.6 Mpc, to show the region of parameter space where existing LIGO searches would not have seen a gravitational wave counterpart to GRB070201 [348] and GRB051103 [339], respectively.

Interestingly, RD templates perform best for comparable mass binaries regardless of total mass for Enhanced LIGO, whereas no such clear general behavior is observed for Advanced LIGO. This can be understood because Enhanced LIGO always has fewer cycles in band than Advanced LIGO, so that the merger-ringdown constitutes a larger fraction of the total SNR, with that fraction further enhanced for comparable masses (since $\rho \propto \eta = m_1 m_2/M^2$ for inspirals, but $\rho \propto \sqrt{\eta}$ for ringdowns [349]). Advanced LIGO shows no such behavior because the number of inspiral cycles is so large that the merger-ringdown rarely dominates the total SNR.

Figures 6.15 and 6.16 again show contours of horizon distance for Enhanced and Advanced LIGO, but as a function of total mass and initial pericenter distance at fixed

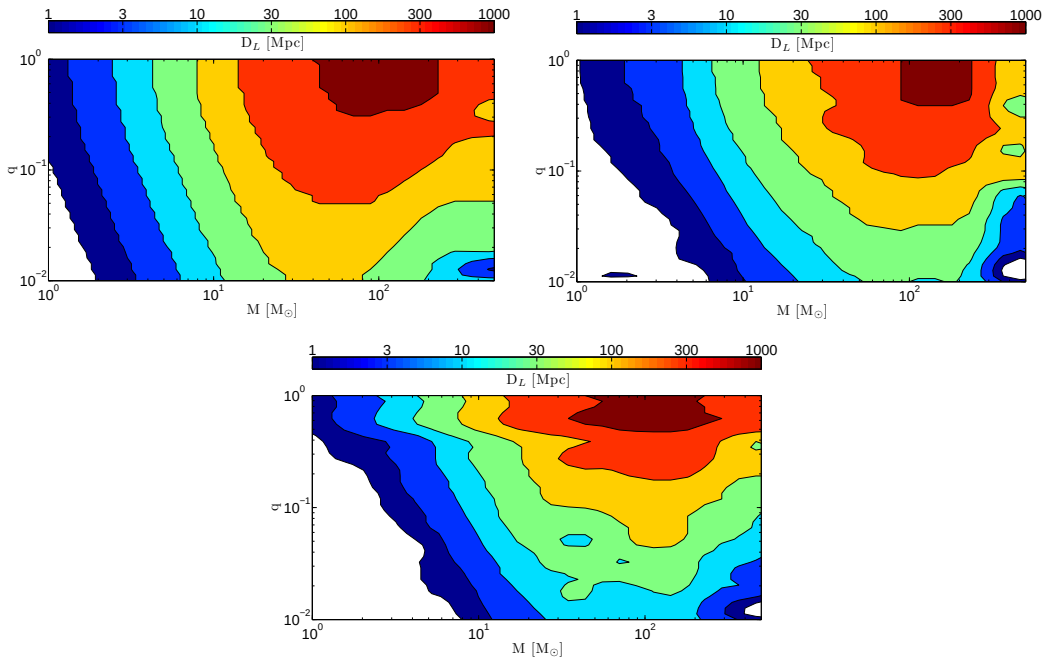

Figure 6.11: Contours of horizon distance as a function of rest mass M and mass ratio q for Enhanced LIGO using an optimal filter (top-left panel), sine-Gaussian templates (top-right panel), and ringdown templates (bottom panel) for an initial pericenter separation of $r_p = 6M$.

$q = 1$. Both q and M rather strongly affect the detectability of sources over the range of masses considered. r_p moderately affects the detectability for lower mass systems ($M \lesssim 20$ M$_\odot$), though very little for higher mass systems (which is expected since the number of bursts varies significantly with r_p in the range $5M < r_p < 10M$, but as the mass increases fewer of the initial bursts are in band). SG templates outperform RD templates for all but the extremely high-mass systems, and a small region of extremely low-mass systems with very small r_p, that merge after $\mathcal{O}(1)$ orbit. This is also clear in Figs. 6.17 and 6.18, which show the corresponding detection probabilities. In addition to SG and RD templates, Figs. 6.16 and 6.18 show the relative performance of a stacked power search, which readily outperforms burst template searches for the full range of parameters. Since this is the case for $q = 1$, it will apply more so for cases with $q < 1$, as they experience more cycles, so that we can conclude that

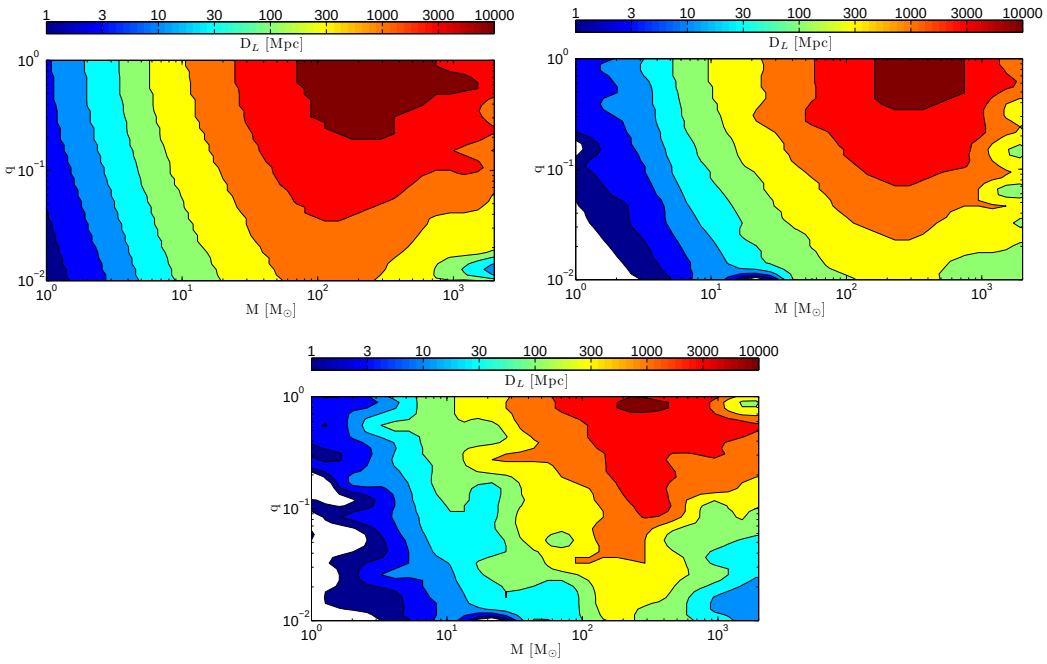

Figure 6.12: Contours of horizon distance as a function of rest mass M and mass ratio q for Advanced LIGO using an optimal filter (top-left panel), sine-Gaussian templates (top-right panel), and ringdown templates (bottom panel) for an initial pericenter separation of $r_p = 6M$.

a power-stacking search will always outperform a burst search and is likely to be the optimal search approach in the absence of a matched-filter bank. SG and RD templates perform best for M in the range 100 $M_\odot$–200 $M_\odot$ for both Enhanced and Advanced LIGO, with the range of horizon distances being the same as in the $M-q$ plots. This is as expected given that setting $q = 1$ maximizes the signal power at fixed M and r_p.

As shown in Fig. 6.18, all three search methods approach optimal-filter performance for large masses, $M \gtrsim 500$ $M_\odot$, since all three methods benefit from having the SNR concentrated in a small number of cycles. However, for lower masses and therefore a larger number of in-band cycles, the SG and RD template performances degrade much more rapidly than power stacking. Whereas SG and RD templates reach detection probabilities as low as 0.01%, power stacking remains above 10% for

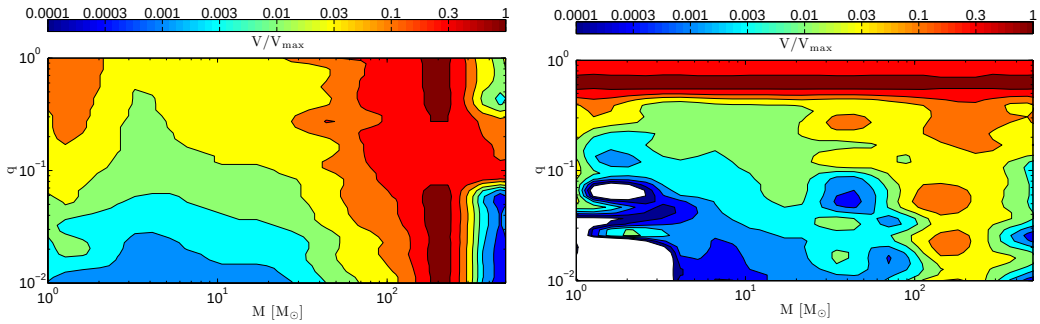

Figure 6.13: Contours of detection probability $p := V/V_{\rm max}$ as a function of rest mass M and mass ratio q for Enhanced LIGO for a source inside the optimal filtering distance horizon, using sine-Gaussian (left panel) and ringdown (right panel) templates for an initial pericenter separation of $r_p = 6M$.

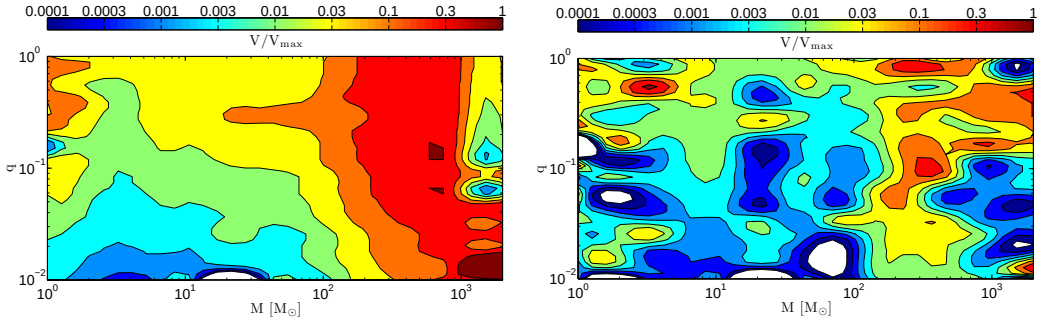

Figure 6.14: Contours of detection probability $p := V/V_{\rm max}$ as a function of rest mass M and mass ratio q for Advanced LIGO for a source inside the optimal filtering distance horizon, using sine-Gaussian (left panel) and ringdown (right panel) templates for an initial pericenter separation of $r_p = 6M$.

the full parameter space considered. Since our power-stacking estimate is an idealization, uncertainties in the timing and frequencies of eccentric bursts may degrade the performance of a true TF power-stacked search. On the other hand, the results of [338] suggest this method is rather robust to timing uncertainties that are smaller than the characteristic time of each burst .

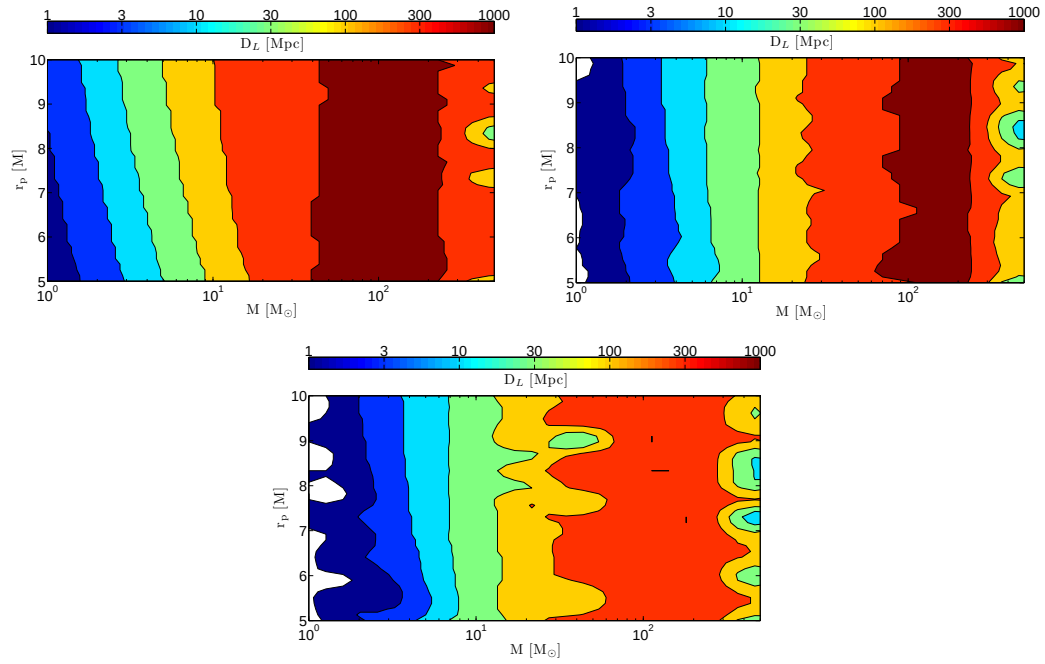

Figure 6.15: Contours of horizon distance as a function of rest mass M and pericenter separation r_p for Enhanced LIGO using an optimal filter (top-left panel), sine-Gaussian templates (top-right panel), and ringdown templates (bottom panel). The mass ratio is $q = 1$.

6.4 Conclusions

We have developed a novel waveform model for eccentric binary gravitational waveforms which can be applied for $r_p \leq 10\,M$, where conventional post-Newtonian waveforms fail. Such binaries may form through dynamical capture in dense stellar environments. Our model is not sufficiently accurate to generate a matched-filter bank, and doing so will be very challenging for large eccentricities. However, the model is adequate to supply mock signals to explore the performance of existing LIGO searches in detecting highly eccentric binary systems. Of existing search strategies, the ringdown and burst searches are best adapted to these systems. However, we find that a large fraction of the parameter space, where we included the impact parameter $5 \leq r_p \leq 10M$ (see [260] for a complementary study of $r_p \geq 10M$), total mass $M \in [1, 2000]\,\mathrm{M}_\odot$ and mass ratio $q \in [0.01, 1]$, has a significantly smaller horizon dis-

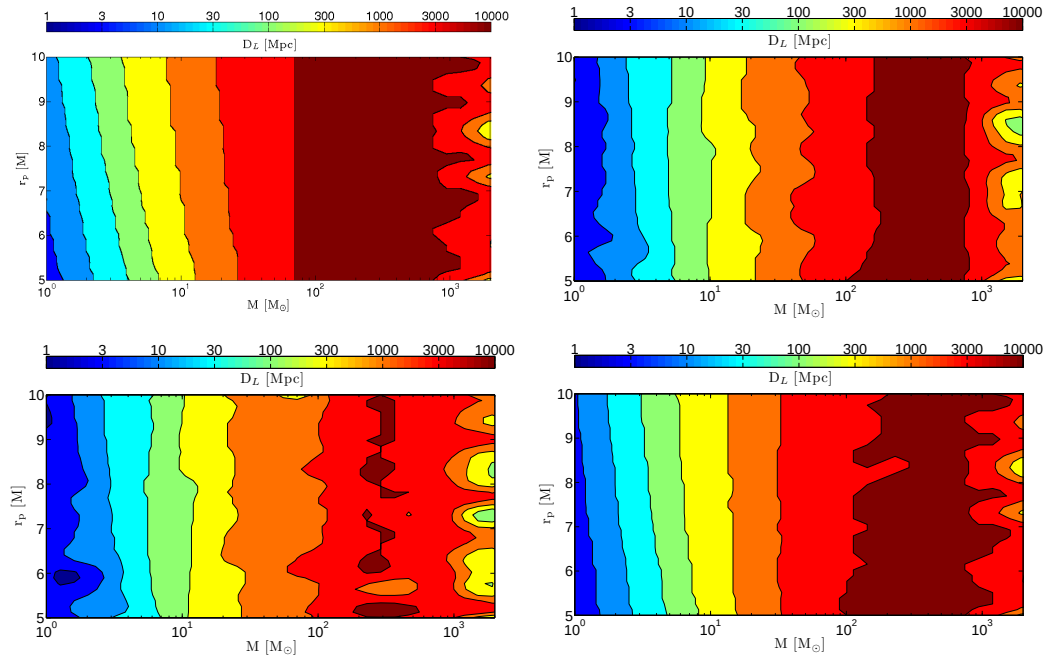

Figure 6.16: Contours of horizon distance as a function of rest mass M and pericenter separation r_p for Advanced LIGO using, from left to right, top to bottom, an optimal filter, sine-Gaussian templates, ringdown templates, and a power-stacking search. The mass ratio is $q = 1$.

tance than what is, in principle, achievable with a matched-filter search. This implies that a corresponding volume of sources could have been missed in prior searches and may be missed in future searches if better adapted strategies are not employed.

Though it may be impractical to construct templates in the near future (via numerical or analytical methods) for these systems that are accurate enough for optimal searches, a refinement of the waveform model presented here should be adequate for informing a power-stacking search. This method has the potential to increase SNR by $\approx N^{1/4}$ for an N-burst event compared to a single-burst search. Though less than the effective $N^{1/2}$ scaling of a full template search, this would still be a significant improvement. Note also that even for systems with larger impact parameters that do evolve to an essentially quasicircular inspiral following the burst phase, for most expected binary parameters the burst phase will be within the band of ground-based

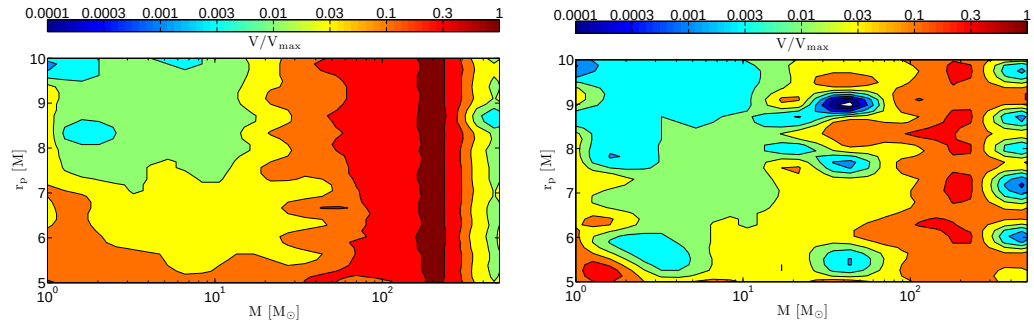

Figure 6.17: Contours of detection probability as a function of rest mass M and pericenter separation r_p for Enhanced LIGO for a source inside the optimal filtering distance horizon, using sine-Gaussian (left panel) and ringdown (right panel) templates. The mass ratio is $q = 1$.

detectors. Thus, the quasicircular inspiral phase will be truncated compared to a primordial quasicircular inspiral, and though such a system may still be detectable with a quasicircular template, it would of course be misidentified, and a bias would be introduced in the estimation of the binary parameters.

For future work, we intend to implement a power-stack search using this waveform model to fully explore the efficacy of this method and its (in)sensitivity to timing errors, as well as continue to refine the model to include (for example) spin precession and finite body effects for neutron stars. We mentioned that the standard PN equations are ill suited to studying the late stages of mergers, in particular for high-eccentricity binaries, motivating our development of the effective Kerr with radiation-reaction model described here. However, the EOB approach [342] is an alternative to the PN expansion that is well behaved all the way to merger for quasicircular orbits. This approach has recently been extended to generic orbits [337], and it will be interesting to explore EOB as the basis for a repeated burst waveform model.

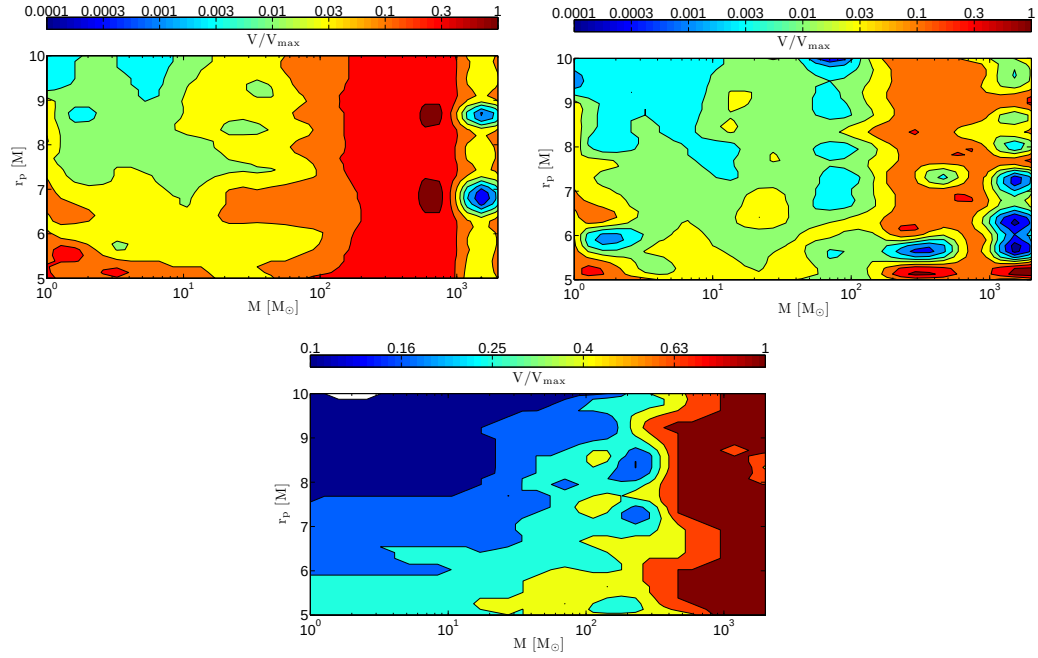

Figure 6.18: Contours of detection probability as a function of rest mass M and initial pericenter separation r_p for Advanced LIGO for a source inside the optimal-filtering horizon distance, using sine-Gaussian (top-left panel) and ringdown (top-right panel) templates and a power-stacking search (bottom panel). The mass ratio is $q = 1$. Note the different scale in the bottom figure.

Chapter 7

Simulating extreme-mass-ratio systems in full general relativity

7.1 Introduction

In recent years, rapid progress has been made in extending the purview of the field of numerical general relativity to a wider class of binary systems. Numerical solutions of the full Einstein equations have been used to study not only compact objects of comparable masses, but also black hole (BH) binaries with mass ratios of up to 100:1 [350, 351], white dwarf-intermediate mass BH systems [66], and neutron star-pseudo white dwarf mergers [352, 104, 353]. In the latter cases, the compaction (ratio of mass to radius in geometric units, $G = c = 1$, which we use throughout) of the white dwarf was $\sim 10^{-4}$, and $\sim 10^{-2}$ for the pseudo white dwarf. Here we are interested in pushing this domain of study even further to BH-stellar systems where the star has compaction $\sim 10^{-6}$, and the mass ratio reaches upwards of 10^6:1. However, simulating these systems with standard methods is very computationally expensive due to the disparate scales in the problem. In order to accurately recover the dynamics of the system, the truncation error from evolving the BH must be reduced

below the level of the star's contribution to the solution. Since the star's contribution to the spacetime metric is many orders of magnitude smaller than that of the BH, this will require exceedingly high resolution compared to the scale that would otherwise be set by the BH alone. In this chapter we introduce a new method for numerically evolving these systems in full general relativity that makes use of the knowledge of the analytic solution of the larger object in order to subtract off the truncation error of the background solution. This method allows extreme-mass-ratio systems to be simulated more efficiently and with greater accuracy at a given resolution.

One of the motivations for the development of this method is the study of tidal disruption of stars by supermassive BHs. Considerable interest in these events has been sparked by the observation in the optical through ultraviolet wavelengths of candidate disruptions and subsequent relativistic outflows associated with the fallback of disrupted material onto the supermassive BH [47, 48, 49, 50, 52, 53, 54, 55, 56, 57, 58, 59, 60]. With more transient surveys [43, 44, 45] beginning operation, the number of observed events should increase significantly, making it important to understand the details of the events across a range of parameters. For BHs with masses around 10^7 to 10^8 $M_\odot$, solar-type stars will be tidally disrupted near the innermost stable circular orbit of the BH. They will therefore be sensitive to strong-field effects including zoom-whirl type behavior and the spin of the BH [354, 355], which may be reflected in observations.

Numerous approaches have been applied to studying tidal disruptions. Analytical approximations include those based on Newtonian dynamics [356, 46, 357, 358, 359, 360], Newtonian dynamics with relativistic corrections [361, 362, 363], and incorporating aspects of Kerr geodesic motion [355]. There have also been particle and grid-based simulations of these events utilizing Newtonian gravity [364, 365, 366]; pseudopotentials to incorporate features of general relativity [367, 368, 369, 370]; or hydrodynamics on a fixed BH spacetime, thus ignoring the self-gravity of the

star [371, 372]. In certain regimes, each of these methods is expected to decently approximate aspects of the desired physics. However, there has yet to be a fully self-consistent calculation within general relativity to investigate this, in particular for the case where disruption occurs near the innermost stable orbit of the BH. The details of the disruption process will depend on the interplay of the strong-field gravity of the black hole, the star's pressure, and the star's self-gravity, which is essentially Newtonian since $M_\odot/R_\odot \sim 2 \times 10^{-6}$. The methods presented here allow us to perform general-relativistic hydrodynamic simulations that self-consistently combine all these components, and hence investigate their importance. As a demonstration, we present results from simulations of the radial infall of a solar-type star into a BH, which can be easily compared to perturbative calculations. We leave the study of the more astrophysically relevant parabolic orbits to future work.

In what follows we explain our method for subtracting background-solution truncation error and its implementation in a general-relativistic hydrodynamics code. We apply this method to simulating the radial infall of a solar-type star into a supermassive BH, illustrating its efficiency and commenting on the tidal effects and resulting gravitational radiation.

7.2 Computational methodology

7.2.1 Background error subtraction technique

In this section we outline our background error subtraction technique (BEST), a method for altering the truncation error in cases where the system can be written in terms of a known background solution, which satisfies the evolution equations on its own, and a small perturbation. The basic idea is straightforward. Say we want to numerically find the solution $y(x,t)$ to some evolution equation $\partial y/\partial t = \mathcal{F}$, where $\mathcal{F}$ is a nonlinear operator. We discretize t as $t_n = n\Delta t$ and let Δ be a discrete evolution

operator (e.g., a Runge-Kutta time stepper) so that we can approximate the evolution as $y_{n+1} = \Delta(y_n)$. Now consider the case where we can write $y(x,t) = \bar{y}(x,t) + \delta(x,t)$, where $\bar{y}$ is itself a known solution to the evolution equation and $|\delta| \ll |\bar{y}|$ in at least part of the domain. In general, even if $\delta(x,t) = 0$, there will be truncation error from evolving $\bar{y}$. In fact, this error can be calculated exactly as $E_n = \Delta(\bar{y}(t = t_n)) - \bar{y}(t = t_{n+1})$. When evolving y, we can therefore explicitly subtract out the truncation error from evolving only $\bar{y}$ at every time step,

$$y_{n+1} = \Delta(y_n) - E_n. \tag{7.1}$$

Since E_n is converging to zero as $\Delta t \to 0$ at whatever order the numerical scheme converges, including this term does not change the overall order of convergence, nor the continuum solution. However, where the truncation error from evolving the background part of the solution dominates, including this term can reduce the magnitude of the truncation error since the remaining error just comes from δ and its nonlinear interaction with $\bar{y}$. Indeed, in the limit of vanishing δ, we merely recover the exact solution $\bar{y}$. In the other limit, supposing $|\bar{y}| \ll |y|$, hence $\delta \approx y$, the contribution from the E_n term in Eq. (7.1) will be negligible, and the solution from the unmodified numerical evolution scheme will be recovered. Though if this were true in the entire domain, there would be no advantage to using this algorithm.[1]

7.2.2 Numerical implementation

We apply the above method to evolving the Einstein equations in the generalized harmonic formulation [79] where the dynamical variables are the metric and its time derivatives, g_{ab} and $\partial_t g_{ab}$. In general, evolution equations can also be specified for

[1] One could also imagine a third limit arising if one inadvertently (or perversely) chose a background exact solution $\bar{y}$ that differed significantly from y, yet was large (i.e. $|\bar{y}| \gtrsim |y|$ and $|\bar{y} - y| \gtrsim |y|$); in that case, subtracting the error term would not help in terms of efficiency, and would in general require more resolution than the unmodified algorithm to get a solution of comparable accuracy.

the source functions $H^a = \Box x^a$, though for simplicity here we restrict ourselves to gauge choices where the source functions are specified as some function of the coordinates and metric variables. We consider cases where the metric is close to a known background solution and hence can be written as $g_{ab} = \tilde{g}_{ab} + h_{ab}$, where $\tilde{g}_{ab}$ is the known background solution and $|h_{ab}| \ll |\tilde{g}_{ab}|$ (in at least part of the domain) and similarly for $\partial_t g_{ab}$. In the example below we take $\tilde{g}_{ab}$ to be the metric of an isolated black hole in a moving frame, though this method will work for an arbitrary metric.

We use a version of the code described in Chap. 2 to numerically evolve the Einstein-hydrodynamics equations with adaptive mesh refinement, modified by BEST. We note that whenever we interpolate, extrapolate, or apply numerical dissipation to the evolution variables, we do so to the quantities h_{ab} and $\partial_t h_{ab}$. From the viewpoint of the adaptive mesh refinement driver, these are treated as the dynamical variables. We evolve the metric in time using fourth-order Runge-Kutta and evolve the fluid variables using second-order Runge Kutta. The fluid variables are evolved using high resolution shock-capturing techniques as described in Chap. 2 with the following modifications. For the conserved fluid quantities we evolve $\tau := -S_t/\alpha - S_i\beta^i - D$ (where D, S_a are the conserved fluid quantities defined in Chap. 2 and α and β^i are the lapse and shift respectively) instead of S_t. This gives better results when the internal energy is small compared to the rest mass. Additionally, when calculating the source terms in the fluid evolution equations that involve $\partial_a g_{bc}$, we numerically compute $\partial_a h_{bc}$ and then add $\partial_a \tilde{g}_{bc}$.

From a programming standpoint, modifying a standard general-relativistic hydrodynamics code to implement BEST is straightforward as it only entails calling the time stepping function twice for every physical time step: once with the background solution $\tilde{g}_{ab}$ and all matter sources set to zero, and again with the full solution g_{ab} and matter sources. These results are then combined following Eq. (7.1). This will essentially double the computational expense of evolving the metric; however, as seen

below, the savings from not having to resolve the background metric at the same level can more than make up for this. If $\tilde{g}_{ab}$ is static then it is only necessary to compute E_n once for a given numerical grid. This algorithm does not depend on the details of the particular numerical time stepper used nor the particular form of the background solution. We also note that with this algorithm the level at which numerical round-off errors come in is still set by the magnitude of g_{ab} and not by the magnitude of h_{ab}.

For the application considered in this paper, we use the axisymmetry of the problem to restrict our computational domain to two spatial dimensions using a modified Cartoon method [125] as described in [79]. However, the methods described here work equally well in three dimensions.

7.2.3 Comoving frame

For the application considered here we use a background solution that is a Galilean transformation of a static BH solution. Specifically, we take an isolated BH solution in coordinates $\{\bar{t}, \bar{x}^i\}$ and transform to the new coordinates $\{t, x^i\}$ where $t = \bar{t}$ and $x^i = \bar{x}^i - p^i(\bar{t})$ where $p^i(\bar{t})$ is some specified function. Below we take p^i to be the geodesic on the isolated BH spacetime with the same initial conditions as the star's center-of-mass. This ensures that in the new coordinates the star's center-of-mass will essentially be at coordinate rest. This is beneficial since the fluid sound speed c_s is much smaller than the speed of light, and letting the star advect across the grid at speeds much greater than c_s can lead to a loss of numerical accuracy (see [366] and references therein). For cases where the geodesic used to compute p^i falls into the BH (as considered below) we transition to a constant p^i after the geodesic crosses the BH's horizon.

7.3 Application

7.3.1 Setup

As an application of BEST we consider a setup with a star of solar-type compaction $m/R_* = 2 \times 10^{-6}$ (where m and R_* are the mass and radius of the star, respectively) that falls radially into a black hole of mass M. The star is modeled as a perfect fluid with a $\Gamma = 5/3$ equation of state. We begin the star at a distance of $50M$ from the BH with the velocity of a geodesic falling from rest at infinity. The initial data is constructed by solving the constraint equations as described in Chap. 3. For the BH we begin with a harmonic solution [144] and then apply a Galilean transformation as described above to keep the star at approximately coordinate rest. We evolve with the gauge choice $H^a = \tilde{\Box}(\tilde{x}^a)$ where all the quantities on the right hand side are from the isolated (and Galilean-transformed) BH solution and hence are not functions of the dynamical variables. This ensures that the background solution does not undergo nontrivial gauge dynamics during evolution.[2] We consider mass ratios of $m/M = 10^{-6}$ and 1.25×10^{-7}.

For the $m/M = 10^{-6}$ case, we use a grid setup with eight levels of mesh refinement (with 2:1 refinement ratio) covering the star's radius with approximately 50, 75, and 100 points for what we will refer to as the low, medium, and high resolutions runs, respectively. Unless otherwise specified, results below are from the high resolution runs with the other two resolutions used to establish convergence. For the $m/M = 1.25 \times 10^{-7}$ case, we add additional refinement levels to achieve the same resolution covering the radius of the star. As described in Chap. 2, during evolution the mesh refinement hierarchy is dynamically adjusted based on truncation error estimates.

[2] In principle, any gauge condition which preserves the desired background solution is allowed. E.g., for a BSSN-puncture evolution, one could use the isotropic Schwarzschild solution with some variation of the $1 + \log$ slicing and gamma-driver condition [373].

7.3.2 Comparison to not using BEST

In Fig. 7.1 we illustrate the benefits of using the background error subtraction technique by plotting the truncation error in the metric component g_{xx} after one coarse time step with and without this technique for the $m/M = 10^{-6}$ case. For this comparison, the same numerical grid at the low resolution is used and the evolution is carried out in exactly the same way except for the inclusion of the second term in Eq. (7.1) when taking a time step. Since there is a lot of resolution concentrated on the star, at the initial separation the truncation error of the BH background solution is negligible in the neighborhood of the star and the use of BEST does not make much difference. However, away from the star, and in particular near the BH, the truncation error from the background solution of an isolated BH moving across the grid is large. The use of BEST makes a significant difference by obviating the need to use high resolution globally.

Whereas in this example the BH is initially resolved at the same level as the wave zone (six refinement levels fewer than the star), in order to achieve the same level of truncation error near the BH after one coarse time step without BEST, the BH must be covered with seven additional levels of refinement. Using the total number of time steps that must be taken at each point in the grid (where, since we use a refinement ratio of two, each successively finer refinement level takes twice as many steps to keep a fixed Courant factor) as an estimate of computational expense, the grid setup necessary without BEST is ~ 40 times more expensive (and would be ~ 140 times more expensive if our computational domain were three- instead of two-dimensional). This far outweighs the computational expense of computing the background error term when taking a time step, which will do no more than double the expense of taking a time step.

We note that high accuracy is required to extract the gravitational wave signal from this system (see Sec. 7.3.4) and when the evolution is performed without using

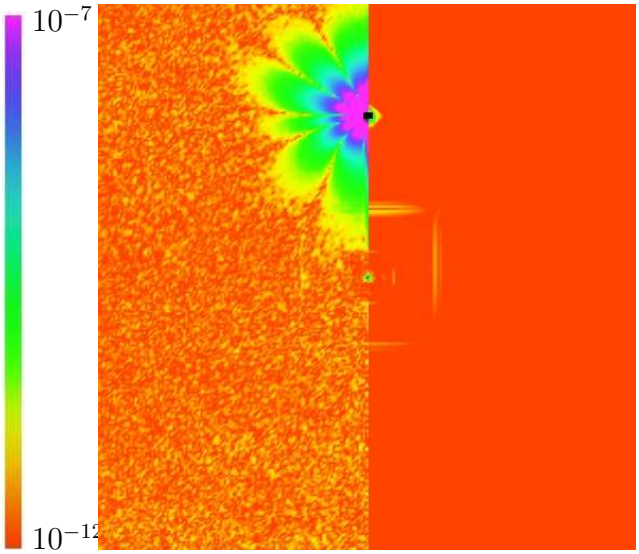

Figure 7.1: Comparison of the absolute magnitude of the truncation error in g_{xx} without (left half) and with (right half) the background subtraction algorithm. Truncation error is calculated by comparing the quantity after one coarse time step ($t \approx 0.4M$) at lower resolution to the same quantity computed with four times the resolution. The inner $[-100M, 100M] \times [0, 100M]$ of the domain which is shown (with the x axis in the vertical direction) is covered entirely by the second level of mesh refinement. The star (center) is covered by 6 additional levels of refinement while the BH (top) is not. The color scale is logarithmic and is saturated in the left panel, which has a maximum of $\sim 10^{-2}$.

BEST, even at the equivalent high resolution, truncation error completely dominates over the physical signal. BEST makes little difference in modeling the star's self-gravity effects noted in Sec. 7.3.3 (which is not surprising as the star is well resolved). However, the accumulation of truncation error from evolving without BEST can cause the star's center-of-mass to drift from the geodesic path as shown in Fig. 7.2.

7.3.3 Effects of self-gravity

To demonstrate the importance of including the star's self-gravity in this calculation, we also consider simulations where we fix the metric to be that of the isolated BH. Without self-gravity to balance the star's pressure, it will expand outwards on timescales of $\sim R_*/c_s$. In Fig. 7.3 we show the maximum rest density as a function

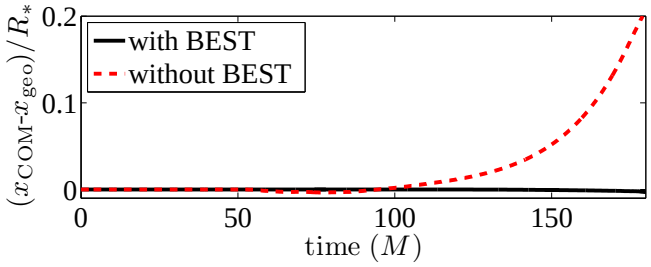

Figure 7.2: The distance of the star's center-of-mass from the equivalent geodesic for $m/M = 1.25 \times 10^{-7}$ with and without the background subtraction algorithm at low resolution.

of time with and without self-gravity. For $m/M = 10^{-6}$ the star's central density drops by more than a factor of two before the star reaches the BH (for this case $R_*/c_s \approx 370M$ at the star's center). For $m/M = 1.25 \times 10^{-7}$, as expected, this drop in density occurs approximately eight times faster in units scaled by the mass of the BH. With self-gravity, the star's central density remains essentially constant in both cases until the star gets close to the BH, at which point it increases. Hence, simply calculating hydrodynamics on a fixed spacetime background will not capture the correct physics.

As the star falls into the BH, the star is stretched in the direction parallel to its motion (i.e., the radial direction) and squeezed in the perpendicular direction by the BH's tidal forces. In Fig. 7.4 we show the coordinate parallel and perpendicular radii of the $0.1\rho_c$ density contour (where ρ_c is the initial central density of the star) that initially contains $\approx 90\%$ of the star's mass. We compare this to the change in separation that two geodesics in the isolated BH spacetime would undergo if they had the same initial velocity and separation. For $m/M = 10^{-6}$, it seems that the combined effect of pressure and self-gravity is small and the change in radii matches the geodesic calculation well. This is not surprising since the star begins at the nominal Newtonian tidal radius of $r_T := R_*(M/m)^{1/3} = 50M$. For $m/M = 1.25 \times 10^{-7}$ the tidal radius

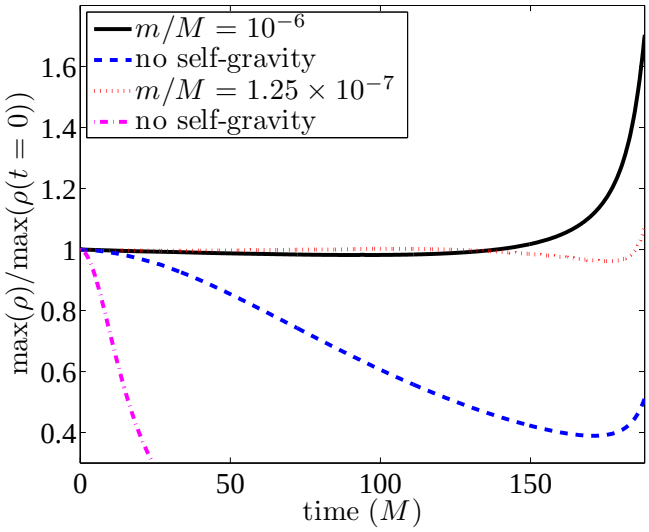

Figure 7.3: Normalized maximum rest density as a function of time with and without self-gravity for the star for $m/M = 10^{-6}$ and $m/M = 1.25 \times 10^{-7}$.

is $r_T = 12.5M$, and there is less of a change in the star's radii compared to freefall at early times.

7.3.4 Gravitational waves

Since we are evolving the full spacetime metric, we can also self-consistently calculate the gravitational wave signal. In Fig. 7.5 we show the gravitational waves emitted from the star-BH interaction for the $m/M = 10^{-6}$ case. We plot spherical harmonics of the Newman-Penrose scalar multiplied by the extraction radius (because of the axisymmetry, only the $m = 0$ components are nonzero). The waveforms are shown multiplied by $M/m = 10^6$, since in the point-particle limit this scaled quantity is independent of the mass ratio. We also show the difference in the computed gravitational wave signal with resolution, which is consistent with second-order convergence.

For comparison, we also show the gravitational wave signal of a point particle falling in a BH, which was calculated in [351] using BH perturbation theory [374]. Though at this mass ratio we are well within the perturbative regime, the star itself

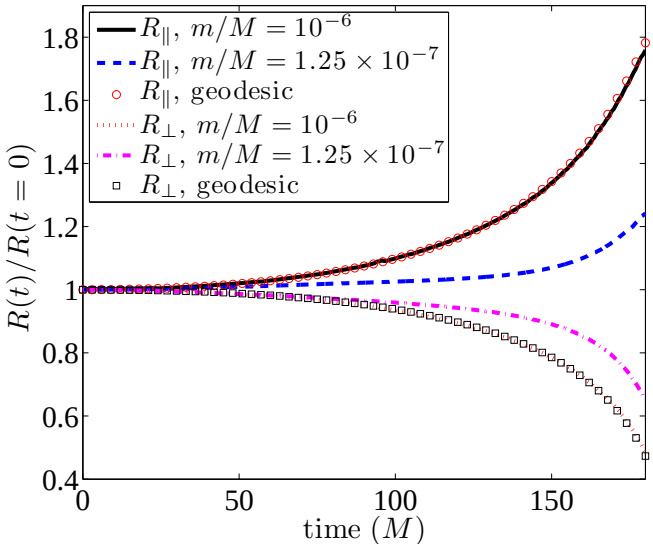

Figure 7.4: Normalized radius of the star perpendicular and parallel to the star's trajectory as a function of time for $m/M = 10^{-6}$ and $m/M = 1.25 \times 10^{-7}$. For comparison we also show the relative position of geodesics starting at corresponding points on the stellar surface and with the same initial velocity as the star's center of mass.

is not that close to a point mass since $R_* = 0.5M$. Nevertheless, we find that our results are well matched by the point-particle results, and the difference between the waveforms is comparable to the truncation error. We also show the power in different harmonics of the gravitational radiation in Fig. 7.6. For the high resolution run, the total energy radiated is 0.0101 (0.0103) m^2/M, where the value in parentheses is the Richardson extrapolated value using all three resolutions and can be used to judge the error. This is compared to 0.0104 m^2/M for the point-particle result [374].

7.4 Conclusions

We have presented a method, BEST, for more efficient solution of the Einstein equations in situations where the metric is dominated by a known background solution. We have demonstrated the utility of this method by applying it to the radial infall of a solar-type star into a supermassive black hole and achieving ~ 40 decrease in

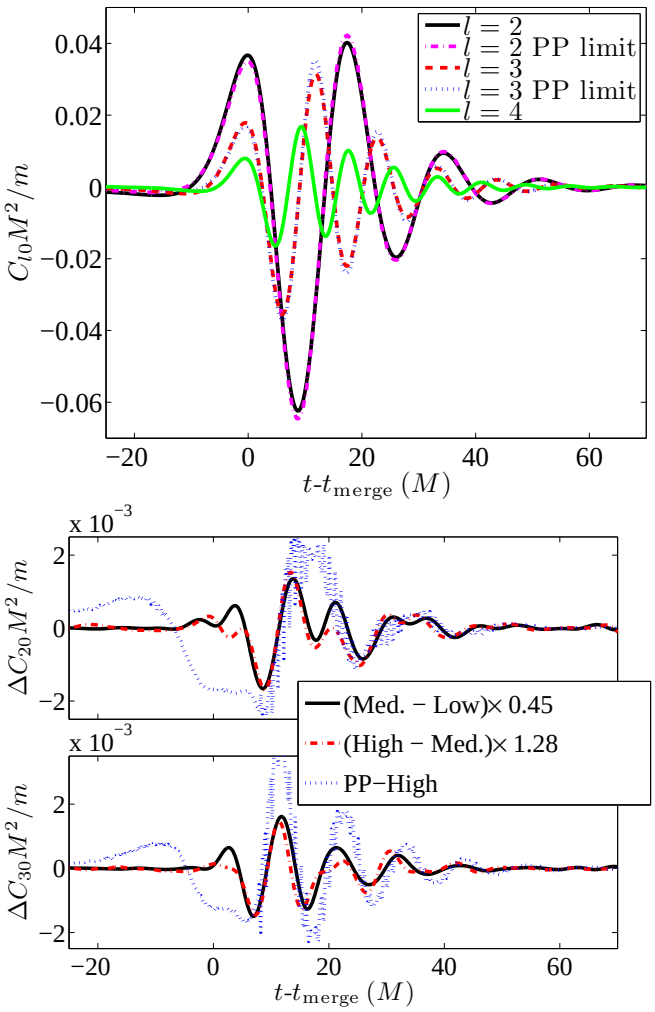

Figure 7.5: Gravitational wave signal from a star falling into a BH with $M = 10^6 m$. *T*op: The first three spin-weight -2 spherical harmonics of $r\Psi_4$ as well as the first two harmonics as calculated using a point-particle approximation, from [351], for comparison. *B*ottom: The difference between the $l = 2$ and $l = 3$ harmonics with resolution, scaled assuming second-order convergence, as well as the difference between the highest resolution run and the point-particle calculation.

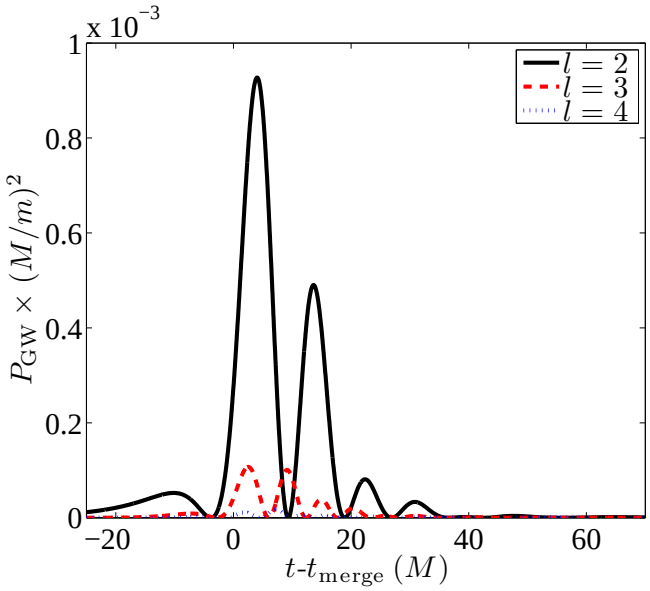

Figure 7.6: The power in each of the first three spin-weight -2 spherical harmonics of the gravitational radiation from the infall of a star into a BH with $M = 10^6 m$.

the computational expense. To our knowledge, this is the first computation within full general relativity of the radial collision problem with such extreme mass ratios and relative compaction between the two objects (upwards of 10^6:1 and 10^5:1, respectively). We found that despite the comparable radius of the star and BH, and the importance of tidal forces in the star, the gravitational waveform from merger matches the point-particle calculation to within the numerical error of a few percent.

The method outlined here is rather general and could be applied to many more problems. An obvious extension, which we will address in future work, is to study tidal disruption of stars on parabolic orbits by supermassive BHs and explore strong-field effects, including the spin of the BH. This technique could also be used to more efficiently study other large-mass-ratio systems, such as binary BHs or a supermassive BH-neutron star merger, where both objects are strongly self-gravitating, but the effect of the small object on the larger one is small. Though the disparate length scales would still be computationally challenging, there would be less need for high global resolution. Other potential applications include simulating stellar-mass compact ob-

ject binaries interacting in some strong-field background, such as near a supermassive BH, or possibly even studying cosmological systems like nonlinear effects of fluctuations on a Friedmann-Robertson-Walker background.

Chapter 8

Ultrarelativistic black hole formation

8.1 Introduction

An important topic in high energy physics that remains poorly understood is the dynamics and outcome of super-Planck scale particle collisions. According to general relativity, kinetic energy, like all forms of energy, gravitates. This implies that at sufficiently high center of mass energies E, the gravitational force will eventually dominate any interaction. Suppose one can localize the particles' wave functions at the moment of interaction to be within a sphere of radius R; then, according to Thorne's hoop conjecture [248] (see also [245, 246, 247]), if R is less than the corresponding Schwarzschild radius $R_s = 2GE/c^2$, the gravitational interaction will be so strong that a black hole (BH) will form. For particles satisfying the de Broglie relationship the threshold for BH formation occurs at Planck energies. There has been much interest in the past decade over the possible relevance of this to proton collisions at the Large Hadron Collider [75, 76] and cosmic ray collisions with the Earth's atmosphere [77], spurred by theories of quantum gravity with small or warped extra

dimensions [72, 73, 74] that present the possibility of a true Planck scale within reach of these processes. To date no evidence for BH formation has been found [249, 250], though since the theories do not make firm predictions for what the true Planck scale is, the high energy scattering problem is worthy (beyond intrinsic theoretical interest) of further study.

In this chapter we explore the purely classical gravitational properties of head-on ultrarelativistic collisions (in four-dimensional asymptotically flat spacetime). This ostensibly gives the leading order description of the process for energies sufficiently above the Planck scale, as all nongravitational interactions will be hidden behind the event horizon, implying that the particular model for the particles is irrelevant. However, part of the motivation for this study is to test this notion, and begin to investigate how it breaks down approaching the threshold of BH formation (though again only at the classical level).

There have been several studies of ultrarelativistic collisions using BHs as model particles. Penrose [375] first considered the head-on collision of two Aichelburg-Sexl metrics [251], each representing the boost $\gamma \to \infty$ limit of the Schwarzschild metric (letting the mass M go to zero such that the energy $E = \gamma M$ is fixed, and note throughout we use geometric units $G = c = 1$). Though the spacetime to the causal future is unknown, a trapped surface is present at the moment of collision, giving an upper bound of 29% for the radiated energy. Perturbative methods [376, 377] allowed a direct calculation, estimating 16.4% energy emitted. In [176], head-on collisions up to $\gamma \approx 3$ were studied using numerical solutions of the field equations; extrapolating the results to $\gamma \to \infty$ gave a value of $14 \pm 3\%$. We briefly mention that studies of BH collisions for general impact parameters using the trapped surface method for infinite boosts [378], and numerical simulations of finite boosts [177, 379] show that considerably more energy can be radiated then.

However, as detailed in [178], the application of the infinite boost results to the collision of massive particles at ultrarelativistic but subluminal speeds is not entirely clear. In this limit, the spacetime loses asymptotic flatness while the non-Minkowski part of the spacetime becomes a two-dimensional shockwave. Moreover, BH collisions at any speed will necessarily produce a larger BH for sufficiently small impact parameter, and are not suitable for studying the threshold or dynamics of BH formation, nor whether BH formation is the generic outcome regardless of the nature or compactness of the colliding particles. Trapped surface calculations, as in [378], can be used to infer the dependence of BH formation on impact parameter (which we do not consider here); however, they do not provide information on the spacetime dynamics postcollision. In [178] a first attempt to address some of these questions was made, where the ultrarelativistic collision of boson stars (solitons of a minimally coupled complex scalar field) was studied numerically. It was found for boson stars with compactness $2M/r \approx 1/20$ that a BH forms for boosts greater than $\gamma \approx 2.9$, roughly one-third the value $\gamma_{\rm h} = 10$ predicted by applying the hoop conjecture at the time of collision. Whether the threshold is generically such a factor smaller than the hoop conjecture estimate was unclear, first because only a single matter model was considered, but also because, though for $\gamma = 2.9$ there is almost twice as much kinetic as rest mass energy in the spacetime, this may not be high enough for the matter dynamics to be irrelevant. Furthermore, due to difficulties disentangling gauge from gravitational wave (GW) dynamics, no estimates of the radiated energy were made.

In this chapter we also study black hole formation in head-on particle collisions. However, we use perfect fluid "stars" as the model particles. To begin with, this allows us to further test the generality of the above arguments in a case where gravity would be opposed by the tendency of the fluid to become highly pressurized on collision and disperse. Second, the nature of fluid stars, not having small-scale internal oscillations as boson stars, as well as a new method for constructing initial data [2], permits us

to explore significantly higher boost collisions where the ratio of kinetic to rest mass energy is of order 10:1. An independent work with the same matter model used here was recently presented in [380], though as with [178] it focuses on regimes where this ratio is at most $\approx$ 2:1.

We find that BHs are formed above a critical boost γ_c that is a factor of a few less than the hoop conjecture estimate. A new phenomenon we present here is, for boosts slightly above γ_c, we observe *two* separate apparent horizons (AHs) form shortly *after* the collision, which some time later are encompassed by a single horizon that rings down to a Schwarzschild BH. We argue that this can be qualitatively understood as due to the strong focusing of the fluid elements of one star by the boosted spacetime of the other, and vice versa, using a geodesic model similar to that in [381] for BH formation in the scattering problem. We also study the GWs emitted in this regime for the first time and find that for the $\gamma = 10$ BH forming case $16 \pm 2\%$ of the energy of the spacetime is radiated (the extrapolation described in [176] suggests this should be 94% of the $\gamma = \infty$ limit). For subthreshold cases, the strong focusing leads to high fluid pressures that cause the stars to explode outward. In what follows, we outline the equations we are solving, the numerical methods for doing so, and the setup of the initial data. We then present the results of our simulations, compare them to geodesic focusing, and end with concluding remarks.

8.2 Methodology

We numerically solve the Einstein field equations, in the generalized harmonic formulation, coupled to a perfect fluid using the code described in Chap. 2. In particular, we use the HLL method for calculating intercell fluxes and the MC slope limiter [85] for reconstructing fluid quantities at cell faces. For simplicity we use the $\Gamma = 2$

equation of state. We use a variation of the damped harmonic gauge [178, 298] that corresponds to equation (A15) in [298] with $p = 1/4$.

We take advantage of the axisymmetry of a head-on collision to reduce the numerical grid to two dimensions and use seven levels of mesh refinement where the finest level covers the equatorial and polar radii of the star by approximately 830 and (due to Lorentz contraction) $830/\gamma$ points, respectively. For the $\gamma = 10$ case, to estimate truncation error we also ran simulations with 1.5 and 2 times the resolution. Unless otherwise stated, results from this case are from the high resolution run.

Initial data are constructed using free data from two identical, boosted solutions of the Tolman-Oppenheimer-Volkoff equations with a polytropic condition, and then solving the constraint equations in the conformal thin-sandwich formulation as described in Chap. 3. With this method, the "spurious" gravitational radiation is much smaller than the physical signal (see Fig. 8.3 below). We choose isolated star solutions with compaction $2M_*/R_* = 1/40$, where M_* and R_* are the gravitational mass and radius, respectively, of the star in its rest frame. They are boosted towards each other with Lorentz factor γ, at an initial separation of $d = 534M_*$. We consider cases with $\gamma = 8$, 8.5, 9, 9.5, 10, and 12, though most of our detailed results are from $\gamma = 8$ and 10.

8.3 Results

We find that BH formation *does* occur in the ultrarelativistic collision of fluid particles with the aforementioned compaction for boost factors $\gamma \geq 8.5 \pm 0.5$ (the uncertainty is from the sampling resolution of our survey in γ). This is ~ 2.4 times smaller than the hoop conjecture threshold of $\gamma_{\rm h} \approx 20$. In Fig. 8.1, we show snapshots of the rest mass density for a subcritical case with $\gamma = 8$ and for a supercritical case with $\gamma = 10$. In the former, after the collision, the matter focuses down into two

high density regions which then explode outward. In the latter, instead of exploding, two identical AHs appear surrounding these regions. (It should be noted that the existence of the initially disjoint AHs does not preclude the possibility of a single encompassing event horizon.) The AHs then fall towards each other with a third, encompassing AH appearing afterwards.

In Fig. 8.2, we show the irreducible mass of the AHs, proper distance between the smaller AHs, and the ratio of the proper equatorial and polar circumferences $C_{\rm eq}/C_{\rm p}$ for $\gamma = 10$. The two smaller AHs are born rather prolate with $C_{\rm eq}/C_{\rm p} \sim 0.6$. Together they have mass $> 0.4M$ where $M \approx 2\gamma M_*$ is the total spacetime mass; i.e., they contain a significant amount of what was originally kinetic energy. When the third encompassing AH appears it initially has less irreducible mass (though greater area) than the sum of the smaller AHs. It is also extremely distorted with $C_{\rm eq}/C_{\rm p} \sim 0.2$ and an equatorial circumference that is less than the smaller AHs, suggesting more of a dumbbell shape. This contrasts with what is found in ultrarelativistic black hole collisions where $C_{\rm eq}/C_{\rm p} \sim 1.5$ initially [176], consistent with a disk shaped AH.

In Fig. 8.3, we show the GW power associated with different spherical harmonics for $\gamma = 10$, and the early part of the GW power for $\gamma = 8$. (Because of the symmetries here only the even l, $m = 0$ harmonics are nonzero.) For $\gamma = 10$, $16 \pm 2\%$ of the initial spacetime energy is radiated as GWs, with a peak luminosity of $0.0137 \pm 1\%$ (the error bars include estimates of the truncation error and finite radius extraction effects). The mass of the final BH is $\approx 0.72M$, suggesting the remaining 12% of the energy is carried off by the $\approx 32\%$ of the initial rest mass that remains outside the final BH by the end of the simulation. Measuring the contributions to the total energy from higher l modes relative to the $l = 2$ component we get that $E_4/E_2 = 0.19 \pm 0.01$, $E_6/E_2 = 0.073 \pm 0.001$, and $E_8/E_2 = 0.040 \pm 0.002$. The substantial amount of energy in higher modes is consistent with results from ultrarelativistic BH collisions. Also, the zero-frequency limit combined with an l-dependent frequency cutoff $\omega_c = l/(3\sqrt{3}M)$ set

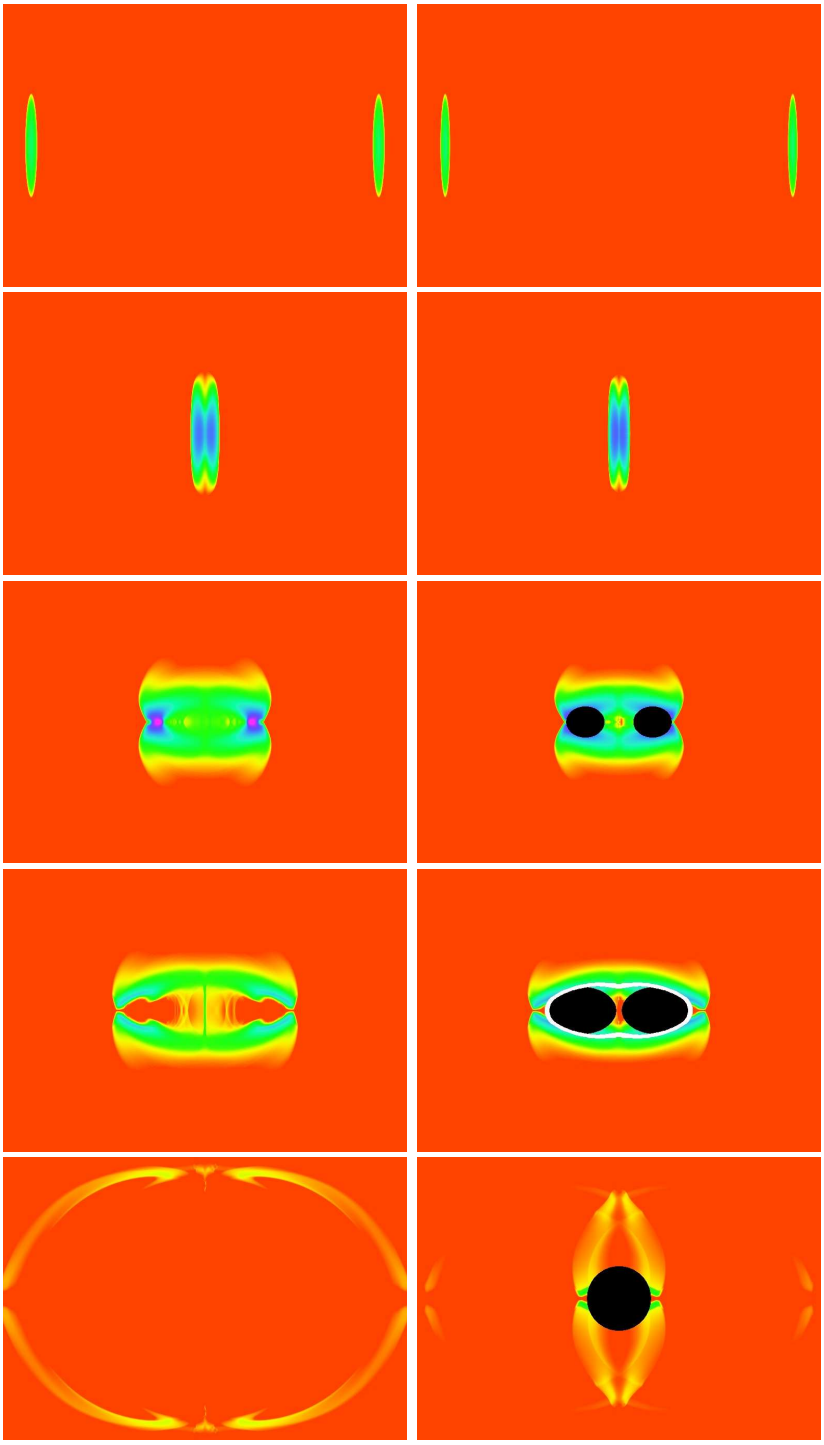

Figure 8.1: Snapshots of rest mass density on a logarithmic scale from 10^{-2} to 10^{2} times the initial maximum density, for simulations with $\gamma = 8$ (left) and $\gamma = 10$ (right) at times (top to bottom) $t = 0$, the initial time; $t = 300M_*$, shortly *after* collision; $t = 375M_*$, after the appearance of the smaller AHs in the $\gamma = 10$ case; $t = 424M_*$, after the appearance of the third, encompassing AH (white outline) in the $\gamma = 10$ case; and $t = 700M_*$. The black regions are best-fit ellipses to the AHs.

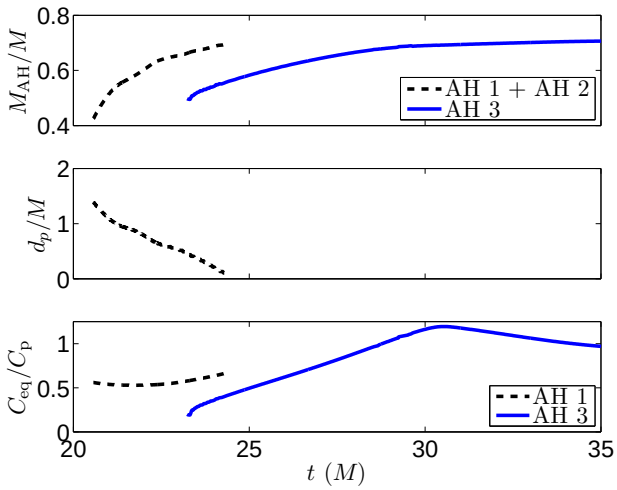

Figure 8.2: Apparent horizon properties for the $\gamma = 10$ case. The AHs labeled 1 and 2 are the two identical (when mirrored about the collision plane) ones that appear first and are later encompassed by AH 3. We show (top to bottom): the irreducible masses, the proper distance d_p between (and exterior to) AHs 1 and 2 measured along the collision axis, and the ratio of the equatorial to polar circumferences.

by BH quasinormal frequencies [382] predicts corresponding values of 0.22, 0.09, and 0.05. For $\gamma = 8$ we can only extract the GW signal before the fluid outflow crosses the extraction sphere. Before this time, the GW signal looks qualitatively similar to the $\gamma = 10$ case and contains 10% of the energy of the spacetime.

Cases with $\gamma = 9.5$, 9.0, and 8.5 also first form two disjoint AHs with increasing initial separation, the smaller the boost. However, we were unable to follow these cases through merger before numerical instabilities set in on the excision surface. The reason, we believe, is the smaller boosts form more distorted AH shapes, and our current approach of excising based on the best-fit ellipse to the AH shape is inadequate. We have also been unable to obtain robust results for significantly higher Lorentz factors due to high frequency numerical instabilities that develop at the surface of the boosted stars; however, it seems that the third AH appears at nearly the same time in this gauge as the first two AHs at $\gamma \sim 12$ for the stars considered here, and for larger boosts we expect a single AH to form at collision.

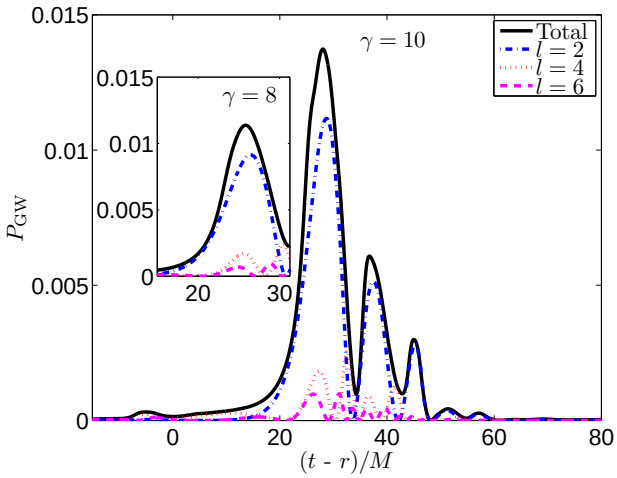

Figure 8.3: Total and spin-weight 2 spherical harmonic decomposition of power in GWs from the $\gamma = 10$ case (with $\gamma = 8$ in the inset). The small feature at $(t - r) < 0$ is an artifact of the initial data and is not included in the estimate of energy.

8.3.1 Geodesic focusing

To illustrate the manner in which a boosted star may act like a gravitational lens and, during collision, focus the matter of the other star, we consider a simplified scenario in a spacetime consisting of a single boosted star. We follow a set of geodesics coming from the opposite direction with the same Lorentz factor, initially distributed to fill out the volume of what would have been the other boosted star (i.e., we replace the second star with tracer particles). These geodesics are shown in Fig. 8.4 for $\gamma = 10$ with the same compaction star described above. As these geodesics pass through the boosted star they become focused in the direction orthogonal to the boost axis while spreading out along the boost axis. The greatest focusing (i.e., when the separation between the geodesics in either direction is smallest) occurs at a distance of $\approx 1.5R_*$ away from the star and reduces the radius by a factor of ≈ 4 (roughly consistent, with the caveat of coordinate differences, with the full problem—see Figs. 8.1 and 8.2). This contraction is sufficient to get to the BH formation threshold if we assume that this focusing also converts sufficient translational energy to radial inflow that it is valid to apply the hoop conjecture to the star's total energy in this frame. Evidence

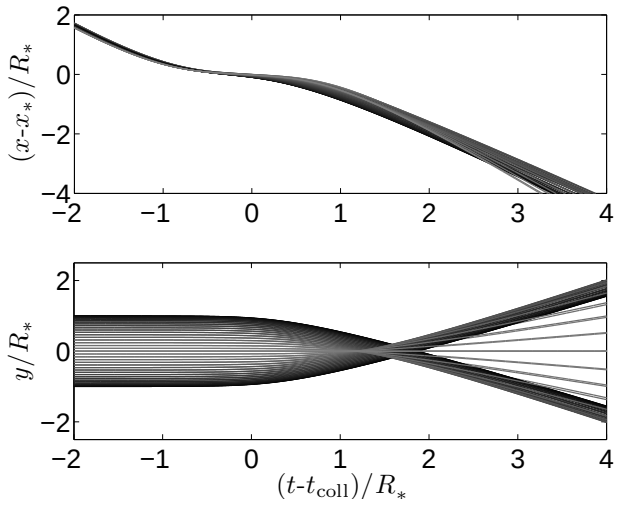

Figure 8.4: Focusing of a set of geodesics in a boosted star spacetime with $\gamma = 10$ and $2M_*/R_* = 1/40$. Shown are the x coordinate relative to the center of the boosted star which is at $x_* = vt$ (top) and the y coordinate (perpendicular to the boost axis) of the geodesics as a function of coordinate time.

for this assumption comes from the temporary slowdown of the translational velocity seen in Fig. 8.4 (though somewhat before maximum focusing), and from the full simulations where in the $\gamma = 10$ case the two AHs move toward each other, and in the $\gamma = 8$ case postcompression the fluid flow is largely radial. In the ultrarelativistic limit, this geodesic focusing factor is mainly a function of the ratio $\gamma M_*/R_*$, and similar results are obtained for larger boosts with correspondingly less compact stars. This can be seen in Fig. 8.5 where the focusing factor in this geodesic model is shown for various values of γ and M_*/R_*. This simplistic treatment of course ignores the effects of pressure and nonlinear gravitational interactions.

8.4 Conclusions

In this chapter, we considered the head-on collision of self-gravitating fluid stars in the regime where the ratio of kinetic to rest mass energy in the spacetime is $\sim$10:1. We find above a critical boost $\gamma_c = 8.5 \pm 0.5$ that BHs do form. The dynamics of the

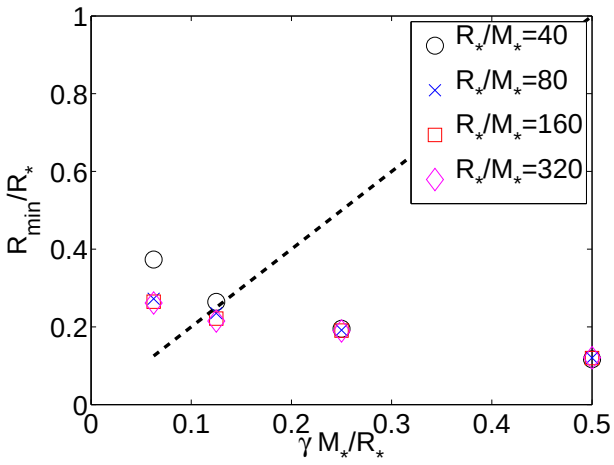

Figure 8.5: Maximum amount of focusing (i.e. the factor by which the radius decreases) an incoming set of geodesics undergoes in a boosted star spacetime plotted against $\gamma M_*/R_*$ for different values of the star's compaction M_*/R_*. Points below the dotted line should form a black hole according to the hoop conjecture.

solution, and a simple geodesic model similar to [381], suggest that near threshold the strong focusing nature of the spacetime sourced by one boosted star on the other, and vice versa, causes the energy to be concentrated postcollision around two focal points on axis. In the subcritical case, the material explodes outward from these points, consistent with [178, 380]; however, just supercritical we find two distinct AHs that initially form around the focal points. This focusing also offers an intuitive explanation for why the threshold in cases studied to date is systematically less than hoop conjecture estimates (here $\gamma_c/\gamma_h \sim 0.4$, with the boson star collisions $\gamma_c/\gamma_h \sim 0.3$ for $\gamma_c \sim 2.9$ [178], and similar factors were found in [383, 384, 385] for the scattering problem using a perturbative model).

For the $\gamma = 10$ supercritical case, we find $16 \pm 2\%$ of the total energy is radiated gravitationally, consistent with results extrapolated from $\gamma \approx 3$ BH collisions [176], and perturbative calculations of the infinite boost limit [376, 377]. Moreover, the leading order spherical-harmonic multipole structure of the waves is consistent with

point-particle approximations and the BH case [382], both super and subcritical, in the latter prior to obscuration of the waveform by matter outflow.

This suggests three different regimes in the head-on collision of ultrarelativistic, nonsingular model particles in general relativity, for sources that have sufficiently *low* compactness such that $\gamma_c \gg 1$. For $\gamma \ll \gamma_c$, gravity plays little role, and the dynamics is governed by that of the matter; for $\gamma \gg \gamma_c$, we expect universal behavior; i.e., any particle model will give the same *quantitative* spacetime dynamics; however, in the intermediate regime $\gamma \sim \gamma_c$ both gravitational and matter dynamics will be important. Ignoring quantum effects and studying the nature of super-Planck scale particles collisions using general relativity is arguably robust only when $\gamma \gg \gamma_c$, though perhaps some insights can still be drawn from classical general relativity in the intermediate regime.

The intermediate regime includes the threshold of BH formation and corresponding, *matter-dependent* critical phenomena [386]. We conjecture approaching γ_c may generically result in two critical solutions unfolding postcollision about the geodesic focal points of the two colliding particles (we speculate the reason why two distinct AHs were not seen in [178, 380] is the compactness is not sufficiently low to have $\gamma_c \gg 1$.) For $\Gamma = 2$ fluid stars, it would be interesting to see whether the critical solution is the type I unstable starlike solution found for lower γ_c's [380], or, as seems more likely, the type II self-similar solution arising in the kinetic energy dominated regime [134]. It would also be interesting to explore collisions with nonzero impact parameters. This would allow a better comparison to BH collisions, which do not have a threshold for BH formation, but do have two distinct end states as a function of impact parameter: a large BH or two unbound BHs.

Chapter 9

Conclusion and directions for future work

In this thesis, we developed methods for numerically simulating hydrodynamics in situations where the effects of dynamical spacetime are important, and used these methods to address several problems in astrophysics and gravitational physics. We presented some of the first work exploring the mergers of black hole-neutron star and neutron star-neutron star binaries formed through dynamical capture. We found that these systems are promising potential sources of gravitational and electromagnetic transients and show a rich variation in dynamics and outcome with impact parameter. Of course, here we have only studied a few points in the parameter space of potential binaries. One area of focus for follow-up work, already underway, is to extend this to include larger mass ratio (up to $7:1$) black hole-neutron star binaries, as well as to study a greater range of black hole spins (up to $a = 0.9$) including spins with different orientations with respect to the orbital angular momentum. This will be interesting since it is expected that black holes are created with various spins [288] that are not generically aligned with the orbital angular momentum. Spin misalignment will complicate the dynamics and give rise to precession effects which will alter the

structure of the accretion disk that forms from the merger. It will also be interesting to leverage increasing computational resources to follow dynamical capture binaries through a larger number of close encounters leading to merger. This will be helpful in tuning improved models of the gravitational wave signals from these binaries.

In addition to expanding the parameter space, it will be important to add new physics to the simulation of these systems, including neutrinos and electromagnetic fields. One direction for future work will be to include magnetic fields in the code presented here. Upgrading the code presented here to ideal magnetohydrodynamics (MHD), which is suitable for simulating the conducting interior of a neutron star, would require extending the same methods already in place to include additional fluid variables. This would be straight-forward, though the primitive inversion, spectral decomposition of the flux Jacobian, etc., would become more complicated. An additional aspect that would need to be addressed is how to enforce the constraint that the divergence of the magnetic field vanish. Several groups have performed general-relativistic simulations of compact object mergers with ideal MHD, which find that magnetic fields do not significantly affect the bulk dynamics (see e.g. [99, 387]). However, even if the bulk dynamics are not affected, it has been suggested that detectable electromagnetic emissions could be created leading up to the merger of a compact object binary when the black hole or other neutron star enters the neutron star's magnetosphere [41, 388], or during the collapse of a hypermassive neutron star to a black hole [40]. This suggests that understanding the behavior of the magnetic field outside the neutron star could be an interesting area to focus on. Simulating the neutron star's magnetosphere requires a more complicated treatment and is an active area of research. One promising approach is using hybrid methods that attempt to combine ideal MHD with a force-free approximation either using matching [40] or within the context of resistive MHD [389]. The code presented here has been recently updated with Maxwell's equations and the force-free approximation.

Constraint violation is controlled using hyperbolic divergence cleaning [390] which is easily implemented within the current framework of the code. It is hoped that the force-free approximation can be combined with suitable boundary conditions in the interior of the neutron star to allow an initial study of the role of magnetic fields in dynamical compact object mergers. However, it will be much more challenging to accurately treat the dynamics of the electromagnetic field across the different regimes going from the neutron star's interior to the magnetosphere to the vacuum, especially in scenarios where the star is significantly distorted.

In this thesis we also presented a numerical technique for efficiently solving the full Einstein equations in situations where the spacetime is dominated by a known background solution. We used this method to study the radial infall of solar-type star into a supermassive black hole. Work is currently underway to study the more astrophysically interesting (though also more computationally expensive) scenario of a star initially in a parabolic orbit being disrupted by a supermassive black hole. Understanding the role of black hole spin in these disruption events will be fruitful, especially if upcoming transient surveys find a number of disruption events which can be used to explore strong-field effects. Incorporating magnetic fields in simulations of these events could also be interesting.

Finally, in this thesis we used general-relativistic hydrodynamics to study the head-on collision of ultrarelativistic fluid particles and found that a gravitational focusing effect could reduce the threshold for black hole formation. For future work, it will be worthwhile to extend these simulations beyond axisymmetry to study collisions with non-zero impact parameters. Besides allowing for a better comparison to ultrarelativistic black hole collision simulations, this will show whether significant gravitational focusing effects remain with increased impact parameter.

Bibliography

[1] William E. East, Frans Pretorius, and Branson C. Stephens. Hydrodynamics in full general relativity with conservative adaptive mesh refinement. *Phys.Rev.*, D85:124010, 2012.

[2] William E. East, Fethi M. Ramazanoglu, and Frans Pretorius. Conformal Thin-Sandwich Solver for Generic Initial Data. *Phys. Rev.*, D86:104053, 2012.

[3] William E. East, Frans Pretorius, and Branson C. Stephens. Eccentric black hole-neutron star mergers: Effects of black hole spin and equation of state. *Phys. Rev. D*, 85:124009, Jun 2012.

[4] Branson C. Stephens, William E. East, and Frans Pretorius. Eccentric Black Hole-Neutron Star Mergers. *Astrophys. J. Lett.*, 737(1):L5, 2011.

[5] William E. East and Frans Pretorius. Dynamical Capture Binary Neutron Star Mergers. *Astrophys.J.*, 760:L4, 2012.

[6] William E. East, Sean T. McWilliams, Janna Levin, and Frans Pretorius. Observing complete gravitational wave signals from dynamical capture binaries. *Phys.Rev.*, D87:043004, 2013.

[7] William E. East and Frans Pretorius. Simulating extreme-mass-ratio systems in full general relativity. *Phys. Rev. D*, 87:101502, May 2013.

[8] William E. East and Frans Pretorius. Ultrarelativistic black hole formation. *Phys.Rev.Lett.*, 110:101101, 2013.

[9] Clifford M. Will. The confrontation between general relativity and experiment. *Living Reviews in Relativity*, 9(3), 2006.

[10] Alex A. Abramovici, William E. Althouse, Ronald W. P. Drever, Yetka Gürsel, Seiji Kawamura, Frederick J. Raab, David Shoemaker, Lisa Sievers, Robert E. Spero, Kip S. Thorne, Rochus E. Vogt, Rainer Weiss, Stanley E. Whitcomb, and Michael E. Zucker. LIGO: The Laser Interferometer Gravitational-Wave Observatory. *Science*, 256:325–333, 1992.

[11] B. Caron, A. Dominjon, C. Drezen, R. Flaminio, X. Grave, et al. The Virgo interferometer. *Class.Quant.Grav.*, 14:1461–1469, 1997.

[12] B. Willke, P. Aufmuth, C. Aulbert, S. Babak, R. Balasubramanian, et al. The GEO 600 gravitational wave detector. *Class.Quant.Grav.*, 19:1377–1387, 2002.

[13] J. Abadie, B. P. Abbott, R. Abbott, T. D. Abbott, M. Abernathy, T. Accadia, F. Acernese, C. Adams, R. Adhikari, C. Affeldt, M. Agathos, P. Ajith, B. Allen, G. S. Allen, E. Amador Ceron, D. Amariutei, R. S. Amin, S. B. Anderson, W. G. Anderson, K. Arai, M. A. Arain, M. C. Araya, S. M. Aston, P. Astone, D. Atkinson, P. Aufmuth, C. Aulbert, B. E. Aylott, S. Babak, P. Baker, G. Ballardin, and S. Ballmer. Search for gravitational waves from low mass compact binary coalescence in ligo's sixth science run and virgo's science runs 2 and 3.

[14] R. van Haasteren, Y. Levin, G.H. Janssen, K. Lazaridis, M. Kramer B.W. Stappers, et al. Placing limits on the stochastic gravitational-wave background using European Pulsar Timing Array data. 2011.

[15] P.B. Demorest, R.D. Ferdman, M.E. Gonzalez, D. Nice, S. Ransom, et al. Limits on the Stochastic Gravitational Wave Background from the North American Nanohertz Observatory for Gravitational Waves. *Astrophys.J.*, 762:94, 2013.

[16] elisa/ngo. *http://www.elisa-ngo.org/*.

[17] J. Abadie, B. P. Abbott, R. Abbott, M. Abernathy, T. Accadia, F. Acernese, C. Adams, R. Adhikari, P. Ajith, B. Allen, and et al. TOPICAL REVIEW: Predictions for the rates of compact binary coalescences observable by ground-based gravitational-wave detectors. *Classical and Quantum Gravity*, 27(17):173001, September 2010.

[18] Fridolin Weber, Rodrigo Negreiros, and Philip Rosenfield. Neutron star interiors and the equation of state of superdense matter. In Werner Becker, editor, *Neutron Stars and Pulsars*, volume 357 of *Astrophysics and Space Science Library*, pages 213–245. Springer Berlin Heidelberg, 2009.

[19] Benjamin D. Lackey, Koutarou Kyutoku, Masaru Shibata, Patrick R. Brady, and John L. Friedman. Extracting equation of state parameters from black hole-neutron star mergers: aligned-spin black holes and a preliminary waveform model. 2013.

[20] Benjamin D. Lackey, Koutarou Kyutoku, Masaru Shibata, Patrick R. Brady, and John L. Friedman. Extracting equation of state parameters from black hole-neutron star mergers. I. Nonspinning black holes. *Phys.Rev.*, D85:044061, 2012.

[21] Y. Sekiguchi, K. Kiuchi, K. Kyutoku, and M. Shibata. Effects of hyperons in binary neutron star mergers. *ArXiv e-prints*, October 2011.

[22] Francesco Pannarale, Luciano Rezzolla, Frank Ohme, and Jocelyn S. Read. Will black hole-neutron star binary inspirals tell us about the neutron star equation of state? *ArXiv e-prints*, 2011.

[23] J. S. Read, C. Markakis, M. Shibata, K. Uryū, J. D. E. Creighton, and J. L. Friedman. Measuring the neutron star equation of state with gravitational wave observations. *Phys. Rev. D*, 79(12):124033, 2009.

[24] R. Oechslin and H.-T. Janka. Gravitational Waves from Relativistic Neutron-Star Mergers with Microphysical Equations of State. *Phys. Rev. Lett.*, 99(12):121102, 2007.

[25] L. K. Tsui, P. T. Leung, and J. Wu. Determination of the internal structure of neutron stars from gravitational wave spectra. *Phys. Rev. D*, 74(12):124025, 2006.

[26] K. D. Kokkotas and N. Stergioulas. Gravitational Waves from Compact Sources. In A. M. Mourão, M. Pimenta, R. Potting, & P. M. Sá , editor, *New Worlds in Astroparticle Physics: Proceedings of the Fifth International Workshop*, page 25, 2006.

[27] M. Shibata. Constraining Nuclear Equations of State Using Gravitational Waves from Hypermassive Neutron Stars. *Phys. Rev. Lett.*, 94(20):201101, 2005.

[28] M. Shibata, K. Taniguchi, and K. Uryū. Merger of binary neutron stars with realistic equations of state in full general relativity. *Phys. Rev. D*, 71(8):084021, 2005.

[29] J. Faber, P. Grandclément, and F. Rasio. Relativistic calculations of coalescing binary neutron stars. *Pramana*, 63:837, 2004.

[30] M. Branchesi, on behalf of the LIGO Scientific Collaboration, the Virgo Collaboration, A. Klotz, and M. Laas-Bourez. Searching for electromagnetic counterparts of gravitational wave transients. *ArXiv e-prints*, October 2011.

[31] The LIGO Scientific Collaboration, Virgo Collaboration: J. Abadie, B. P. Abbott, R. Abbott, T. D. Abbott, M. Abernathy, T. Accadia, F. Acernese, C. Adams, R. Adhikari, and et al. Implementation and testing of the first prompt search for electromagnetic counterparts to gravitational wave transients. *ArXiv e-prints*, September 2011.

[32] Ramesh Narayan, Bohdan Paczynski, and Tsvi Piran. Gamma-ray bursts as the death throes of massive binary stars. *Astrophys. J.*, 395:L83, 1992. astro-ph/9204001.

[33] N. Gehrels *et al.* A short γ-ray burst apparently associated with an elliptical galaxy at redshift z = 0.225. *Nature*, 437:851–854, October 2005.

[34] W. H. Lee, E. Ramirez-Ruiz, and J. Granot. A Compact Binary Merger Model for the Short, Hard GRB 050509b. *Astrophys. J. Lett.*, 630:L165–L168, September 2005.

[35] Ehud Nakar. Short-hard gamma-ray bursts. *Physics Reports*, 442(16):166 – 236, 2007. The Hans Bethe Centennial Volume 1906-2006.

[36] J. M. Lattimer and D. N. Schramm. Black-hole-neutron-star collisions. *Astrophys. J. Lett.*, 192:L145–L147, September 1974.

[37] S. Rosswog, F. K. Thielemann, M. B. Davies, W. Benz, and T. Piran. Coalescing Neutron Stars: a Solution to the R-Process Problem? In W. Hillebrandt and E. Muller, editors, *Nuclear Astrophysics*, page 103, 1998.

[38] Li-Xin Li and Bohdan Paczynski. Transient events from neutron star mergers. *Astrophys.J.*, 507:L59, 1998.

[39] E. Nakar and T. Piran. Detectable radio flares following gravitational waves from mergers of binary neutron stars. *Nature*, 478:82–84, October 2011.

[40] Luis Lehner, Carlos Palenzuela, Steven L. Liebling, Christopher Thompson, and Chad Hanna. Intense Electromagnetic Outbursts from Collapsing Hypermassive Neutron Stars. 2011.

[41] Sean T. McWilliams and Janna J. Levin. Electromagnetic extraction of energy from black hole-neutron star binaries. *Astrophys. J.*, 742:90, 2011. arXiv:1101.1969 [astro-ph.HE].

[42] David Tsang, Jocelyn S. Read, Tanja Hinderer, Anthony L. Piro, and Ruxandra Bondarescu. Resonant shattering of neutron star crusts. *Phys. Rev. Lett.*, 108:011102, Jan 2012.

[43] Arne Rau, Shrinivas R. Kulkarni, Nicholas M. Law, Joshua S. Bloom, David Ciardi, George S. Djorgovski, Derek B. Fox, Avishay Gal-Yam, Carl C. Grillmair, Mansi M. Kasliwal, Peter E. Nugent, Eran O. Ofek, Robert M. Quimby, William T. Reach, Michael Shara, Lars Bildsten, S. Bradley Cenko, Andrew J. Drake, Alexei V. Filippenko, David J. Helfand, George Helou, D. Andrew Howell, Dovi Poznanski, and Mark Sullivan. Exploring the Optical Transient Sky with the Palomar Transient Factory. *PASP*, 121:1334–1351, December 2009.

[44] N. Kaiser. Pan-STARRS: a wide-field optical survey telescope array. volume 5489 of *SPIE Conference Series*, pages 11–22, October 2004.

[45] LSST Science Collaborations, P. A. Abell, J. Allison, S. F. Anderson, J. R. Andrew, J. R. P. Angel, L. Armus, D. Arnett, S. J. Asztalos, T. S. Axelrod, and et al. LSST Science Book, Version 2.0. *ArXiv e-prints*, December 2009.

[46] M. J. Rees. Tidal disruption of stars by black holes of 10 to the 6th-10 to the 8th solar masses in nearby galaxies. *Nature*, 333:523–528, June 1988.

[47] N. Bade, S. Komossa, and M. Dahlem. Detection of an extremely soft X-ray outburst in the HII-like nucleus of NGC 5905. *Astron. and Astrophys.*, 309:L35–L38, May 1996.

[48] S. Komossa and J. Greiner. Discovery of a giant and luminous X-ray outburst from the optically inactive galaxy pair RX J1242.6-1119. *Astron. and Astrophys.*, 349:L45–L48, September 1999.

[49] S. Gezari, J. P. Halpern, S. Komossa, D. Grupe, and K. M. Leighly. Follow-Up Hubble Space Telescope/Space Telescope Imaging Spectroscopy of Three Candidate Tidal Disruption Events. *Astrophys. J.*, 592:42–51, July 2003.

[50] S. Gezari, D. C. Martin, B. Milliard, S. Basa, J. P. Halpern, K. Forster, P. G. Friedman, P. Morrissey, S. G. Neff, D. Schiminovich, M. Seibert, T. Small, and T. K. Wyder. Ultraviolet Detection of the Tidal Disruption of a Star by a Supermassive Black Hole. *Astrophys. J. Lett.*, 653:L25–L28, December 2006.

[51] P. Esquej, R. D. Saxton, M. J. Freyberg, A. M. Read, B. Altieri, M. Sanchez-Portal, and G. Hasinger. Candidate tidal disruption events from the XMM-Newton slew survey. *Astron. and Astrophys.*, 462:L49–L52, February 2007.

[52] S. Gezari, S. Basa, D. C. Martin, G. Bazin, K. Forster, B. Milliard, J. P. Halpern, P. G. Friedman, P. Morrissey, S. G. Neff, D. Schiminovich, M. Seibert, T. Small, and T. K. Wyder. UV/Optical Detections of Candidate Tidal Disruption Events by GALEX and CFHTLS. *Astrophys. J.*, 676:944–969, April 2008.

[53] N. Cappelluti, M. Ajello, P. Rebusco, S. Komossa, A. Bongiorno, C. Clemens, M. Salvato, P. Esquej, T. Aldcroft, J. Greiner, and H. Quintana. A candidate tidal disruption event in the Galaxy cluster Abell 3571. *Astron. and Astrophys.*, 495:L9–L12, February 2009.

[54] S. van Velzen, G. R. Farrar, S. Gezari, N. Morrell, D. Zaritsky, L. Östman, M. Smith, J. Gelfand, and A. J. Drake. Optical Discovery of Probable Stellar Tidal Disruption Flares. *Astrophys. J.*, 741:73, November 2011.

[55] J. S. Bloom, D. Giannios, B. D. Metzger, S. B. Cenko, D. A. Perley, N. R. Butler, N. R. Tanvir, A. J. Levan, P. T. O'Brien, L. E. Strubbe, F. De Colle, E. Ramirez-Ruiz, W. H. Lee, S. Nayakshin, E. Quataert, A. R. King, A. Cucchiara, J. Guillochon, G. C. Bower, A. S. Fruchter, A. N. Morgan, and A. J. van der Horst. A Possible Relativistic Jetted Outburst from a Massive Black Hole Fed by a Tidally Disrupted Star. *Science*, 333:203–, July 2011.

[56] A. J. Levan, N. R. Tanvir, S. B. Cenko, D. A. Perley, K. Wiersema, J. S. Bloom, A. S. Fruchter, A. d. U. Postigo, P. T. O'Brien, N. Butler, A. J. van der Horst, G. Leloudas, A. N. Morgan, K. Misra, G. C. Bower, J. Farihi, R. L. Tunnicliffe, M. Modjaz, J. M. Silverman, J. Hjorth, C. Thöne, A. Cucchiara, J. M. C. Cerón, A. J. Castro-Tirado, J. A. Arnold, M. Bremer, J. P. Brodie, T. Carroll, M. C. Cooper, P. A. Curran, R. M. Cutri, J. Ehle, D. Forbes, J. Fynbo, J. Gorosabel, J. Graham, D. I. Hoffman, S. Guziy, P. Jakobsson, A. Kamble, T. Kerr, M. M. Kasliwal, C. Kouveliotou, D. Kocevski, N. M. Law, P. E. Nugent, E. O. Ofek,

D. Poznanski, R. M. Quimby, E. Rol, A. J. Romanowsky, R. Sánchez-Ramírez, S. Schulze, N. Singh, L. van Spaandonk, R. L. C. Starling, R. G. Strom, J. C. Tello, O. Vaduvescu, P. J. Wheatley, R. A. M. J. Wijers, J. M. Winters, and D. Xu. An Extremely Luminous Panchromatic Outburst from the Nucleus of a Distant Galaxy. *Science*, 333:199–, July 2011.

[57] B. A. Zauderer, E. Berger, A. M. Soderberg, A. Loeb, R. Narayan, D. A. Frail, G. R. Petitpas, A. Brunthaler, R. Chornock, J. M. Carpenter, G. G. Pooley, K. Mooley, S. R. Kulkarni, R. Margutti, D. B. Fox, E. Nakar, N. A. Patel, N. H. Volgenau, T. L. Culverhouse, M. F. Bietenholz, M. P. Rupen, W. Max-Moerbeck, A. C. S. Readhead, J. Richards, M. Shepherd, S. Storm, and C. L. H. Hull. Birth of a relativistic outflow in the unusual γ-ray transient Swift J164449.3+573451. *Nature*, 476:425–428, August 2011.

[58] S. B. Cenko, J. S. Bloom, S. R. Kulkarni, L. E. Strubbe, A. A. Miller, N. R. Butler, R. M. Quimby, A. Gal-Yam, E. O. Ofek, E. Quataert, L. Bildsten, D. Poznanski, D. A. Perley, A. N. Morgan, A. V. Filippenko, D. A. Frail, I. Arcavi, S. Ben-Ami, A. Cucchiara, C. D. Fassnacht, Y. Green, I. M. Hook, D. A. Howell, D. J. Lagattuta, N. M. Law, M. M. Kasliwal, P. E. Nugent, J. M. Silverman, M. Sullivan, S. P. Tendulkar, and O. Yaron. PTF10iya: a short-lived, luminous flare from the nuclear region of a star-forming galaxy. *Mon. Not. Roy. Astron. Soc.*, 420:2684–2699, March 2012.

[59] S. B. Cenko, H. A. Krimm, A. Horesh, A. Rau, D. A. Frail, J. A. Kennea, A. J. Levan, S. T. Holland, N. R. Butler, R. M. Quimby, J. S. Bloom, A. V. Filippenko, A. Gal-Yam, J. Greiner, S. R. Kulkarni, E. O. Ofek, F. Olivares E., P. Schady, J. M. Silverman, N. R. Tanvir, and D. Xu. Swift J2058.4+0516: Discovery of a Possible Second Relativistic Tidal Disruption Flare? *Astrophys. J.*, 753:77, July 2012.

[60] S. Gezari, R. Chornock, A. Rest, M. E. Huber, K. Forster, E. Berger, P. J. Challis, J. D. Neill, D. C. Martin, T. Heckman, A. Lawrence, C. Norman, G. Narayan, R. J. Foley, G. H. Marion, D. Scolnic, L. Chomiuk, A. Soderberg, K. Smith, R. P. Kirshner, A. G. Riess, S. J. Smartt, C. W. Stubbs, J. L. Tonry, W. M. Wood-Vasey, W. S. Burgett, K. C. Chambers, T. Grav, J. N. Heasley, N. Kaiser, R.-P. Kudritzki, E. A. Magnier, J. S. Morgan, and P. A. Price. An ultraviolet-optical flare from the tidal disruption of a helium-rich stellar core. *Nature*, 485:217–220, May 2012.

[61] P. J. Montero, O. Zanotti, J. A. Font, and L. Rezzolla. Dynamics of magnetized relativistic tori oscillating around black holes. *Mon. Not. Roy. Astron. Soc.*, 378:1101–1110, July 2007.

[62] O. Korobkin, E. B. Abdikamalov, E. Schnetter, N. Stergioulas, and B. Zink. Stability of general-relativistic accretion disks. *Phys. Rev. D*, 83(4):043007, February 2011.

[63] B. D. Farris, Y. T. Liu, and S. L. Shapiro. Binary black hole mergers in gaseous disks: Simulations in general relativity. *Phys. Rev. D*, 84(2):024024, July 2011.

[64] T. Bode, T. Bogdanović, R. Haas, J. Healy, P. Laguna, and D. Shoemaker. Mergers of Supermassive Black Holes in Astrophysical Environments. *Astrophys. J.*, 744:45, January 2012.

[65] V. Paschalidis, Y. T. Liu, Z. Etienne, and S. L. Shapiro. Merger of binary white dwarf–neutron stars: Simulations in full general relativity. *Phys. Rev. D*, 84(10):104032, November 2011.

[66] R. Haas, R. V. Shcherbakov, T. Bode, and P. Laguna. Tidal Disruptions of White Dwarfs from Ultra-close Encounters with Intermediate-mass Spinning Black Holes. *Astrophys. J.*, 749:117, April 2012.

[67] Christian D. Ott, Ernazar Abdikamalov, Philipp Msta, Roland Haas, Steve Drasco, et al. General-Relativistic Simulations of Three-Dimensional Core-Collapse Supernovae. *Astrophys.J.*, 768:115, 2013.

[68] Paul M. Chesler and Laurence G. Yaffe. Horizon formation and far-from-equilibrium isotropization in supersymmetric Yang-Mills plasma. *Phys.Rev.Lett.*, 102:211601, 2009.

[69] Hans Bantilan, Frans Pretorius, and Steven S. Gubser. Simulation of Asymptotically AdS5 Spacetimes with a Generalized Harmonic Evolution Scheme. *Phys.Rev.*, D85:084038, 2012.

[70] Alex Buchel, Luis Lehner, and Robert C. Myers. Thermal quenches in N=2* plasmas. 2012.

[71] Carsten Gundlach and Jose M. Martin-Garcia. Critical phenomena in gravitational collapse. *Living Reviews in Relativity*, 10:5, 2007.

[72] Nima Arkani-Hamed, Savas Dimopoulos, and G. R. Dvali. The hierarchy problem and new dimensions at a millimeter. *Phys. Lett.*, B429:263–272, 1998.

[73] Ignatios Antoniadis, Nima Arkani-Hamed, Savas Dimopoulos, and G. R. Dvali. New dimensions at a millimeter to a Fermi and superstrings at a TeV. *Phys. Lett.*, B436:257–263, 1998.

[74] Lisa Randall and Raman Sundrum. Large mass hierarchy from a small extra dimension. *Phys. Rev. Lett.*, 83:3370–3373, 1999.

[75] S. Dimopoulos and G. Landsberg. Black Holes at the Large Hadron Collider. *Physical Review Letters*, 87(16):161602, October 2001.

[76] S. B. Giddings and S. Thomas. High energy colliders as black hole factories: The end of short distance physics. *Phys. Rev. D*, 65(5):056010, March 2002.

[77] Jonathan L. Feng and Alfred D. Shapere. Black hole production by cosmic rays. *Phys. Rev. Lett.*, 88:021303, Dec 2001.

[78] D. Garfinkle. Harmonic coordinate method for simulating generic singularities. *Phys. Rev. D*, 65(4):044029, 2002.

[79] Frans Pretorius. Numerical relativity using a generalized harmonic decomposition. *Class. Quantum Grav.*, 22:425–452, 2005.

[80] M. Shibata and T. Nakamura. Evolution of three-dimensional gravitational waves: Harmonic slicing case. *Phys. Rev. D*, 52:5428, 1995.

[81] T. W. Baumgarte and S. L. Shapiro. Numerical integration of Einstein's field equations. *Phys. Rev. D*, 59(2):024007, 1999.

[82] James R. Wilson. Numerical Study of Fluid Flow in a Kerr Space. *Astrophys. J.*, 173:431, 1972.

[83] James R. Wilson. Stellar collapse and supernovae. In Larry L. Smarr, editor, *Sources of Gravitational Radiation*, pages 335–344. Cambridge University Press, Cambridge, U.K., 1979.

[84] José A. Font, Mark Miller, Wai-Mo Suen, and Malcolm Tobias. Three-dimensional numerical general relativistic hydrodynamics: Formulations, methods, and code tests. *Phys. Rev. D*, 61:044011, Jan 2000.

[85] E.F. Toro. *Riemann Solvers and Numerical Methods for Fluid Dynamics*. Springer, Berlin, Germany, 1997.

[86] H. Lück *et al.* The geo-600 project. *Class. and Quant. Grav.*, 15:1471, 1997.

[87] M. Ando *et al.* Stable operation of a 300-m laser interferometer with sufficient sensitivity to detect gravitational-wave events within our galaxy. *Phys. Rev. Lett.*, 86:3950, 2001. astro-ph/0105473.

[88] B. D. Metzger and E. Berger. What is the Most Promising Electromagnetic Counterpart of a Neutron Star Binary Merger? *Astrophys. J.*, 746:48, February 2012.

[89] Jos A. Font. Numerical hydrodynamics and magnetohydrodynamics in general relativity. *Living Reviews in Relativity*, 11:7, 2008.

[90] M. D. Duez, Y. T. Liu, S. L. Shapiro, and B. C. Stephens. Relativistic magnetohydrodynamics in dynamical spacetimes: Numerical methods and tests. *Phys. Rev. D*, 72(2):024028, 2005.

[91] Tetsuro Yamamoto, Masaru Shibata, and Keisuke Taniguchi. Simulating coalescing compact binaries by a new code (sacra). *Phys. Rev. D*, 78:064054, Sep 2008.

[92] Bruno Giacomazzo and Luciano Rezzolla. WhiskyMHD: a new numerical code for general relativistic magnetohydrodynamics. *Class. Quantum Grav.*, 24:S235–S258, 2007.

[93] M. Thierfelder, S. Bernuzzi, and B. Brügmann. Numerical relativity simulations of binary neutron stars. *Phys. Rev. D*, 84(4):044012, August 2011.

[94] Tanja Bode, Roland Haas, Tamara Bogdanovic, Pablo Laguna, and Deirdre M. Shoemaker. Relativistic mergers of supermassive black holes and their electromagnetic signatures. *Astrophys. J.*, 715:1117–1131, 2010.

[95] M. D. Duez, F. Foucart, L. E. Kidder, H. P. Pfeiffer, M. A. Scheel, and S. A. Teukolsky. Evolving black hole-neutron star binaries in general relativity using pseudospectral and finite difference methods. *Phys. Rev. D*, 78(10):104015, 2008.

[96] M. Anderson, E. W. Hirschmann, S. L. Liebling, and D. Neilsen. Relativistic MHD with adaptive mesh refinement. *Class. and Quant. Grav.*, 23:6503, 2006.

[97] L. Lindblom, M. A. Scheel, L. E. Kidder, R. Owen, and O. Rinne. A new generalized harmonic evolution system. *Class. and Quant. Grav.*, 23:447, 2006.

[98] Sarvnipun Chawla, Matthew Anderson, Michael Besselman, Luis Lehner, Steven L. Liebling, Patrick M. Motl, , and David Neilsen. Mergers of Magnetized Neutron Stars with Spinning Black Holes: Disruption, Accretion, and Fallback. *Phys. Rev. Lett.*, 105:111101, 2010.

[99] Z. B. Etienne, Y. T. Liu, and S. L. Shapiro. Relativistic magnetohydrodynamics in dynamical spacetimes: A new adaptive mesh refinement implementation. *Phys. Rev. D*, 82(8):084031, October 2010.

[100] Z. B. Etienne, V. Paschalidis, Y. T. Liu, and S. L. Shapiro. Relativistic MHD in dynamical spacetimes: Improved EM gauge condition for AMR grids. *ArXiv e-prints*, October 2011.

[101] Matthew D. Duez, Francois Foucart, Lawrence E. Kidder, Christian D. Ott, and Saul A. Teukolsky. Equation of state effects in black hole-neutron star mergers. *Class. Quant. Grav.*, 27:114106, 2010.

[102] K. Kiuchi, Y. Sekiguchi, M. Shibata, and K. Taniguchi. Exploring Binary-Neutron-Star-Merger Scenario of Short-Gamma-Ray Bursts by Gravitational-Wave Observation. *Phys. Rev. Lett.*, 104(14):141101, April 2010.

[103] K. Kyutoku, H. Okawa, M. Shibata, and K. Taniguchi. Gravitational waves from spinning black hole-neutron star binaries: dependence on black hole spins and on neutron star equations of state. *Phys. Rev. D*, 84(6):064018, September 2011.

[104] Vasileios Paschalidis, Zachariah Etienne, Yuk Tung Liu, and Stuart L. Shapiro. Head-on collisions of binary white dwarf–neutron stars: Simulations in full general relativity. *Phys.Rev.*, D83:064002, 2011.

[105] Yuichiro Sekiguchi, Kenta Kiuchi, Koutarou Kyutoku, and Masaru Shibata. Gravitational waves and neutrino emission from the merger of binary neutron stars. *Phys. Rev. Lett.*, 107:051102, Jul 2011.

[106] M. Shibata, K. Kiuchi, Y. Sekiguchi, and Y. Suwa. Truncated Moment Formalism for Radiation Hydrodynamics in Numerical Relativity. *Prog. Theor. Phys.*, 125:1255–1287, June 2011.

[107] B. Müller, H.-T. Janka, and H. Dimmelmeier. A New Multi-dimensional General Relativistic Neutrino Hydrodynamic Code for Core-collapse Supernovae. I. Method and Code Tests in Spherical Symmetry. *Astrophys. J. Supp.*, 189:104–133, July 2010.

[108] P. Cerdá-Durán, J. A. Font, L. Antón, and E. Müller. A new general relativistic magnetohydrodynamics code for dynamical spacetimes. *Astron. and Astrophys.*, 492:937–953, December 2008.

[109] W. H. Lee and W. Kluźniak. Newtonian Hydrodynamics of the Coalescence of Black Holes with Neutron Stars. I. Tidally Locked Binaries with a Stiff Equation of State. *Astrophys. J.*, 526:178–199, November 1999.

[110] S. Rosswog and D. Price. MAGMA: a three-dimensional, Lagrangian magnetohydrodynamics code for merger applications. *Mon. Not. Roy. Astron. Soc.*, 379:915–931, August 2007.

[111] J. A. Faber, P. Grandclément, and F. A. Rasio. Mergers of irrotational neutron star binaries in conformally flat gravity. *Phys. Rev. D*, 69(12):124036, June 2004.

[112] R. Oechslin, H.-T. Janka, and A. Marek. Relativistic neutron star merger simulations with non-zero temperature equations of state. I. Variation of binary parameters and equation of state. *Astron. and Astrophys.*, 467:395–409, May 2007.

[113] P. Laguna, W. A. Miller, and W. H. Zurek. Smoothed particle hydrodynamics near a black hole. *Astrophys. J.*, 404:678–685, February 1993.

[114] S. Rosswog. Conservative, special-relativistic smoothed particle hydrodynamics. *Journal of Computational Physics*, 229:8591–8612, November 2010.

[115] M.J. Berger and P. Colella. Local adaptive mesh refinement for shock hydrodynamics. *Journal of Computational Physics*, 82(1):64, 1989.

[116] J. M. Stone, T. A. Gardiner, P. Teuben, J. F. Hawley, and J. B. Simon. Athena: A New Code for Astrophysical MHD. *Astrophys. J. Supp.*, 178:137, 2008.

[117] A. S. Almgren, V. E. Beckner, J. B. Bell, M. S. Day, L. H. Howell, C. C. Joggerst, M. J. Lijewski, A. Nonaka, M. Singer, and M. Zingale. CASTRO: A New Compressible Astrophysical Solver. I. Hydrodynamics and Self-gravity. *Astrophys. J.*, 715:1221–1238, June 2010.

[118] D. C. Collins, H. Xu, M. L. Norman, H. Li, and S. Li. Cosmological Adaptive Mesh Refinement Magnetohydrodynamics with Enzo. *Astrophys. J. Supp.*, 186:308–333, February 2010.

[119] B. Fryxell, K. Olson, P. Ricker, F. X. Timmes, M. Zingale, D. Q. Lamb, P. MacNeice, R. Rosner, J. W. Truran, and H. Tufo. FLASH: An Adaptive Mesh Hydrodynamics Code for Modeling Astrophysical Thermonuclear Flashes. *Astrophys. J. Supp.*, 131:273–334, November 2000.

[120] K. Beckwith and J. M. Stone. A Second-order Godunov Method for Multi-dimensional Relativistic Magnetohydrodynamics. *Astrophys. J. Supp.*, 193:6, March 2011.

[121] Helmut Friedrich. On the hyperbolicity of einstein's and other gauge field equations. *Communications in Mathematical Physics*, 100:525–543, 1985. 10.1007/BF01217728.

[122] Carsten Gundlach, José M. Martín-García, Gioel Calabrese, and Ian Hinder. Constraint damping in the Z4 formulation and harmonic gauge. *Class. Quantum Grav.*, 22:3767–3774, 2005.

[123] F. Pretorius. Evolution of Binary Black-Hole Spacetimes. *Phys. Rev. Lett.*, 95(12):121101, 2005.

[124] C. F. Gammie, J. C. McKinney, and G. Tóth. HARM: A Numerical Scheme for General Relativistic Magnetohydrodynamics. *Astrophys. J.*, 589:444–457, May 2003.

[125] Miguel Alcubierre, Steve R. Brandt, Bernd Brügmann, Daniel E. Holz, Edward Seidel, Ryoji Takahashi, and Jonathan Thornburg. Symmetry without Symmetry: Numerical Simulation of Axisymmetric Systems using Cartesian Grids. *Int. J. Mod. Phys. D*, 10:273–290, 2001.

[126] A. Harten, P.D. Lax, and B.J. van Leer. *SIAM Rev.*, 25:35, 1983.

[127] F. Eulderink and G. Mellema. General relativistic hydrodynamics with a ROE solver. *Astron. and Astrophys. Supp.*, 110:587, 1995.

[128] R. Donat and A. Marquina. Capturing shock reflections: An improved flux formula. *J. Comput. Phys.*, 125:42–58, 1996.

[129] Chi-Wang Shu and Stanley Osher. Efficient implementation of essentially non-oscillatory shock-capturing schemes, ii. *Journal of Computational Physics*, 83(1):32 – 78, 1989.

[130] P. Colella and P. R. Woodward. The Piecewise Parabolic Method (PPM) for Gas-Dynamical Simulations. *Journal of Computational Physics*, 54:174, 1984.

[131] José Ma Martí and Ewald Müller. Extension of the piecewise parabolic method to one-dimensional relativistic hydrodynamics. *Journal of Computational Physics*, 123(1):1 – 14, 1996.

[132] Guang-Shan Jiang and Chi-Wang Shu. Efficient implementation of weighted eno schemes. *Journal of Computational Physics*, 126(1):202 – 228, 1996.

[133] A. Tchekhovskoy, J. C. McKinney, and R. Narayan. WHAM: a WENO-based general relativistic numerical scheme - I. Hydrodynamics. *Mon. Not. Roy. Astron. Soc.*, 379:469, 2007.

[134] Scott C. Noble and Matthew W. Choptuik. Type II critical phenomena of neutron star collapse. *Phys. Rev. D*, 78(6):064059, Sep 2008.

[135] H. Shen, H. Toki, K. Oyamatsu, and K. Sumiyoshi. Relativistic equation of state of nuclear matter for supernova and neutron star. *Nuclear Physics A*, 637:435, 1998.

[136] H. Shen, H. Toki, K. Oyamatsu, and K. Sumiyoshi. Relativistic Equation of State of Nuclear Matter for Supernova Explosion. *Progress of Theoretical Physics*, 100:1013, 1998.

[137] R.P. Brent. *Algorithms for minimization without derivatives.* Prentice-Hall, Englewood Cliffs, N.J., 1972.

[138] J. M. Ibanez, M. A. Aloy, J. A. Font, J. M. Marti, J. A. Miralles, and J. A. Pons. Riemann Solvers in General Relativistic Hydrodynamics. *ArXiv Astrophysics e-prints*, November 1999.

[139] Marsha J Berger and Joseph Oliger. Adaptive mesh refinement for hyperbolic partial differential equations. *Journal of Computational Physics*, 53(3):484, 1984.

[140] F. Pretorius and M. W. Choptuik. Adaptive mesh refinement for coupled elliptic-hyperbolic systems. *Journal of Computational Physics*, 218:246–274, October 2006.

[141] Frans Pretorius. Simulation of binary black hole spacetimes with a harmonic evolution scheme. *Class. Quantum Grav.*, 23:S529–S552, 2006.

[142] Dieter R. Brill. On the positive definite mass of the bondi-weber-wheeler time-symmetric gravitational waves. *Annals of Physics*, 7(4):466 – 483, 1959.

[143] Evgeny Sorkin. On critical collapse of gravitational waves. *Classical and Quantum Gravity*, 28(2):025011, 2011.

[144] Gregory B. Cook and Mark A. Scheel. Well-behaved harmonic time slices of a charged, rotating, boosted black hole. *Phys. Rev. D*, 56:4775–4781, 1997.

[145] W. Zhang and A. I. MacFadyen. RAM: A Relativistic Adaptive Mesh Refinement Hydrodynamics Code. *Astrophys. J. Supp.*, 164:255, 2006.

[146] B. Giacomazzo and L. Rezzolla. The exact solution of the Riemann problem in relativistic magnetohydrodynamics. *Journal of Fluid Mechanics*, 562:223–259, September 2006.

[147] B. Giacomazzo, L. Rezzolla, and L. Baiotti. Can magnetic fields be detected during the inspiral of binary neutron stars? *Mon. Not. Roy. Astron. Soc.*, 399:L164, 2009.

[148] Luciano Rezzolla and Olindo Zanotti. New relativistic effects in the dynamics of nonlinear hydrodynamical waves. *Phys. Rev. Lett.*, 89:114501, Aug 2002.

[149] Ashley F. Emery. An evaluation of several differencing methods for inviscid fluid flow problems. *Journal of Computational Physics*, 2(3):306 – 331, 1968.

[150] Arturo Lucas-Serrano, Jose A. Font, Jose M. Ibanez, and Jose M. Marti. Assessment of a high-resolution central scheme for the solution of the relativistic hydrodynamics equations. *Astron. Astrophys.*, 428:703–715, 2004.

[151] Stuart L. Shapiro and Saul A. Teukolsky. *Black holes, white dwarfs, and neutron stars : the physics of compact objects*. Wiley, New York, 1983.

[152] Phillip Colella and Michael D. Sekora. A limiter for ppm that preserves accuracy at smooth extrema. *Journal of Computational Physics*, 227(15):7069 – 7076, 2008.

[153] Roman Gold, Sebastiano Bernuzzi, Marcus Thierfelder, Bernd Brugmann, and Frans Pretorius. Eccentric binary neutron star mergers. *Phys.Rev.*, D86:121501, 2012.

[154] Kentaro Somiya. Detector configuration of KAGRA - the Japanese cryogenic gravitational-wave detector. *Class.Quant.Grav.*, 29:124007, 2012.

[155] B. Sathyaprakash, M. Abernathy, F. Acernese, P. Ajith, B. Allen, et al. Scientific Objectives of Einstein Telescope. *Class.Quant.Grav.*, 29:124013, 2012.

[156] Harald P Pfeiffer. Numerical simulations of compact object binaries. *Classical and Quantum Gravity*, 29(12):124004, 2012.

[157] Frans Pretorius. Binary Black Hole Coalescence. 2007.

[158] Mark D. Hannam. Status of black-hole binary simulations for gravitational-wave detection. *Class. Quantum Grav.*, 26:114001, 2009.

[159] Joan M. Centrella, John G. Baker, Bernard J. Kelly, and James R. van Meter. Black-hole binaries, gravitational waves, and numerical relativity. *Rev. Mod. Phys.*, 82:3069–3119, 2010.

[160] Sean T McWilliams. The status of black-hole binary merger simulations with numerical relativity. *Classical and Quantum Gravity*, 28(13):134001, 2011.

[161] Joshua A. Faber and Frederic A. Rasio. Binary neutron star mergers. *Living Reviews in Relativity*, 15:8, 2012.

[162] Masaru Shibata and Keisuke Taniguchi. Coalescence of black hole-neutron star binaries. *Living Reviews in Relativity*, 14(6), 2011.

[163] Matthew D. Duez. Numerical relativity confronts compact neutron star binaries: a review and status report. *Class.Quant.Grav.*, 27:114002, 2010.

[164] Ian Hinder, Frank Herrmann, Pablo Laguna, and Deirdre Shoemaker. Comparisons of eccentric binary black hole simulations with post-Newtonian models. *Phys. Rev. D*, 82:024033, 2010.

[165] James Healy, Frank Herrmann, Ian Hinder, Deirdre M. Shoemaker, Pablo Laguna, and Richard A. Matzner. Superkicks in hyperbolic encounters of binary black holes. *Phys. Rev. Lett.*, 102:041101, 2009.

[166] Ulrich Sperhake, Emanuele Berti, Vitor Cardoso, José A. González, Bernd Brügmann, and Marcus Ansorg. Eccentric binary black-hole mergers: The transition from inspiral to plunge in general relativity. *Phys. Rev. D*, 78:064069, Sep 2008.

[167] Frans Pretorius and Deepak Khurana. Black hole mergers and unstable circular orbits. *Class. Quantum Grav.*, 24:S83–S108, 2007.

[168] Matthew C. Washik, James Healy, Frank Herrmann, Ian Hinder, Deirdre M. Shoemaker, Pablo Laguna, and Richard A. Matzner. Binary-black-hole encounters, gravitational bursts, and maximum final spin. *Phys. Rev. Lett.*, 101:061102, Aug 2008.

[169] Ian Hinder, Birjoo Vaishnav, Frank Herrmann, Deirdre M. Shoemaker, and Pablo Laguna. Circularization and final spin in eccentric binary-black-hole inspirals. *Phys. Rev. D*, 77:081502, Apr 2008.

[170] Roman Gold and Bernd Bruegmann. Eccentric black hole mergers and zoom-whirl behavior from elliptic inspirals to hyperbolic encounters. 2012.

[171] Christian D. Ott. The Gravitational Wave Signature of Core-Collapse Supernovae. *Class.Quant.Grav.*, 26:063001, 2009.

[172] Chris L. Fryer and Kimberly C.B. New. Gravitational waves from gravitational collapse. *Living Reviews in Relativity*, 14:1, 2011.

[173] Beverly K. Berger. Numerical approaches to spacetime singularities. *Living Reviews in Relativity*, 5:1, 2002.

[174] David Garrison. Numerical Relativity as a tool for studying the Early Universe. 2012.

[175] V. et al. Cardoso. NR/HEP: roadmap for the future. *ArXiv e-prints*, January 2012.

[176] Ulrich Sperhake, Vitor Cardoso, Frans Pretorius, Emanuele Berti, and José A. González. High-energy collision of two black holes. *Phys. Rev. Lett.*, 101:161101, 2008.

[177] Masaru Shibata, Hirotada Okawa, and Tetsuro Yamamoto. High-velocity collision of two black holes. *Phys. Rev. D*, 78:101501(R), 2008.

[178] Matthew W. Choptuik and Frans Pretorius. Ultrarelativistic particle collisions. *Phys. Rev. Lett.*, 104:111101, 2010.

[179] Hirotada Okawa, Ken-ichi Nakao, and Masaru Shibata. Is super-Planckian physics visible? – Scattering of black holes in 5 dimensions. *Phys.Rev.*, D83:121501, 2011.

[180] Helvi Witek, Vitor Cardoso, Leonardo Gualtieri, Carlos Herdeiro, Ulrich Sperhake, et al. Head-on collisions of unequal mass black holes in D=5 dimensions. *Phys.Rev.*, D83:044017, 2011.

[181] Paul M. Chesler and Laurence G. Yaffe. Holography and colliding gravitational shock waves in asymptotically AdS_5 spacetime. *Phys.Rev.Lett.*, 106:021601, 2011.

[182] Paul M. Chesler and Derek Teaney. Dynamical Hawking Radiation and Holographic Thermalization. 2011.

[183] Toby Wiseman. Numerical construction of static and stationary black holes. 2011.

[184] Masaru Shibata and Hirotako Yoshino. Nonaxisymmetric instability of rapidly rotating black hole in five dimensions. *Phys. Rev. D*, 81:021501(R), 2010.

[185] Luis Lehner and Frans Pretorius. Black Strings, Low Viscosity Fluids, and Violation of Cosmic Censorship. *Phys.Rev.Lett.*, 105:101102, 2010.

[186] Piotr Bizon and Andrzej Rostworowski. On weakly turbulent instability of anti-de Sitter space. *Phys.Rev.Lett.*, 107:031102, 2011.

[187] James W. York. Conformal "thin-sandwich" data for the initial-value problem of general relativity. *Phys. Rev. Lett.*, 82:1350–1353, Feb 1999.

[188] J. W. York, Jr. *Frontiers in Numerical Relativity*, pages 89–109. Cambridge University Press, 1989.

[189] Gregory B. Cook. Initial data for numerical relativity. *Living Reviews in Relativity*, 3:5, 2000.

[190] H. P. Pfeiffer. The initial value problem in numerical relativity. *ArXiv General Relativity and Quantum Cosmology e-prints*, December 2004.

[191] E. Gourgoulhon. Construction of initial data for 3+1 numerical relativity. *Journal of Physics Conference Series*, 91(1):012001, November 2007.

[192] J. M. Bowen and J. W. York, Jr. Time-asymmetric initial data for black holes and black-hole collisions. *Phys. Rev. D*, 21:2047–2056, April 1980.

[193] A. Garat and R. H. Price. Nonexistence of conformally flat slices of the Kerr spacetime. *Phys. Rev. D*, 61(12):124011, June 2000.

[194] G. B. Cook and J. W. York, Jr. Apparent horizons for boosted or spinning black holes. *Phys. Rev. D*, 41:1077–1085, February 1990.

[195] G. Lovelace, R. Owen, H. P. Pfeiffer, and T. Chu. Binary-black-hole initial data with nearly extremal spins. *Phys. Rev. D*, 78(8):084017, October 2008.

[196] G. B. Cook, M. W. Choptuik, M. R. Dubal, S. Klasky, R. A. Matzner, and S. R. Oliveira. Three-dimensional initial data for the collision of two black holes. *Phys. Rev. D*, 47:1471–1490, February 1993.

[197] Gregory B. Cook. Three-dimensional initial data for the collision of two black holes. II. Quasi-circular orbits for equal-mass black holes. *Phys. Rev. D*, 50(8):5025–5032, 1994.

[198] J. R. Wilson, G. J. Mathews, and P. Marronetti. Relativistic numerical model for close neutron-star binaries. *Phys. Rev. D*, 54:1317–1331, July 1996.

[199] T. W. Baumgarte, G. B. Cook, M. A. Scheel, S. L. Shapiro, and S. A. Teukolsky. Binary Neutron Stars in General Relativity: Quasiequilibrium Models. *Physical Review Letters*, 79:1182–1185, August 1997.

[200] Silvano Bonazzola, Eric Gourgoulhon, and Jean-Alain Marck. Relativistic formalism to compute quasiequilibrium configurations of nonsynchronized neutron star binaries. *Phys. Rev. D*, 56:7740–7749, 1997.

[201] Gregory B. Cook. Corotating and irrotational binary black holes in quasicircular orbits. *Phys. Rev. D*, 65:084003, Mar 2002.

[202] Eric Gourgoulhon, Philippe Grandclément, and Silvano Bonazzola. Binary black holes in circular orbits. i. a global spacetime approach. *Phys. Rev. D*, 65:044020, Jan 2002.

[203] Philippe Grandclément, Eric Gourgoulhon, and Silvano Bonazzola. Binary black holes in circular orbits. ii. numerical methods and first results. *Phys. Rev. D*, 65:044021, Jan 2002.

[204] Wolfgang Tichy and Bernd Brügmann. Quasi-equilibrium binary black hole sequences for puncture data derived from helical Killing vector condition. *Phys. Rev. D*, 69:024006, 2004.

[205] Gregory B. Cook and Harald P. Pfeiffer. Excision boundary conditions for black-hole initial data. *Phys. Rev. D*, 70:104016, Nov 2004.

[206] Marcus Ansorg, Bernd Brügmann, and Wolfgang Tichy. A single-domain spectral method for black hole puncture data. *Phys. Rev. D*, 70:064011, 2004.

[207] Marcus Ansorg. A Double-domain spectral method for black hole excision data. *Phys.Rev.*, D72:024018, 2005.

[208] M. Shibata, K. Uryū, and J. L. Friedman. Deriving formulations for numerical computation of binary neutron stars in quasicircular orbits. *Phys. Rev. D*, 70(4):044044, August 2004.

[209] P. Grandclément. Accurate and realistic initial data for black hole neutron star binaries. *Phys. Rev. D*, 74(12):124002, December 2006.

[210] F. Foucart, L. E. Kidder, H. P. Pfeiffer, and S. A. Teukolsky. Initial data for black hole neutron star binaries: A flexible, high-accuracy spectral method. *Phys. Rev. D*, 77(12):124051, June 2008.

[211] Keisuke Taniguchi, Thomas W. Baumgarte, Joshua A. Faber, and Stuart L. Shapiro. Quasiequilibrium sequences of black-hole˘neutron-star binaries in general relativity. *Phys. Rev. D*, 74:041502, Aug 2006.

[212] Jason D. Grigsby and Gregory B. Cook. Measuring eccentricity in binary black-hole initial data. *Phys. Rev. D*, 77:044011, Feb 2008.

[213] Harald P. Pfeiffer, Gregory B. Cook, and Saul A. Teukolsky. Comparing initial-data sets for binary black holes. *Phys. Rev. D*, 66:024047, Jul 2002.

[214] Mark D. Hannam, Sascha Husa, Bernd Brügmann, José A. González, and Ulrich Sperhake. Beyond the Bowen-York extrinsic curvature for spinning black holes. *Class. Quantum Grav.*, 24:S15–S24, 2007.

[215] Richard A. Matzner, Mijan F. Huq, and Deirdre Shoemaker. Initial data and coordinates for multiple black hole systems. *Phys. Rev. D*, 59:024015, Dec 1998.

[216] Pedro Marronetti and Richard A. Matzner. Solving the initial value problem of two black holes. *Phys. Rev. Lett.*, 85:5500–5503, Dec 2000.

[217] Geoffrey Lovelace. Reducing spurious gravitational radiation in binary-black-hole simulations by using conformally curved initial data. *Classical and Quantum Gravity*, 26(11):114002, 2009.

[218] Yuk Tung Liu, Zachariah B. Etienne, and Stuart L. Shapiro. Evolution of near-extremal-spin black holes using the moving puncture technique. *Phys.Rev.*, D80:121503, 2009.

[219] Wolfgang Tichy, Bernd Brügmann, Manuela Campanelli, and Peter Diener. Binary black hole initial data for numerical general relativity based on post-newtonian data. *Phys. Rev. D*, 67:064008, Mar 2003.

[220] Samaya Nissanke. Post-newtonian freely specifiable initial data for binary black holes in numerical relativity. *Phys. Rev. D*, 73:124002, Jun 2006.

[221] Nicolás Yunes, Wolfgang Tichy, Benjamin J. Owen, and Bernd Brügmann. Binary black hole initial data from matched asymptotic expansions. *Phys. Rev. D*, 74:104011, 2006.

[222] Nathan K. Johnson-McDaniel, Nicolás Yunes, Wolfgang Tichy, and Benjamin J. Owen. Conformally curved binary black hole initial data including tidal deformations and outgoing radiation. *Phys. Rev. D*, 80:124039, 2009.

[223] G. Reifenberger and W. Tichy. Alternatives to standard puncture initial data for binary black hole evolution. *ArXiv e-prints*, May 2012.

[224] G. Lovelace, M. A. Scheel, and B. Szilágyi. Simulating merging binary black holes with nearly extremal spins. *Phys. Rev. D*, 83(2):024010, January 2011.

[225] M. Shibata, K. Uryū, and J. L. Friedman. Erratum: Deriving formulations for numerical computation of binary neutron stars in quasicircular orbits [Phys. Rev. D 70, 044044 (2004)]. *Phys. Rev. D*, 70(12):129901, December 2004.

[226] Koji Uryu, Francois Limousin, John L. Friedman, Eric Gourgoulhon, and Masaru Shibata. Binary neutron stars in a waveless approximation. *Phys.Rev.Lett.*, 97:171101, 2006.

[227] Gregory B. Cook and Thomas W. Baumgarte. Excision boundary conditions for the conformal metric. *Phys. Rev. D*, 78:104016, Nov 2008.

[228] K. Uryū, F. Limousin, J. L. Friedman, E. Gourgoulhon, and M. Shibata. Nonconformally flat initial data for binary compact objects. *Phys. Rev. D*, 80(12):124004, December 2009.

[229] Mark Hannam, Sascha Husa, Denis Pollney, Bernd Brügmann, and Niall Ó Murchadha. Geometry and regularity of moving punctures. *Phys. Rev. Lett.*, 99:241102, Dec 2007.

[230] Mark Hannam, Sascha Husa, Frank Ohme, Bernd Brügmann, and Niall Ó Murchadha. Wormholes and trumpets: Schwarzschild spacetime for the moving-puncture generation. *Phys. Rev. D*, 78:064020, Sep 2008.

[231] Mark Hannam, Sascha Husa, and Niall Ó Murchadha. Bowen-york trumpet data and black-hole simulations. *Phys. Rev. D*, 80:124007, Dec 2009.

[232] Jason D. Immerman and Thomas W. Baumgarte. Trumpet-puncture initial data for black holes. *Phys. Rev. D*, 80:061501(R), 2009.

[233] Steve R. Brandt and Bernd Brügmann. A simple construction of initial data for multiple black holes. *Phys. Rev. Lett.*, 78(19):3606–3609, 1997.

[234] Thomas W. Baumgarte. An alternative approach to solving the Hamiltonian constraint. *Phys.Rev.*, D85:084013, 2012.

[235] A. Arbona, C. Bona, J. Carot, L. Mas, J. Massó, and J. Stela. Stuffed black holes. *Phys. Rev. D*, 57:2397–2402, Feb 1998.

[236] David Brown, Olivier Sarbach, Erik Schnetter, Manuel Tiglio, Peter Diener, Ian Hawke, and Denis Pollney. Excision without excision. *Phys. Rev. D*, 76:081503, Oct 2007.

[237] David Brown, Peter Diener, Olivier Sarbach, Erik Schnetter, and Manuel Tiglio. Turduckening black holes: An analytical and computational study. *Phys. Rev. D*, 79:044023, Feb 2009.

[238] Maurice H. P. M. van Putten. Approximate black holes for numerical relativity. *Phys. Rev. D*, 54:R5931–R5934, Nov 1996.

[239] Pedro Marronetti, Mijan F. Huq, Pablo Laguna, Luis Lehner, Richard A. Matzner, and Deirdre M. Shoemaker. Approximate analytical solutions to the initial data problem of black hole binary systems. *Phys. Rev. D*, 62:024017, 2000.

[240] Frans Pretorius and Matthew W. Choptuik. Adaptive mesh refinement for coupled elliptic-hyperbolic systems. *J.Comput.Phys.*, 218:246–274, 2006.

[241] William H. Press, Saul A. Teukolsky, William T. Vetterling, and Brian P. Flannery. *Numerical Recipes: The Art of Scientific Computing*. Cambridge University Press, 3rd edition, 2007.

[242] Harald P Pfeiffer, Duncan A Brown, Lawrence E Kidder, Lee Lindblom, Geoffrey Lovelace, and Mark A Scheel. Reducing orbital eccentricity in binary black hole simulations. *Classical and Quantum Gravity*, 24(12):S59, 2007.

[243] Sascha Husa, Mark Hannam, José A. González, Ulrich Sperhake, and Bernd Brügmann. Reducing eccentricity in black-hole binary evolutions with initial parameters from post-newtonian inspiral. *Phys. Rev. D*, 77:044037, Feb 2008.

[244] M. A. Scheel, M. Boyle, T. Chu, L. E. Kidder, K. D. Matthews, and H. P. Pfeiffer. High-accuracy waveforms for binary black hole inspiral, merger, and ringdown. *Phys. Rev. D*, 79(2):024003, January 2009.

[245] G. 't Hooft. Graviton dominance in ultra-high-energy scattering. *Physics Letters B*, 198:61–63, November 1987.

[246] T. Banks and W. Fischler. A Model for High Energy Scattering in Quantum Gravity. *ArXiv High Energy Physics - Theory e-prints*, June 1999.

[247] E. Kohlprath and G. Veneziano. Black holes from high-energy beam–beam collisions. *Journal of High Energy Physics*, 6:57, June 2002.

[248] K. S. Thorne. In J. Klauder, editor, *Magic Without Magic: John Archibald Wheeler*, page 231, San Francisco, 1972. Freeman.

[249] (Ed.) de los Heros, C. Proceedings of the First Workshop on Exotic Physics with Neutrino Telescopes, EPNT06. 2007.

[250] Serguei Chatrchyan et al. Search for microscopic black holes in pp collisions at sqrt(s) = 7 TeV. *JHEP*, 1204:061, 2012.

[251] Peter C. Aichelburg and R. U. Sexl. On the gravitational field of a massless particle. *Gen. Rel. Grav.*, 2:303–312, 1971.

[252] A. Rendall. Local and Global Existence Theorems for the Einstein Equations. *Living Reviews in Relativity*, 5:6, September 2002.

[253] Harald P. Pfeiffer and James W. York. Extrinsic curvature and the einstein constraints. *Phys. Rev. D*, 67:044022, Feb 2003.

[254] H. P. Pfeiffer and J. W. York. Uniqueness and Nonuniqueness in the Einstein Constraints. *Physical Review Letters, vol. 95, Issue 9, id. 091101*, 95(9):091101, August 2005.

[255] N. Dalal, D. E. Holz, S. A. Hughes, and B. Jain. Short GRB and binary black hole standard sirens as a probe of dark energy. *Phys. Rev. D*, 74(6):063006, 2006.

[256] W. H. Press and S. A. Teukolsky. On formation of close binaries by two-body tidal capture. *Astrophys. J.*, 213:183–192, April 1977.

[257] P. C. Peters and J. Mathews. Gravitational radiation from point masses in a Keplerian orbit. *Phys. Rev.*, 131:435–440, 1963.

[258] C. Hopman and T. Alexander. The Effect of Mass Segregation on Gravitational Wave Sources near Massive Black Holes. *Astrophys. J. Lett.*, 645:L133–L136, July 2006.

[259] Ryan M. O'Leary, Bence Kocsis, and Abraham Loeb. Gravitational waves from scattering of stellar-mass black holes in galactic nuclei. *Mon. Not. R. Astron. Soc.*, 395:2127–2146, 2009.

[260] B. Kocsis and J. Levin. Repeated bursts from relativistic scattering of compact objects in galactic nuclei. *Phys. Rev. D*, 85(12):123005, June 2012.

[261] Uri Keshet, Clovis Hopman, and Tal Alexander. Analytic study of mass segregation around a massive black hole. *Astrophys. J. Lett.*, 698(1):L64, 2009.

[262] A. C. Fabian, J. E. Pringle, and M. J. Rees. Tidal capture formation of binary systems and X-ray sources in globular clusters. *Mon. Not. R. Astron. Soc.*, 172:15P–+, August 1975.

[263] D. Pooley, W. H. G. Lewin, S. F. Anderson, H. Baumgardt, A. V. Filippenko, B. M. Gaensler, L. Homer, P. Hut, V. M. Kaspi, J. Makino, B. Margon, S. McMillan, S. Portegies Zwart, M. van der Klis, and F. Verbunt. Dynamical Formation of Close Binary Systems in Globular Clusters. *Astrophys. J. Lett.*, 591:L131–L134, July 2003.

[264] W. H. Lee, E. Ramirez-Ruiz, and G. van de Ven. Short Gamma-ray Bursts from Dynamically Assembled Compact Binaries in Globular Clusters: Pathways, Rates, Hydrodynamics, and Cosmological Setting. *Astrophys. J.*, 720:953–975, September 2010.

[265] S. R. Kulkarni, P. Hut, and S. McMillan. Stellar black holes in globular clusters. *Nature*, 364:421–423, July 1993.

[266] S. Sigurdsson and L. Hernquist. Primordial black holes in globular clusters. *Nature*, 364:423–425, July 1993.

[267] Simon F. Portegies Zwart and Stephen L. W. McMillan. Black hole mergers in the universe. *Astrophys. J. Lett.*, 528(1):L17, 2000.

[268] R. M. O'Leary, F. A. Rasio, J. M. Fregeau, N. Ivanova, and R. O'Shaughnessy. Binary Mergers and Growth of Black Holes in Dense Star Clusters. *Astrophys. J.*, 637:937–951, February 2006.

[269] Sverre Aarseth. Mergers and ejections of black holes in globular clusters. 2012.

[270] B. W. Murphy, H. N. Cohn, and P. M. Lugger. Fokker-Planck Models for M15 Without a Central Black Hole: The Role of the Mass Function. *Astrophys. J.*, 732:67, May 2011.

[271] J. D. Dull, H. N. Cohn, P. M. Lugger, B. W. Murphy, P. O. Seitzer, P. J. Callanan, R. G. M. Rutten, and P. A. Charles. The Dynamics of M15: Observations of the Velocity Dispersion Profile and Fokker-Planck Models. *Astrophys. J.*, 481:267–+, May 1997.

[272] E. Pfahl, S. Rappaport, and P. Podsiadlowski. A Comprehensive Study of Neutron Star Retention in Globular Clusters. *Astrophys. J.*, 573:283–305, July 2002.

[273] J. Grindlay, S. Portegies Zwart, and S. McMillan. Short gamma-ray bursts from binary neutron star mergers in globular clusters. *Nature Physics*, 2:116–119, February 2006.

[274] D. Clausen, S. Sigurdsson, and D. F. Chernoff. Black hole-neutron star mergers in globular clusters. *Mon. Not. Roy. Astron. Soc.*, 428:3618–3629, February 2013.

[275] Linqing Wen. On the Eccentricity Distribution of Coalescing Black Hole Binaries Driven by the Kozai Mechanism in Globular Clusters. *Astrophys. J.*, 598:419–430, 2003.

[276] M. Coleman Miller and Douglas P. Hamilton. Four-body effects in globular cluster black hole coalescence. *Astrophys. J.*, 576(2):894, 2002.

[277] Fabio Antonini and Hagai B. Perets. Secular evolution of compact binaries near massive black holes: Gravitational wave sources and other exotica. *Astrophys. J.*, 757(1):27, 2012.

[278] Todd A. Thompson. Accelerating Compact Object Mergers in Triple Systems with the Kozai Resonance: A Mechanism for 'Prompt" Type Ia Supernovae, Gamma-Ray Bursts, and Other Exotica. *Astrophys.J.*, 741:82, 2011.

[279] S. Naoz, B. Kocsis, A. Loeb, and N. Yunes. Resonant Post-Newtonian Eccentricity Excitation in Hierarchical Three-body Systems. *ArXiv e-prints*, June 2012.

[280] B. Katz and S. Dong. The rate of WD-WD head-on collisions may be as high as the SNe Ia rate. *ArXiv e-prints*, November 2012.

[281] K. Belczynski, M. Dominik, T. Bulik, R. O'Shaughnessy, C. Fryer, and D. E. Holz. The Effect of Metallicity on the Detection Prospects for Gravitational Waves. *Astrophys. J. Lett.*, 715:L138–L141, June 2010.

[282] E. Berger. A Short Gamma-ray Burst "No-host" Problem? Investigating Large Progenitor Offsets for Short GRBs with Optical Afterglows. *Astrophys. J.*, 722:1946–1961, October 2010.

[283] R. P. Church, A. J. Levan, M. B. Davies, and N. Tanvir. Implications for the origin of short gamma-ray bursts from their observed positions around their host galaxies. *Mon. Not. Roy. Astron. Soc.*, pages 355–+, March 2011.

[284] J. D. M. Dewi, P. Podsiadlowski, and O. R. Pols. The spin period-eccentricity relation of double neutron stars: evidence for weak supernova kicks? *Mon. Not. Roy. Astron. Soc.*, 363:L71–L75, October 2005.

[285] J. P. Norris, N. Gehrels, and J. D. Scargle. Heterogeneity in Short Gamma-Ray Bursts. *Astrophys. J.*, 735:23, July 2011.

[286] W. F. Domainko. Finding short GRB remnants in globular clusters: the VHE gamma-ray source in Terzan 5. *Astron. and Astrophys.*, 533:L5, September 2011.

[287] B. D. Metzger, G. Martínez-Pinedo, S. Darbha, E. Quataert, A. Arcones, D. Kasen, R. Thomas, P. Nugent, I. V. Panov, and N. T. Zinner. Electromagnetic counterparts of compact object mergers powered by the radioactive decay of r-process nuclei. *Mon. Not. Roy. Astron. Soc.*, 406:2650–2662, August 2010.

[288] Charles F. Gammie, Stuart L. Shapiro, and Jonathan C. McKinney. Black Hole Spin Evolution. *Astrophys. J.*, 602:312–319, 2004.

[289] J. M. Miller, M. C. Miller, and C. S. Reynolds. The Angular Momenta of Neutron Stars and Black Holes as a Window on Supernovae. *ArXiv e-prints*, 2011.

[290] Z. B. Etienne, Y. T. Liu, S. L. Shapiro, and T. W. Baumgarte. General relativistic simulations of black-hole-neutron-star mergers: Effects of black-hole spin. *Phys. Rev. D*, 79(4):044024, 2009.

[291] Francois Foucart, Matthew D. Duez, Lawrence E. Kidder, , and Saul A. Teukolsky. Black hole-neutron star mergers: Effects of the orientation of the black hole spin. *Phys. Rev. D*, 83:024005, 2011.

[292] Koutarou Kyutoku, Hirotada Okawa, Masaru Shibata, and Keisuke Taniguchi. Gravitational waves from spinning black hole-neutron star binaries: dependence on black hole spins and on neutron star equations of state. *Phys. Rev.*, D84:064018, 2011.

[293] M. Shibata and K. Uryū. Merger of black hole-neutron star binaries: Nonspinning black hole case. *Phys. Rev. D*, 74(12):121503, 2006.

[294] K. Kyutoku, M. Shibata, and K. Taniguchi. Gravitational waves from nonspinning black hole-neutron star binaries: Dependence on equations of state. *Phys. Rev. D*, 82(4):044049–+, August 2010.

[295] Z. B. Etienne, Y. T. Liu, V. Paschalidis, and S. L. Shapiro. General relativistic simulations of black hole-neutron star mergers: Effects of magnetic fields. *ArXiv e-prints*, December 2011.

[296] F. Foucart, M. D. Duez, L. E. Kidder, M. A. Scheel, B. Szilagyi, and S. A. Teukolsky. Black hole-neutron star mergers for 10 solar mass black holes. *ArXiv e-prints*, November 2011.

[297] F. Löffler, L. Rezzolla, and M. Ansorg. Numerical evolutions of a black hole-neutron star system in full general relativity: Head-on collision. *Phys. Rev. D*, 74(10):104018, 2006.

[298] Lee Lindblom and Bela Szilagyi. An Improved Gauge Driver for the GH Einstein System. *Phys. Rev.*, D80:084019, 2009.

[299] R. M. O'Leary, B. Kocsis, and A. Loeb. Gravitational waves from scattering of stellar-mass black holes in galactic nuclei. *Mon. Not. Roy. Astron. Soc.*, 395:2127–2146, June 2009.

[300] G. D. Quinlan and S. L. Shapiro. The collapse of dense star clusters to supermassive black holes - Binaries and gravitational radiation. *Astrophys. J.*, 321:199–210, October 1987.

[301] James M. Lattimer and M. Prakash. What a Two Solar Mass Neutron Star Really Means. *ArXiv e-prints*, 2010.

[302] Feryal Ozel, Dimitrios Psaltis, Ramesh Narayan, and Jeffrey E. McClintock. The Black Hole Mass Distribution in the Galaxy. *ArXiv e-prints*, 2010.

[303] M. Turner. Gravitational radiation from point-masses in unbound orbits - Newtonian results. *Astrophys. J.*, 216:610–619, 1977.

[304] Paul Demorest, Tim Pennucci, Scott Ransom, Mallory Roberts, and Jason Hessels. Shapiro delay measurement of a two solar mass neutron star. *Nature*, 467:1081–1083, 2010.

[305] Kostas Glampedakis and Daniel Kennefick. Zoom and whirl: Eccentric equatorial orbits around spinning black holes and their evolution under gravitational radiation reaction. *Phys. Rev. D*, 66:044002, 2002.

[306] W. Kastaun, B. Willburger, and K. D. Kokkotas. Saturation amplitude of the f-mode instability. *Phys. Rev. D*, 82(10):104036, November 2010.

[307] K.D. Kokkotas, T.A. Apostolatos, and N. Andersson. The Inverse problem for pulsating neutron stars: A 'Fingerprint analysis' for the supranuclear equation of state. *Mon.Not.Roy.Astron.Soc.*, 320:307–315, 2001.

[308] Christopher P. L. Berry and Jonathan R. Gair. Gravitational wave energy spectrum of a parabolic encounter. *Phys. Rev.*, D82:107501, 2010.

[309] Neil J. Cornish and Janna J. Levin. Lyapunov timescales and black hole binaries. *Class.Quant.Grav.*, 20:1649–1660, 2003.

[310] L. F. Roberts, D. Kasen, W. H. Lee, and E. Ramirez-Ruiz. Electromagnetic transients powered by nuclear decay in the tidal tails of coalescing compact binaries. *The Astrophysical Journal Letters*, 736(1):L21, 2011.

[311] T. Piran, E. Nakar, and S. Rosswog. The Electromagnetic Signals of Compact Binary Mergers. *ArXiv e-prints*, April 2012.

[312] S. Rosswog, T. Piran, and E. Nakar. The multi-messenger picture of compact object encounters: binary mergers versus dynamical collisions. *ArXiv e-prints*, April 2012.

[313] T. Fischer, S. C. Whitehouse, A. Mezzacappa, F.-K. Thielemann, and M. Liebendörfer. Protoneutron star evolution and the neutrino-driven wind in general relativistic neutrino radiation hydrodynamics simulations. *A&A*, 517:A80, 2010.

[314] A. Arcones and H.-Th. Janka. Nucleosynthesis-relevant conditions in neutrino-driven supernova outflows. *A&A*, 526:A160, 2011.

[315] C. J. Horowitz and Kai Kadau. Breaking strain of neutron star crust and gravitational waves. *Phys. Rev. Lett.*, 102:191102, May 2009.

[316] D. J. Price and S. Rosswog. Producing ultrastrong magnetic fields in neutron star mergers. *Science*, 312(5774):719–722, 2006.

[317] Bruno Giacomazzo, Luciano Rezzolla, and Luca Baiotti. Accurate evolutions of inspiralling and magnetized neutron stars: Equal-mass binaries. *Phys. Rev. D*, 83:044014, Feb 2011.

[318] M. Anderson, E. W. Hirschmann, L. Lehner, S. L. Liebling, P. M. Motl, D. Neilsen, C. Palenzuela, and J. E. Tohline. Magnetized Neutron-Star Mergers and Gravitational-Wave Signals. *Phys. Rev. Lett.*, 100(19):191101, 2008.

[319] Steven A. Balbus and John F. Hawley. Instability, turbulence, and enhanced transport in accretion disks. *Rev. Mod. Phys.*, 70:1–53, Jan 1998.

[320] S. R. Kulkarni. Modeling Supernova-like Explosions Associated with Gamma-ray Bursts with Short Durations. *ArXiv Astrophysics e-prints*, October 2005.

[321] D. Kasen. Radioactively powered transients from compact object mergers. In *work presented at KITP 'Rattle and Shine' conference*, 2012.

[322] C. Thompson and R. C. Duncan. The soft gamma repeaters as very strongly magnetized neutron stars - I. Radiative mechanism for outbursts. *Mon. Not. Roy. Astron. Soc.*, 275:255–300, July 1995.

[323] E. Troja, S. Rosswog, and N. Gehrels. Precursors of short gamma-ray bursts. *Astrophys. J.*, 723(2):1711, 2010.

[324] Masatake Ohashi. Gravitational wave detection in Japan. *Prog.Theor.Phys.Suppl.*, 190:335–338, 2011.

[325] P. C. Peters. Gravitational radiation and the motion of two point masses. *Phys. Rev.*, 136:B1224–B1232, 1964.

[326] J. Abadie et al. Search for Gravitational Waves from Low Mass Compact Binary Coalescence in LIGO's Sixth Science Run and Virgo's Science Runs 2 and 3. *Phys.Rev.*, D85:082002, 2012.

[327] E.A. Huerta and Duncan A. Brown. Effect of eccentricity on binary neutron star searches in Advanced LIGO. 2013.

[328] Bence Kocsis, Merse E. Gaspar, and Szabolcs Marka. Detection rate estimates of gravity waves emitted during parabolic encounters of stellar black holes in globular clusters. *Astrophys. J.*, 648(1):411, 2006.

[329] Roman Gold and Bernd Brügmann. Radiation from low-momentum zoom-whirl orbits. *Class. Quantum Grav.*, 27:084035, 2010.

[330] John G. Baker, William D. Boggs, Joan M. Centrella, Bernard J. Kelly, Sean T. McWilliams, and James R. van Meter. Mergers of non-spinning black-hole binaries: Gravitational radiation characteristics. *Phys. Rev. D*, 78:044046, 2008.

[331] Bernard J. Kelly, John G. Baker, William D. Boggs, Sean T. McWilliams, and Joan M. Centrella. Mergers of black-hole binaries with aligned spins: Waveform characteristics. *Phys. Rev. D*, 84:084009, 2011.

[332] Kostas Glampedakis, Scott A. Hughes, and Daniel Kennefick. Approximating the inspiral of test bodies into Kerr black holes. *Phys.Rev.*, D66:064005, 2002.

[333] Stanislav Babak, Hua Fang, Jonathan R. Gair, Kostas Glampedakis, and Scott A. Hughes. 'Kludge' gravitational waveforms for a test-body orbiting a Kerr black hole. *Phys.Rev.*, D75:024005, 2007.

[334] Nicolas Yunes, Carlos F. Sopuerta, Louis J. Rubbo, and Kelly Holley-Bockelmann. Relativistic Effects in Extreme Mass Ratio Gravitational Wave Bursts. *Astrophys.J.*, 675:604–613, 2008.

[335] Carlos F. Sopuerta and Nicolas Yunes. New Kludge Scheme for the Construction of Approximate Waveforms for Extreme-Mass-Ratio Inspirals. *Phys.Rev.*, D84:124060, 2011.

[336] R. Ruffini and M. Sasaki. On a Semi-Relativistic Treatment of the Gravitational Radiation from a Mass Thrusted into a Black Hole. *Progress of Theoretical Physics*, 66:1627–1638, November 1981.

[337] Donato Bini and Thibault Damour. Gravitational radiation reaction along general orbits in the effective one-body formalism. 2012.

[338] P. Kalmus, K. C. Cannon, S. Márka, and B. J. Owen. Stacking gravitational wave signals from soft gamma repeater bursts. *Phys. Rev. D*, 80(4):042001, 2009.

[339] K. Hurley, A. Rowlinson, E. Bellm, D. Perley, I. G. Mitrofanov, D. V. Golovin, A. S. Kozyrev, M. L. Litvak, A. B. Sanin, W. Boynton, C. Fellows, K. Harshmann, M. Ohno, K. Yamaoka, Y. E. Nakagawa, D. M. Smith, T. Cline, N. R. Tanvir, P. T. O'Brien, K. Wiersema, E. Rol, A. Levan, J. Rhoads, A. Fruchter, D. Bersier, J. J. Kavelaars, N. Gehrels, H. Krimm, D. M. Palmer, R. C. Duncan, C. Wigger, W. Hajdas, J.-L. Atteia, G. Ricker, R. Vanderspek, A. Rau, and A. von Kienlin. A new analysis of the short-duration, hard-spectrum grb 051103, a possible extragalactic soft gamma repeater giant flare. *Mon. Not. R. Astron. Soc.*, 403:342–352, 2010.

[340] B. P. Abbott, R. Abbott, F. Acernese, R. Adhikari, P. Ajith, B. Allen, G. Allen, M. Alshourbagy, R. S. Amin, S. B. Anderson, and et al. Search For Gravitational-wave Bursts Associated with Gamma-ray Bursts using Data from LIGO Science Run 5 and Virgo Science Run 1. *Astrophys. J.*, 715:1438–1452, 2010.

[341] J. Abadie, B. P. Abbott, R. Abbott, T. Accadia, F. Acernese, R. Adhikari, P. Ajith, B. Allen, G. Allen, E. Amador Ceron, and et al. Search for Gravitational-wave Inspiral Signals Associated with Short Gamma-ray Bursts During LIGO's Fifth and Virgo's First Science Run. *Astrophys. J.*, 715:1453–1461, 2010.

[342] Alessandra Buonanno and Thibault Damour. Effective one-body approach to general relativistic two-body dynamics. *Phys. Rev. D*, 59:084006, 1999.

[343] J. N. Goldberg, A. J. MacFarlane, Ezra T. Newman, F. Rohrlich, and E. C. G. Sudarshan. Spin-s spherical harmonics and edth. *J. Math. Phys.*, 8:2155–2161, 1967.

[344] Thibault Damour, Bala R. Iyer, and Bangalore S. Sathyaprakash. Improved filters for gravitational waves from inspiralling compact binaries. *Phys. Rev. D*, 57:885–907, 1998.

[345] Janna Levin, Sean T McWilliams, and Hugo Contreras. Inspiral of generic black hole binaries: spin, precession and eccentricity. *Class. Quantum Grav.*, 28(17):175001, 2011.

[346] Kip S. Thorne. *in 300 Years of Gravitation.* Cambridge University Press, Cambridge, 1987.

[347] Thibault Damour, Bala R. Iyer, and Bangalore S. Sathyaprakash. Frequency-domain P-approximant filters for time-truncated inspiral gravitational wave signals from compact binaries. *Phys. Rev. D*, 62:084036, 2000.

[348] E. P. Mazets, R. L. Aptekar, T. L. Cline, D. D. Frederiks, J. O. Goldsten, S. V. Golenetskii, K. Hurley, A. von Kienlin, and V. D. Pal'shin. A giant flare from a soft gamma repeater in the andromeda galaxy (m31). *Astrophys. J.*, 680:545, 2008.

[349] Sean T. McWilliams, Bernard J. Kelly, and John G. Baker. Observing mergers of nonspinning black-hole binaries. *Phys. Rev. D*, 82:024014, 2010.

[350] Carlos O. Lousto and Yosef Zlochower. Orbital evolution of extreme-mass-ratio black-hole binaries with numerical relativity. *Phys. Rev. Lett.*, 106:041101, 2011.

[351] Ulrich Sperhake, Vitor Cardoso, Christian D. Ott, Erik Schnetter, and Helvi Witek. Collisions of unequal mass black holes and the point particle limit. *Phys. Rev. D*, 84:084038, 2011.

[352] Vasileios Paschalidis, Morgan MacLeod, Thomas W. Baumgarte, and Stuart L. Shapiro. Merger of white dwarf-neutron star binaries: Prelude to hydrodynamic simulations in general relativity. *Phys.Rev.*, D80:024006, 2009.

[353] Vasileios Paschalidis, Yuk Tung Liu, Zachariah Etienne, and Stuart L. Shapiro. The merger of binary white dwarf–neutron stars: Simulations in full general relativity. *Phys.Rev.*, D84:104032, 2011.

[354] Nicholas Stone and Abraham Loeb. Observing Lense-Thirring Precession in Tidal Disruption Flares. *Phys.Rev.Lett.*, 108:061302, 2012.

[355] Michael Kesden. Black-Hole Spin Dependence in the Light Curves of Tidal Disruption Events. *Phys.Rev.*, D86:064026, 2012.

[356] B. Carter and J.-P. Luminet. Tidal compression of a star by a large black hole. I Mechanical evolution and nuclear energy release by proton capture. *Astron. and Astrophys.*, 121:97–113, May 1983.

[357] E. S. Phinney. Manifestations of a Massive Black Hole in the Galactic Center. In M. Morris, editor, *The Center of the Galaxy*, volume 136 of *IAU Symposium*, page 543, 1989.

[358] P. Diener, A. G. Kosovichev, E. V. Kotok, I. D. Novikov, and C. J. Pethick. Non-linear effects at tidal capture of stars by a massive black hole - II. Compressible affine models and tidal interaction after capture. *Mon. Not. Roy. Astron. Soc.*, 275:498–506, July 1995.

[359] A. Ulmer. Flares from the Tidal Disruption of Stars by Massive Black Holes. *Astrophys. J.*, 514:180–187, March 1999.

[360] L. E. Strubbe and E. Quataert. Optical flares from the tidal disruption of stars by massive black holes. *Mon. Not. Roy. Astron. Soc.*, 400:2070–2084, December 2009.

[361] J.-P. Luminet and J.-A. Marck. Tidal squeezing of stars by Schwarzschild black holes. *Mon. Not. Roy. Astron. Soc.*, 212:57–75, January 1985.

[362] M. Brassart and J.-P. Luminet. Relativistic tidal compressions of a star by a massive black hole. *Astron. and Astrophys.*, 511:A80, February 2010.

[363] Nicholas Stone, Re'em Sari, and Abraham Loeb. Consequences of Strong Compression in Tidal Disruption Events. 2012.

[364] R. A. Nolthenius and J. I. Katz. The passage of a star by a massive black hole. *Astrophys. J.*, 263:377–385, December 1982.

[365] M. MacLeod, J. Guillochon, and E. Ramirez-Ruiz. The Tidal Disruption of Giant Stars and their Contribution to the Flaring Supermassive Black Hole Population. *Astrophys. J.*, 757:134, October 2012.

[366] J. Guillochon and E. Ramirez-Ruiz. Hydrodynamical Simulations to Determine the Feeding Rate of Black Holes by the Tidal Disruption of Stars: The Importance of the Impact Parameter and Stellar Structure. *ArXiv e-prints*, June 2012.

[367] C. R. Evans and C. S. Kochanek. The tidal disruption of a star by a massive black hole. *Astrophys. J. Lett.*, 346:L13–L16, November 1989.

[368] P. Diener, V. P. Frolov, A. M. Khokhlov, I. D. Novikov, and C. J. Pethick. Relativistic Tidal Interaction of Stars with a Rotating Black Hole. *Astrophys. J.*, 479:164, April 1997.

[369] Kimitake Hayasaki, Nicholas Stone, and Abraham Loeb. Finite, Intense Accretion Bursts from Tidal Disruption of Stars on Bound Orbits. 2012.

[370] Kimitake Hayasaki, Nicholas Stone, and Abraham Loeb. Tidal disruption flares from stars on eccentric orbits. 2012.

[371] P. Laguna, W. A. Miller, W. H. Zurek, and M. B. Davies. Tidal disruptions by supermassive black holes - Hydrodynamic evolution of stars on a Schwarzschild background. *Astrophys. J. Lett.*, 410:L83–L86, June 1993.

[372] T. Bogdanović, M. Eracleous, S. Mahadevan, S. Sigurdsson, and P. Laguna. Tidal Disruption of a Star by a Black Hole: Observational Signature. *Astrophys. J.*, 610:707–721, August 2004.

[373] Miguel Alcubierre, Bernd Brügmann, Peter Diener, Michael Koppitz, Denis Pollney, Edward Seidel, and Ryoji Takahashi. Gauge conditions for long-term numerical black hole evolutions without excision. *Phys. Rev. D*, 67:084023, 2003.

[374] M. Davis, Remo Ruffini, William H. Press, and Richard H. Price. Gravitational Radiation from a Particle Falling Radially into a Schwarzschild Black Hole. *Phys. Rev. Lett.*, 27:1466–1469, 1971.

[375] R. Penrose. *unpublished*, 1971.

[376] P. D. D'Eath. High Speed Black Hole Encounters and Gravitational Radiation. *Phys. Rev.*, D18:990, 1978.

[377] P. D. D'Eath and P. N. Payne. Gravitational radiation in black-hole collisions at the speed of light. iii. results and conclusions. *Phys. Rev. D*, 46:694–701, Jul 1992.

[378] Douglas M. Eardley and Steven B. Giddings. Classical black hole production in high-energy collisions. *Phys. Rev. D*, 66:044011, 2002.

[379] Ulrich Sperhake, Vitor Cardoso, Frans Pretorius, Emanuele Berti, Tanja Hinderer, et al. Cross section, final spin and zoom-whirl behavior in high-energy black hole collisions. *Phys.Rev.Lett.*, 103:131102, 2009.

[380] Luciano Rezzolla and Kentaro Takami. Black-hole production from ultrarelativistic collisions. *Class. Quant. Grav.*, 30:012001, 2013.

[381] Nemanja Kaloper and John Terning. How black holes form in high energy collisions. *Int. J. Mod. Phys.*, D17:665–672, 2008.

[382] Emanuele Berti, Vitor Cardoso, Tanja Hinderer, Madalena Lemos, Frans Pretorius, Ulrich Sperhake, and Nicolás Yunes. Semianalytical estimates of scattering thresholds and gravitational radiation in ultrarelativistic black hole encounters. *Phys. Rev. D*, 81:104048, May 2010.

[383] D. Amati, M. Ciafaloni, and G. Veneziano. Towards an S-matrix description of gravitational collapse. *JHEP*, 0802:049, 2008.

[384] G. Veneziano and J. Wosiek. Exploring an S-matrix for gravitational collapse. *JHEP*, 0809:023, 2008.

[385] Giuseppe Marchesini and Enrico Onofri. High energy gravitational scattering: A Numerical study. *JHEP*, 0806:104, 2008.

[386] M. W. Choptuik. Universality and scaling in gravitational collapse of a massless scalar field. *Phys. Rev. Lett.*, 70:9, 1993.

[387] S. Chawla, M. Anderson, M. Besselman, L. Lehner, S. L. Liebling, P. M. Motl, and D. Neilsen. Mergers of Magnetized Neutron Stars with Spinning Black Holes: Disruption, Accretion and Fallback. *ArXiv e-prints*, 2010.

[388] Carlos Palenzuela, Luis Lehner, Marcelo Ponce, Steven L. Liebling, Matthew Anderson, et al. Gravitational and electromagnetic outputs from binary neutron star mergers. 2013.

[389] Carlos Palenzuela. Modeling magnetized neutron stars using resistive MHD. *Mon. Not. R. Aston. Soc.*, 431:, 1853–1865 (2013), 2.

[390] A. Dedner, F. Kemm, D. Kröner, C.-D. Munz, T. Schnitzer, and M. Wesenberg. Hyperbolic divergence cleaning for the MHD equations. *Journal of Computational Physics*, 175(2):645 – 673, 2002.